

A STUDY OF THE HEAT TRANSFER IN HYDROGEN FUELED
INTERNAL COMBUSTION ENGINE

The logo of the University of Malaysia Pahang (UMP) is a large, stylized shield shape. It is divided into four quadrants: top-left is light blue, top-right is light purple, bottom-left is light blue, and bottom-right is light purple. In the center is a white diamond shape. Above the diamond is a yellow diamond. A green and blue swoosh curves around the top of the shield.

KHALAF IBRAHIM HAMADA

Thesis submitted in fulfilment of the requirements for the award of the degree of Doctor
of Philosophy (Automotive Engineering)

UMP
Faculty of Mechanical Engineering
UNIVERSITI MALAYSIA PAHANG

JANUARY 2012

SUPERVISORS' DECLARATION

We hereby declare that we have checked this thesis and in our opinion, this thesis is adequate in terms of scope and quality for the award of the degree of Doctor of Philosophy (Automotive Engineering).

Signature

Name of Supervisor: DR. MD. MUSTAFIZUR RAHMAN

Position: ASSOCIATE PROFESSOR

Date:

Signature

Name of Field-supervisor: DR. ABD RASHID BIN ABD AZIZ

Position: ASSOCIATE PROFESSOR – UNIVERSITI TEKNOLOGI PETRONAS

Date:

UMP

STUDENT'S DECLARATION

I hereby declare that the work in this thesis is my own except for quotations and summaries which have been duly acknowledged. The thesis has not been accepted for any degree and is not concurrently submitted for award of other degree.

Signature

Name:

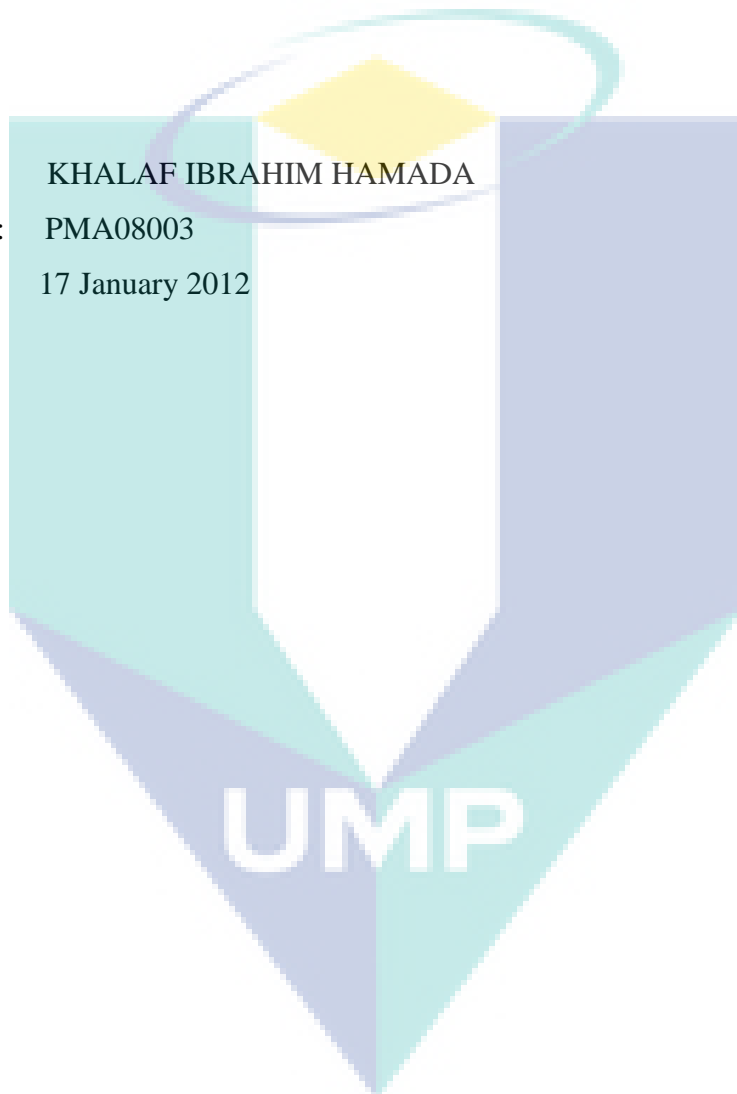
KHALAF IBRAHIM HAMADA

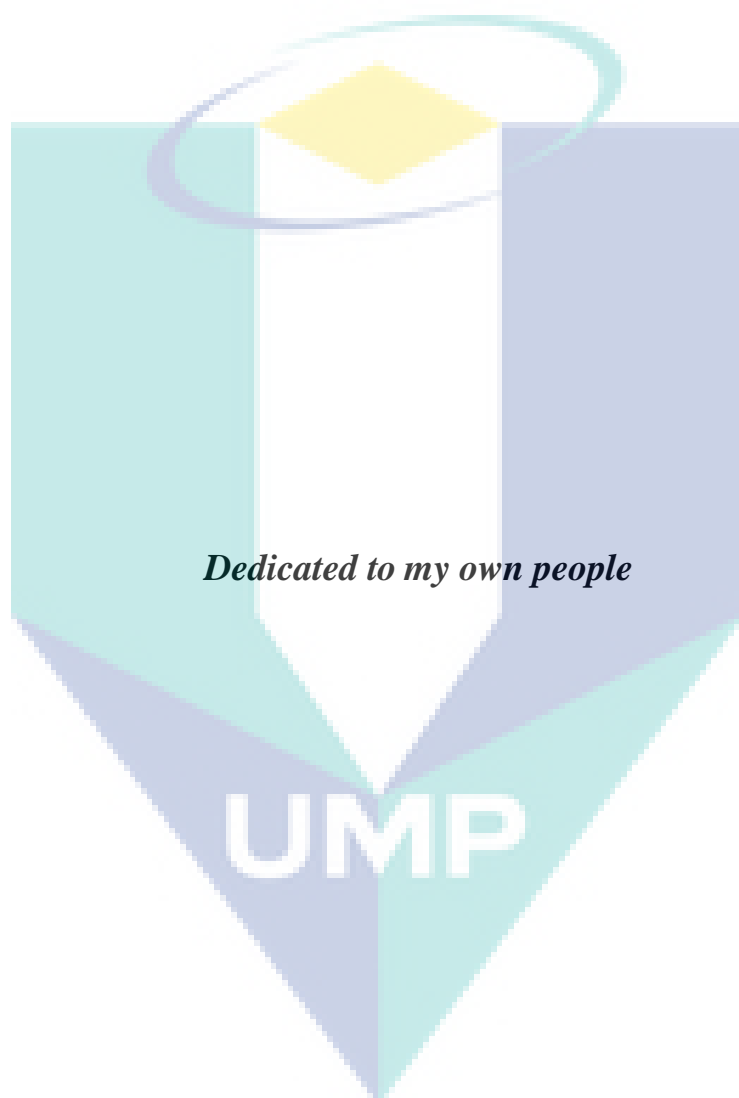
ID Number:

PMA08003

Date:

17 January 2012





ACKNOWLEDGEMENTS

In the name of Allah, the Most Gracious, the Most Merciful. Praise be to Allah, the Lord of the Worlds; peace and blessings of Allah be upon the noblest of the Prophets and Messengers, our Prophet Mohammed and upon his family, companions and who follows him until the last day. I am truly and deeply indebted to so many people that there is no way to acknowledge them all or even any of them properly. Thus, I offer my sincerest apologies to anyone I ungratefully omitted from explicit mention.

First of all, I wish to express my deep sense of gratitude and indebtedness to my Supervisors Associate Professor Dr. Md. Mustafizur Rahman and Associate Professor Dr. Abd Rashid Abd Aziz, who have been a constant source of inspiration and guidance to me throughout my doctoral study. I wish to thank them for their valuable time and resources, to make this thesis a success. I wish to express my warm and sincere thanks to my close friend Dr. Mohammed Kamil for guiding me to study in Malaysia. His perpetual energy and enthusiasm in research had motivated me to complete my Ph.D. Special thanks to Dr. Medhat Elkelawy for his consultancy regarding the manipulating of KIVA code.

I would like to express my sincere gratitude to Universiti Malaysia Pahang (UMP) for granting me a doctoral scholarship, without their support, my ambition to study abroad can hardly be realized. I want to thank all the people at UMP. It was a wonderful place to work, and they are very dedicated people. I gained so much from it. Furthermore, special thanks to the academic, management and technical staff in Faculty of Mechanical Engineering and the staff of Center of Graduate Studies (CGS) in UMP. I wish to thank everyone who has helped me throughout my attachment period at Universiti Teknologi PETRONAS, especially the staff in Centre of Automotive Research. I thank all my friends and colleagues for every bit of support; I thank to all Malaysian people whom I met, for their openness, friendship and hospitality.

I express my indebtedness to Iraqi Ministry of Higher Education and Scientific Research and University of Tikrit for giving me the permission for this study. Many special thanks go to Asst. Prof. Dr. Farouq Al-Salmani and Dr. Hazim Khalil for their help and support. Words are not enough to show my gratitude to you, except almighty Allah should assist me in rewarding you abundantly; I say Jazakumullahukhaeran for both of you.

At last and most importantly, I would like to thank my parents, wife and all family members for their open-mindedness and endless support. They are always close to my heart. Without the help and support of all these people, this thesis would not be completed.

ABSTRACT

Heat transfer in the internal-combustion engine is a crucial phenomenon because of it affects the engine performance, efficiency and emissions. The aim of this thesis is to characterize the time-averaged heat-transfer and instantaneous heat-transfer of the direct-injection hydrogen-fueled engine. A one-dimensional model was developed based on the gas dynamic and heat-transfer concepts for characterizing the time-averaged heat-transfer. This model was developed using the real engine specifications with the capabilities of GT-POWER software. The dimensionless analysis for TAHT was performed based on the output results from one-dimensional model. The multidimensional model based on the finite volume approach for characterizing the instantaneous heat-transfer. The structural three-dimensional model was constructed and then discretized using the structured hexahedron mesh. The governing equations for reactive flow with the accompanied physical phenomena were solved numerically. A novel subroutine was integrated to simulate the hydrogen-injection process. Simplified single-step mechanism was considered for estimating the reaction rate of hydrogen oxidation. The modified wall-function was used for resolving the near wall transport. Arbitrary Lagrangian-Eulerian algorithm was adopted for solving the governing equations. Whereas the sub-models were solved utilizing the operator splitting approach, then it was incorporated with the main program. The influences of the engine speed, equivalence ratio and start of injection timing were investigated. Experimental study shows that the time-averaged heat-transfer and instantaneous heat-transfer models are adequately accurate. The equivalence ratio and engine speed were observed to have significant impacts on characteristics of the time-averaged heat-transfer as well as instantaneous heat transfer. It was demonstrated that ignoring the impact of the equivalence ratio on the time-averaged heat-transfer is unjustifiable, especially on the heat-transfer correlation. Accordingly, the equivalence ratio was established in a new correlation form of the time-averaged heat-transfer. The reliability of the newly developed correlation was verified using the Taylor's correlation. The relative error was reduced from 70 % to around 10 %. Thermal field analysis was used for demonstrating the trends of the instantaneous heat transfer. It was observed that there is a crucial distinction between the lean and ultra-lean mixture as well as the engine speed. Furthermore, a non-uniform behavior was found for the impact of the equivalence ratio on the temperature distributions. Moreover, the heat release rate, instantaneous rate of heat loss, cumulative heat loss and heat transfer coefficient were used for monitoring the behaviour of the instantaneous heat transfer. The instantaneous heat transfer parameters were increased around 35% when increasing the equivalence ratio within the range of the finest operation while these parameters are acquired within 10% increase for the entire engine speed range. It can be comprehended that the developed models are powerful tools for estimating the heat transfer of hydrogen-fueled engine. The developed predictive correlation is highly recommended for predicting the heat transfer of hydrogen-fueled engine.

ABSTRAK

Pemindahan haba di dalam enjin pembakaran dalam adalah suatu fenomena penting kerana ia mempengaruhi prestasi, kecekapan, dan emisi enjin. Tesis ini bertujuan untuk menentukan ciri pemindahan haba berpurata masa dan juga pemindahan haba seketika bagi enjin suntikan terus berbahan api hidrogen. Sebuah model satu dimensi telah dibangunkan berasaskan dinamik gas dan konsep pemindahan haba bagi mencirikan pemindahan haba berpurata masa manakala model berbilang dimensi pula telah dibangunkan berasaskan kaedah isipadu sehingga bagi mencirikan pemindahan haba seketika. Model berstruktur tiga dimensi telah dibangunkan dan dibahagikan kepada isipadu kecil dengan menggunakan elemen struktur heksahedron. Persamaan menakluk untuk medan aliran bertindakbalas **beserta model fenomena fizikal** telah diselesaikan dengan menggunakan kaedah berangka. **Sebuah sub-atucara asli** telah disepadukan bagi mensimulasi proses suntikan hydrogen. **Persamaan fungsi dinding** yang telah diubahsuai telah digunakan untuk menyelesaikan aliran berhampiran dinding. Kesan kelajuan enjin, nisbah kesetaraan dan permulaan pemaasan suntikan telah dikaji. Kajian eksperimen menunjukkan bahawa pemindahan haba berpurata masa dan pemindahan haba seketika menghasilkan ketepatan yang memadai. Nisbah kesetaraan dan kelajuan enjin didapati mempunyai kesan yang ketara terhadap ciri pemindahan haba berpurata masa dan pemindahan haba seketika. Telah ditunjukkan bahawa dengan mengabaikan kesan nisbah kesetaraan ke atas pemindahan haba berpurata masa adalah tidak disokong khususnya keatas korelasi pemindahan haba. Sehubungan dengan itu, nisbah kesetaraan telah dihasilkan dalam bentuk korelasi baru dalam sebutan pemindahan haba berpurata masa. Kebolehpercayaan korelasi yang baru dibangunkan telah disahkan dengan menggunakan korelasi Taylor. Ralat relatif telah dikurangkan daripada 70% kepada sekitar 10%. Analisis medan haba telah digunakan bagi mempamerkan ciri pemindahan haba seketika. Berdasarkan pemerhatian, terdapat kesan perbezaan ketara antara campuran udara-bahan api yang rendah dan sangat rendah termasuk juga kelajuan enjin. Lebih-lebih lagi, terdapat juga sifat-sifat yang tidak seragam telah dikesan hasil daripada kesan nisbah kesetaraan ke atas taburan haba. Tambahan pula kadar pembebasan haba, kadar kehilangan haba seketika, kehilangan haba kumulatif dan pekali pemindahan haba telah digunakan bagi memantau ciri pemindahan haba seketika. Parameter-parameter pemindahan haba seketika telah meningkat pada tahap 35% apabila nilai nisbah kesetaraan ditingkatkan di dalam julat operasi terbaik sementara julat peningkatan yang dikehendaki adalah dalam lingkungan 10% bagi keseluruhan julat operasi halaju enjin. Dapat difahami bahawa, model yang telah dibangunkan adalah suatu penemuan yang berguna yang mampu menganggarkan pemindahan haba di dalam enjin. Korelasi jangkaan yang telah dibangunkan adalah sangat disyorkan bagi menganggarkan pemindahan haba di dalam enjin pembakaran dalam berbahan api hidrogen.

CONTENTS

	Page
SUPERVISORS' DECLARATION	ii
STUDENT'S DECLARATION	iii
ACKNOWLEDGEMENTS	v
ABSTRACT	vi
ABSTRAK	vii
CONTENTS	viii
LIST OF TABLES	xi
LIST OF FIGURES	xii
NOMENCLATURES	xvii
LIST OF ABBREVIATIONS	xxiii
 CHAPTER I INTRODUCTION	
1.1 Introduction	1
1.2 Hydrogen as a Fuel	3
1.3 Problem Statement	5
1.4 Objectives of the Study	6
1.5 Scope of the Study	7
1.6 Organisation of Thesis	8
 CHAPTER II LITERATURE SURVEY	
2.1 Introduction	9
2.2 Trends of H ₂ ICE	9
2.3 Hydrogen Combustion	11
2.4 Heat Transfer in SI Engines	14
2.4.1 Heat Transfer Correlations	16
2.4.2 Heat Transfer Models	25
2.5 Heat Transfer Correlations Applicable for H ₂ ICE	29
2.6 Conclusions	35

CHAPTER III EXPERIMENTAL DETIALS AND COMPUTATIONAL MODELING

3.1	Introduction	37
3.2	Strategy of Work Frame	37
3.3	Experimental Details	39
3.3.1	Experimental Setups	39
3.3.2	Engine Combustion Analysis	46
3.4	One-Dimensional Engine Model	49
3.4.1	Model Setup	49
3.4.2	Governing Equations	55
3.4.3	Convergence Criteria	62
3.4.4	Time-Averaged Heat Transfer Correlation	64
3.5	Multidimensional Engine Model	65
3.5.1	Computational Meshing	66
3.5.2	Governing Equations	69
3.5.3	The Main Sub-models	72
3.5.4	Algorithm for Multidimensional Model	79
3.5.5	Boundary and Initial Conditions	82
3.6	Summary	83

CHAPTER IV RESULTS AND DISCUSSION

4.1	Introduction	84
4.2	Experimental Analysis of Hydrogen Combustion	85
4.2.1	In-Cylinder Pressure Traces	85
4.2.2	Mass Fraction Burned	89
4.2.3	Heat Release Rate	91
4.3	One-Dimensional Model	93
4.3.1	Model Validation	94
4.3.2	Analysis of Time-Averaged Heat Transfer	101
4.3.3	Correlations between Dimensionless Parameters	108
4.4	MULTIDIMENSIONAL MODEL	117
4.4.1	Model Validation	117
4.4.2	Parametric Analysis	122
4.5	Summary	147

CHAPTER V CONCLUSIONS AND FUTURE WORK

5.1	Introduction	149
5.2	Summary of Findings	149
	5.2.1 One-dimensional Modelling	149
	5.2.2 Multidimensional Modelling	151
5.3	Contributions of the Study	152
5.4	Recommendations for Future Work	153

REFERENCES	154
-------------------	-----

APPENDICES

A	IPREP File	167
B	Calibration and Testing Procedure	182
B.1	Calibration	182
	B.1.1 Dynamometer	182
	B.1.2 Pressure data acquisition systems	182
	B.1.3 Fuel injector	183
	B.1.4 Exhaust gas analyzer	185
B.2	Procedure for the Experimental Testing	186
C	List of Publications	187

UMP

LIST OF TABLES

Table No.	Title	Page
1.1	Types of heat transfer correlations for ICE applications	2
1.2	Physical properties of hydrogen versus fossil fuels	3
2.1	Summary of the sources of ignition energy for abnormal	13
2.2	Coefficients of Woschni's Correlation	22
3.1	PROTON CAMPRO engine specifications	40
3.2	Fuel Injector specifications	41
3.3	Hydrogen fuel specifications	43
3.4	Micro-motion flow meter specifications	44
3.5	Pressure sensor specifications	44
3.6	Specifications of the GASMET Oxygen Analyzer	46
3.7	Piping system components specifications	51
3.8	Engine valves specifications	51
3.9	Parts wall temperature	52
3.10	Coefficients of Woschni's Correlation	57
3.11	Values of The constants for k - ϵ turbulent model	72
4.1	Calibration parameters considered for the one-dimensional model	94
4.2	TAHT Correlations constants	112
4.3	Squares differences analysis	113
4.4	Constants of the newly developed TAHT correlations	113
4.5	The experimental operating points of the cases utilized for validating of the multidimensional model	120
B.1	Load Sequence for Dynamometer Calibration Process	184

LIST OF FIGURES

Figure No.	Title	Page
2.1	Identification of the combustion anomalies in DIH ₂ ICE	14
2.2	Schematic distribution for the engine energy	15
2.3	An example correlation of time-averaged heat transfer based on wide range of measurements for several engines	18
2.4	Comparison of predicted heat transfer coefficient for several correlations	23
2.5	Instantaneous heat transfer coefficient measured comparing to those of empirical equations	31
2.6	Comparison between the apparent heat release $\frac{dQ}{dt}$ and the in-cylinder pressure difference ($p-p_m$)	33
2.7	Comparison between the real cooling loss (estimated by Wiebe's function) and that one predicted by the new correlation	34
3.1	Strategy of the work frame for the current research methodology	38
3.2	Schematic of the test cell for the experimental set up	39
3.3	Details of the PROTON CAMPRO research engine	40
3.4	The engine cylinder head showing the injector, pressure transducer and sparkplug positions as well as the intake and exhaust valves	41
3.5	Schematic of the integrated fuelling system	42
3.6	Experimental setup of the fuelling system	43
3.7	The test-cell (a) Overview of the tested engine coupled with the eddy current dynamometer (b) Dynamometer control console	45
3.8	The GASMET gas analyzers system	46
3.9	One dimensional gas dynamic model for single cylinder four strokes SI DIH ₂ ICE	50
3.10	Engine cylinder with engine crank train details	52

3.11	Illustration of component discretization with staggered grids	59
3.12	Physical domain for the multidimensional engine model	66
3.13	Computational grid domain with hexahedral element	67
3.14	(a) Typical finite-difference cell; (b) The portion of a momentum cell lying within the regular cell; (c) Momentum cell (i,j), shown in dashed lines, and its associated regular cell	68
3.15	Flowchart for the injection program SETVELIN	73
3.16	Algorithm for the multidimensional model	81
4.1	Experimental traces of the in-cylinder pressure for at 3000 rpm, $\phi=0.93$ and $SOI = 130$ deg BTDC at the full-load condition	86
4.2	Experimental traces of the in-cylinder pressure for different equivalence ratio at 3000 rpm and $SOI = 130$ deg BTDC at the full-load condition	87
4.3	Experimental traces of the in-cylinder pressure traces for different injection timing at 1800 rpm and stoichiometric mixture condition ($\phi=1.0$) at the full-load condition	88
4.4	Variation of the mass fraction burned for different equivalence ratio at 3000 rpm and $SOI = 130$ deg BTDC at full-load condition	91
4.5	Variation of the mass fraction burned for different injection timing at 1800 rpm and stoichiometric condition ($\phi = 1.0$) at full-load condition	91
4.6	Variation of the heat release rate profiles for different equivalence ratio at 3000 rpm and $SOI = 130$ deg BTDC at full-load condition	92
4.7	Variation of the heat release rate for different injection timing at 1800 rpm and stoichiometric mixture condition ($\phi=1.0$) at full-load condition	93
4.8	Comparison between predicted (simulated) and experimental results of <i>IMEP</i> for the baseline hydrogen engine at $SOI = 130$ deg BTDC	95
4.9	Comparison between predicted (simulated) with experimental results of the maximum in-cylinder pressure for the baseline hydrogen engine at $SOI = 130$ deg BTDC	96

4.10	Comparison between predicted (simulation) and experimental brake torque for the baseline hydrogen engine at $SOI = 130$ deg BTDC	97
4.11	Comparison between measured and simulated volumetric efficiency for the baseline hydrogen engine at different engine speed and SOI	98
4.12	Comparison between measured and simulated engine brake torque for the baseline hydrogen engine at different engine speed and SOI	99
4.13	Comparison between measured and simulated engine brake power for the baseline hydrogen engine at different engine speed and SOI	100
4.14	Variation of heat transfer rate against the engine speed and equivalence ratio for different SOI	102
4.15	Variation of PRHT against the engine speed and equivalence ratio for different SOI	104
4.16	Variation of Nusselt number against the engine speed and equivalence ratio for different SOI	106
4.17	Variation of Reynolds number against the engine speed and equivalence ratio for different SOI	107
4.18	Comparison of the predicted (simulation) with Taylor's correlation results	109
4.19	Relative error of the predicted results based on results of Taylor's correlation	110
4.20	Comparison of simulation results and proposed correlation for $70 \text{ deg BTDC} \leq SOI \leq 85 \text{ deg BTDC}$	114
4.21	Comparison of simulation results and proposed correlation for $100 \text{ deg BTDC} \leq SOI \leq 130 \text{ deg BTDC}$	115
4.22	Relative error of predicted (simulation) results based on newly developed correlations (model1 and model2)	116
4.23	Computational domain with hexahedral element for multidimensional engine model at TDC position	118
4.24	Effect of mesh size on the comparison between simulated and experimental in-cylinder pressure under the motoring condition with (2000 rpm)	119

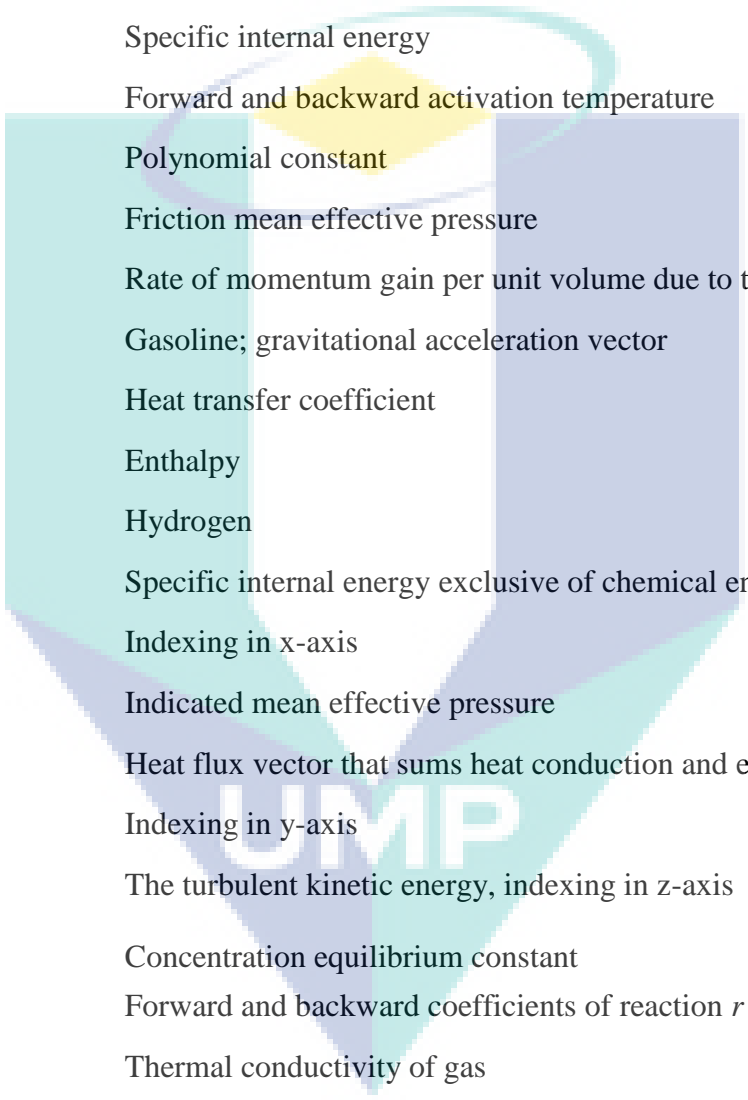
4.25	Comparison between the experiment and predicted (simulation) results of the in-cylinder pressure traces for different engine speed and mixture strength under WOT and full-load conditions	121
4.26	The flow field with hydrogen concentration of the injection process for different engine speed, $\phi = 0.7$ and $SOI = 100$ deg BTDC at 80 deg BTDC. (Isometric view)	124
4.27	The flow field with hydrogen concentration of the injection process for different instants, 3000 rpm, $\phi = 0.5$ and $SOI = 100$ deg BTDC. (Isometric view)	126
4.28	The flow field with hydrogen concentration of the injection process for different equivalence ratio, 3000 rpm and $SOI = 100$ deg BTDC at 80 deg BTDC. (Isometric view)	127
4.29	The temperature contour at TDC position (isometric view)	128
4.30	The temperature contours for different engine speed and instants at $\phi = 0.7$, IT = TDC and $SOI = 100$ deg BTDC	129
4.31	The temperature contours for different equivalence ratio and instants at engine speed of 3000 rpm, IT = TDC and $SOI = 100$ deg BTDC	131
4.32	The temperature contours for different SOI and instants at engine speed of 3000 rpm, $\phi = 0.7$ and IT = TDC	133
4.33	Variation of heat release rate against crank angle for different engine speed at $\phi = 0.7$, IT = TDC and $SOI = 100$ deg BTDC	134
4.34	Variation of heat release rate against crank angle for different equivalence ratio at engine speed of 3000 rpm, IT = TDC and $SOI = 100$ deg BTDC	135
4.35	Variation of heat release rate against crank angle for different SOI at engine speed of 3000 rpm, $\phi = 0.7$ and IT = TDC	136
4.36	Variation of the instantaneous rate of heat loss against crank angle for different engine speed at $\phi = 0.7$, IT = TDC and $SOI = 100$ deg BTDC	137
4.37	Variation of the instantaneous rate of heat loss against crank angle for different equivalence ratio at engine speed of 3000 rpm, IT = TDC and $SOI = 100$ deg BTDC	138
4.38	Variation of the instantaneous rate of heat loss against crank angle for different SOI at engine speed of 3000 rpm, $\phi = 0.7$ and IT = TDC	140

4.39	Variation of the cumulative heat loss against crank angle for different engine speed at $\phi = 0.7$, IT = TDC and $SOI = 100$ deg BTDC	141
4.40	Variation of the cumulative heat loss against crank angle for different equivalence ratio at engine speed of 3000 rpm, IT = TDC and $SOI = 100$ deg BTDC	142
4.41	Variation of the cumulative heat loss against crank angle for different SOI at engine speed of 3000 rpm, $\phi = 0.7$ and IT = TDC	143
4.42	Variation of the heat transfer coefficient against crank angle for different engine speed at $\phi = 0.7$, IT = TDC and $SOI = 100$ deg BTDC	144
4.43	Variation of the heat transfer coefficient against crank angle for different equivalence ratio at engine speed of 3000 rpm, IT = TDC and $SOI = 100$ deg BTDC	145
4.44	Variation of the heat transfer coefficient against crank angle for different SOI at engine speed of 3000 rpm, $\phi = 0.7$ and IT = TDC	147
B.1	The set up for calibration of the injector and the ECU system	186
B.2	Hydrogen mass flow rate against the injection duration for injector calibration test	186
B.3	Calibration spectrums on FTIR system for emission analysis	187

NOMENCLATURES

List of Symbols

Symbol	Meaning
a	Crank radius; Adjustable factor in Wiebe's function; dimensionless number used for low Mach number flows
A	Area
A_{eff}	Effective area
AFR	Air/fuel ratio
A_{fr} and A_{br}	Empirical constants
a_{mr}	Integral stoichiometric coefficient of the species m appearing as a reactant
a'_{mr}	Reaction order
A_o	Flow regime flag, laminar (0), or (1) for turbulence models
A_r	Reference flow area; polynomial constant
B	Karmann's model's constant
b_{mr}	Integral stoichiometric coefficient of the species m appearing as a product
b'_{mr}	Reaction order
B_r	Polynomial constant
C	Constant
c	Speed of sound
C_1 and C_2	Constants in Woschni's correlation
C_D	Discharge coefficient
C_f	Friction factor
C_m	Mean piston speed
c_m	Concentration of species m
C_p	Specific heat at constant pressure
C_{pl}	Pressure loss coefficient



C_r	Polynomial constant
c_μ	Karmann's model's constant
d	Diameter of the cylinder bore
D	Diameter of flow element
D_m	Mass diffusion coefficient from Fick's law of binary diffusion
D_r	Polynomial constant
e	Specific internal energy
E_{fr} and E_{br}	Forward and backward activation temperature
E_r	Polynomial constant
$FMEP$	Friction mean effective pressure
F^s	Rate of momentum gain per unit volume due to the spray
g	Gasoline; gravitational acceleration vector
h	Heat transfer coefficient
H	Enthalpy
H_2	Hydrogen
I	Specific internal energy exclusive of chemical energy
i	Indexing in x-axis
$IMEP$	Indicated mean effective pressure
J	Heat flux vector that sums heat conduction and enthalpy diffusion
j	Indexing in y-axis
k	The turbulent kinetic energy, indexing in z-axis
$K_c^r(T)$	Concentration equilibrium constant
k_{fr} and k_{br}	Forward and backward coefficients of reaction r
k_g	Thermal conductivity of gas
k_l	Laminar thermal conductivity
k_t	Turbulent thermal conductivity
l	connecting rod length
L	Piston stroke
LHV	Lower heating value
m	Mass; exponent for Re in TAHT correlation

m_b	Burning mass
\dot{m}	Mass flow rate
\dot{m}_a	Air mass flow rate
$\dot{m}_{delivery}$	Injector delivery rate
MFB	Mass fraction burned
M_m	Molecular weight of species m
$MPSF$	Mean piston speed factor
$MPSSF$	Mean piston speed squared factor
n	Wiebe form parameter; exponent for φ in TAHT correlation
N	Engine speed
Nu	Nusselt number
p	Pressure
P	Engine brake power
p_1 and p_2	Inlet and outlet pressure
PF	Peak cylinder pressure factor
p_m	Motored cylinder pressure
p_{max}	Maximum cylinder pressure
p_r	Reference point pressure
Pr	Prandtl number
p_{ratio}	Absolute pressure ratio
Pr_l	Laminar Prandtl number
Q	Heat rate
\bar{Q}	Time-averaged convection heat transfer rate
\dot{Q}^c	Source term of chemical heat release
\dot{Q}^s	Source term of spray interaction
q_w	Wall heat flux
R	Gas constant
R^2	Coefficient of determination
Re	Reynolds number
R_o	Universal gas constant

RPR	Reciprocal of the turbulent Prandtl number
t	Time
T	Temperature
T_A	Normalised temperature ($T/1000$)
T_g	Cylinder gases temperature
T_o	Upstream stagnation temperature
T_r	Reference point temperature
T_w	Cylinder wall temperature
u	Fluid velocity vector
u_l	Inlet fluid velocity
U_{ise}	Isentropic velocity
v	Characteristic velocity in Reynolds number
V	Volume
V_c	Clearance volume
V_d	Cylinder displacement volume
V_r	Reference volume for Woschni's correlation
w	Average cylinder gas velocity
\dot{W}^s	Turbulent eddies rate of work on spray dispersion
x	Dimension in x-axis
\bar{x}	Averaged spatially dimension
x_b	Mass burned fraction
y	Dimension in y-axis; distance from the wall in the normal direction
z	The distance between the crank axis and the piston pin axis; roughness height; dimension in z-axis

Greek Symbols

Symbol

Meaning

 $\Delta\theta_{inj}$

Injection duration

 Δp_c

Pressure rise due to combustion

 $(\Delta h_f^o)_m$

Heat of formation of species m at absolute zero

 Δt

Computational time step

 Δx

Discretised length

 δ_{ml}

Dirac delta function

 η_v

Volumetric efficiency

 θ_d

Crankshaft position at combustion end

 θ_s

Crankshaft position at combustion start

 μ

Dynamic viscosity

 ν_l

Laminar kinematic viscosity

 ρ

Density

 ρ_r

Reference density

 ρ_{ise}

Isentropic density

 ρ_o

Upstream stagnation density

 ρ_m

mass density of species m

 $\dot{\rho}^s$

Source term of spray

 $\dot{\rho}_m^c$

Source term of chemistry

 ∇

Differential operator

 Ψ

General quantity for formulating of governing equations

 κ

Karmann's model's constant

 γ

Specific heat ratio

 ε

Turbulence energy dissipation rate

 σ

Viscous stress tensor

 θ

Crankshaft angle

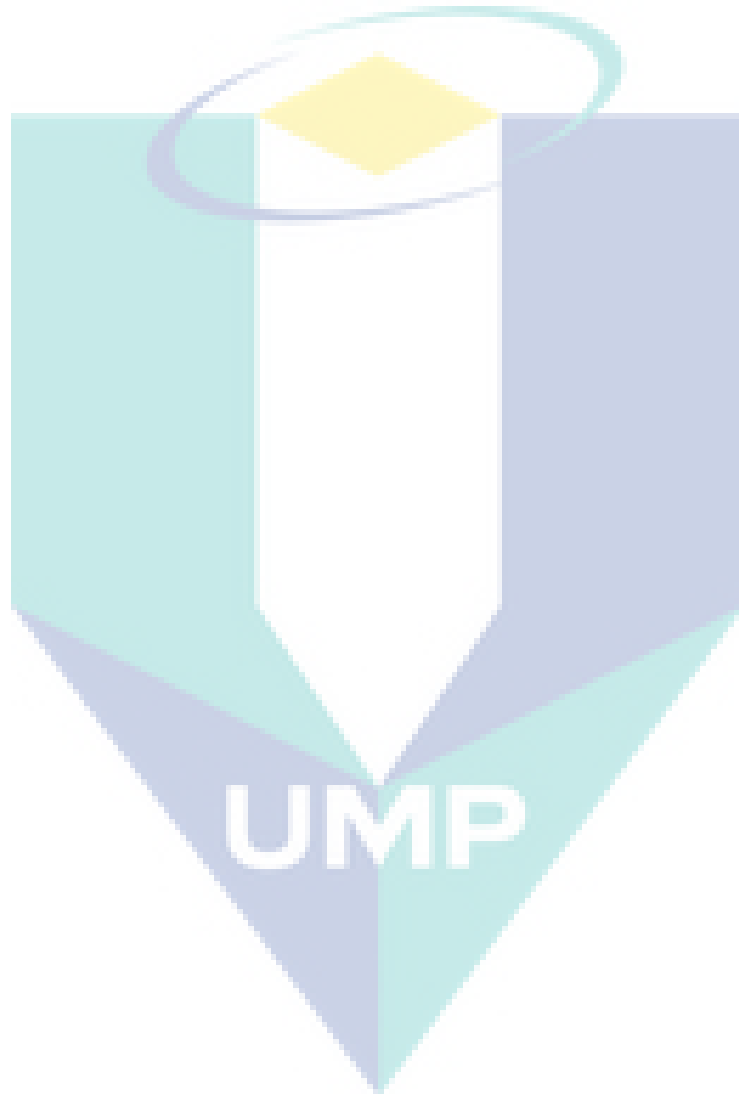
 λ

Air/fuel relative ratio

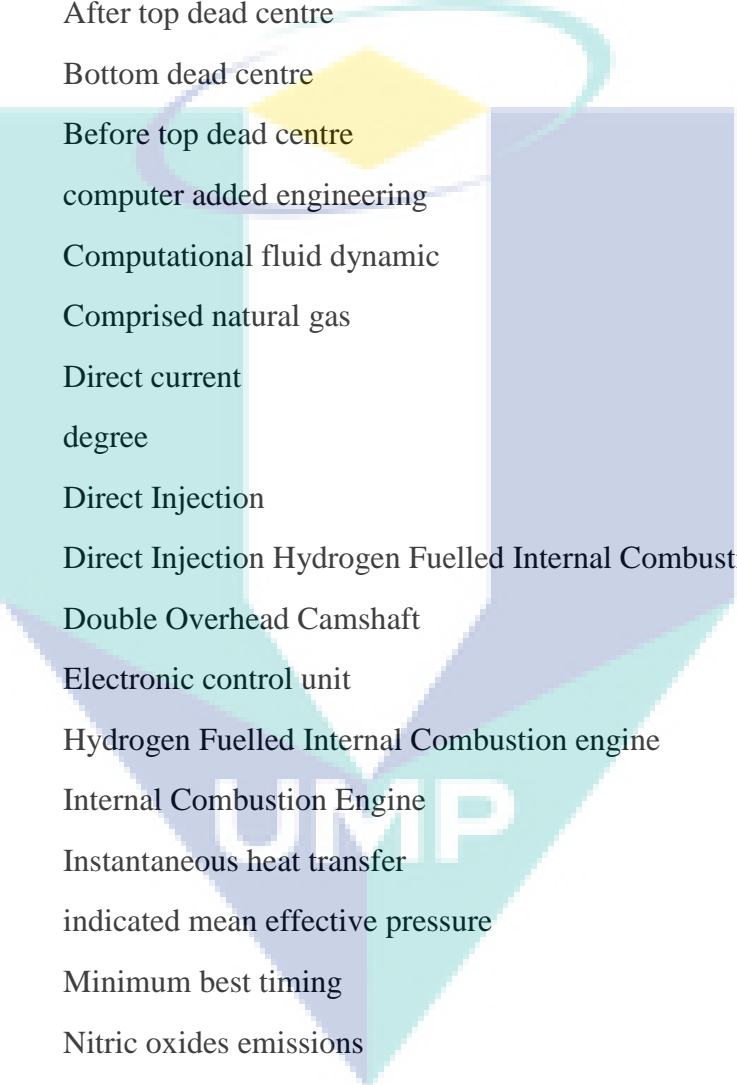
 ρ

Density

ω_r	Rate at which reaction proceeds
φ	Fuel/air equivalence ratio
τ	Engine brake torque
χ_m	one mole of species m
ζ	Ratio of the heat transfer (hydrogen/gasoline) in Eq. 2.1 and Eq. 2.2
ζ_{fr} and ζ_{br}	Empirical constants

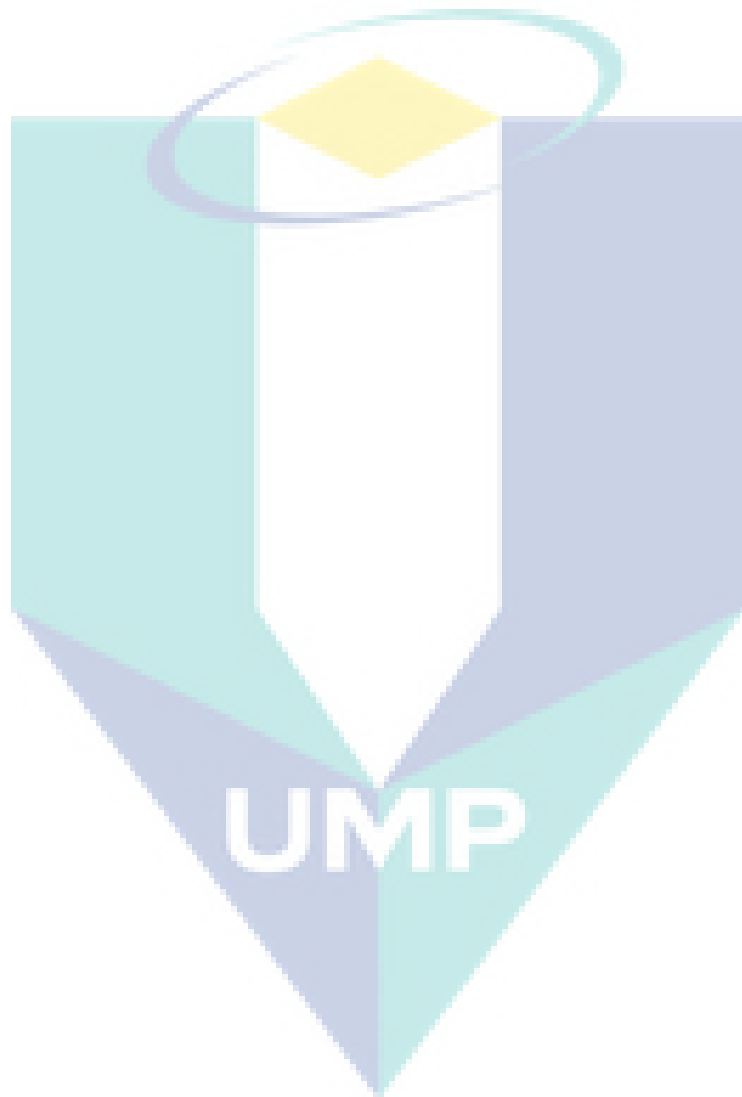


LIST OF ABBREVIATIONS



1D	One dimensional
3D	Three dimensional
<i>AFR</i>	Air Fuel Ratio
ALE	Arbitrary Lagrangian-Eulerian
ATDC	After top dead centre
BDC	Bottom dead centre
BTDC	Before top dead centre
CAE	computer added engineering
CFD	Computational fluid dynamic
CNG	Comprised natural gas
DC	Direct current
deg	degree
DI	Direct Injection
DIH ₂ ICE	Direct Injection Hydrogen Fuelled Internal Combustion engine
DOHC	Double Overhead Camshaft
ECU	Electronic control unit
H ₂ ICE	Hydrogen Fuelled Internal Combustion engine
ICE	Internal Combustion Engine
IHT	Instantaneous heat transfer
<i>IMEP</i>	indicated mean effective pressure
MBT	Minimum best timing
NO _x	Nitric oxides emissions
<i>PRHT</i>	Percentage ratio of heat transfer
QSOU	Quasi-Second-Order Upwind
rpm	revolution per minute
SI	Spark ignition
SIMPLE	Semi Implicit Method for Pressure-Linked Equations
<i>SOI</i>	Start of injection

TAHT	Time-averaged heat transfer
TDC	top dead center
WOT	wide open throttle



CHAPTER ONE

INTRODUCTION

1.1 INTRODUCTION

The global utilization of fossil fuels has almost doubled in the last three decades. Fossil fuels are currently meeting more than 90% of the total energy demand (EIA, 2011). It is expected to increase the utilization energy resources due to the rapid rate of developments, as well as the requirements of human comfort. This causes the vast depletion of resources as well as the undesirable emissions. The main source for emitting of CO₂ is the fossil fuel. The CO₂ is a main gas caused the green house phenomena. The concentration of CO₂ has increased by about one-third since industrialization began and the average surface temperature of the earth is increasing because of the global warming phenomenon (Subramanian et al., 2007). Fuels with higher hydrogen to carbon ratio are the world target for the next energy development. The motivation for substituting the fossil fuel by the alternative fuels comes from the energy crisis and global warming phenomenon (Crabtree et al., 2004). Therefore, the vitality of alternative fuel research for internal combustion engines (ICEs) has been an upsurge. Up to two decades ago, the availability of fossil fuels and their well-established infrastructure support exiled hydrogen fuel away from the cycle of interest. However, when the problems of hydrocarbon fuel availability and their destructive influence on nature had been aggregating in the last two decades, hydrogen fuel returned back strongly and seized most of the lights among the possible alternatives. Hydrogen represents one of the main alternatives available at the long-term use in internal combustion engine applications. A lot of attention at present is directed to hydrogen fuel utilization, mainly because of its abundance and non-polluting nature. It was pointed out that hydrogen has excellent

characteristics as a spark ignition (SI) engine fuel (Eichlseder et al., 2003; Subramanian et al., 2005 and Kahraman et al., 2007). The studies on the performance of hydrogen-fuelled engines (H_2 ICEs) are voluminous (White et al., 2006); however, there is some lacking in the investigation of heat transfer (Verhelst and Wallner, 2009).

The heat transfer is one of the noteworthy issues in the studies of ICEs. It has a direct effect on the main distinguishing parameters for the engine, such as in-cylinder pressure and temperature. The effort was devoted to developing a highly efficient global heat transfer model for ICEs applications (Bohac et al., 1996). An overview of the state-of-the-art shows abundance of correlations for estimation of heat transfer in ICEs (Sanli et al., 2009). The behavior of the in-cylinder heat transfer is a function of location and time. According to this fact, all the empirical correlations were developed from modeling of heat transfer can be categorized into three groups. Table 1.1 summarizes the type of heat transfer correlations for ICEs application depending on the averaging methods in the estimation of the heat transfer coefficient (Heywood, 1988).

Table 1.1: Types of heat transfer correlations for ICEs applications

Category of heat transfer coefficient	Averaging method	Field of Application
Time averaged $h(\bar{x}, \bar{t})$	Averaged over time and space	Overall steady state energy balance calculations
Instantaneous spatially averaged $h(\bar{x}, t)$	Instantaneous, space average	Analysis of engine performance
Instantaneous local $h(x, t)$	Instantaneous, local	Local calculations of thermal stress

Over the last past decade, the heat-transfer issue was arisen as one of the crucial affairs for modeling of the hydrogen-fueled engine (H_2 ICE). The importance of heat transfer investigation for H_2 ICE is due to the vast differences in the properties compared with hydrocarbon fuels (Wei et al., 2001 and Demuynck et al., 2008). The differences are not only for the quantity of the liberated heat transfer from the

combustion process but also the unique behavior for the hydrogen combustion (Shudo and Suzuki, 2002a).

1.2 HYDROGEN AS A FUEL

Hydrogen as a fuel has unique characteristics (wide flammability limit, small quenching distance, high flame speed, etc) compared to fossil fuel. Understanding of these properties provides keys for developing and improving of design strategies for H₂ICE. The benefits and technical challenge of the heat-transfer issues for H₂ICE revealed through investigation of hydrogen properties relevant to engine heat loss and thermal efficiency. Hydrogen and other fossil fuels properties are listed in Table 1.2 (Wimmer et al., 2005; White et al., 2006 and Verhelst and Wallner, 2009). Hydrogen has a high specific energy, high flame speed, small quenching distance, high diffusion coefficient, wide range of flammability and cleans burning characteristics. These properties are the possibility of high performance in ICE (Verhelst and Sierens, 2001a and Cordaway, 2004).

Table 1.2: Physical properties of hydrogen versus fossil fuels

Parameter	Unit	Diesel	Gasoline	Methane	Hydrogen
Density	kg/m ³	830 ¹	730-780 ¹	0.72 ¹	0.089 ¹ , 71 ^{2,3}
Stoich. air demand	kg _{air} / kg _{fuel}	14.5	14.7	17.2	34.3
Lower heating value	MJ/kg _{fuel}	42.5	43.5	50	120
Mixture calorific value ⁵	MJ/m ³	3.83 ⁷	3.82 ⁷	3.4 ⁷	3.2 ⁷
		3.83 ⁸	3.83 ⁸	3.76 ⁸	4.53 ⁸
Boiling temp. ³	°C	180-360	25-215	-162	-253
Ignition limits ⁴	λ	0.5-1.3	0.4-1.4	0.7-2.1	0.2-10
Min. ignition energy ^{3,4,5}	mJ	0.24	0.24	0.29	0.02
Self ignition temp.	°C	≈250	≈350	540	585
Quenching distance ^{3,4,6}	mm	-	2	2.03	0.64
Lam. flame speed ^{4,5}	cm/s	40-80	40-80	40	200
Conductivity ⁹	mW/m ² .K	-	-	34	182
Diffusion coeff. ^{1,4}	m ² /s	-	-	1.9×10 ⁻⁶	8.5×10 ⁻⁶
Carbone content	Mass (%)	86	86	75	0

Note

¹ at 1.013 bar and 0 °C

² at -253

³ at 1.013 bar

⁴ in air

⁵ λ=1

⁶ at 20 °C

⁷ mixture aspiration

⁸ air aspiration

⁹ at 300 K

The quenching distance describes the flame extinguishing properties of a fuel when used in an ICE. It is the distance of the flame quenches due to heat losses from the cylinder wall. The quenching distance for hydrogen fuel is smaller than other fuels (Shudo and Nabetani, 2001). Therefore, the flame front can escape from the combustion chamber through the intake valve more easily and backfire occurred (Halmari, 2005). As can be seen in Table 1.2, the quenching distance of hydrogen fuel is about one-third compared to methane and gasoline. Because of this, the cooling losses are high and the thermal efficiency of H₂ICE is lower than fossil-fueled engines (Shudo et al., 2003 and Shudo, 2007).

Hydrogen has higher flame speed compared to all other fuels. At a stoichiometric condition, the hydrogen flame speed is nearly 4 times higher than hydrocarbon fuels (Wei et al., 2001). This means that hydrogen engines are more likely the thermodynamically ideal engine cycle (Eichlseder et al., 2003). However, it causes the increase of heat transfer due to intensify the turbulence level. Hence, thermal boundary layer is very thin then increases the amount of heat transfer from combustion gas to combustion chamber walls (Shudo, 2005). At leaner mixtures, however, the flame speed decreases significantly (Natkin et al., 2003).

The wide flammability range of hydrogen can be combusted in an ICE over a wide range of hydrogen-air mixtures ($0.1 < \text{fuel/air equivalence ratio } (\varphi) < 7.1$) (Demuynck et al., 2008). A significant advantage of this, hydrogen can run on a lean mixture. It is easy to get an engine to start on hydrogen (Padiyar, 1985). Under this wide flammability range, it is expected to introduce φ for expressing of heat transfer correlations.

Hydrogen is a remarkably light gaseous fuel that requires the least amount of air for stoichiometric combustion (2.39 versus 59.6 for iso-octane) on the volume basis while the highest relative mass of air on the mass basis (Yamin, 2007). The combustion of hydrogen is also associated with a substantial molar contraction of around 15%. Its heating value on the mass basis is the highest but lowest on the volume basis (Yamin and Hamdan, 2010). In addition, there is the significant difference between its higher and lower heating values since its product of

combustion in the air is mainly water. However, its energy release by combustion per unit mass of the stoichiometric mixture is one of the highest.

The thermal conductivity of hydrogen is 5 times higher than methane. As well as, the diffusion coefficient for hydrogen is 4 times higher than methane. As results, a better homogeneity of the mixture for H₂ICE compared to the hydrocarbon fuels engine (Wimmer et al., 2005). However, the hydrogen disperses rapidly when its leak develops. Thus, unsafe conditions can be minimized (Stefaan et al., 2005).

1.3 PROBLEM STATEMENT

Development of ICE with hydrogen as an alternative fuel has achieved considerable progress. However, still many challenges are facing. Therefore, enormous efforts are continuously paid to resolve these barriers (White et al., 2006 and Verhelst and Wallner, 2009). Several efforts are directed to develop realistic thermodynamic models of the engine cycle. These types of the model enable a cheap and fast optimistic of engine settings for an operation with hydrogen fuel (Demuynck et al., 2011). Several sub-models are required to solve the equations governing the conservation of energy and mass, for example, the combustion, turbulence and heat transfer models. Numerous correlations in the literature were developed to model the heat transfer in fossil fuel engines (Eichelberg, 1939; Annand, 1963 and Woschni, 1967). The existed models based on the empirical formulation for heat transfer in hydrocarbon fuelled ICEs. However, the heat-transfer phenomenon in the hydrogen and fossil-fuel ICEs are different in the rate and behaviour of heat release as well as heat loss due to the different properties (Wei et al., 2001; Shudo and Suzuki, 2002a; Verhelst, 2005; Shudo, 2007; Demuynck et al., 2008 and Demuynck et al., 2011). New heat transfer model applicable to H₂ICE was proposed by Shudo and Suzuki (2002b) based on Woschni's model. It was contained two calibration parameters depends on the ignition timing and equivalence ratio. Therefore, dependency of heat transfer correlation on the equivalence ratio is stated to be the subject of further studies (Verhelst, 2005; Safari et al., 2009; Verhelst and Wallner, 2009 and Demuynck et al., 2011). It was unable to accurately predict the trends with a variation in the equivalence ratio with a recalibration of Annand and Woschni

correlations (Demuynck et al., 2011). Applicability of a quasi-dimensional heat transfer model for H₂ICE was presented by Nefischer et al. (2009). This model is based on the realistic description of the characteristic velocity for the turbulent flow field proposed by Schubert et al., (2005). It was predicted of heat transfer with the reasonable agreement with experiment for port injection; however, the direct-injection effect was not predictable.

The recent development for the analysis of heat transfer in H₂ICE was focused only on the instantaneous spatially averaged. This is due to the importance of heat transfer correlation for modelling engine cycle (Verhelst and Sierens, 2007, and Demuynck et al., 2011). However, the evaluation of heat transfer characteristics based on the time-average analysis introduces valuable information in case of H₂ICE. There is no study performed to assess the applicability of existing time-averaged correlations for hydrogen-fueled engine.

The present study attempts to address the influence of the equivalence ratio on heat transfer in direct injection H₂ICE. Two types of heat transfer analysis namely time-averaged heat transfer (TAHT) and instantaneous heat transfer (IHT) are considered in the present study. The time averaged heat transfer is dedicated to including the equivalence ratio as a governing variable within correlation form. For this purpose, diagnostic study is a prerequisite for assessing the effect of operation parameters on TAHT characteristics. The IHT is devoted to weighting the influence of operation parameters on heat transfer. Therefore, the parametric study of heat transfer is essential to investigate the trends of IHT. The outcome of the present study is expected to establish a technical contribution for the automotive sectors.

1.4 OBJECTIVES OF THE STUDY

The objectives of this study are summarized as follows:

- i. To characterize time-averaged heat transfer based on one-dimensional model using gas dynamics approach.

- ii. To develop multidimensional model for the different processes in DIH₂ICE using finite volume approach.
- iii. To validate one-dimensional as well as multidimensional model based on experimental results.
- iv. To develop a new correlation and assess the time-averaged heat transfer for hydrogen fuelled engine.
- v. To investigate the parametric study of instantaneous heat transfer based on multidimensional model.

1.5 SCOPE OF THE STUDY

This thesis attempts to develop one- and multidimensional models for analysing of heat transfer in DIH₂ICE. Several points are declared herein to clarify the scope of study. These points are as follows:

- i. The models are developed for spark ignited, direct injection ICEs.
- ii. The developed engine models are suited only for normal engine operation. Abnormal combustion phenomena such as knock, pre-ignition or backfire are out of the scope.
- iii. In the multidimensional model, the modified wall function is used for resolving near wall transport.
- iv. The experimental work is conducted to provide a set of data for model's validations as well as to clarify the combustion characteristics of DIH₂ICE under various operation parameters.
- v. The one-dimensional model is mainly dedicated to develop a new predictive correlation to estimate the rate of TAHT in DIH₂ICE. Therefore, a diagnostic study is required to assess the influence of operation parameters on TAHT characteristics.
- vi. In the multidimensional model, the concentration is devoted, foremost, for investigating the impact of the various operation parameters on IHT trends. Secondly, the concern is given for evaluating hydrogen injection process under different conditions.

1.6 ORGANISATION OF THESIS

This thesis is arranged to provide details on the facts, observations, arguments, and procedures in order to meet its objectives. Four chapters excluding the introduction are composed to present the sequence of logical thoughts. Chapter 2 includes a brief review of the heat transfer in SI engine combustion concepts and theories. In addition, the heat transfer analysis inside of H₂ICE is also reviewed in details. Chapter 3 presents to explain the adopted methods for achieving the objectives. The one-dimensional and multidimensional approaches that applied in building up the models are described. Furthermore, it summarizes a brief description for the experimental setup and facilities, which is utilized for engine testing program and database collection. In Chapter 4, the results and discussion of the one-dimensional and multidimensional models for DIH₂ICE are illustrated. The results of one-dimensional and multidimensional models are validated with experimental results. The time-averaged heat transfer is characterized based on the one-dimensional model. A new correlation for TAHT is developed and assessed. The instantaneous heat transfer (IHT) is parameterized based on the multidimensional modelling. Finally, the conclusions as well as recommendations for the future work are presented in Chapter 5. References and Appendices are given at the end of this thesis.

CHAPTER TWO

LITERATURE SURVEY

2.1 INTRODUCTION

This chapter discusses a survey of past research efforts related to the heat transfer for hydrogen-fueled internal-combustion engine. The trends of H₂ICE and combustion of hydrogen with its associated problems were reviewed in brief. A review of other relevant research studies is also provided. The basic concept for the heat-transfer analysis in spark ignition (SI) engine was reviewed in terms of types the correlations and models. The efforts for improving and developing of heat transfer correlations applicable to H₂ICE were reviewed. However, a little information can be found on assessment of the existing correlations for time averaged heat transfer, as well as the parameterization of instantaneous heat transfer in H₂ICE. The review is organized chronologically to offer insight to how past research efforts have laid the groundwork for subsequent studies, including the present research effort. The present research effort can be properly tailored to add to the present body of the literature as well as to justify the scope and direction of the present research effort.

2.2 TRENDS OF H₂ICE

Fossil fuels are being depleted rapidly due to the huge consumption in the wide applications of the world today. In addition, the fossil-fuels combustion produces the main elements for the global environmental problems, such as the greenhouse effect, ozone layer depletion and acid rain (Kahraman, 2005 and Kahraman et al., 2007). According to the best estimates, the world's fossil fuel (coal, petroleum and natural gas) production meets about 80% of our energy requirements

today, will start to decline in 20-30 years time (Yamin and Hamdan, 2010). On the other hand, since the demand for energy is ever increasing as the nations of the world try to improve their living standards; alternative energy sources are being considered. The growth of alternatives to the fossil-fueled internal-combustion engines (ICEs) for personal transportation proposes significant prospects. It directs to reduce the dependence of the world on fossil fuels (depleted resources) and the adverse environmental effects of the fossil fuels. The challenge is to find highly efficient ways to produce, deliver, and use energy that enhanced the quality of life. Nevertheless, it is threatened the environment and climate. The energy carrier hydrogen is an alternative to fossil fuels with the potential to achieve these goals (Dresselhaus et al., 2003 and Crabtree et al., 2004).

Picardo was introduced hydrogen as fuel for internal-combustion engines through the late 1800's. An excellent technical and historical survey of literatures on H₂ICE research was accomplished by several researchers (Das, 1990; White et al., 2006 and Ball and Wietschel, 2008). These reviews were deals with the major effect, difficulties, technical problems and economy of utilizing hydrogen as fuel for ICEs. Hydrogen is a promising alternative for fossil fuel due to the near-zero emissions and higher thermal efficiency compared to hydrocarbon fueled engine (Das, 1991 and Tang et al., 2002). The hydrogen-fueled engine operates at the significantly leaner air fuel ratio so that the higher efficiency compared to gasoline can be achieved (Grabner et al., 2006). This is due to the low lean limit ($0.1 < \phi < 7.1$) and ignition energy of hydrogen (0.02 mJ) that allows the engine to be run with stable combustion with little or no throttling (Subramanian et al., 2006).

Efficiency improvement for the alternative fueled engine is one of the crucial research aspects. Within this field, many studies were presented to characterize of the combustion process, overall performance and emissions for hydrogen-fueled engines (Yi et al., 1996; Natkin et al., 2003; Subramanian et al., 2005; Knop et al., 2008 and Ma et al., 2011). Hydrogen fuel tolerates different mixture formation techniques and combustion processes (Eichlseder et al., 2003 and Nefischer et al., 2009). The hydrogen-fueled engine is being developed with a port injection (Lee et al., 1995; Sierens and Verhelst, 2003 and Liu et al., 2008), direct injection (Yi et al., 1996;

Berckmüller et al., 2003; Mohammadi et al., 2007 and Abdullah and Rashid, 2009) and dual injection (Yi et al., 2000 and Kim et al., 2006) system. The combustion chamber design would require little amendment for converting from gasoline to hydrogen engines with port-fuel-injected system through the transitional period (Verhelst et al., 2008 and Verhelst et al., 2010). The power densities of port fuel injected hydrogen engines are diminished relative to fossil-fueled engines due to the low density of hydrogen (Verhelst et al., 2008 and Vudumu and Koylu, 2011). The hydrogen fuel injects directly into the cylinder at very high pressures in case of direct injection technique. This technique offers a very high degree of freedom for optimization (Wimmer et al., 2005 and Grabner et al., 2006). It is practically difficult for the injector to survive such an extreme thermal environment of the combustion chamber over a prolonged operation period (Polasek et al., 2002). Besides that, the possibility of formation the NO_x emission is higher relative to the port injection systems due to the relatively short fuel/air mixing time (Jorach et al., 1997). However, more recent studies using new concepts of mixture formation have shown that the direct injection can be used to its advantage and lower NO_x emissions (Verhelst et al., 2006; White et al., 2006; Verhelst and Wallner, 2009 and Verhelst et al., 2010). As a result, the recent developments for H₂ICE are focused on the direct-injection technique. It can be concluded that developing an injection model applicable to DIH₂ICE would be a significant contribution to the automotive industry.

2.3 HYDROGEN COMBUSTION

Hydrogen gas can burn in two modes. Firstly, deflagration that is the flame travel through the mixture at the subsonic speed. Another mode is called detonation that is a flame and shock wave travel together through the mixture at the supersonic speed. Even though, the ignition is caused by minimal ignition energy (Das, 1996). Combustion within ICEs is usually classified into the normal and the abnormal combustion. In normal mode, the combustion initiates solely by a controlled spark event, the flame front propagates entirely across the combustion chamber, and the flame propagation is relatively uniform and consistent. Abnormal combustion refers to a variety of situations in which one or more of the above definitions are not held.

Hydrogen fuel demonstrates the desirable characteristics for combustion in SI engines (White, 2006). The low spark energy requirement would lower the cyclic combustion fluctuation (Abdel-Aal et al., 2005). The high burning velocity of hydrogen contributes to the relatively high thermal efficiency with a shorter combustion period at the ignition timing close to the top dead centre (Masood et al., 2007 and Mohammadi et al., 2007). Wide range of flammability limits enables a smooth engine operation at a very lean mixture with low NO_x level (Gadallah et al., 2009). The throttle control is unnecessary even at the idling condition in hydrogen engines (Ma et al., 2011). In particular, these unique properties can result in undesired combustion phenomena generally summarized as combustion anomalies. These anomalies include surface ignition and backfire as well as auto-ignition (knock) (Ringler et al., 2004 and Verhelst and Wallner, 2009).

Numerous studies and experiments to understand and solve the problem of pre-ignition and backfire were conducted over the past 70 years (Heffel, 2003). From the literature, the furthestmost issues regarding the spark-ignited H₂ICE combustion are the backfire and/or pre-ignition occurring as a lean fuel/air ratio approaches stoichiometric, which limits the torque output of the engine (Tang et al., 2002). Backfire is the condition when the fresh charge of hydrogen is ignited in intake ports while the pre-ignition is the condition when the hydrogen charge is ignited after the intake valve closes and before the spark plug fires in the cylinder (Liu, et al., 2008). These anomalies were identified in case of DIH₂ICE by Abdullah (2009). Backfire was appeared to start before the intake valve closed at the early injection timing and air fuel ratio close to stoichiometric (Figure 2.1a). The damage to the engine intake systems would be ensued when the engine continues to operate with this abnormal combustion. The backfire was eliminated by retarding the ignition timing during the tests, especially at air fuel ratios close to the stoichiometric.

The pinging noise was detected accompanied by a sharp rise in cylinder pressure and the corresponding pressure ripple when the engine was operated under certain conditions (Figure 2.1b). Combustion started prior to the spark. Thus, the knocking observed was thought to be due to pre-ignition caused by hot spots in the engine. These were characteristics of the engine pre-ignition. The pre-ignition was

reduced by cleaning the engine prior to the test program. Therefore, the existence of hot-spots from engine deposits was ruled out. There is ambiguity concerning the source of ignition. The wide ranges of the stated justification are summarized in Table 2.1. Based on these conditions, the backfire and pre-ignition limits are engine specifics. Direct-injection technique for hydrogen-fuel prevents the backfire phenomenon. However, the thermal efficiency and output power are limited by knock due to the reduction in volumetric efficiency (Mohammadi et al, 2007). The exact heat source of the initial pre-ignition is unclear and may have several sources depend on the operating conditions (Swain et al., 1988). The most promising approach is to avoid these anomalies for the combustion of the hydrogen-fueled engine is the optimized injection technique.

Table 2.1: Summary of the sources of ignition energy for abnormal combustion

Pre-ignition source energy	References
<i>Hot spots in combustion chambers</i> (the surfaces of the exhaust valve and spark plugs)	(Sierens and Verhelst, 2003 and Fiene et al., 2002)
<i>Hot particles</i>	(Verhelst et al., 2006; Das, 1996)
<i>Metal asperities</i> (such as edges of head cavities or piston bowls)	(Tang et al., 2002)
<i>The inert dust</i> (in the intake air as well as probably forgetting the function of the air filter)	(Das, 1996; Verhelst et al., 2006)
<i>Residual gases</i>	(Watson and Milkins, 1978; Li and Karim, 2006; Boretti et al., 2007)
<i>The overlap</i> (the opening between the intake and exhaust valves)	(He, 2001; Fiene et al., 2002)
<i>The pyrolysis</i> (chemical decomposition, which is brought out by heat, of oil suspended in the combustion chamber or in the crevices just above the top piston ring)	(Stockhausen et al., 2002; Boretti et al., 2007)
<i>The intense high voltage</i> (induced from the set of spark leads in the adjacent one)	(Verhelst et al. 2006)
<i>The residual energy</i> (in the ignition circuit)	(Kim et al. 2006)

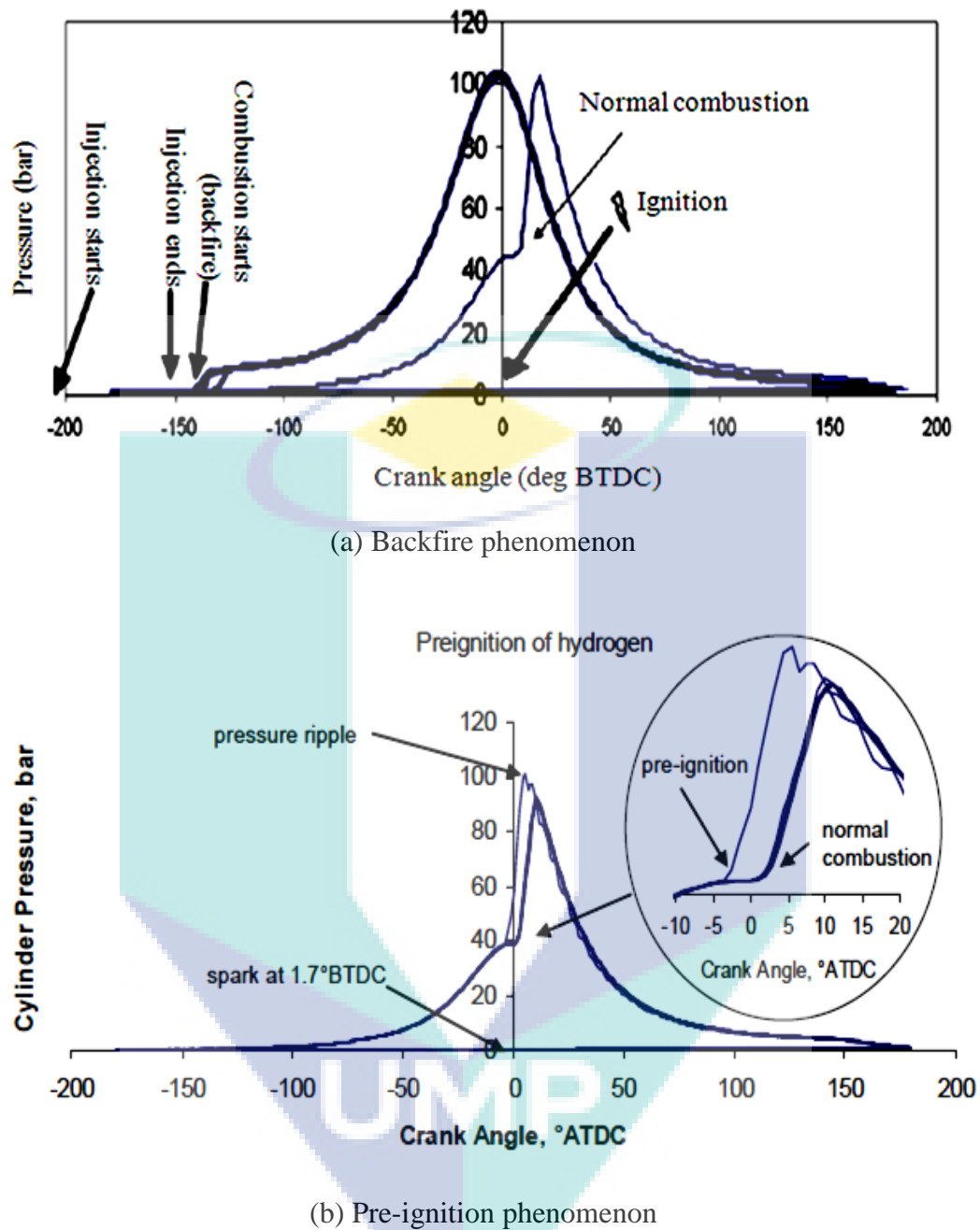


Figure 2.1: Identification of the combustion anomalies in DIH₂ICE

Source: Abdullah, 2009

2.4 HEAT TRANSFER IN SI ENGINES

During the last 40 years, the heat-transfer process between the working fluid and the combustion chamber walls and its noticeable effects on engine performance,

efficiency and emissions were intensively investigated and reported (Chiodi, 2011). The three modes of heat transfer (conduction, convection and radiation) are involved in the process of energy transmission from the gases to the engine components (Heywood, 1988). From the gases to metal, the forced convection is the main mechanism for heat transfer with a contribution by radiation (Suzuki et. al, 2000). It is known that the radiation contribution in compression ignition engines is more significant than the spark ignition engines due to the formation of highly soot particles during combustion (Stone, 1999 and Finol Parra, 2008). Conduction mechanism also contributes indirectly in heat transfer from the gases to the cylinder bores through the piston rings and skirts (Sanli et al., 2009). The heat transfer in internal combustion engines is one of the most crucial factors stirring the engine energy distribution in any operating conditions (see Figure 2.2). In case of a SI engine, the percentage of heat transfer to the fuel heating energy content is approximately 20-25 % for full load and even more than 30 % for low load (Chiodi and Bargende, 2001 and Chiodi, 2011). Therefore, the high accuracy in the determination of the engine heat transfer is a prerequisite for a realistic computational analysis.

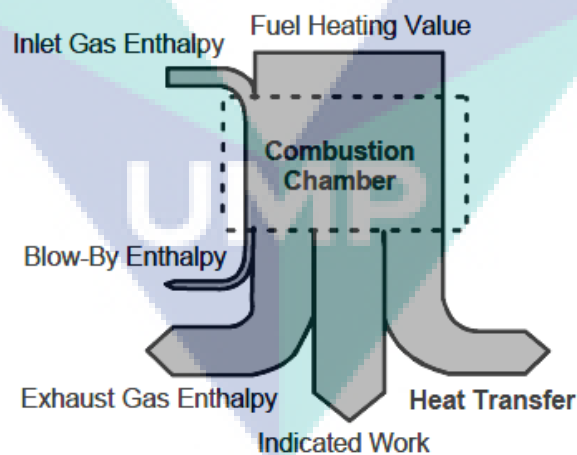


Figure 2.2: Schematic distribution for the engine energy.

Source: Chiodi and Bargende, 2001

Heat transfer in reciprocating engines is a non-uniform and unsteady phenomenon since the heat flux between the gases and walls vary during engine

operating cycle in time and space (Lounici et al., 2011). The heat flux from the in-cylinder gases to the walls has a wide range of change during the working cycle. It is varied from small negative values during charge exchange to positive values, in the order of MW/m^2 , during the combustion period (Borman and Nishiwaki, 1987). The heat flux into the wall has in general a convective as well as a radiation component. Numerous works were concentrated on the correlating and modeling of the heat transfer process for the internal combustion engine applications. The heat transfer correlations and models are reviewed in the following sub-sections.

2.4.1 Heat Transfer Correlations

Estimation of the heat transfer coefficient in ICE is a complicated due to the cyclic nature of the process. Many correlations were proposed based on the dimensionless analysis of the forced convection in turbulent flow inside circular tubes (Finol and Robinson, 2011). There are three categories of heat transfer correlations in ICEs according to the adopted method for averaging. For the first category, heat transfer coefficient is averaging over both time and position domains. Sometimes it is called a steady-state analysis. This analysis represents a simplified approach for the heat-transfer estimation in internal-combustion engine applications. Even that, it provides highly useful information when the interest focused on the total quantity of heat transfer rather than on the local and instantaneous values of heat flow. Results obtained by this approach considered to estimate the coolant thermal load in the engine design.

A detailed of steady-state investigations based on rigorous dimension analysis approach were presented by Taylor (1985). It was considered the independent influence of parameters such as ignition timing, mixture strength, engine size and speed (Stone, 1999). Taylor and Toong (1957) were derived time-averaged heat transfer correlation based on heat transfer measurements taken from 19 commercial engines of various sizes and configurations within three different types (Sanli et al., 2009 and Lounici et al., 2011), namely, water-cooled compression ignition engines, water-cooled spark ignition engines and air-cooled spark ignition engines (Finol and Robinson, 2006). The authors were followed a stricter approach for dimension

analysis. This correlation is often used for calculation of space, and time averaged heat transfer coefficient. The authors were proposed a power law of 0.75 for their correlation form with adjusting constant (a) varied from 7.7 to 15.5 approximately, depending on the engine type. It was highest for compression ignition water-cooled engines and lower for compression ignition air-cooled engines than for spark ignition water-cooled engines (Finol Parra, 2008). As commented by Annand (1986) and Heywood (1988), a relationship was correlated the data acquired from engines operation based on a wide range of piston speeds, intake charge densities and fuel-air ratios, Eq. (2.1):

$$Nu = a \times Re^m \quad (2.1)$$

Three different lines were identified by Annand (1986) based on the engine group in the original plot of Nusselt (Nu) versus Reynolds (Re) presented by Taylor and Toong (1957) as shown in Figure 2.3. Taylor (1985) was taken an averaged value of the factor a based on the experimental data. It was found that the expression corresponds very well to the averaged line as described in Eq. (2.2):

$$Nu = 10.4 \times Re^{0.75} \quad (2.2)$$

The accuracy of Eq. (2.2) to predict the heat flux coefficients depends mainly on the selection of the critical parameters, including the speed, characteristic length and thermodynamic properties (Heywood, 1988). Ideally, the speed is taken into account for the contribution of piston movement and combustion. It is also worth mentioning that the values used for the thermo-physical properties of gases (viscosity and thermal conductivity) depend strongly on temperature. This correlation was developed based on the measurements of the heat loss to the coolant, the lubricant oil, and less consideration for the heat of friction. However, most of the considered measurements were based only on the heat loss to the coolant. Thus, it was not fully coordinated with the concept of energy balance. As commented by Shayler *et al.*, (1997), in the best case no indirect heat contributions were considered. It was reported that the improvements of the energy balance were presented the better

predictions of steady-state heat transfer rate. It is relatively difficult to use a single correlation to determine the overall steady-state heat flux of different types of engines (Finol and Robinson, 2006). The dependency of factor a on the engine type revealed the possibility of obtaining better results simply by adjusting the correlation for a particular engine group (Stone, 1999). This correlation was commonly used for the estimation of the overall cycle of heat transfer rate to the wall. However, it was empirically developed from observations of engines fueled with gasoline and diesel fuel. There are no assessments for the capability of the existing correlation of time-averaged heat transfer in case of H_2ICE .

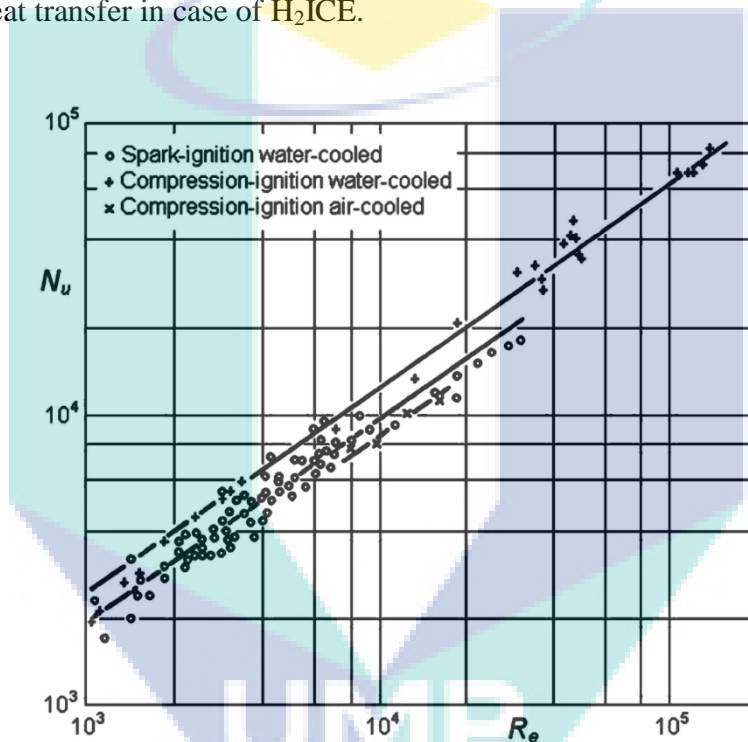


Figure 2.3: An example correlation of time-averaged heat transfer based on wide range of measurements for several engines.

Source: Annand, 1986

For the instantaneous correlations, the heat-transfer coefficient is usually averaging over an entire combustion chamber domain instantaneously (Mohammadi et al., 2008). Estimation of the instantaneous heat transfer coefficient is based on the quasi-steady assumptions for analyzing the in-cylinder heat transfer process. Thus, the heat transfer rate considers as proportional to the temperature difference between the working fluid and the metal surface at any instant. It also assumes a uniform

distribution of the instantaneous gas temperature in the cylinder (Suzuki et al., 2000). Even this approach was accepted it is not justified to consider a quasi-steady analysis of heat transfer from any rigorous theoretical or experimental point of view (Annand, 1963). This is because of the cyclic nature of heat transfer variation in a reciprocating engine. Moreover, there is a phase lag caused by the heat capacity of the fluid between the leading gas-to-wall temperature difference and the corresponding heat fluxes (Nijeweme et al., 2001).

A numerous of correlations was earlier suggested for estimating the instantaneous heat transfer coefficient between the charge and the confining surfaces. Among of these, the three correlations proposed by Eichelberg (1939), Annand (1963) and Woschni (1967) are most frequently used in cycle computations (Alkidas, 1980 and Demuynck et al., 2010). Annand's and Woschni's correlations were formulated based on the Newton's heat transfer equation and the theory of similarity, while Eichelberg's correlation was used Nusselt's equation for interpreting the heat transfer in a spherical bomb (Wu et al., 2006 and Sanli et al., 2009). The correlation proposed by Eichelberg (1939) was one of the early efforts to estimate the heat loss to the cylinder walls in reciprocating engines. The heat-transfer coefficient is expressed as Eq. (2.3):

$$h = 2.43 \times C_m^{\frac{1}{3}} \times (p T_g)^{\frac{1}{2}} \quad (2.3)$$

where h is the instantaneous heat transfer coefficient for combustion chamber.
 C_m is the mean piston speed.
 p is the instantaneous pressure of the in-cylinder gaseous.
 T_g is the instantaneous temperature of the in-cylinder gaseous.

It was distinguished by easy handling for expression of the characteristic velocity. It is based on Nusselt formula utilizing the experiments of heat transfer in diesel engines. The Nusselt formula take accounted for the convection and radiation separately, while Eichelberg version is not included the radiation effect (Oguri, 1960

and Wu et al., 2006). Essentially, both formulae interpret the heat transfer under conditions of free convection, which is, basically, another mechanism of heat transfer in a reciprocating engine (Lounici et al., 2011). In an internal-combustion engine, the heat is transferred from the gases mainly by forced convection with a contribution of radiation after ignition and during the expansion stroke (Rakopoulos et al., 2010). Therefore, these formulas are not theoretically appropriate to describe the in-cylinder heat transfer process, in particular, during the combustion (Woschni, 1967). Besides that, the lack of theoretical soundness, Eichelberg's correlation is mismatched in the dimension consistence. A considerable care is required for using exactly the specified unit. Otherwise, it has a different value for correlation's constant (Stone, 1999). Thus, it was expelled from the general usage.

Annand (1963) was proposed the first widely used correlation of the forced convection type, including an explicit radiation term. Annand was reviewed the existing correlations and analyzed the available data at the time, which included results from experiments in two different compression-ignition engines, one being a two-stroke and the other a four-stroke (Finol Parra, 2008). Annand's correlation was constructed based on the instantaneous heat flux measurements at selected location within the cylinder head (Wu et al., 2006 and Wu et al., 2009). Even that, it was often utilized to estimate instantaneous spatial-average heat fluxes for entire combustion chamber. The heat flux for Annand's correlation is expressed as Eq. (2.4):

$$\frac{\dot{Q}}{A} = a \times \frac{k_g}{d} \times Re^b (T_g - T_s) \quad (2.4)$$

where \dot{Q} is the instantaneous heat transfer rate.

A is the heat transfer area.

k_g is the thermal conductivity.

d is the cylinder diameter.

T_g is the instantaneous temperature of the in-cylinder gaseous.

T_s is the surface wall temperature.

a and b are the correlation coefficients.

The mean-bulk temperature was considered to evaluate the gas properties. The mean-bulk temperature was derived from cylinder pressure, charge mass and cylinder volume (Verhelst, 2005). Correlation coefficients were estimated based on the statistical regression methods and it used fit the given data. The proposed correlation was matched with previously published of experimental data. It was found the value of the empirical coefficients (a) varied with intensity of charge motion and engine design (Heywood, 1988). The variation of correlation's coefficients confirmed that significant factors were still ignored and presumably the relationship between piston speed and gas velocity was not strong enough (Watson and Janota, 1982 and Finol and Robinson, 2006). Another well-known correlation proposed by Woschni (1967) is widely used to estimate the instantaneous heat fluxes. This correlation is based on the power law expression for the steady forced convection heat transfer in turbulent flow, which is expressed as Eq. (2.5) (Incropera and DeWitt, 1990):

$$Nu = 0.035 \times Re^{0.8} \quad (2.5)$$

The exponent for Re is equal to that one for turbulent flow in pipes. The characteristic length was taken as the cylinder bore. The unknown gas velocity in the cylinder was empirically defined to be the characteristic velocity. It was correlated with measured data of the total heat transfer obtained from a heat balance in a test engine under motored and firing conditions (Finol and Robinson, 2006). The formula of heat transfer coefficient was established to describe the heat transfer data adequately described as Eq. (2.6) (Lounici et al., 2011):

$$h = 129.9 \times d^{-0.2} \times p^{0.8} \times T_g^{-0.53} \times \left[C_1 \times C_m + C_2 \times \frac{V_s \times T_r}{p_r \times V_r} \times (p - p_m) \right]^{0.8} \quad (2.6)$$

where h is the instantaneous heat transfer coefficient for combustion chamber.

d is the cylinder bore diameter.

p is the instantaneous pressure of the in-cylinder gaseous.

T_g is the instantaneous temperature of the in-cylinder gaseous.

C_m is the mean piston speed.

C_1 and C_2 are the adjustable constants.

V_s is the clearance volume of the combustion chamber.

r is the reference point (usually it is considered as the IVC)

The constants C_1 and C_2 are essential to take into account the changes in gas velocity over the engine cycle. On the other hand, C_1 and C_2 have to be consistent physical units. The suggested values for C_1 and C_2 are listed in Table 2.2. The prerequisite evaluation of the motored pressure p_m during combustion and expansion is a disadvantage of this correlation. Watson and Janota (1982) were suggested a method of calculating this pressure based on the energy equation. However, it is also proposed that assuming isentropic compression and expansion processes, with appropriate index, to compute of p_m based on the known reference conditions introduces no significant error and is simpler.

Table 2.2: Coefficients of Woschni's Correlation

Period	C_1	C_2
The scavenging period	6.18	0
Compression stroke	2.28	0
combustion and expansion stroke	2.28	3.24×10^{-3}

Several correlations were derived based on the original correlations of Woschni's and Annand's (Borman and Nishiwaki, 1987). The review of some of the most common correlations for the case of instantaneous heat fluxes illustrates the different methods and experimental approaches used to derive and validate the correlations (Finol and Robinson, 2006). It reveals a substantial difference in predictions of the instantaneous heat transfer coefficient as shown in Figure 2.4. It is not surprising to appear this wide variation in prediction values. This is because of various approaches were used for manipulating the velocity term.

Evaluation of these correlations based on the experimental measurements was not fully accurate. Even that, most of the subsequent investigations for modelling of

ICEs were used these correlations. Besides that, Woschni's correlation represents the generic form for most of the recent development of heat transfer correlation in an internal-combustion engine (Chang et al., 2004 and Soyhan et al., 2009). In spite of the limitations of empirical correlation in predicting the instantaneous heat transfer coefficient over the engine cycle, the correlations based on zero-dimensional models in which the flow field is not adequately considered (Finol and Robinson, 2006; Finol Parra, 2008 and Buttsworth et al., 2009). These correlations are still the benchmark for analyzing the engines heat transfer and the improvement of more advanced models, mainly because of their simplicity (Demuynck et al., 2011).

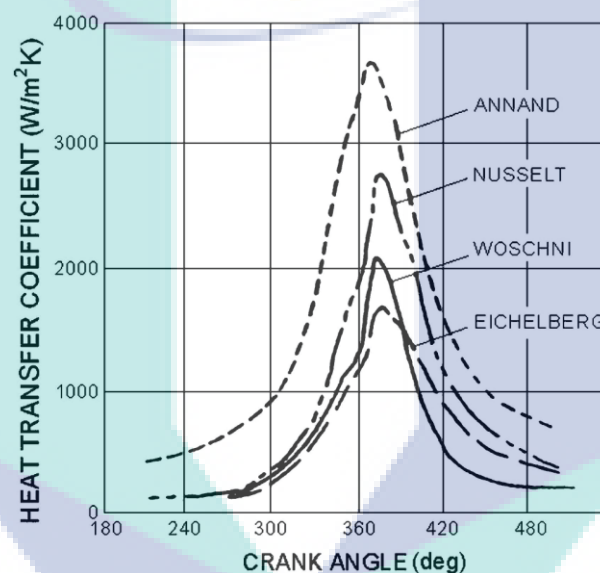


Figure 2.4: Comparison of predicted heat transfer coefficient for several correlations

Source: Watson and Janota, 1982

The local prediction of heat fluxes in the combustion chamber requires some knowledge of the local conditions, either from theoretical considerations or by experience. The comprehension correlation of the spatial and time variation for the engine heat transfer is required in case of computing thermal analysis. It is required solution of three-dimensional, unsteady Navier-Stoke's equations coupled to the energy equation, atom conservation equations, a turbulence model, equation of state, and chemical kinetic rate equations (Ferguson, 1986).

Earlier, the experimental measurements were performed at several positions within the combustion chamber to develop these kinds of correlations. Later, an alternative approach has been arisen, which is using the zonal modeling (Heywood, 1988). With limited application to firing engines, LeFeuvre et al., (1969) were proposed a correlation to predict the instantaneous wall heat flux on the cylinder head or piston at different radial distances from the bore axis (Heywood, 1988). This correlation was intended for convective heat transfer. Therefore; it was not expected to predict the total heat flux in a fired engine with high accuracy (Finol and Robinson, 2006). However, it was subsequently used to predict the heat transfer under the motored and fired conditions. The correlation was revealed a reasonable agreement with experimental measurements in some locations; however, it was over-predicted at other locations for most of the cycle, particularly during combustion (Nishiwaki, 1998). The observed differences in heat transfer between different locations challenge the hypotheses of mass-averaged gas properties and uniform gas temperature throughout the combustion chamber being implemented as the basis temperature for heat flux to the cylinder walls. This correlation was modified by Dent and Suliaman (1977) using the engine with higher swirl ratios than those considered by LeFeuvre et al. (1969). An identical correlation form was proposed to the previous one, but with the higher coefficients due to the higher swirl velocity along with different engine specifications, and the consideration of radiation heat transfer.

With progress in development of CFD approach, the more accurate and meaningful formulation for the heat transfer becomes achievable. In the last two decades, CFD as a high speed and low cost advantage tool is being widely used in various platforms of engine design and optimization. One of the most valuable aspects, for heat transfer in the engine combustion chamber, is the estimation of the instantaneous convection coefficient at various locations (Nijeweme et al., 2001). Currently, the CFD tools are utilized for prediction of the instantaneous convection coefficient at various locations with the combustion chamber.

2.4.2 Heat Transfer Models

Numerous models, with the different level of complexity, were proposed to quantify heat fluxes arising from combustion. A comprehensive review of heat transfer models for engine applications was presented by Borman and Nishiwaki (1987). It was particularly based on the analytical and experimental investigations to classify the models of heat transfer in case of spark ignition engine into three categories namely global, zonal, one-dimensional and multidimensional models. This division was based on the spatial resolution of the core region. With global models, the instantaneous heat transfer coefficient was estimated according to the steady heat transfer correlations found in flows over flat plates and pipes (Torregrosa et al., 2008). In this convection dominated flows, the boundary layers are fully developed and in equilibrium with each other. Therefore, an analogy between the transport of energy and momentum is valid (Borgnakke et al., 1986). Empirical correlations with non-dimensional groups as parameters were introduced based on the quasi steady-state assumption for denoting the global models (such as Annand 1963; Woschni, 1967 and Han et al., 1997). With these models, the averaged heat transfer coefficient supposed identically for all the surfaces of the combustion chamber (Bohac et al., 1996). Global models were considered the dimensionless correlations to estimate the overall heat transfer coefficient. The global models are inadequate to describe the details of local and unsteady heat transfer impacts. It is commonly used to address the overall impacts on the state of the entire cylinder gas. These models are suitable for simulation purposes of the engine cycle (Galindo et al., 2006 and Xin et al., 2009).

The main drawback of global models is unable to differentiate between the hottest and coolest region inside the combustion chamber. At least the two-zone combustion models are needed to distinguish between the fresh air zone and the burned zone (Ciulli et al., 1993). This is required to obtain knowledge of the temperature's history in order to evaluate the two transfer mechanisms separately (Guezennec and Hamama, 1999). Multi-zone (zonal) models (such as Krieger and Borman, 1966; Poulos and Heywood, 1983 and Morel et al. 1985), were developed to promote more benefits for ICEs applications. The main difference between global

and zonal models is the adopted approach for description of the study domain (combustion chamber). The global models are considered the combustion chamber as a single region filled with air-fuel mixture has the regular properties. While in case of the zonal, for example, in two-zonal models (Krieger and Borman, 1966 and Poulos and Heywood, 1983), the combustion chamber was divided into an unburned and a burned zone. The inherent dependence of the convective heat transfer on the actual flow velocities and the spatial resolution represent the main features of the zonal models. The Colburn analogy was considered for calculation of the heat transfer coefficient (Morel and Keribar, 1985). Zonal models are able to address the effect of flame propagation on the heat transfer variation. This advantage for the zonal model due to each unburned and burned zone has its own history of the heat transfer coefficient for the estimation of heat flux of each zone (Bargende, 1991). However, some applications require more specific local information of heat transfer, temperature and flow field. The disadvantage for the global and zonal models is unpredictable for these requirements. Besides that, these models need adjustable parameter that is robustly subordinated on tentative constants. The validity of these models is confined to the operating range from which the correlation is acquired. These models are suitable for engineering applications that require only global amounts (Ciulli et al., 1993).

Heat transfer takes place through the thermal boundary layers of the combustion chamber and the solid walls with the steepest temperature gradient at the wall (Borman, 1990). One-dimensional heat transfer approach is distinct from global and zonal models in the representation of the boundary layer's nature due to include the energy equation within the assumption and solution scheme for that approach (Nijeweme et al., 2001 and Buttsworth et al., 2009). The computation of wall heat flux for one-dimensional models is performed based on the energy equation for thermal boundary layer without employing the heat transfer coefficient (Isschiki and Nishiwaki, 1970; Grief et al., 1979; Yang and Martin, 1989 and Han and Reitz, 1997). Both cores and the near-wall regions were identified. The detailed solution based on the assumptions of thermal boundary layers was considered for the near wall region calculations. The core region was dealt as a global region with uniform characteristics in the absence of spatial variation or multidimensional core regions. It

is not correct to represent the core region by using the global approach because of the local variation existence due to turbulence, swirling, tumbling motions and combustion impacts with the flame propagation. From this point of view, employment of the multidimensional approach for the core region is justifiable in case of one-dimensional heat transfer models for a comprehensive and an advanced analysis of heat transfer.

Multidimensional modelling represents the general approach for all modern computational codes (CFD). It provides very valuable and complete information, as compare with experiments or simple models, of the in-cylinder flow pattern. It is difficult to simulate the heat fluxes adequately through the cylinder walls due to the unsteady and highly inhomogeneous temperature distribution of the cylinder charge as well as the uncertainty existing in the determination of the initial and boundary conditions of the problem (Rakopoulos et al., 2010). The CFD codes become an efficient tool for the heat transfer calculations in ICEs applications. Most of the current CFD codes utilize either a wall function or a near wall modelling approach to describe near the wall flow conditions in the heat transfer calculations. The abundances of literature are revealed for various heat transfer models, which are based on the wall-function hypothesis. The basic formula for all available models is developed by Launder and Spalding, (1974). This approach is extensively considered in multidimensional simulations, because it provides a robust technique of computing the thermal boundary layer without increasing the computational nodes that are placed within this layer (Han and Reitz, 1997). Of course, the various formulations can be found where the number of nodes in the boundary layer is increased and the law-of-the-wall is applied there with satisfactorily results (Nishiwaki, 1998 and Rakopoulos et al., 2010).

Rakopoulos et al. (2010) presented a critical evaluation of current heat transfer models used in CFD in-cylinder engine simulations. It is included the establishment of a comprehensive wall-function formulation for estimation the heat fluxes. It was differentiated which wall-function formulation is more suitable for each engine type and under what operating conditions. The model of Launder and Spalding, (1974) revealed its weaknesses in all cases considered, as has also been

demonstrated by many researchers so far (Han and Reitz, 1997 and Nishiwaki, 1998). However, its improved version was acquired best estimation of wall heat loss (Amsden, 1997 and Xin et al., 2003). Therefore, it will be considered later on for multidimensional modelling in this study.

Both local and instantaneous characteristics are easily identified by using the multidimensional modelling and CFD codes. As well as, the parametric investigations become more achievable due to including several sub-models, which describe each phenomenon. The three dimensional compressible averaged Navier-Stoke's equations are solved on a moving mesh. Turbulent fluxes are modeled by an eddy viscosity concept using κ - ϵ model (Torregrosa, 2008). There are a number of commercial CFD packages such as FIRE, Fluent, KIVA and STAR-CD, which provide superior combustion engine multidimensional capability. However, the most widely used for the engine simulation is KIVA family of programs originally developed at Los Alamos National Laboratory. The basic features of the code were well-documented (Amsden et al., 1989 and Amsden, 1997). KIVA family is a three-dimensional, multi-component model capable of simulating multiphase flow under steady state and transient conditions. The code solves an unsteady three-dimensional compressible average Navier-Stoke's equations coupled to a k - ϵ turbulence model. The k - ϵ model uses the wall function.

In all CFD codes, the chamber wall temperatures, the refinement and accuracy of the supplied information are vital parameters for determining the magnitude of the heat flux. If an accurate wall temperature distribution is unavailable as input data to the CFD code, even with improved temperature wall functions, it is still impossible to obtain accurate heat flux results (Liu and Reitz, 1997). Multidimensional modelling has a vast scope due to including many aspects of physics. The depth of the review is limited to heat transfer aspect in SI engine application. For more comprehensive details related to multidimensional modelling and CFD codes can be found in the supporting references for the commercial CFD programs.

2.5 HEAT TRANSFER CORRELATIONS APPLICABLE FOR H₂ICE

Evaluation of the existing heat transfer correlations represents a prerequisite step for improving and developing an enhanced correlation for any application. It is useful to make some crucial comments here for the validity of the existing correlations in H₂ICE application. Regarding the time-averaged correlation was proposed by Taylor and Toong (1957), one would expect that the various constants base on data collected on engines from fifty years ago would be different when the data are taken from more efficient, modern engines were used (Finol and Robinson, 2006). Moreover, the hydrogen properties have vast differences in the compared with fossil fuels (Wei et al., 2001). The differences are not for the quantity of the liberated heat transfer from the combustion process but also the unique behavior for the hydrogen combustion (Shudo and Suzuki, 2002a). Thus, updating this equation would yield to more accurate heat balance calculations and enhance definitions of engine cooling requirements even at the design stage of H₂ICE.

The applicability of instantaneous spatially averaged correlations for H₂ICE was evaluated. The best known of these correlations are considered during the previous evaluation studies. Most of the correlations intended for this purpose are based on Eichelberg (1939), Annand (1963) and Woschni (1967) correlations. Woschni's correlation was under predicted of the heat-transfer loss based on the experimental of H₂ICE. However, multiplication of the original correlation's constants by 1.8 acquired a better match with the experimental data (Smith and Aceves, 1997).

An experimental investigation was performed by Wei et al., (2001) to clarify the effect of fuel type on the heat transfer coefficient. Instantaneous measurement for the heat-transfer coefficient was conducted for hydrogen and gasoline on the same test rig. It was noticed that instantaneous heat transfer coefficient was differentiated according to the fuel properties. In terms of absolute values, heat transfer coefficient for hydrogen-fueled engine was about twice higher than that of the gasoline-fueled engine within most of the cycle. Besides that, the reliability of using the existing empirical correlations was evaluated for hydrogen and gasoline fuel. Comparisons

between the measurements and predictions of the empirical correlations are demonstrated in Figure 2.5. In case of gasoline, it was consistent with remarks of the previous investigations for hydrocarbon fuels. However, predictions of the empirical correlations were significantly different from the experimental results of the hydrogen-fueled engine. Woschni's correlation was under predicted results for the heat-transfer coefficient by a factor of two while closer results were obtained from Annand's correlation. Furthermore, it was found the transient heat transfer coefficients during hydrogen combustion to be twice as high as during gasoline combustion. Accordingly, an equation was suggested for describing the impact of fuel properties on the heat-transfer coefficient, which is expressed as Eq. (2.7):

$$\zeta = \frac{C_{H_2}}{C_g} = \frac{h_{H_2} / (p_{H_2} \times T_{H_2})^{0.5}}{h_g / (p_g \times T_g)^{0.5}}$$

$$\zeta = 2.556 \times \exp(-0.0197 \times \theta) \quad (2.7)$$

where

ζ is the ratio of heat transfer for hydrogen to that one for gasoline

C is the term that includes the effect of fuel properties, gas velocity, geometry shape factor etc.

h is the instantaneous heat transfer coefficient for combustion chamber.

p is the instantaneous pressure of gaseous within combustion chamber.

T is the instantaneous temperature of gaseous within combustion chamber

g and H_2 are the subscript refers to gasoline and hydrogen respectively.

θ is the crank angle (deg).

Eq. (2.7) is expected to provide a reasonable inspection for enhancing the empirical correlation of the heat transfer. However, authors were not performed any assessment for the heat-transfer correlations. In actual, this formula accounts on the differences caused by fuel properties without improving the correlation itself.

Shudo and Suzuki, (2002a) were analyzed applicability of existing correlations to estimate the amount of heat loss from H₂ICE. The instantaneous heat transfer coefficient and the cumulative cooling loss were considered for the evaluation process. The weakness in prediction of heat transfer rate was detected in case the hydrogen combustion. It was found that the actual cooling loss in hydrogen stoichiometric combustion is four times higher than the value calculated by Woschni's equation. Therefore, the existing correlations were not applicable to hydrogen combustion due to the significant differences in properties (Demuynck et al., 2008).

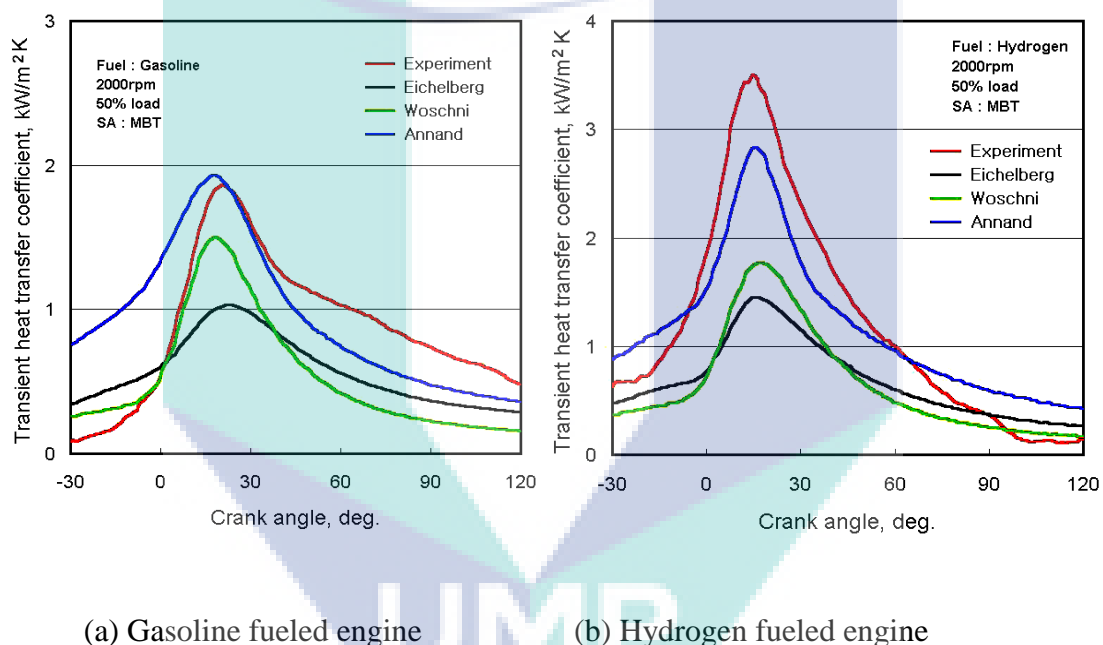


Figure 2.5: Instantaneous heat transfer coefficient measured comparing to those of empirical equations

Source: Wei et al., 2001

A modified correlation was suggested based on the Woschni's correlation for an instantaneous spatially heat transfer estimation in the hydrogen-fueled engine (Shudo and Suzuki, 2002b). It was considered the specific heat ratio as a variable during estimation of the apparent rate of the heat release. The specific heat ratio was calculated from the composition and average temperature of the gaseous within the combustion chamber. This is because of the combustion of hydrogen accompanying with a large variation in the specific heat ratio (Shudo et al., 2001b). The validity of

the modified correlation was performed based on the curve of cooling loss. It was estimated based on the experimental measurements combining with the Wiebe's function for the heat release calculations (Shudo and Suzuki, 2002c). That means, it is an independent character with respect to the estimated the heat transfer rate. The gas velocity term in Woschni's correlation was corrected in order to produce the same rate of cooling loss. The correction was included the constants as well as the distinguishing factor $(p-p_m)$ in the gas velocity expression. It was revealed that the constants' corrections were insufficient to describe the rapid increase in cooling loss during a combustion period of hydrogen. Even it was increased the value of the total cooling loss per cycle (Shudo and Suzuki, 2002a). The total cooling loss for the cycle was controlled by adjusting the second constant in gas velocity term only. However, the trend of the calculated cooling loss in the early part of combustion was remained inadequate (Shudo and Suzuki, 2002b). Consequently, the apparent rate of the heat release term $(\frac{dQ}{dt})$ was used as a distinguishing factor instead of the in-cylinder pressure difference $(p-p_m)$. Because of it is more responsive to the rapid combustion of hydrogen (Figure 2.6). Finally, the modified heat transfer correlations were proposed to be applicable to H₂ICE as Eq. (2.8) to Eq. (2.10) (Shudo and Suzuki, 2002b):

$$h = C_1 \times d^{-0.2} \times p^{0.8} \times T_g^{-0.53} \times w^{0.8} \quad (2.8)$$

$$w = C_m + C_2 \times \frac{dQ}{dt} \times \frac{T_r}{p_r \times V_r} \quad (2.9)$$

$$\frac{dQ}{dt} = \frac{V}{\gamma-1} \times \frac{dp}{dt} + \frac{\gamma}{\gamma-1} \times \frac{dV}{dt} - \frac{pV}{(\gamma-1)^2} \frac{d\gamma}{dt} \quad (2.10)$$

where h is the instantaneous heat transfer coefficient for combustion chamber.

C_1 and C_2 are the adjustable constants.

d is the cylinder bore diameter.

p is the instantaneous pressure of the in-cylinder gaseous.

T_g is the instantaneous temperature of the in-cylinder gaseous.

w is the instantaneous velocity of the in-cylinder gaseous.

C_m is the mean piston speed.

Q is the heat release.

t is the instantaneous time.

V is the instantaneous volume of the combustion chamber.

γ is the specific heat ratio for the in-cylinder gaseous.

r is the reference point (usually it is considered as the IVC)

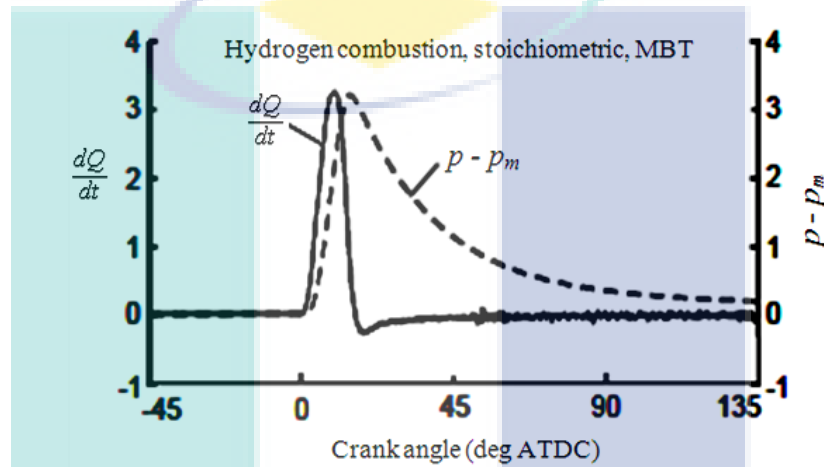


Figure 2.6: Comparison between the apparent heat release $\frac{dQ}{dt}$ and the in-cylinder pressure difference ($p - p_m$)

Source: Shudo and Suzuki 2002b

The values of constants, C_1 and C_2 , were supposed to be a function of the ignition timing and excess air ratio. The influence of an excess air ratio on the constants was larger than that of the ignition timing (Shudo and Suzuki, 2002b). The modified correlation was successfully described the cooling loss curve of hydrogen combustion without a delay in the increase of the cooling loss in the early part of combustion (see Figure 2.7). However, the correlation contains two calibration parameters C_1 and C_2 , dependent on the ignition timing and equivalence ratio. These dependencies are stated to be the subject of further studies (Safari et al., 2009 and Verhelst and Wallner, 2009). Moreover, the modified correlation needs to recalibrate for every measurement in order to match the measured heat flux (Verhelst, 2005; Demuynck et al., 2009 and Demuynck et al., 2011). Thus, this correlation is still under development and not widely use, until now.

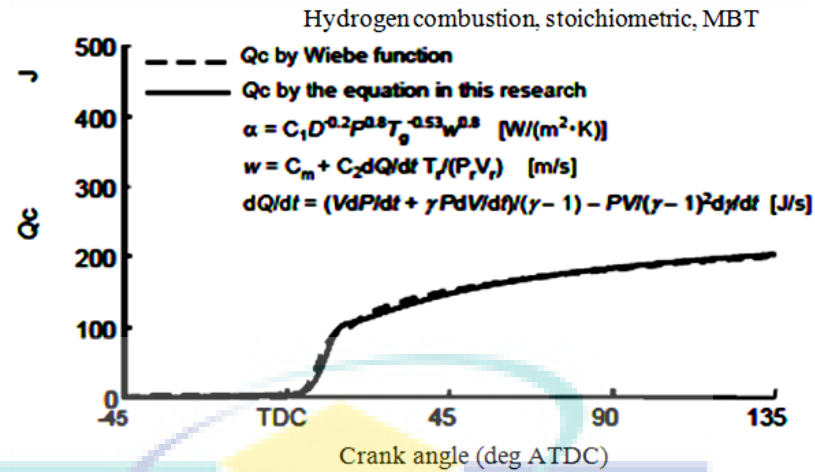


Figure 2.7: Comparison between the real cooling loss (estimated by Wiebe's function) and that one predicted by the new correlation

Source: Shudo and Suzuki, 2002b

Clearly, there is a difference in the heat-transfer process between hydrogen and a fossil fuel (Demuynck et al., 2011). The existing heat transfer correlations need to be evaluated for the hydrogen fuel (Demuynck et al., 2009 and Demuynck et al., 2010). Accordingly, Demuynck et al., (2011) were tested several hypotheses regarding the amount of necessary calibrations. The evaluation tests were based on two criteria namely the maximum in the heat flux traced and the total cycle heat loss. Well correlations' performance is important on both values. The maximum gas temperature is mainly depending on the maximum heat flux. Hence, an accurate estimation of it is essential for a better determination of NO_x emissions. An accurate prediction of the total cycle heat loss is essential for an exact computation of the engine's power and efficiency.

Annand's and Woschni's correlations were tested to take account of the influence of the fuel properties. Both correlations were failed to predict the heat flux and total heat loss accurately for the hydrogen combustion at all (Demuynck et al., 2011). Therefore, the correlations were recalibrated for the hydrogen combustion and their ability to estimate the influence of a variation the equivalence ratio was evaluated. It was revealed that the correlations lack some parameters that have an influence on the heat transfer process in an engine. Consequently, it was suggested to be recalibrated every time and need to be improved. For hydrogen, the correlations

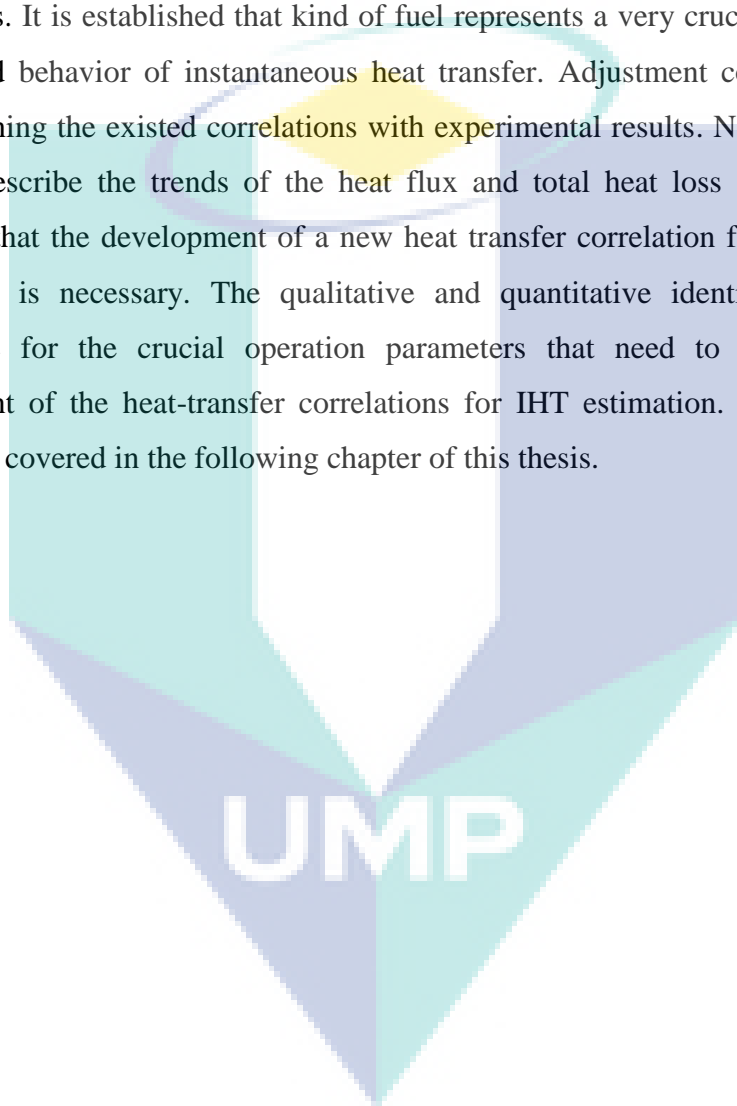
were not even capable of simulating a variance in the air-to-fuel equivalence ratio after a calibration.

For instance, in a recent work by Nefischer et al. (2009), the applicability of the quasi-dimensional heat transfer model developed by Schubert et al. (2005) was investigated. This model was developed based on a comprehensive description of the turbulent flow field in the combustion chamber of the compression ignition engine. It was provided a better selection approach for the significant parameters, in particular, the characteristic velocity. Therefore, it yields accurate results for the local heat flux. It was realistically described the required characteristic velocity considering the influence of the injection on the global turbulence and on the in-cylinder flow field. However, the model's prediction was deviated from the experimental measurements at higher engine speed (5000 rpm). A better prediction of the wall heat transfer was during the compression stroke and for operations with multiple injections. While, the increased wall heat transfer caused by an inhomogeneous mixture was unpredictable by the tendency of the flow field model. This is because of the uncertainty in estimation of the characteristic velocity which is directly related to the flame speed.

2.6 CONCLUSIONS

The significant progress in heat transfer of engines research was apparently reviewed. In parallel, several uncertainties were revealed in applicability of the developed correlations and models in case of H_2ICE . The recent developments for H_2ICE are focused on the direct-injection technique. It can be concluded that developing an injection model applicable to DIH_2ICE would be a good contribution to the automotive sectors. Hydrogen combustion within ICEs has some anomalies namely the backfire and pre-ignition. The backfire is practically avoided using the direct-injection technique. However, the energy sources of pre-ignition are unclear. The most promising approach to avoid these anomalies for combustion of H_2ICE is the optimized injection technique. The time-averaged correlation with various constants was proposed by Taylor and Toong based on data collected on engines from fifty years ago. It would be different when the data are taken from more efficient, modern engines were used. Moreover, the vast differences of hydrogen

properties and the unique behavior for the hydrogen combustion compared with fossil fuels are another motivated to evaluate this correlation. The present review showed that although the best known of the instantaneous spatially-averaged correlations, proposed by Annand, and Woschni over forty years ago, have been validated by other authors against more recent data. The applications of these correlations to the modern engine are questionable, especially for H₂ICEs applications. It is established that kind of fuel represents a very crucial factor on the amount and behavior of instantaneous heat transfer. Adjustment coefficients were used for tuning the existed correlations with experimental results. Nevertheless, it is failed to describe the trends of the heat flux and total heat loss accurately. It is concluded that the development of a new heat transfer correlation for the hydrogen combustion is necessary. The qualitative and quantitative identifications are a prerequisite for the crucial operation parameters that need to be included in development of the heat-transfer correlations for IHT estimation. There are more issues to be covered in the following chapter of this thesis.



CHAPTER THREE

COMPUTATIONAL MODELING AND EXPERIMENTAL DETAILS

3.1 INTRODUCTION

This chapter is dedicated to explain the adopted methods in this research. The numerical and experimental works were performed in order to specify the heat-transfer characteristics of SI engine operating on the hydrogen fuel. The experimental setup and facilities that were utilized for the engine-testing program and database collection was presented. The numerical work includes both one-dimensional as well as multidimensional modeling. Detail aspects for the one-dimensional model based on the gas dynamics approaches are stated. The multidimensional modeling based on the finite volume approach is also explained.

3.2 STRATEGY OF WORK FRAME

The flowchart of the strategy framework for the current research methodology is described in Figure 3.1. It shows three main implements, including the one-dimensional modeling, three-dimensional modeling and the experimental work. According to this framework, the results are clarified in a logical manner. The outcomes of this framework strategy are summarized in the conclusions and recommendations for future studies.

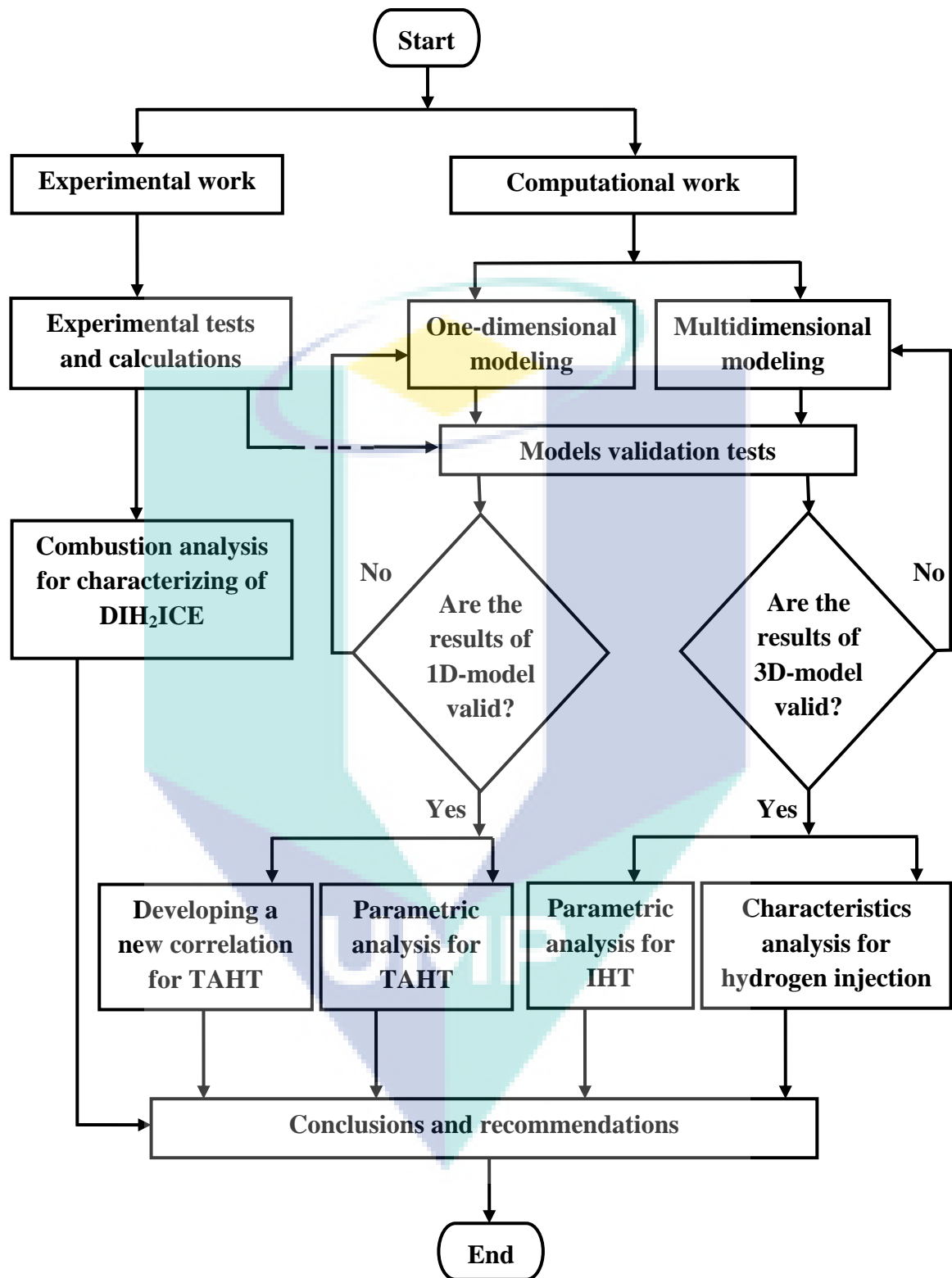


Figure 3.1: Strategy of the work frame for the current research methodology

3.3 EXPERIMENTAL DETAILS

This section is devoted to describe the major experimental setups and the approach for engine combustion analysis. Experimental setups describe the experimental engine test-rig and the important equipments for measurement, including the cylinder pressure, fuel injection, engine speed, engine torque and *AFR*. Approach of the engine combustion analysis defines the time-averaged and instantaneous indicators.

3.3.1 Experimental Setup

A schematic of the experimental setup in details of the main components are presented in Figure 3.2. The experimental tests are conducted based on the PROTON CAMPRO research engine. The engine specifications are listed below in Table 3.1.

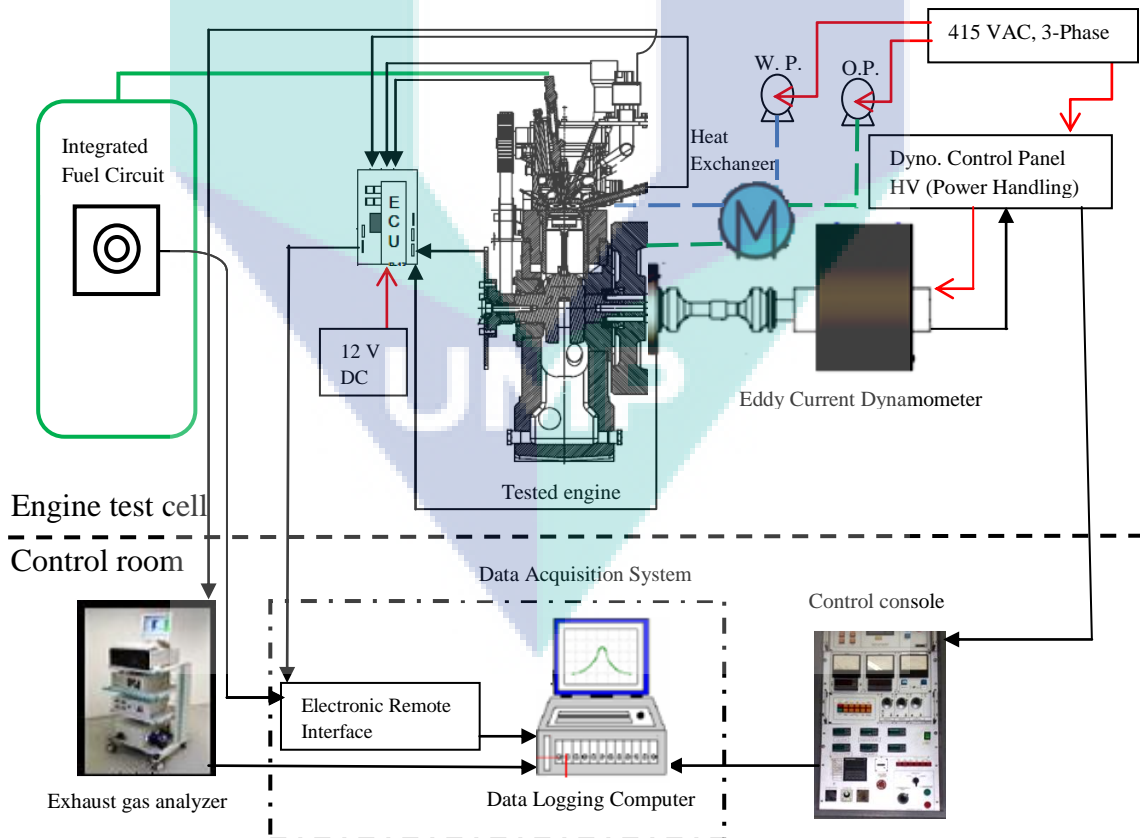
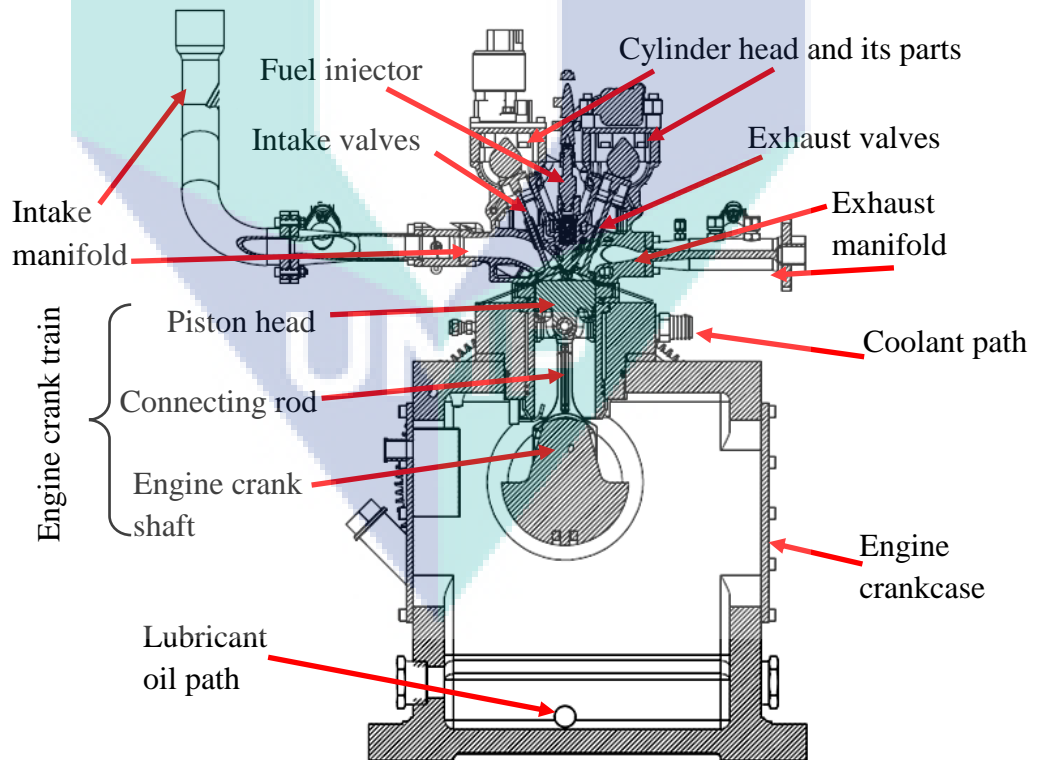


Figure 3.2: Schematic of the test cell for the experimental setup

Table 3.1: PROTON CAMPRO engine specifications

Parameter	Value	Unit
Bore	76.0	mm
Stroke	88.0	mm
Displacement	399.25	cm ³
Geometric compression ratio	14.0	
Connecting rod length	131.0	mm
Intake valve open (BTDC)	12	deg
Intake valve close (ABDC)	48	deg
Exhaust valve open (BBDC)	45	deg
Exhaust valve close (ATDC)	10	deg
Intake valve diameter	30.0	mm
Exhaust valve diameter	27.0	mm

Figure 3.3 shows the details of this engine, which is also used for developing the computational models. It is a single cylinder, four stroke, direct injection, water-cooled SI engine.

**Figure 3.3:** Details of the PROTON CAMPRO research engine.

The aluminum cylinder head has a pent-roof configuration for the combustion chamber with a center-mounted sparkplug. The cylinder head has dual intake and exhaust valves actuated by a double overhead camshaft (DOHC) through direct attack tappets. The cylinder head for PROTON CAMPRO engine is shown in Figure 3.4.

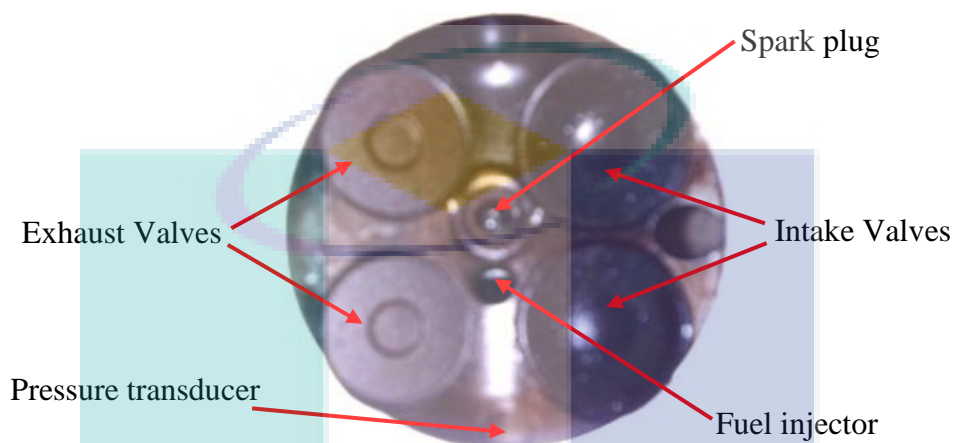


Figure 3.4: The engine cylinder head showing the injector, pressure transducer and sparkplug positions as well as the intake and exhaust valves.

Fuel is injected into the combustion chamber by a single fuel injector located at the cylinder head as shown in Figure 3.4. Details of the fuel injector are listed in Table 3.2.

Table 3.2: Fuel Injector specifications

Specification	Description
Manufacturer	Synerject
Part number/designation	37-152CNG
Nozzle spray angle	30 deg
Spring	33.0 N
Stroke	0.135mm
Maximum operating pressure	2.0 Mpa (high pressure)
Turn on time	1.05 ms
Turn off time	0.95 ms
Operating voltage	14.0 VDC
Coil resistance	1.3 ohm

The fuel injector is considered with a narrow angle for injection (30 deg) to provide a proper fuel spray penetration. This is because of hydrogen has low density and viscosity as well as high diffusivity. The injection pressure for experiments is considered 18 bar. Injector is fed with hydrogen fuel by utilizing an integrated fuel system as shown schematically in Figure 3.5. The integrated fuel system is consisted of the hydrogen gas bottles at 200 bar pressure, pressure regulators, pressure gages, pneumatic valve, compressor and micro-motion flow meter.

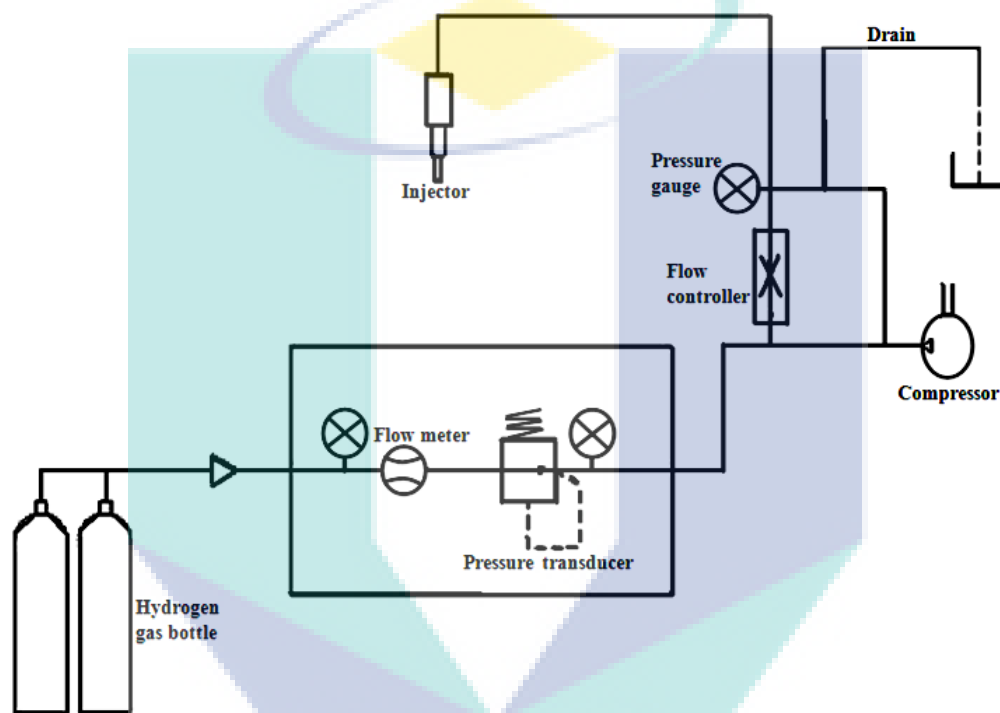


Figure 3.5: Schematic of the integrated fueling system

Figure 3.6 demonstrates the experimental setup of the integrated fueling systems. Table 3.3 provides the specifications of the utilized hydrogen gas in this experiment. The specifications of micro-motion flow meter for fuel are listed in Table 3.4. The engine cooling system was modified in order to carry out the experiment. The generated heat by the combustion is transferred to the open cooling circuit fed by tap water. A specified heat exchanger is used to transfer the heat. The coolant of the engine is circulated through an external pump (0.18 kW) which is derived by electric motor. The coolant temperature is maintained at $(70 \pm 5 \text{ }^{\circ}\text{C})$. The oil circulation system consists of the oil pump, filter and connection pipes with a

specified heat exchanger. The oil temperature is controlled utilizing the same external cooling circuit to be within range (90 ± 5 °C).

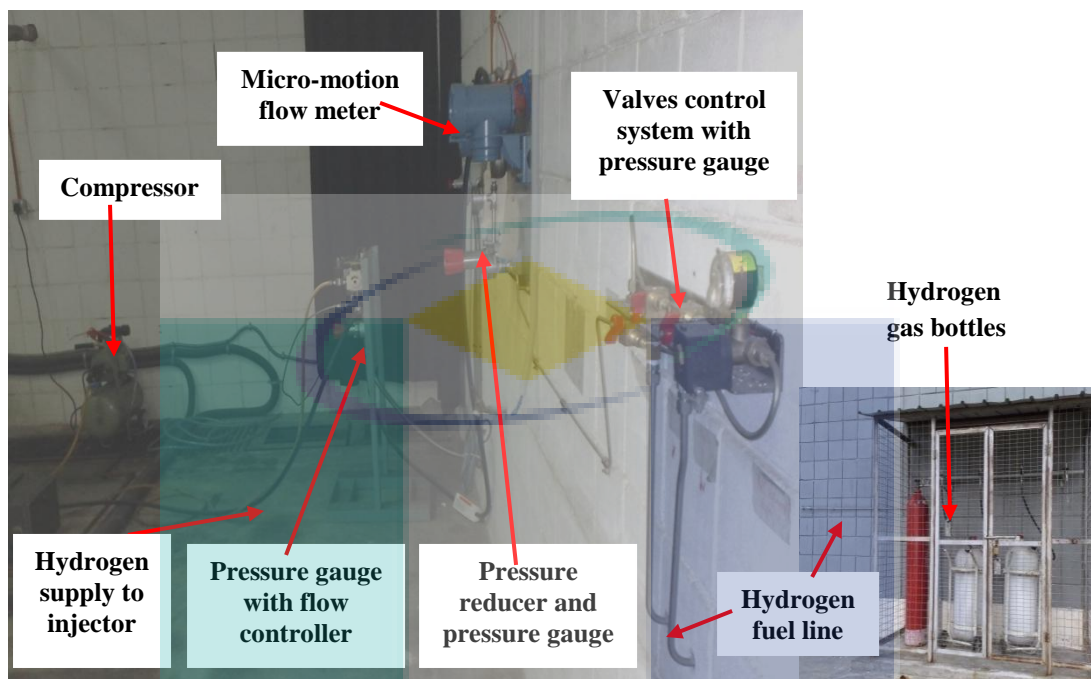


Figure 3.6: Experimental setup of the fueling system

Table 3.3: Hydrogen fuel specifications (Abdullah, 2009)

Parameter	Value
Purity	99.999%
Moisture	<3 vpm
Oxygen	<3 vpm
Hydrocarbon	<1 ppm
Carbon monoxide	<1 ppm
Carbon dioxide	<1ppm

The in-cylinder pressure trace is instantaneously measured by using piezoelectric transducer for pressure measurement. It is a Kistler ThermoComp[®], water cool type pressure transducer. A special threaded hole was made in the cylinder head to accept the pressure transducer as shown in Figure 3.4. The specifications of the pressure sensor are listed in Table 3.5.

Table 3.4: Micro-motion flow meter specifications (EPM, 2006)

Specification	Description
Make and model	Micro-motion™ CMF010 ELITE Series fuel flow meter
Flow accuracy	± 0.05 % of flow rate
Gas accuracy	± 0.35 % of flow rate
Density accuracy	± 0.0002 g/cc
Wetted materials	304 L, 316 L Stainless Steel or Nickel Alloy
Temperature rating	-240 to 427 °C
Pressure rating	100 to 413 bar

Table 3.5: Pressure sensor specifications

Specification	Description
Make and model	Kistler ThermoCOMP®
Range	0-250 bar
Linearity all ranges	$< \pm 0.5$ % FSO
Sensitivity shift, cooled 50 ± 35 °C	$< \pm 0.5$ %

A crank angle encoder is used to specify the angular position of the engine. A Hall Effect sensor has been mounted at the end of the engine's shaft provides the clock signal for crank angle measurement. The signal from the crank angle encoder is arrived at the signal conditional and then transferred to the combustion analyzer for recording. The crank angle encoder and pressure sensors are connected to a computerized based combustion analyzer, completed with data acquisition system. Combustion analyzer unit is employed for pressure data collection in crank angle domain.

A programmable ECU (Orbital Inc.) is used to control the engine. It is controlled of the injection timing and duration, the spark timing, *AFR* and throttle position. The ECU is connected to ECU Remote Interface (ERI) installed in the personal computer for data collection. The power for the ECU board is supplied from 12 V DC source as shown in Figure 3.7a.

The test cell includes an eddy current dynamometer for loading the engine. An eddy current dynamometer (David McClure DC30) is utilized for power absorption and engine speed regulation. This dynamometer is a bi-directional, dry

type. Dynamometer capacity is 30 kW with a maximum rated speed 6000 rpm and attached with an external blower. The 30 kW DC dynamometer is coupled to the PROTON CAMPRO test engine as shown in Figure 3.7a.

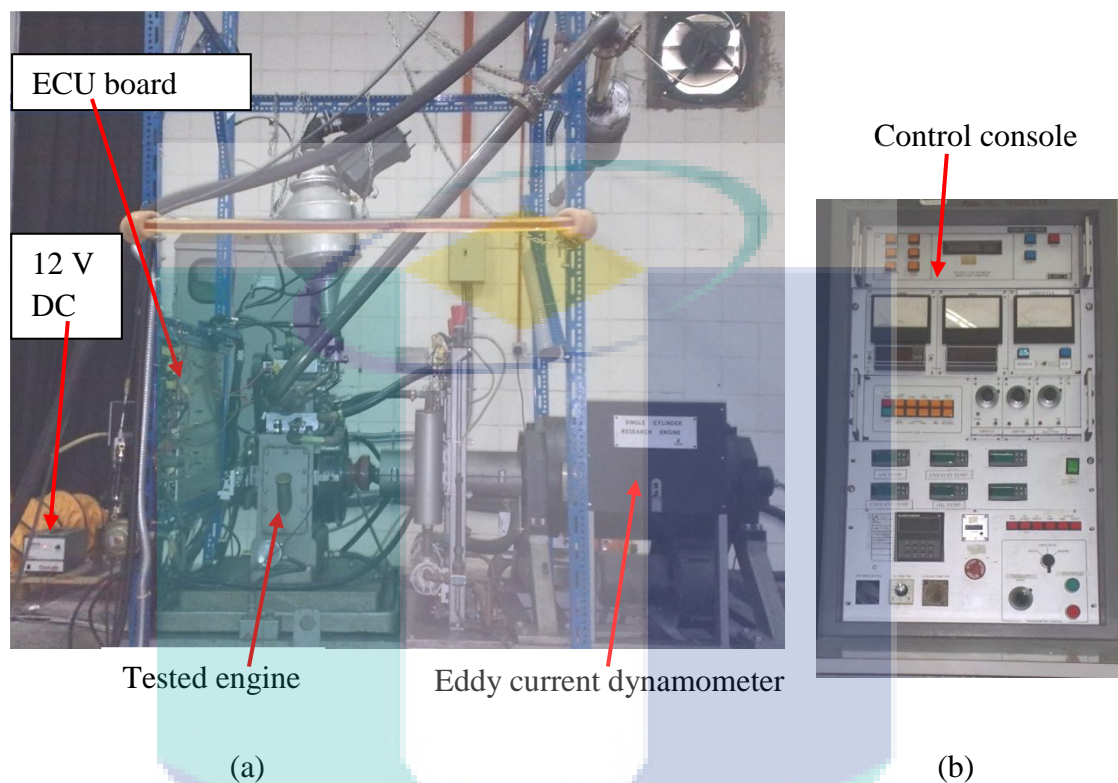


Figure 3.7: The test-cell (a) Overview of the tested engine coupled with the eddy current dynamometer (b) Dynamometer control console

The dynamometer electromechanically absorbs the power delivered by the engine. The heat generated by the applied torque has been removed by utilizing the attached external blower. The engine speed can be control at the desired level. Brake torque as the engine output is measured by eddy current dynamometer and display through a control console. Another data such as the speed, engine oil temperature, coolant temperature and intake air temperature are collected from the dynamometer control console. The control console of dynamometer is shown in Figure 3.7b.

At last, a GASMETTM analyzer is used for conducting measurements of the exhaust flue gases constituent. It is based on the Zirconia cell measurement. The output is a voltage proportion to the oxygen concentration. The oxygen concentration

measurement is utilized for estimation of the equivalence ratio (ϕ). A GASMET Oxygen Analyzer is used for that propose, as shown in Figure 3.8. Specifications of the GASMET Oxygen Analyzer are listed in Table 3.6. The apparatuses had been calibrated before proceeding to conduct the tests. Details of the calibration and experimental testing procedure are stated in Appendix B.

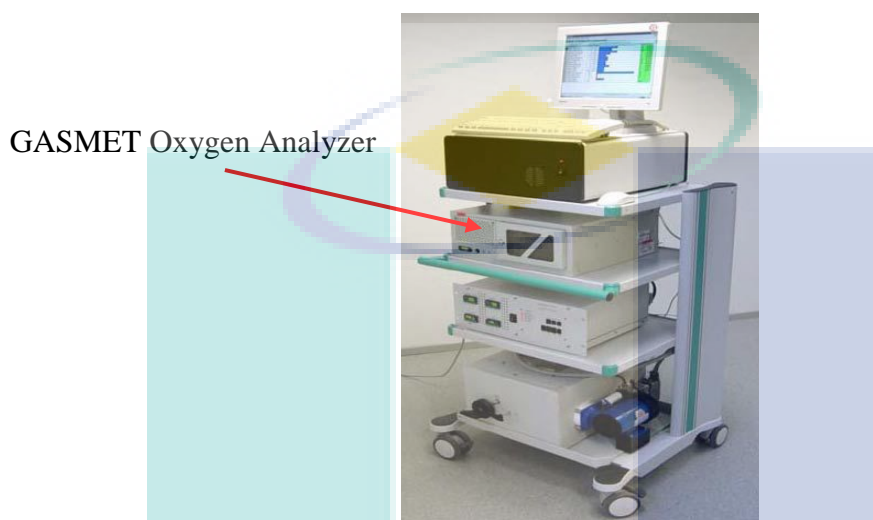


Figure 3.8: The GASMET gas analyzers system.

Table 3.6: Specifications of the GASMET Oxygen Analyzer

Specification	Description
Measuring principle	ZrO ₂ measuring cell
Detection limit	< 1 ppm O ₂
Response time	< 1 second
Sample gas temp.	120 °C to 300 °C, non condensing
Environment temp.	20 °C to + 40 °C
Reference gas	instruments air, dew point less than – 40 °C, no oil, about 30 l/h
Measuring gas	dry or wet, no combustibles
Calibration gas	instrument air as above or test gas from bottles

3.3.2 Engine Combustion Analysis

The experimental indicators are used to analyze the combustion process for DIH₂ICE. The time-averaged (cyclic resolved) and instantaneous (crank angle resolved) indicators are considered for one and multidimensional models

respectively. Sections below explain each indicator in details. Time-averaged indicators are used for validation of the one-dimension gas dynamics model. The *IMEP* is calculated from the analysis of the cylinder pressure. The *IMEP* is expressed as Eq. (3.1) (Burnt and Emtage, 1997):

$$IMEP = \frac{\Delta\theta}{V_d} \times \sum_{i=n_1}^{n_2} p(i) \frac{dV(i)}{d\theta} \quad (3.1)$$

where $p(i)$ is the cylinder pressure at crank angle i
 $V(i)$ is the cylinder volume at crank angle i
 V_d is the cylinder displacement volume
 θ is the crank angle
 n_1 and n_2 refers to the BDC crank angle position

Besides the *IMEP*, the peak cylinder pressure is utilized as another gain from the cylinder pressure. Both of the *IMEP* and peak cylinder pressure are based on the combustion analyzer measurement. The engine brake torque is recorded directly from the control console as the engine output. According to the output torque, the engine brake power is computed as Eq. (3.2):

$$P = \frac{2\pi N \tau}{60} \quad (3.2)$$

where P is the engine brake power
 τ is the engine brake torque
 N is the engine speed

Volumetric efficiency represents one of the crucial characteristics for the H_2ICE , due to the low density for hydrogen fuel. It is considered as one of the time-averaged indicators for validation. In case of four strokes direct injection engine, the definition of the volumetric efficiency is reduced to Eq. (3.3):

$$\eta_v = \frac{2\dot{m}_a}{\rho_r V_d N} \quad (3.3)$$

where η_v is the volumetric efficiency

\dot{m}_a is the air mass flow rate

ρ_r is the reference air density (at the intake manifold conditions)

The instantaneous indicators are used for validation of the multi-dimension model. A pressure sensor measures the cylinder pressure and the crank angle position is specified from the crank angle encoder. The cylinder pressure and the corresponding crank angle were captured through a high speed data acquisition system. The output of these measurements is the pressure crank angle diagrams, which are used for pressure trace validation. The mass burned fraction and heat release rate are estimated based on the cylinder pressure measurements.

The mass burned fraction profile is estimated by using a very well known model developed by (Rassweiler and Withrow, 1938). According to the definitions and assumptions for that model, the mass burned fraction at the end of the i th interval is given by Eq. (3.4)

$$x_b(\theta) = \frac{m_{b(i)}}{m_{b(total)}} = \frac{\sum_{j=0}^i \Delta p_c}{\sum_{j=0}^{n'} \Delta p_c} \quad (3.4)$$

where x_b is the mass burned fraction

m_b is the burning mass

Δp_c is the pressure rise due to combustion

n' is the total number of crank angle intervals

For the calculation of heat release rate the suggested approach by (Krieger and Borman, 1966) is adopted during current experimental work. Accordingly, the form of heat release rate is expressed in Eq. (3.5):

$$\frac{dQ}{d\theta} = \frac{1}{\gamma-1} \times \frac{Vdp}{d\theta} + \frac{\gamma}{\gamma-1} \times \frac{pdV}{d\theta} \quad (3.5)$$

where Q is the apparent heat release

γ is the specific heat ratio (1.33)

V is the instantaneous volume for the combustion chamber

p is the instantaneous pressure for the combustion chamber

The pressure crank angle traces and pressure-volume diagrams are used for computation the *IMEP*, heat release rate and mass burned fraction. A special MACRO code was developed in Microsoft Excel to analyze the data (Abdullah, 2009).

3.4 ONE-DIMENSIONAL ENGINE MODEL

One-dimensional modeling represents one of the most widely used approach due to less effort needed compared to multidimensional approach. One-dimensional model is developed based on gas dynamic approach. A single cylinder four strokes direct injection SI engine model is developed using GT-Power as shown in Figure 3.9. The real engine specifications are used as listed in Table 3.1. This model is employed for analysing of TAHT in DIH₂ICE. The model setup, governing equations, convergence criteria and TAHT correlation are described in following sections.

3.4.1 Model Setup

The developed model is composed of three main parts: intake system, engine crank train and exhaust system. The intake system consists of an end environment part, air cleaner, throttle, plenum, intake manifold and valves. The end environment part is used to describe the boundary values for pressure, temperature and inlet gas composition. These conditions are assumed the same values for the surrounding environment conditions. Atmospheric pressure, temperature (300 K) and standard air composition (76.7% N₂ and 23.3% O₂) are used for initialization of all the simulation

executions. These conditions also are used as a reference state for evaluation of the volumetric efficiency.

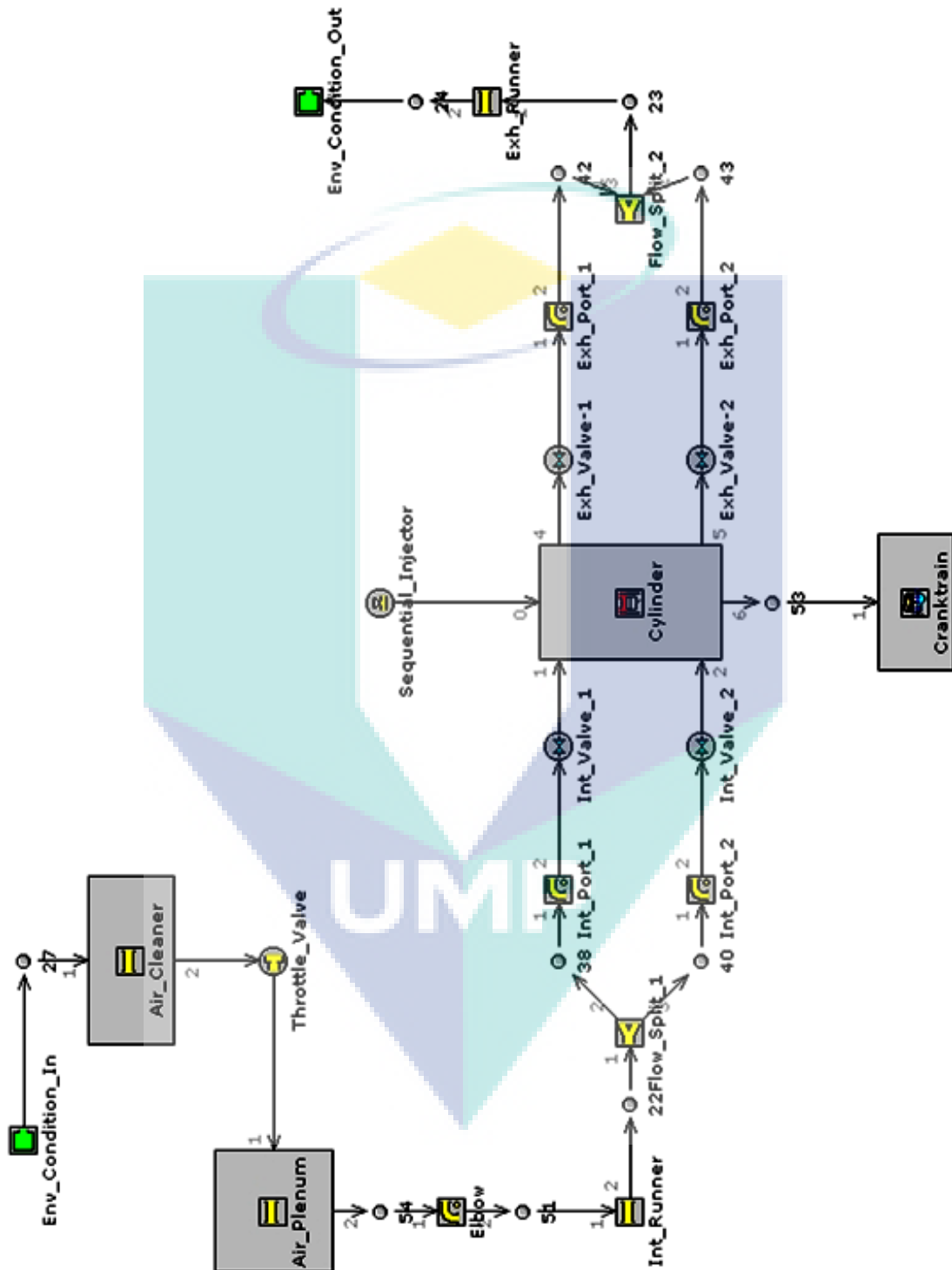


Figure 3.9: One-dimensional gas dynamic model for single cylinder four strokes SI DIH₂ICE.

The end environment part is connected to air cleaner which is connected to throttle and plenum. The air is taken to the air cleaner which is modeled as a pipe with restriction in the way of the intake air. The plenum is connected to the intake manifold which consists of the intake elbow, runner, flow split and two ports. The flow split is used in the intake system to divide the intake charge between the two intake ports. The intake system components are connected by using the orifices connection. The discharge coefficients of the orifices are set to 1 to ensure the smooth transition as in the real engine. The specifications of the intake system components are listed in Table 3.7. The intake ports are connected directly to the intake valves. Two intake valves are used to connect the intake manifolds with engine cylinder. It is utilized by defining valves geometries and timing as in Table 3.8.

Table 3.7: Piping system components specifications.

Part Name	Diameter(mm)		Length (mm)	Volume (mm ³)	Surface roughness (mm)
	Inlet	Outlet			
Air cleaner	30	35	240	-	0.0025
Plenum	35	22	720	-	0.25
Intake runner	22	22	75	-	0.25
Intake Flow split	-	-	-	17300	0.25
Intake port	26	30	120	-	0.2
Exhaust runner	30	30	164	-	0.25
Exhaust flow split	-	-	-	12500	0.2
Exhaust port	27	27	40	-	0.2

Table 3.8: Engine valves specifications.

Parameter	Value	Unit
Intake valve open	12	deg BTDC
Exhaust valve open	45	deg BBDC
Intake valve close	48	deg ABDC
Exhaust valve close	10	deg ATDC
Intake valve diameter	30.0	mm
Exhaust valve diameter	27.0	mm
Number of intake valve	2	-
Number of exhaust valve	2	-

Intake valves are delivered the intake charge to cylinder which is connected to the engine crank train. Cylinder of the engine is the main element in the model.

The cylinder geometry is specified according to the real engine details. These details are common between the cylinder and crank train. The most important details are shown in Figure 3.10, while the dimensions are specified according to the real engine details in Table 3.1. Additionally, there are several sub-models should be specified for setting of the engine cylinder. The most crucial sub-models for current study are: wall temperature, fluid flow, heat transfer and combustion models. To specify the in-cylinder chamber's surface temperature for heat transfer calculations the overall temperature of the head (including valves), piston and cylinder are specified. A wall temperature model is used where the overall temperature of the head, piston and cylinder can be given in as a boundary condition. Therefore, according to the literatures (Demuynck et al., 2009 and Mohammadi et al., 2008), these temperature values are chosen, as that listed in Table 3.9. The temperature of the piston is higher than the cylinder head and cylinder block wall temperature because this part is not directly cooled by the cooling liquid or oil. The details of other models are stated with details in Section 3.4.2.

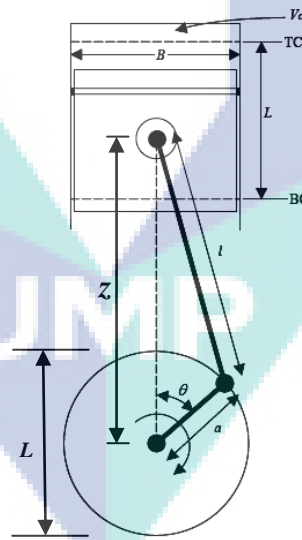


Figure 3.10: Engine cylinder with engine crank train details

Table 3.9: Parts wall temperature

Part	Temperature (K)
Cylinder head	550
Piston	600
Cylinder wall	460

Engine crank train includes the crank train, the crank slider mechanisms and crankshaft. All these parts are used for action force transmission from the piston into the crankshaft output brake power. It is used to identify the engine specifications, where the four-stroke engine, single cylinder is considered. Besides the indication of the simulation model is prescribed by choosing engine speed specification, while the corresponding load variation is determined. The engine speed is used as one of the main parameters for the present investigation. Description of the engine friction model is adjusted for the engine cylinder. Engine friction is calculated using Chen-Flynn friction model (Chen and Flynn, 1965). The $FMEP$ is expressed as Eq. (3.6):

$$FMEP = C + (PF \times p_{max}) + (MPSF \times C_m) + (MPSSF \times C_m^2) \quad (3.6)$$

where C is the constant part of the $FMEP$

PF is the peak cylinder pressure factor

p_{max} is the maximum in-cylinder pressure

$MPSF$ is the mean piston speed factor

$MPSSF$ is the mean piston speed squared factor

C_m is the mean piston speed

Those factors are considered as calibration parameters within the current model for best matching with experimental results.

The direct-injection is modeled using a single sequential pulse fuel injector. The injector is linked directly to the engine head. The injection of gas hydrogen fuel was located in the top of the cylinder. Fuel injector is specified by AFR , fuel delivery rate, and injection timing. A fuel delivery is estimated according to the engine specifications, volumetric efficiency and engine speed. The AFR is imposed for the injector; then the injected fuel rate was estimated according to Eq. (3.7) (Ferguson and Kirkpatrick, 2001):

$$\dot{m}_{delivery} = \rho_r \times N \times \eta_v \times V_d \times \frac{3}{AFR \times 2\Delta\theta_{inj}} \quad (3.7)$$

where $\dot{m}_{delivery}$ is the injector delivery rate (g/s)

ρ_r is the reference density (kg/m³)

N is the engine speed (rpm)

V_d is the volume displacement (cm³)

AFR is the air fuel ratio

$\Delta\theta_{inj}$ is the injection duration (deg)

Fuel injector is implicitly governed of the most important parameters during the present study. These parameters are the equivalence ratio (ϕ) through the AFR and injection timing, where the start of injection (SOI) is chosen as the marking flag. For all the simulations, the AFR is selected for a wide range, from ultra-lean to rich mixture. The injection timing is varied to be consisting with remarking of the previous studies regarding the sensitivity of the H₂ICE for occurrence of the backfire phenomena and lowest NO_x level (Mohammadi et al., 2007 and Gadallah et al., 2009), as well as to be comparable with the available experimental database.

The exhaust system consists of two exhaust valves, two exhaust ports, exhaust flow split, exhaust runner and end environment part. Two exhaust valves are modeled to joined the exhaust manifolds with engine cylinder. It is utilized by defining valves geometries and timing as in Table 3.8. The exhaust valves are connected directly to the exhaust ports. Exhaust ports are modeled as pipe with specific dimensions as in Table 3.7. Flow split is used to collect the expelled exhaust gases in the exhaust ports. Exhaust flow split is joined to runner which is modelled as a pipe. The exhaust system components are connected by using the orifices connection. Orifice is identified by a diameter, forward and reverse discharge coefficients. The discharge coefficients of the orifices are set to 1 to ensure the smooth transition as in the real engine. All dimensions for the exhaust system components are listed in Table 3.7.

3.4.2 Governing Equations

The physical phenomena including the fluid flow, heat transfer and combustion are most related to the present study. These phenomena are formulated to

simulate the one-dimensional gas dynamics model for characterizing of TAHT in DIH₂ICE. More effort is focused on treatment of the heat transfer phenomenon inside engine components. This is due to the differences in fuel properties between hydrogen and fossil fuel types. The engine system consists of three sub-systems namely cylinder, manifolds and valves. The details of these components related to the TAHT are discussed in the following sections.

The nature of the in-cylinder flow dynamics is more complicated compared to the manifolds and valves. The complexities come from the opening and closing of the intake and exhaust valves simultaneously combined with the reciprocating motion for the piston (Heywood, 1988). One-dimension flow analysis is performed using a combustion model to reduce the simulation time and accounts for the in-cylinder fluid motion. The widely used approach for combustion modeling in SI engine is Wiebe's function. It was previously applied for H₂ICE (Takats et al., 1998; Polasek et al., 2002; Shudo and Suzuki, 2002a,b and Ma et al., 2003). It is a functional form for the mass fraction-burning rate. It is defined as the ratio of the cumulative heat release to the total heat release. A Wiebe's function is expressed as Eq. (3.8) (Ferguson and Kirkpatrick, 2001):

$$x_b(\theta) = 1 - \exp \left[-a \left(\frac{\theta - \theta_s}{\theta_d} \right)^n \right] \quad (3.8)$$

where x_b is the mass burned fraction

θ is crank angle degrees

θ_s is the corresponding crank angle to the initialization of burning process

θ_d is the corresponding crank angle to the duration of burn

n is the Weibe's form factor

a is the Weibe's efficiency factor

The Weibe's function factors are adjusted as calibration parameters according to literature (Takats et al., 1998; Polasek et al., 2002; Shudo and Suzuki, 2002a,b and Ma et al., 2003).

The rate of heat release is obtained by differentiating the cumulative heat release of Weibe's function as Eq. (3.9):

$$\frac{dQ}{d\theta} = LHV \times \frac{dx_b}{d\theta} = n \times a \times \frac{LHV}{\theta_d} (1 - x_b) \left(\frac{\theta - \theta_s}{\theta_d} \right)^{n+1} \quad (3.9)$$

where Q is the heat release

LHV is the lower heating value

The forced convection mechanism represents the dominant heat transfer mode from the bulk gas to combustion chamber walls. Due to the reduction in the soot production from SI engine compare with the diesel engine (especially for hydrogen fuel), the radiation effect can be neglected (Demuynck et al., 2011). The instantaneous heat transfer coefficient represents the prerequisite for accounting of the amount of heat transferred to the combustion chamber. Therefore, the instantaneous heat transfer coefficient from bulk gas to cylinder wall was extensively studied over the years (Borman and Nishiwaki, 1987 and Ollivier et al., 2006). Heat transfer inside the cylinder is modeled using a formula that closely emulates the classical Woschni's correlation. In particular, Woschni's correlation has frequently been used for SI engine investigations, even though the correlations were developed under the direct-injection diesel engine (Heywood, 1988). The classical Woschni's correlation the heat transfer coefficient can be expressed as Eq. (3.10):

$$h = 129.9 \times d^{-0.2} \times p^{0.8} \times T_g^{-0.53} \times \left[C_1 \times C_m + C_2 \times \frac{V_s \times T_r}{p_r \times V_r} \times (p - p_m) \right]^{0.8} \quad (3.10)$$

where h is the instantaneous heat transfer coefficient for combustion chamber.

d is the cylinder bore diameter.

p is the instantaneous pressure of the in-cylinder gaseous.

T_g is the instantaneous temperature of the in-cylinder gaseous.

C_m is the mean piston speed.

C_1 and C_2 are the adjustable constants.

V_s is the clearance volume of the combustion chamber.

r is the reference point (usually it is considered as the IVC)

The constants C_1 and C_2 are essential to take into account the changes in gas velocity over the engine cycle. On the other hand, C_1 and C_2 have to be consistent physical units. The suggested values for C_1 and C_2 are listed in Table 3.10.

Table 3.10: Coefficients of Woschni's Correlation

Period	C_1	C_2
The scavenging period	6.18	0
Compression stroke	2.28	0
combustion and expansion stroke	2.28	3.24×10^{-3}

It was extensively demonstrated that Woschni's correlation produces considerable error where used for H₂ICE (Wei et al., 2001; Shudo and Suzuki, 2002b and Demuynck et al., 2011). To overcome this obstacle, an additional multiplier is added to Woschni's correlation as calibration parameter. This parameter is used for adapting Woschni's correlation for best matching with experimental observations.

Flow pattern is yielded through solving of one-dimensional flow equation across the pipes. A pipe is discretized into smaller elements and the flow equations are solved at these elements level. The scalar properties of a fluid include pressure, temperature, density and internal energy are assumed to be constant. Each element has vector properties (mass flux and fluid velocity) that are transferred across its boundaries. Figure 3.11 illustrates the difference between vector and scalar properties and their locations. Since it is one-dimensional flow, variables are uniform at pipe cross section. Each scalar variable is assumed to be uniform over each element. Vector variable is calculated at each boundary. Accordingly, the governing equations are defined as follows:

Continuity equation:

$$\frac{dm}{dt} = \sum_{boundaries} m_{flux} \quad (3.12)$$

Momentum equation:

$$\frac{d(m_{flux})}{dt} = \frac{dpA + \sum_{boundaries} (m_{flux}u) - 4C_f \frac{\rho u^2 A dx}{2D} - C_{pl}(\frac{1}{2}\rho u^2)A}{dx} \quad (3.13)$$

Energy equation:

$$\frac{d(m_{flux}e)}{dt} = p \frac{dV}{dt} + \sum_{boundaries} m_{flux}H - hA(T_g - T_w) \quad (3.14)$$

where A is the cross sectional area.

e is the specific internal energy.

V is the element volume.

H is the enthalpy

Gas properties are computed by solving the above governing equations simultaneously based on explicit technique for integration in the time domain. All pipes are assumed constant conditions for one-dimensional model. Accuracy improvements was considered by choosing a finer discretisation length. However, the discretisation length is limited by the size of the time step. The criteria for element's discretisation are used 40% of diameter on the intake side and 50% of diameter on the exhaust side (Gama Technologies Inc., 2004). The solver stability is reached by using the Courant's condition for time step calculation. The time integration step for the set of the governing equations is specified as Eq. (3.16) (Courant et al., 1928):

$$\frac{\Delta t}{\Delta x} (u + c) \leq 0.8 \quad (3.16)$$

where Δt is the time step

Δx is the discretised length

u is the fluid velocity

c is the speed of sound

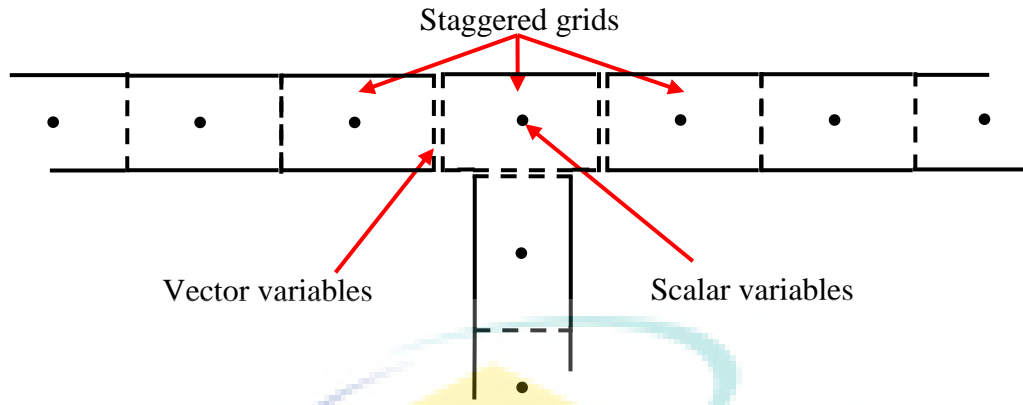


Figure 3.11: Illustration of component discretization with staggered grids

To complete the simulation model other additional formulas beside of the main governing equations are used for calculations of the pressure loss coefficient and friction coefficient. The pressure loss coefficient (C_{pl}) is defined by Eq. (3.17):

$$C_{pl} = \frac{p_1 - p_2}{\frac{1}{2} \rho u_1^2} \quad (3.17)$$

where p_1 and p_2 are the inlet and outlet pressure respectively

ρ is the density

u_1 is the inlet velocity

Friction loss factor is based on the Reynolds number (Re) and the surface roughness of the walls. The friction coefficient is related to Re as Eq. (3.18) and Eq. (3.19) (Nikuradse, 1937):

For smooth walls:

$$C_f = \frac{16}{Re} \quad Re < 2000; \quad Re = \frac{\rho \times v \times d}{\mu} \quad (3.18)$$

$$C_f = \frac{0.08}{Re^{0.25}} \quad Re > 4000$$

For rough walls:

$$C_{f(rough)} = \frac{0.25}{\left(2 \log_{10} \left(\frac{d}{2 \times z} \right) + 1.74 \right)^2} \quad (3.19)$$

where d is the pipe diameter

z is the roughness height

v is characteristic velocity (m/sec)

The roughness height is represented by the equivalent sand roughness of the wall material. Value of the equivalent roughness height depends on the material of each part from the manifold. The considered values in present study for each part are listed in Table 3.7 (Gama Technologies Inc., 2004).

The heat transfer from gases flowing inside of pipes to their walls is estimated using a heat transfer coefficient. From the experimental observation, the amount of heat transfer rate depends on the heat transfer coefficient, the predicted gas temperature and the internal wall temperature. The heat transfer coefficient is calculated every time step. It is a function of fluid velocity, thermo-physical properties and wall surface roughness. The heat transfer coefficient is defined according to the Reynolds-Colburn analogy, which is based on boundary layer theory and describes the correlation between fluid friction and heat transfer. This analogy is valid to use for turbulent, laminar as well as transitional flow. The heat transfer coefficient is defined by Eq. (3.20):

$$h = \frac{1}{2} \times \rho \times U_{eff} \times C_p \times C_f \times Pr^{-\frac{2}{3}} \quad (3.20)$$

where h is the heat transfer coefficient

U_{eff} is the effective speed outside boundary layer

C_p is the specific heat

C_f is the smooth pipe friction coefficient

Pr is the Prandtl number

The important phenomenon for valve is the gas flow. The estimation of the discharge coefficients for forward and reversed flow is a prerequisite for valves flow simulation. Discharge coefficient is defined as the ratio of effective flow area to the reference flow area. Values of discharge coefficient are obtained from solution of velocity equation for flow through an orifice under isentropic assumption. Friction losses and errors in assumptions of velocity profiles are included in the orifice equations. For gases, discharge coefficient is calculated as Eq. (3.21) (Ferguson and Kirkpatrick, 2001):

$$\dot{m} = A_{eff} \rho_{ise} U_{ise} = C_D A_r \rho_{ise} U_{ise} \quad (3.21)$$

$$\rho_{ise} = \rho_o (p_{ratio})^{\frac{1}{\gamma}}$$

$$U_{ise} = \sqrt{RT_o \left(\frac{2\gamma}{\gamma-1} \left(1 - p_{ratio}^{\frac{\gamma-1}{\gamma}} \right) \right)}$$

where \dot{m} is the mass flow rate

A_{eff} is the effective flow area

ρ_{ise} is the isentropic density at the valve

ρ_o is the upstream stagnation density

U_{ise} is the isentropic velocity at the valve

C_D is the discharge coefficient

A_r is the reference flow area

p_{ratio} is the absolute pressure ratio

R is the gas constant

T_o is the upstream stagnation temperature

γ is the specific heat ratio

3.4.3 Convergence Criteria

The periodic type simulation with explicit flow solver is adopted. Since the current application concerns reciprocating system. During the iterative solution, convergence is assessed at the end of each cycle according to the convergence criteria. The convergence criteria is based on mass flow rate, pressure and temperature. The fluid flow and temperature tolerance are used for convergence criteria. The simulation stops if the convergence tolerances are met for every connection and flow sub-volume element in the model. The convergence tolerances for fluid flow and temperature are specified by Eq. (3.22) and Eq. (3.23):

$$dF_{\max} < \text{Fluid flow convergence tolerance} \quad (3.22)$$

$$dT_{\max} < \text{Fluid temperature tolerance} \quad (3.23)$$

where dF_{\max} is the maximum relative change of the average mass flow rate for all flow connections during that cycle update

dT_{\max} is the maximum change of the average fluid temperature for all fluid sub-volumes during that cycle update

The relative change of the average mass flow rate is calculated at the end of the recent cycle update by Eq. (3.24):

$$dF = \frac{|F_{\text{new}} - F_{\text{old}}|}{|F_{\text{new}}|} \quad (3.24)$$

where F_{new} is the average mass flow rate of the most recent cycle update

F_{old} is the average mass flow rate of the previous cycle update

The change of the average fluid temperature is calculated at the end of the recent cycle update by Eq. (3.25):

$$dT = |T_{new} - T_{old}| \quad (3.25)$$

where T_{new} is the average fluid temperature of the most recent cycle update

T_{old} is the average fluid temperature of the previous cycle update

The fluid flow and temperature convergence tolerances are considered less than 10^{-3} and 0.05 respectively. The convergence of pressure as dp_{max} is reported for one-dimensional model. The convergence criterion for pressure is defined as Eq. (3.26):

$$dp_{max} = \left| \frac{p_{new} - p_{old}}{p_{max}} \right| \quad (3.26)$$

The flow criterion expressed in Eq. (3.27) is applicable when the convergence criterion for pressure $\leq 1\%$.

$$\left| \frac{F_{new} - F_{old}}{F_{new}} \right| < 0.25 \times \text{Fluid flow convergence tolerance} \quad (3.27)$$

Moreover, the brake power for five consecutive cycles is considered as an overall cycle convergence criterion. The simulations were executed until the brake power met the minimum convergence tolerance (relative change $\leq 0.2\%$ value).

3.4.4 Time-Averaged Heat Transfer Correlation

The characteristics of TAHT for DIH₂ICE are carried out for one-dimensional gas dynamic model. TAHT describes the heat transfer using dimensionless parameters including Nusselt (Nu) and Reynolds (Re) numbers. The dimensionless parameters are defined as Eq. (3.28) and Eq. (3.29):

$$Nu = \frac{h \times d}{k_g} \quad (3.28)$$

$$Re = \frac{\rho \times v \times d}{\mu} \quad (3.29)$$

where h is heat transfer coefficient ($\text{W/m}^2 \cdot \text{K}$)

d is diameter of cylinder (m)

k_g is working gases thermal conductivity ($\text{W/m} \cdot \text{K}$)

ρ is density of gases (kg/m^3)

v is characteristic velocity (m/sec)

μ is dynamic viscosity of the working gases ($\text{kg/m} \cdot \text{sec}$)

These parameters are used for predicting the time-averaged heat transfer to the combustion chamber walls. The thermal conductivity and dynamic viscosity of gases are defined as Eq. (3.30) and Eq. (3.31) respectively (Blair, 1999):

$$k_g = 6.1944 \times 10^{-3} + 7.3814 \times 10^{-5} T_f - 1.2491 \times 10^{-8} T_f^2 \quad (3.30)$$

$$\mu = 7.457 \times 10^{-6} + 4.1547 \times 10^{-8} T_f - 7.4793 \times 10^{-12} T_f^2 \quad (3.31)$$

where T_f is the wall film temperature in Kelvin.

The average effective gas temperature over the engine cycle is used as the cylinder gases temperature to account for the variations in the *AFR* (Taylor and Toong, 1957). The *AFR* is considered as one of the significant parameters in this study. The average in-cylinder gas temperature is selected to estimate the convection heat transfer, which is expressed in Eq. (3.32):

$$\bar{Q} = h \times A (T_g - T_w) \quad (3.32)$$

The Nu and Re are manipulated based on the heat transfer coefficient (h) and mass flows rate (\dot{m}). The mass flow rate is determined based on the characteristic velocity. Accordingly, the non-dimensional quantities are given as Eq. (3.33) and Eq. (3.34):

$$Nu = \frac{4 \times \bar{\dot{Q}}}{\pi \times d \times k_g (T_g - T_w)} \quad (3.33)$$

$$Re = \frac{4 \times \dot{m}}{\pi \times \mu \times d} \quad (3.34)$$

where $\bar{\dot{Q}}$ is the time-averaged convection heat transfer rate

T_g is the averaged in-cylinder gas temperature (K)

T_w is the in-cylinder surface wall temperature (K)

\dot{m} is the mass flow rate (m³/sec)

3.5 MULTIDIMENSIONAL ENGINE MODEL

Multidimensional modeling represents a rapid and cost effective tool in different stages of engine design and optimization. It can be utilized to estimate of the heat transfer rate at various positions in an engine cylinder (Mohammadi and Yaghoubi, 2010). The multidimensional model is used to characterize of instantaneous heat transfer (IHT) for SI DIH₂ICE. This model is based on computational fluid dynamics (CFD) approach using finite volume (FV) technique. The KIVA code is utilized to carry out CFD analysis. The computational domain definition, grid generation, governing equations, main sub-models, algorithm and boundary as well as initial conditions of the multidimensional model are described in the following sections.

3.5.1 Computational Meshing

The physical domain includes the intake port, exhaust port and combustion chamber. This is embraced the intake valves, the exhaust valves and piston within the combustion chamber as shown in Figure 3.12. The engine has a dual intake and exhaust valves per cylinder with a circular shape for runners. The combustion chamber is a pent roof configuration with a piston which has a small cup in the

centre of the crown. Furthermore, a new distinct region is defined in order to simulate the fuel inlets.

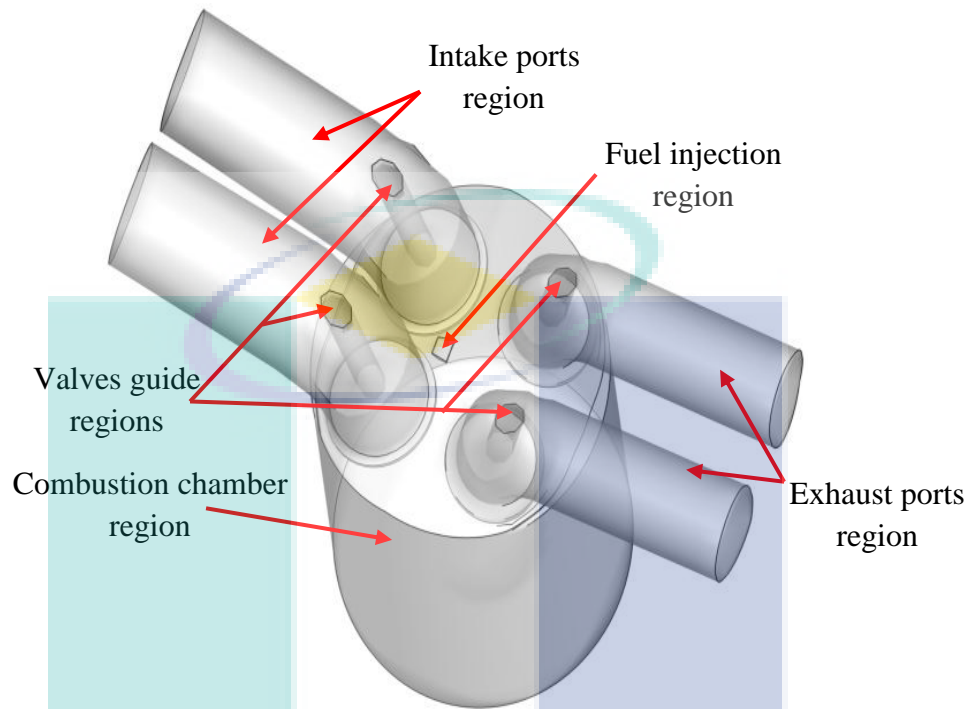


Figure 3.12: Physical domain for the multidimensional engine model

The preprocessor (K3PREP) is used for mesh generation. The physical domain of the engine is discretized with a structured hexahedral grid. K3PREP has been expanded to support the generation of grids with valves, along with the shaping of valve ports and runners (Amsden, 1997). It employs a multi-block structured grid to model the complex geometries. Then the individual blocks of regions are patched together to construct the required structure. Accordingly, the complex geometries are created block by block with assistance of the patching approach. Details of the patching approach have been fully described in KIVA code documentation (Amsden, 1993). K3PREP exported an input file IPREP for generating the computational mesh. The refinement process for the mesh size is adjusted within the IPREP file. The input data file is presented in appendix A. It contains the configuration details for the components of the combustion chamber. As well as the details for all the blocks are produced from the conformal division for the combustion chamber.

Formulation of multidimensional model is based on the Cartesian coordinates system (x, y, z). Each block has six bounding faces. Although each block initially has its own (i, j, k) structure. Global (i, j, k) structure disappears when the blocks are patched together and storage is sorted. Patching allows complex geometries to be created block by block, while minimizing the number of deactivated zones (Amsden, 1999). In fact, the deactivated zones are only the ghosts that surround the final mesh. The ghosts enable the application of boundary conditions at inflow/outflow cell faces. For meshing process, the physical domain is divided into three main regions: the intake, exhaust and the combustion chamber regions. Each region is composed of several blocks and each block sub-divided into many small volumes. The current model is used to simulate the fuel supply into the combustion chamber. The familiar snapper technique is used for simulating the piston and valves motion. They are considered as solid objects moving through the meshing domain.

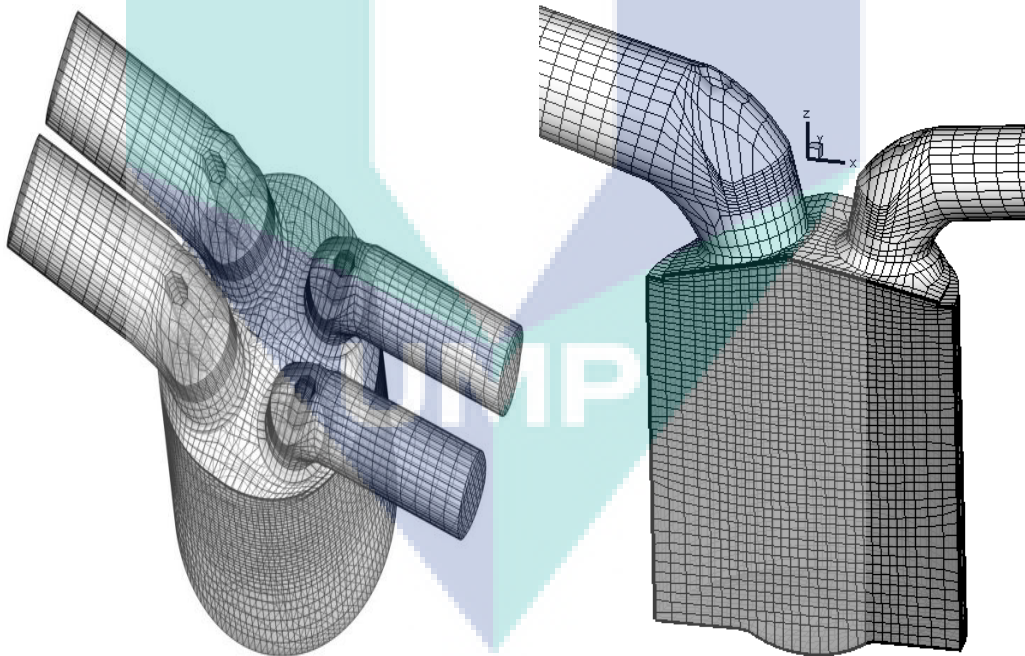


Figure 3.13: Computational grid domain with hexahedral element

Nevertheless, there is a one basic difference between the methods of manipulating of piston and valves motion. In case of piston motion, some planes in the mesh are activated (with the piston moving down) or deactivated (piston moving up). On the contrary, for valve repositioning within the mesh, the planes are simply

passing from the bottom valve face to the top one (valve moving down) and vice versa. By adopting this type of modeling for valve and piston motion as well as the shape description a higher grid resolution is achievable. The computational grid domain is displayed in Figure 3.13. This computational grid is related to the PROTON CAMPRO single cylinder research engine.

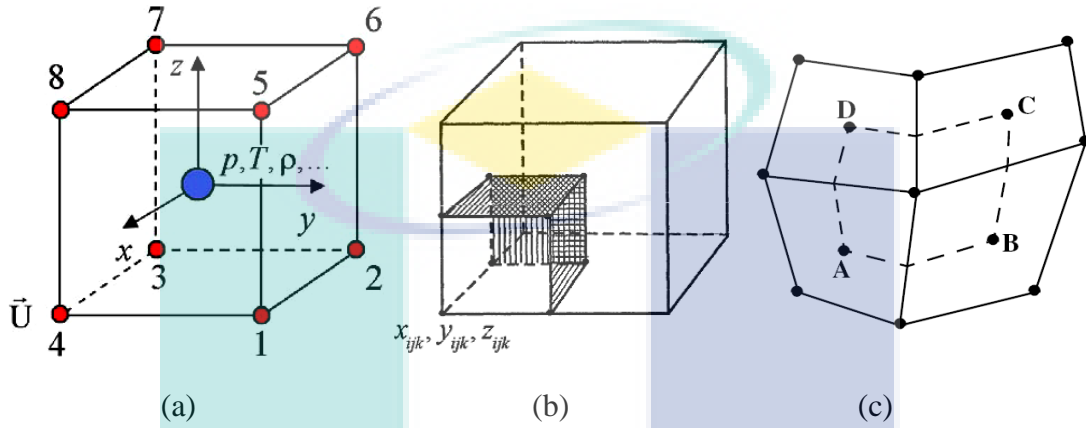


Figure 3.14: (a) Typical finite-difference cell; (b) The portion of a momentum cell lying within the regular cell; (c) Momentum cell (i,j) , shown in dashed lines, and its associated regular cell.

The mesh can conform to curved boundaries and can move in order to follow changes in the combustion chamber geometry (Amsden, 1989). Figure 3.14(a) illustrates a typical cell is adopted within multidimensional modeling. The conventional numbering for the vertices is depicted. The cells are indexed by integers (i, j, k) , which are its coordinates in logical space. The indices (i, j, k) also label the vertices, with the understanding that vertex (i, j, k) is vertex 4 of cell (i, j, k) . In addition to the regular cells, auxiliary cells, named momentum cells, are used for differencing the momentum equations. Auxiliary cells are described as circumfusing a vertex (i, j, k) , with cell edges meeting the midpoint of the surrounding regular cell edges. The vertices are placed appropriately within the surrounding regular cells to cover one quarter of each of the surrounding regular cell areas. Figure 3.14(b) shows the portion of a momentum cell lying within a regular cell. The momentum cell (i, j, k) is located at the center of the vertex (i, j, k) . Figure 3.14(c) demonstrates an example for the momentum cell in cross section of a standard finite-difference cell.

3.5.2 Governing Equations

Equations of motion for unsteady, turbulent and chemical reactive flow govern the multidimensional model. The equations of motion for the fluid phase are solved for both laminar and turbulent flows. The mass, momentum and energy equations for the two cases differ primarily in the form and magnitude of the transport coefficients (i.e. viscosity, thermal conductivity and species diffusivity) (Amsden, 1989 and Mohammadi and Yaghoubi, 2010). Turbulent cases are much larger than laminar because of the additional transport caused by turbulent fluctuations. The transport coefficients are derived from a turbulent diffusivity that depends on the kinetic energy and its dissipation rate.

The continuity equation for species m is defined by Eq. (3.35):

$$\begin{aligned} \frac{\partial \rho_m}{\partial t} + \nabla \cdot (\rho_m u) &= \nabla \cdot \left[\rho D_m \nabla \left(\frac{\rho_m}{\rho} \right) \right] + \dot{\rho}_m^c + \dot{\rho}^s \delta_{m1} \\ \frac{\partial \rho}{\partial t} + \nabla \cdot (\rho u) &= \dot{\rho}^s \end{aligned} \quad (3.35)$$

where ρ_m is the mass density of species m

ρ is the total mass density

t is the time variable

u is the fluid velocity vector

D_m is the mass diffusion coefficient from Fick's law of binary diffusion

$\dot{\rho}_m^c$ is the source term of chemistry

$\dot{\rho}^s$ is the source term of spray

δ_{m1} is the Dirac delta function

The momentum equation for the fluid mixture is described by Eq. (3.36):

$$\frac{\partial(\rho u)}{\partial t} + \nabla \cdot (\rho u u) = -\frac{1}{a^2} \nabla p - A_o \nabla \left[\frac{2}{3} \rho k \right] + \nabla \cdot \sigma + F^s + \rho g \quad (3.36)$$

where p is the fluid pressure

k is the turbulent kinetic energy per unit mass

a is a dimensionless number used for low Mach number flows

A_o is the flow regime flag, laminar (0), or (1) for turbulence models

σ is the viscous stress tensor

F^s is the rate of momentum gain per unit volume due to the spray

g is the gravitational acceleration vector

The internal energy is expressed as Eq. (3.37):

$$\frac{\partial(\rho I)}{\partial t} + \nabla \cdot (\rho u I) = -p \nabla \cdot u + (1 - A_o) \sigma : \nabla u - \nabla \cdot J + A_o \rho \varepsilon + \dot{Q}^c + \dot{Q}^s \quad (3.37)$$

where I is the specific internal energy exclusive of chemical energy

J is the heat flux vector that sums heat conduction and enthalpy diffusion

ε is the dissipation rate of turbulent kinetic energy k

\dot{Q}^c is the source term of chemical heat release

\dot{Q}^s is the source term of spray interaction

$:$ is the double-dot product

The ideal gas relationships are defined as Eq. (3.38) to Eq. (3.40):

$$p = R_o T \sum_m \left(\frac{\rho_m}{M_m} \right) \quad (3.38)$$

$$I(T) = \sum_m \left(\frac{\rho_m}{\rho} \right) I_m(T) \quad (3.39)$$

$$I_m(T) = h_m(T) - \frac{R_o}{M_m} T \quad (3.40)$$

where R_o is the universal gas constant

M_m is the molecular weight of species, (m)

$I_m(T)$ is the specific internal energy of species, (m) at temperature, (T) taken from the JANAF thermodynamic tables

$h_m(T)$ is the specific enthalpy of species, (m) at temperature, (T) taken from the JANAF thermodynamic tables

Two additional transport equations are solved for the turbulent kinetic energy k and its dissipation rate ε . The most widely used turbulence model (k - ε model) is defined by Eq. (3.41) and Eq. (3.42):

$$\frac{\partial(\rho k)}{\partial t} + \nabla \cdot (\rho u k) = -\frac{2}{3} \rho k \nabla \cdot \sigma + \sigma : \nabla u + \nabla \cdot \left[\left(\frac{\mu}{Pr_k} \right) \nabla k \right] - \rho \varepsilon + \dot{W}^s \quad (3.41)$$

$$\begin{aligned} \frac{\partial(\rho \varepsilon)}{\partial t} + \nabla \cdot (\rho u \varepsilon) = & -\left(\frac{2}{3} c_{\varepsilon 1} - c_{\varepsilon 3} \right) \rho \varepsilon \nabla \cdot \sigma + \sigma : \nabla u \\ & + \nabla \cdot \left[\left(\frac{\mu}{Pr_\varepsilon} \right) \nabla \varepsilon \right] + \frac{\varepsilon}{k} \left[c_{\varepsilon 1} \sigma : \nabla u - c_{\varepsilon 2} \rho \varepsilon + c_s \dot{W}^s \right] \end{aligned} \quad (3.42)$$

where \dot{W}^s is the turbulent eddies rate of work on spray dispersion

Pr is the Prandtl number, with constant model values for k and ε

c is the model constants

The quantities $c_{\varepsilon 1}$, $c_{\varepsilon 2}$, $c_{\varepsilon 3}$, c_s , Pr_k , and Pr_ε are constants. Suggested values of the above constants are listed in Table 3.11 (Launder and Spalding, 1974).

Table 3.11: Values of the constants for k - ε turbulent model

Constant	Value
$c_{\varepsilon 1}$	1.44
$c_{\varepsilon 2}$	1.92
$c_{\varepsilon 3}$	-1
c_s	1.5
Pr_k	1.0
Pr_ε	1.3

3.5.3 The Main Sub-models

Numerous additional sub-models are used besides the main governing equations. These include models for describing the in-cylinder processes such as fuel injection, combustion, ignition and heat transfer. For solving the governing equations, the Arbitrary Lagrangian-Eularian (ALE) method is adopted (Amsden, 1993). Whereas the sub-models are solved by utilizing the operator splitting approach, then it is incorporated with the main program. A description of the main utilized sub-models is reported in following sections.

The original fuel injection model is replaced by developing a new particular program. The name of the newly developed program is a “SETVELIN”, and it is described in flowchart as shown Figure 3.15. It was incorporated with the main KIVA code to complete the multidimensional modeling. SETVELIN simulates the hydrogen injection process as a boundary condition. SETVELIN sets the inlet velocity to value from experimental tests at the beginning of gas injection through the velocity open boundary. It is set to zero when time to stop the gas injection. The injection parameters include the injection velocity based on the experimental mass flow rate according to calibration curve of injector (see Figure B.2), mass of hydrogen fuel based on the equivalence ratio and injection duration based on the *SOI* are considered as boundary conditions at the injection region shown in Figure 3.12.

Both kinetically controlled and equilibrium reactions are considered for the combustion of multidimensional model. The forward and backward reactions are specified the rate constants for the kinetically controlled reactions. The progress rates (ω_r) for the kinetic reactions are computed for each reaction (r) and every participating species either inert ($a_{mr} = b_{mr}$) or appears on only one side of the reaction ($a_{mr}b_{mr} = 0$) (Amsden et al., 1989). The chemical reactions occurring in the system is described by Eq. (3.43):

$$\sum_m a_{mr} \times \chi_m \Leftrightarrow \sum_m b_{mr} \times \chi_m \quad (3.43)$$

where χ_m is represent one mole of species, (m)

a_{mr} and b_{mr} are the integral stoichiometric coefficients of the species, (m) appearing as a reactant and as a product, respectively, in the individual reversible reaction, (r).

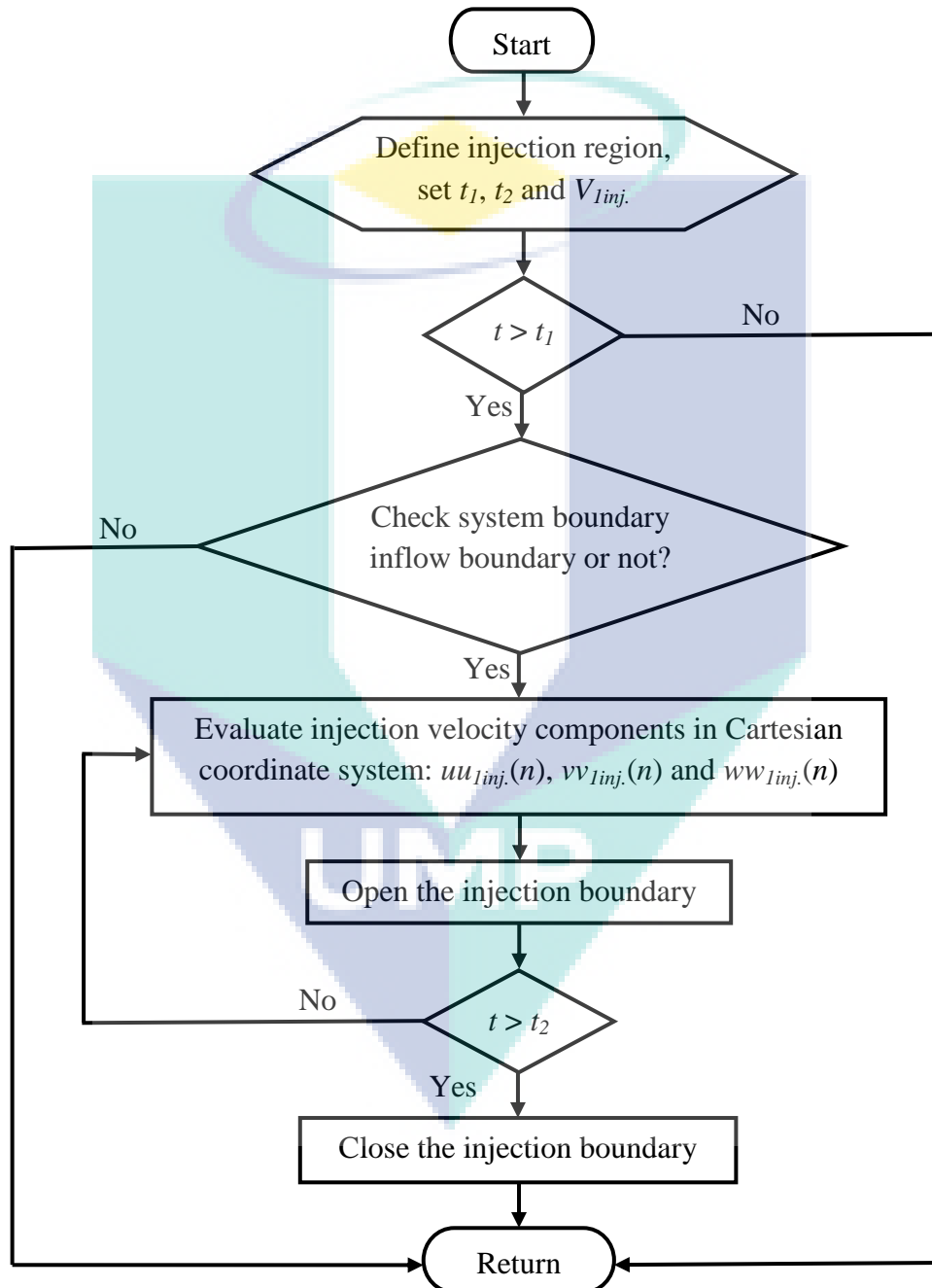


Figure 3.15: Flowchart for the injection program SETVELIN

Hydrogen combustion are produced the following species: H₂, NO, O, N₂, O₂, N, OH, and H. The rate of change for the species concentration due to chemical reaction is given by Eq. (3.44):

$$\left. \frac{d(c_m)}{dt} \right|_{react} = \sum_m (a_{mr} - b_{mr}) \times \omega_r \quad (3.44)$$

where ω_r is the rate at which reaction proceeds and c_m is the concentration of species (m).

The specific reaction rate (ω_r) is related to the concentrations of the reactants by the phenomenological law of mass action applied to the forward and backward reactions. Chemical reactions are divided into kinetically and equilibrium. A kinetic reaction (r) proceeds at a rate (ω_r) is given by Eq. (3.45):

$$\omega_r = k_{fr} \prod_m (c_m)^{a'_{mr}} - k_{br} \prod_m (c_m)^{b'_{mr}} \quad (3.45)$$

where k_{fr} and k_{br} are the forward and backward coefficients of reaction (r)

a'_{mr} and b'_{mr} are the reaction orders

The coefficients k_{fr} and k_{br} are expressed as Eq. (3.46) and Eq. (3.47):

$$k_{fr} = A_{fr} \times T^{\zeta_{fr}} \exp[-E_{fr}/T] \quad (3.46)$$

$$k_{br} = A_{br} \times T^{\zeta_{br}} \exp[-E_{br}/T] \quad (3.47)$$

where A_{fr} , A_{br} , ζ_{fr} and ζ_{br} are an empirical constants

E_{fr} and E_{br} are the forward and backward activation temperature

The source terms due to the kinetically controlled reactions are explicitly computing from Eq. (3.44)-Eq. (3.47). It is prevented species mass fractions from being driven negative. The rates of equilibrium reactions are implicitly determined according to the constraint condition expressed by Eq. (3.48):

$$\prod_m (c_m)^{(b_{mr}-a_{mr})} = K_c^r(T) \quad (3.48)$$

where $K_c^r(T)$ is the concentration equilibrium constant.

The concentration equilibrium constant is defined as Eq. (3.49):

$$K_c^r = \exp\left(A_r \ln T_A + B_r/T_A + C_r + D_r \times T_A + E_r T_A^2\right) \quad (3.49)$$

where A_r , B_r , C_r , D_r and E_r are the polynomial constants.

T_A is the normalised temperature ($T/1000$)

Equilibrium reactions are handled by using an iterative numerical technique. It is iteratively solved the reaction progress increments until achieving the equilibrium condition in Eq. (3.48). This numerical technique has an advantage over the standard procedure through accounting for the heat release of the equilibrium reactions. Accordingly, it is more accurate. The chemical source term in the species continuity equation is evaluated according to the reactions rate determined by Eq. (3.45) or Eq. (3.48), as follows:

$$\dot{\rho}_m^c = M_m \sum_r (b_{mr} - a_{mr}) \times \omega_r \quad (3.50)$$

where M_m is the molecular weight of species m

Chemical heat release term in the energy equation is given by Eq. (3.51) and Eq. (3.52):

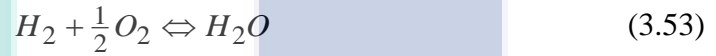
$$\dot{Q}^c = \sum_r Q_r \times \omega_r \quad (3.51)$$

$$Q_r = \sum_m (b_{mr} - a_{mr}) \times (\Delta h_f^o)_m \quad (3.52)$$

where Q_r is the negative of the heat of reaction at absolute zero

$(\Delta h_f^o)_m$ is the heat of formation of species m at absolute zero

A simplified single-step oxidation model is considered for conversion the hydrogen fuel and oxygen to the water vapour as Eq. (3.53):



The reaction rate for this single step is the global one-step hydrogen oxidation reaction rate as Eq. (3.54) (Marinov et al., 1995 and Kumar et al., 2011):

$$\frac{dH_2}{dt} = 1.8 \times 10^{22} \times \exp\left[\frac{1.44 \times 10^5}{RT}\right] \times [H_2]^{1.0} \times [O_2]^{0.5} \quad (3.54)$$

Multidimensional model is simulated the ignition and combustion process in conjunction with the fluid flow for DIH₂ICE. Modeling of the spark ignition is provided by a special energy deposition at the end of the kinetic chemistry subroutine. The ignition process is specified within the crank angle domain by adjusting the initiation of the ignition process at MBT point. During ignition, the internal energy in the specified ignition cell(s) is increased by a factor of $(1.0 + \text{XIGNIT} \times \Delta t)$ on each time step. XIGNIT is the reciprocal time constant for ignition energy addition to spark cell(s). The special energy deposition is terminated when the temperature in the ignition cells reached 1600 K.

Definition of wall function for the velocity and temperature within the region vicinity to the walls is used in the multidimensional model. This is due to the thin boundary layer thickness adjusting to the wall. Therefore, it is unpractical to apply

the computational grid size for determining the shear stress and heat transfer close to the wall. Wall functions are analytic solutions to simplify turbulence equations and are used to conclude wall shear stresses and heat losses (Rakopoulos et al., 2010). It is used instead of numerical solution near walls of complete turbulence equations. The heat transfer model is derived based on assumptions of incompressible flows with perturbation theory (Amsden et. al, 1989). Accordingly, the thermal boundary layers are modeled as a one-dimensional flow based on following assumptions:

- i) The flow is quasi-steady;
- ii) the fluid velocity is directed parallel to a flat wall and varies only in the direction normal to the wall;
- iii) there are no stream-wise pressure gradients;
- iv) there are no chemical reactions in the gas or on the wall surface;
- v) there is no spray source;
- vi) the dimensionless wall heat loss is small compared to unity;
- vii) Reynolds number is large and laminar viscosity is very smaller than eddy viscosity; and
- viii) Mach number is small, so that dissipation of turbulent kinetic energy is a negligible source to the internal energy.

The energy equation near a wall based on above assumptions is expressed as Eq. (3.55):

$$q_w = (k_l + k_t) \frac{dT}{dy} \quad (3.55)$$

where q_w is the wall heat flux

k_l is the laminar thermal conductivity

k_t is the turbulent thermal conductivity

$\frac{dT}{dy}$ is the temperature gradient in the normal direction to the wall

Improved wall function is used to solve the transport equations (continuity, momentum and energy) near to the wall. This improved wall function is obtained the best estimation of wall heat loss (Amsden, 1997 and Xin et al., 2003). It is employed the logarithmic law-of-the-wall to define the velocity and temperature profiles in the near-walls regions. Due to dominant of the turbulent mode, the laminar thermal conductivity (k) is negligible. The definition for the turbulent thermal conductivity is combined with the closure definition of k - ε model eddy viscosity. After the rearrangement, the heat flux is defined as Eq. (3.56):

$$q_w = \frac{\rho \times C_p \times \nu_l \times F \times (T - T_w)}{Pr_l \times y} \quad (3.56)$$

$$F = \begin{cases} 1.0 & \text{for } R' \leq 11.05 \\ \frac{R' \times Pr_l \times RPR}{\frac{1}{\kappa} \times \ln R' + B + 11.05 \times (Pr_l \times RPR - 1)} & \text{for } R' > 11.05 \end{cases}$$

where $R' = \frac{c_\mu^{0.25} \times k^{\frac{1}{2}} \times y}{\nu_l}$

ρ is the density of the in-cylinder gaseous

C_p is the specific heat for in-cylinder gaseous

ν_l is the laminar kinematic viscosity for the in-cylinder gaseous

y is the distance from the wall in the normal direction

Pr_l is the laminar Prandtl number

RPR is the reciprocal of the turbulent Prandtl number

T is the gaseous temperature

T_w is the wall temperature

B , c_μ and κ are the Karman's model's constants

k is the kinetic energy

3.5.4 Algorithm for Multidimensional Model

The governing equations are discretised within the space and time domains. The discretisation process involves a combination of the ALE and variably implicit time-discretisation methods (Holst, 1992). The time derivatives are approximated by the first-order difference. Accordingly, any quantity (Ψ) within governing equations is formulated as Eq. (3.57):

$$\frac{\partial \Psi}{\partial t} \cong \frac{\Psi^{n+1} - \Psi^n}{\Delta t^n} \quad (3.57)$$

where $\Delta t^n = t^{n+1} - t^n$ is the time step

$n = 0, 1, 2 \dots$ is the number of iteration cycle

Each computational cycle is executed in three separated phases: A, B and C. Phase A is a Lagrangian method, where the mesh and control volumes are not moved. The impact of the fuel injection and chemical reactions on gas quantities are calculated within phase A. Phase B is also a Lagrangian method, but the control volume moves with the fluid. Fluid diffusion computations are involved within phase B. Therefore, the governing equations are solved in Lagrangian method using a finite volume scheme. Phase C is a rezoning/remapping phase where the fluid field is static frozen and the mesh moves to a new position. The Eulerian method or the rezoning process is considered within phase C. It includes the grid movement to new positions as well as exchanging the fluxes of mass, momentum, energy and turbulence quantities. The combination of these three phases is equivalent to the process that the mesh moves to a new position in a time step (dt) and the fluid also moves. Figure 3.16 illustrates the comprehensive framework of the numerical algorithm for multidimensional model.

The adopted procedure for solving the governing equations is the SIMPLE technique (Patankar, 1980). This approach is solved the individual equations utilising the conjugate residual method (O'Rourke and Amsden, 1986). The SIMPLE algorithm adopts an iterative routine. It consists of two steps; the pressure field frosts

and solves the other flow quantities. The acquired terms are frosted and solve the implicit finite difference equations for the pressure correction term. Furthermore, it compares the predicted and corrected pressure fields as a condition for convergence criteria. The Lagrangian equations for phase B quantities, namely species density, velocity, temperature, pressure, turbulent kinetic energy and turbulent dissipation rate are solved using the conjugate residual method (O'Rourke and Amsden, 1986). The species and turbulence equations are solved independently. This is because of the weakly coupling between the species and turbulence equations with the flow field solution. Determining of the time step Δt in phase B is based on the accuracy rather than stability conditions. This is due to the implicitly difference for the diffusion terms as well as the sub-cycling of the convective terms. Hence there are no stability restrictions on (Δt) . The flow field is frosted during phase C, as well as the computational mesh moves to new positions. Therefore, the convective transport associated with the moving mesh relative to the fluid is calculated. The convection time step is derived using the Courant stability condition, as Eq. (3.58):

$$\frac{u_r \times \Delta t}{\Delta x} < 1 \quad (3.58)$$

where u_r is the fluid velocity relative to the grid velocity

Δt is the size of time step

Δx is the discretization length for the space domains

The updating of the cell properties is carried out through employing the state equations, and the individual species densities are summed to estimate the density. The Quasi-Second-Order Upwind (QSOU) scheme is used for approximating the difference equations. It is evident that this scheme has more accuracy achievements (Van Leer, 1979).

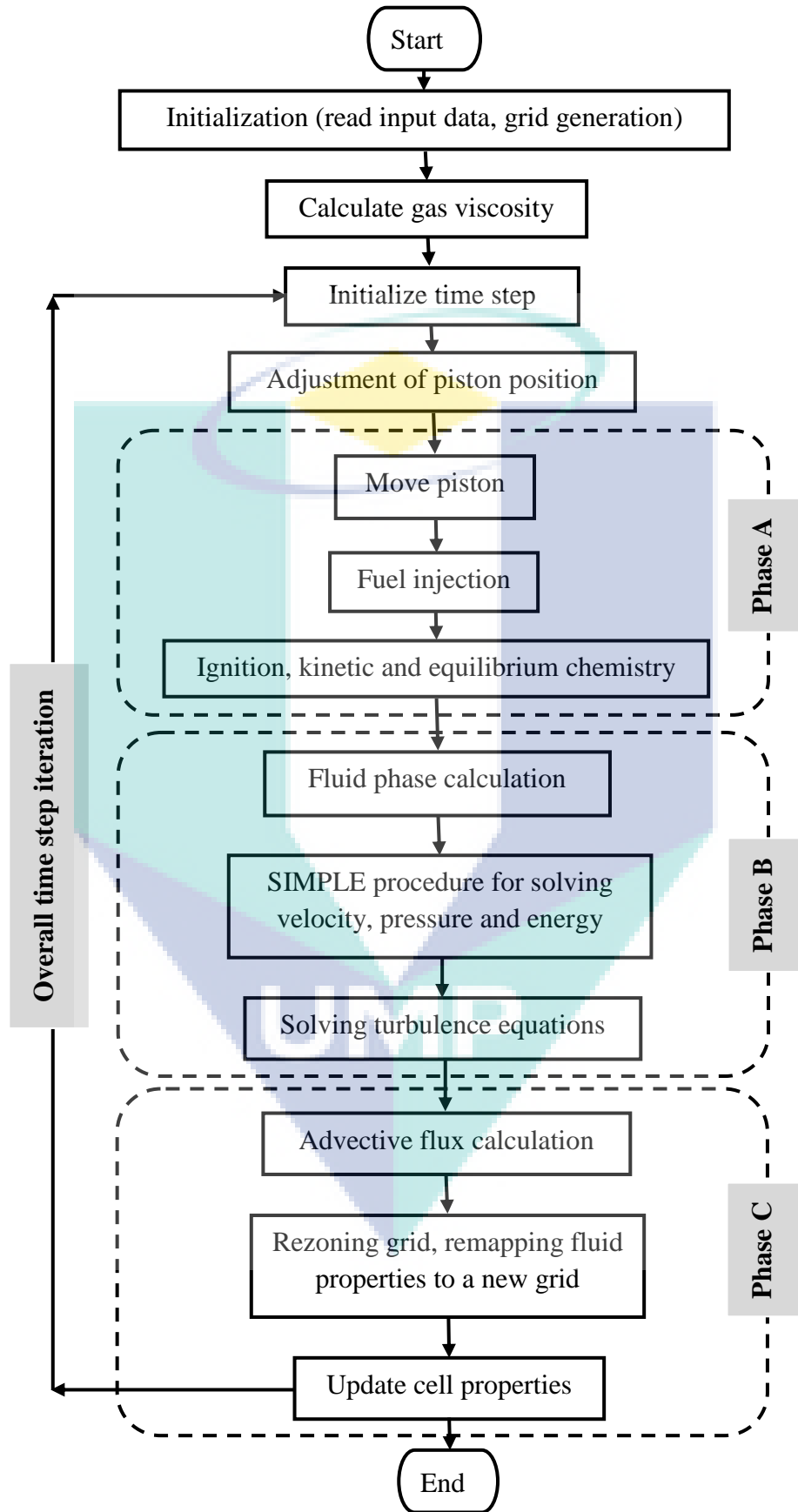


Figure 3.16: Algorithm for the multidimensional model.

The conservation equations are discretized by the finite volume technique on an arbitrary hexahedral mesh applying ALE approach (Hirt, 1974 and Pracht, 1975). The spatial differences are created on a mesh, which subdivides the computational field into a number of small hexahedrons. The vertices are moved with the fluid (Lagrangian), which is kept fixed (Eulerian). In the ALE method, no interpolation is required for determining vertex motion in the Lagrangian phase of calculation. A staggered grid mode is adopted in the multidimensional model. That means, thermodynamic (p , ρ , T , I , ρ_m) and turbulent (k , ε) quantities are stored at the cell centers while velocity is stored at vertexes at the cell corner. Quantities needed at points where they are not fundamentally located are obtained by averaging neighboring values. Spatial difference is carried out by integrating the differential term over the volume of a standard cell.

3.5.5 Boundary and Initial Conditions

The CFD computations consider the compression stroke, including the hydrogen injection process and the combustion/expansion phase. Initial and boundary conditions of the computational model are derived from experimental results of engine measurements as well as from a preliminary cycle simulation. Turbulent law-of-wall velocity conditions with fixed temperature walls are used in this study. The normal gas velocity is equaled to the normal wall velocity while the tangential components are determined by matching to a logarithmic profile. Constant wall temperature is used as the condition at the solid surfaces throughout the computation. The heat flux to the walls is calculated using a modified Reynolds analogy formula. Uniform values are assumed for the in-cylinder pressure and temperature, species concentration, turbulent kinetic energy, and turbulence length scale at the time of the start of computations. A preliminary cycle simulation has been executed to generate the initial conditions for pressure, temperature, and species concentration. The initial value of turbulent kinetic energy (k) is assumed to be 10 % of the total kinetic energy based on mean piston speed. The initial value of dissipation rate (ε) is calculated using standard procedures (Das and Dent, 1995). Besides that, the injection parameters (injection velocity, mass of hydrogen fuel and injection duration) are used as boundary conditions at the injection region shown in

Figure 3.12. Multidimensional model is executed for engine speed $2000 \leq \text{rpm} \leq 5000$ with interval 1000 rpm and equivalence ratio $0.3 \leq \phi \leq 0.9$ with interval 0.2 and start of injection $70 \text{ deg BTDC} \leq \text{SOI} \leq 130 \text{ deg BTDC}$ with interval 30 deg. The same operating parameters are considered in one dimension model.

3.6 SUMMARY

This chapter presented modelling and experimental tools for investigating of heat transfer in DIH₂ICE. The experimental facilities are used for testing and collecting of data is presented. The one-dimensional model based on gas dynamic approach is developed. This model is designated for analyzing of TAHT in DIH₂ICE. It is modeled various processes that take place during the engine cycle. Engine geometry, fluid flow, heat transfer, intake, compression, combustion, expansion and friction were included in this model. Dimensionless analysis is implemented to develop a new TAHT correlation applicable to DIH₂ICE. The multidimensional model based on finite volume approach is developed. This model is developed to perform CFD analysis for the reactive flow within DIH₂ICE. This model is designated for analyzing of IHT in DIH₂ICE. It is modeled various phenomena and processes that take place during the engine cycle. Engine geometry, fluid flow, injection, reaction, ignition and heat transfer were included in this model. It is also composed the whole engine physicochemical process, including flow interaction with hydrogen direct injection and the homogeneity of fuel and air during compression stroke. In the next chapter, these models will be calibrated and validated using several routes and the results will be presented.

CHAPTER FOUR

RESULTS AND DISCUSSION

4.1 INTRODUCTION

This chapter presents the characteristics of the combustion, time-averaged heat transfer (TAHT) and instantaneous heat transfer (IHT) for the direct-injection hydrogen-fueled engine. The combustion characteristics for DIH₂ICE are shown in terms of the experimental results. One-dimensional and multidimensional models were developed for characterizing TAHT and IHT with the assessment of experimental tests. The baseline engine models with the hydrogen-fuel are verified with experimental results then proceed for further investigations. Models validations are performed for the various operation parameters, including the engine speed, equivalence ratio and *SOI*. The grid sensitivity analysis is carried out for geometry of the multidimensional model.

One-dimensional model is used to study the effect of engine speed, equivalence and *SOI* on TAHT in DIH₂ICE. The heat transfer rate, the percentage ratio of heat transfer and dimensionless parameters (*Nu* and *Re* numbers) are used for characterising of TAHT. New predictive correlations for TAHT are developed and assessed. Hydrogen injection process and IHT are characterised based on the multidimensional model analysis. Hydrogen injection process is clarified through using the flow field. Influence of the operation parameters on IHT is presented through a thermal field. The heat release, instantaneous rate and cumulative heat loss are used for monitoring the behavior of IHT. A trend of the heat-transfer coefficient is revealed in terms of the operation parameters.

4.2 EXPERIMENTAL ANALYSIS OF HYDROGEN COMBUSTION

The experimental tests were performed on a direct injection, single cylinder engine with a compression ratio of 14:1. The high compression ratio was intended to take advantage of the high auto ignition temperature of hydrogen fuel (585°C) in order to maximize the thermal efficiency. However, abnormal combustion in the form of 'knocking' was observed during the tests with hydrogen. This is because of starting the combustion by hot spots (pre-ignition) prior to the spark events. Many possible sources were stated that caused the pre-ignition in the engine such as the deposits, spark plug tip and sharp edges in the combustion chamber or because of pyrolysis of engine oil. Moreover, there was a tendency for the backfire to start before the intake valve closed at early injection timing and near to stoichiometric condition.

This section presents the results obtained from the experimental tests. It is devoted to provide clear understanding for the behavior of the instantaneous characteristics of hydrogen combustion. The experimental tests for the instantaneous analysis were carried out for engine speed of 1800 and 3000 rpm, the equivalence ratio of 0.63 and 0.93 and injection timing of 130 and 150 deg BTDC. All tests were conducted to produce the maximum brake torque at the wide-open throttle (WOT) and MBT. The in-cylinder pressure traces are collected from the experimental tests. Then, the trends of the mass fraction burned and heat release rates are investigated based on the in-cylinder pressure traces. The parametric analysis of the in-cylinder pressure traces, mass fraction burned and heat release rates are presented in the following sections.

4.2.1 In-Cylinder Pressure Traces

The assessment of the combustion process in SI engines is based on the in-cylinder pressure traces. There are several parameters directly influenced on the trends of the in-cylinder pressure trace. The equivalence ratio, injection timing and engine speed are considered in the present study. The in-cylinder pressure-crank angle traces are identified using the peak pressure and the corresponding crank angle. The instantaneous in-cylinder pressure was tracked for crank angle of -180 to 180 deg (see

Figure 4.1) includes the compression, combustion and expansion strokes using 100 consecutive cycles to reduce the cyclic variation. However, the crucial part (-30 to 30 deg) is presented for pressure traces analysis .

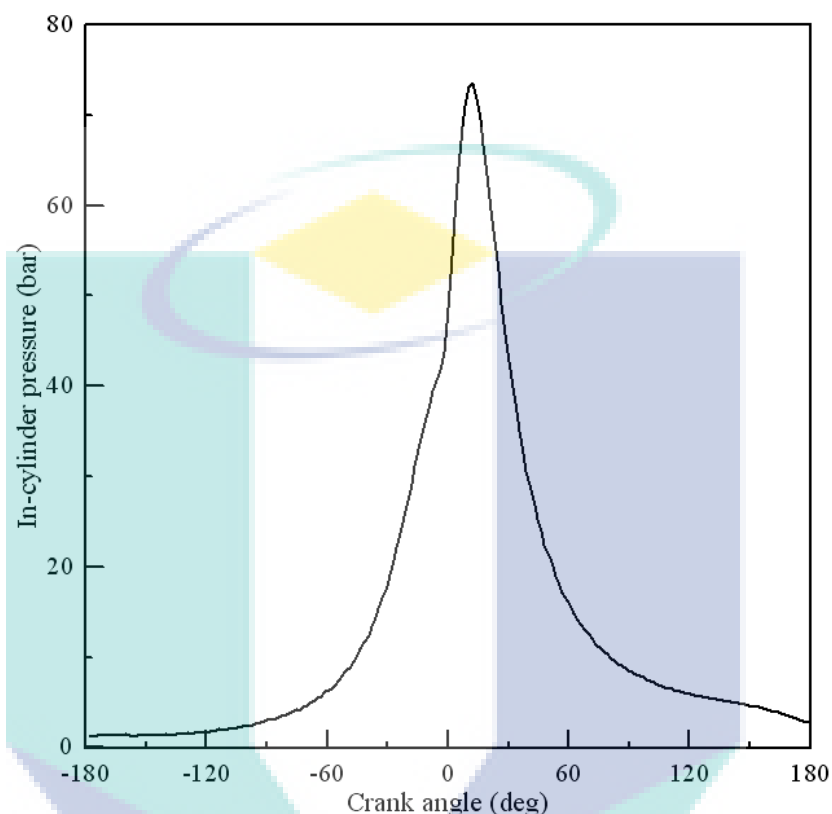


Figure 4.1: Experimental traces of the in-cylinder pressure for at 3000 rpm, $\phi=0.93$ and $SOI = 130$ deg BTDC at the full-load condition.

Two different values of the equivalence ratio (0.63 and 0.93) are selected for experimental tests, which is the range of near to stoichiometric until lean mixture strength. This represents the most promising range for optimization of DIH₂ICE operation (Mohammadi et al., 2007; Berckmüller et al., 2003 and Eichlseder et al., 2003). Figure 4.2 presents the in-cylinder pressures traces for the different equivalence ratio ($\phi = 0.63$ and $\phi = 0.93$) at engine speed of 3000 rpm, $SOI = 130$ deg BTDC and the full-load condition. The in-cylinder pressure traces are identical during compression and expansion strokes. However, there is a significant difference during the combustion stroke. The peak pressure is reached up to 75 bar at 15 deg ATDC at ($\phi = 0.93$), while it is reduced to 57 bar at 15 deg ATDC for ($\phi=0.63$). This difference (24 %) is due to the reduction for the fuel amount per the intake charge. The desired peak

pressure appears close to TDC (5-10 deg ATDC) in case of fossil fuel (Pulkrabek, 2003). However, all the measured timing of peak pressure appears beyond that desired range. This delay in peak pressure timing is due to the retarding of the spark ignition timing (7 deg ATDC) to avoid the abnormal combustion. This is because of the unique characteristics for combustion of hydrogen fuel in comparison with the fossil fuel.

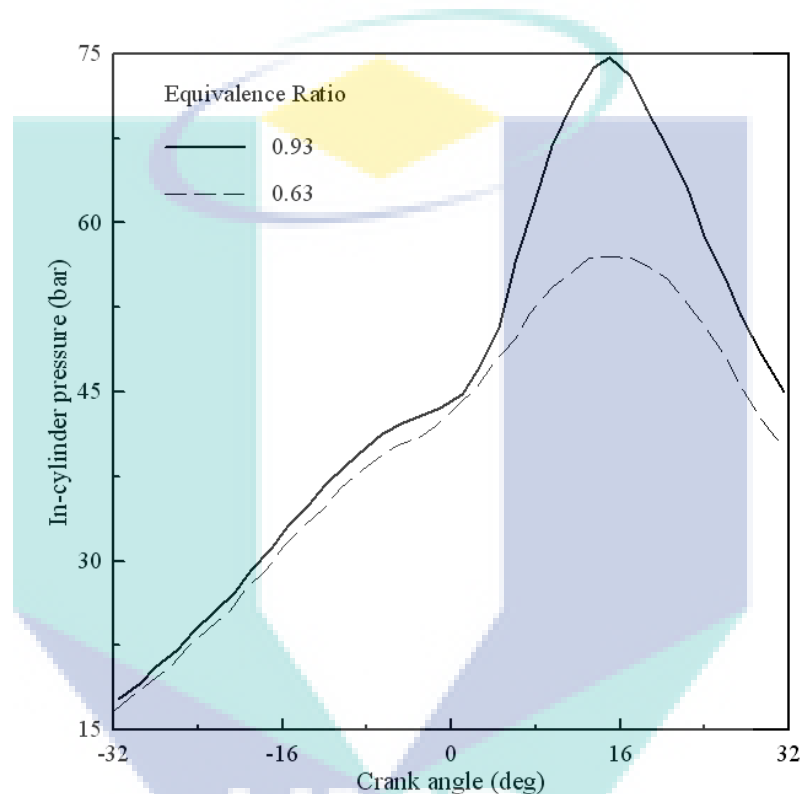


Figure 4.2: Experimental traces of the in-cylinder pressure for different equivalence ratio at 3000 rpm and $SOI = 130$ deg BTDC at the full-load condition.

Another significant observation can be notice in Figure 4.2. At $\phi = 0.93$, a higher combustion rate is detected due to increase the flame speed as the equivalence ratio increases. The energy content of the mixture reduces as the equivalence ratio decreases (Boretti and Watson, 2009). Consequently, the flame speed degraded. Therefore, the combustion rate deteriorates and the spark timing is advanced to neutralize the minimization of combustion rate reduces. Moreover, the ignition event was occurred at the same time. Accordingly, it is not surprising to yield the identical timing for peak pressure because of the interaction between all the parameters.

Figure 4.3 demonstrates the experimental in-cylinder pressure traces against crank angle degree for different injection timing ($SOI = 130$ and 150 deg BTDC) at the engine speed of 1800 rpm, the equivalence ratio ($\phi=1.0$) and the full-load condition. The direct injection ($SOI = 130$ deg BTDC) as well as partially direct injection ($SOI = 150$ deg BTDC) are considered this analysis. The detonation behavior for hydrogen fuel is clearer in Figure 4.3 compared to Figure 4.2 due to the higher flame propagation with an increase of the equivalence ratio (Das, 1996 and Natkin et al. 2003). The in-cylinder pressure traces are identical during compression and expansion strokes. However, there is a significant difference during the combustion stroke. The peak pressure is reached up to 93 bar at 12 deg ATDC at $SOI = 130$ deg BTDC, while it is reduced to 88 bar at 15 deg ATDC for $SOI = 150$ deg BTDC. This difference is due to earlier and faster rate of combustion for $SOI = 130$ deg BTDC. This is because of the direct injection ($SOI = 130$ deg BTDC) produces a stratified mixture (Grabner et al., 2006; Wimmer et al., 2005 and Eichlseder et al., 2003), while the partially direct injection ($SOI = 150$ deg BTDC) produces a homogeneous mixture (Mohammadi et al., 2007 and Grabner et al., 2006).

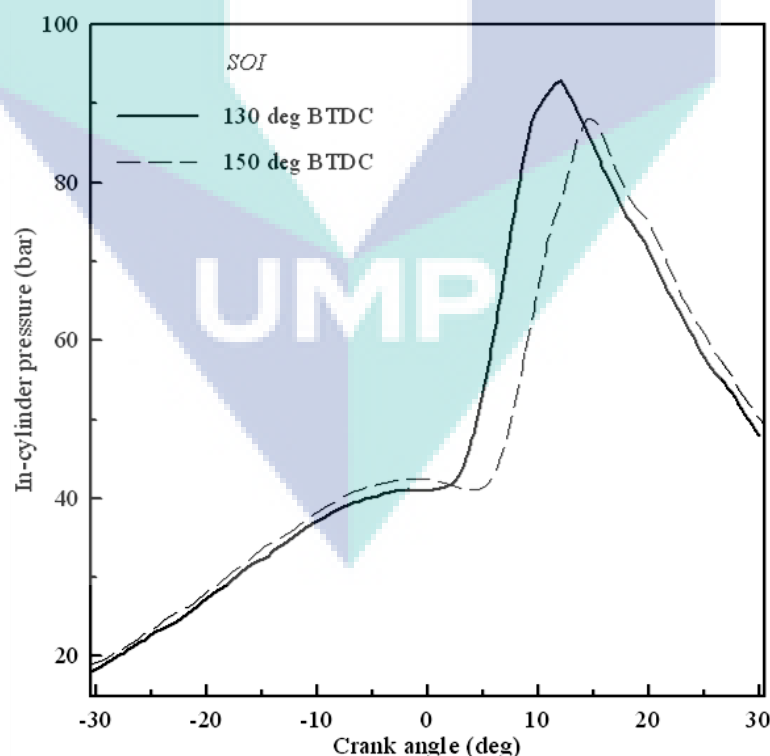


Figure 4.3: Experimental traces of the in-cylinder pressure for different injection timing at 1800 rpm and stoichiometric mixture condition ($\phi=1.0$) at the full-load condition.

Moreover, the combustion is initiated a slightly earlier for direct injection due to advancing the ignition timing (1.6 deg ATDC) compared to partially direct injection (2.4 deg ATDC). It is expected that, the earlier injection timing produce lower torque due to the reduction in the volumetric efficiency (Liu, et al., 2008; White, 2006 and Wimmer et al., 2005). However, the same torque (29.6 Nm) was obtained for the injection timing of 130 and 150 deg BTDC. This is because of the volumetric efficiency loss was not significant ($< 5\%$) due to the charge cooling effect of hydrogen expansion (Abdullah, 2009). Therefore, a more fuel-air mixture is drawn into the combustion chamber.

4.2.2 Mass Fraction Burned

The mass fraction burned (MFB) is derived based on measurement of the in-cylinder pressure traces. Characterization of MFB is based on the ignition delay period, flame propagation period and flame termination. These specifications are typically used for distinguishing different stages of the SI engine combustion process (Ferguson and Kirkpatrick, 2001 and Heywood, 1988). The MFB is calculated using the well-known model developed by Rassweiler and Withrow (1938). Figure 4.4 shows MFB against crank angle for the different equivalence ratio ($\phi = 0.63$ and $\phi = 0.93$) at the engine speed of 3000 rpm, $SOI = 130$ deg BTDC and the full-load condition. The MFB has an identical flame termination period while a small reduction (around 2 deg) is revealed for the ignition delay as the equivalence increased. However, there is a significant difference in the flame propagation period where a sharper trend for ($\phi = 0.93$) is observed. This is because of increasing the burning velocity as the mixture strength shifted from the lean to stoichiometric condition (Boretti and Watson, 2009).

Figure 4.5 shows the MFB against crank angle for different injection timing ($SOI = 130$ and 150 deg BTDC) at the engine speed of 1800 rpm, equivalence ratio ($\phi = 1.0$) and the full-load condition. The MFB has an identical flame termination period while a small reduction (around 2 deg) is revealed for the ignition delay and flame propagation periods as the SOI retarded ($SOI = 130$ deg BTDC). The reduction of the ignition delay period is because of advancing the ignition timing (1.6 deg ATDC). The reduction of the flame propagation periods is due to the faster rate of combustion with

the stratified mixture ($SOI = 130$ deg BTDC). This is because of a bit stratification occurs for the mixture with direct injection ($SOI = 130$ deg BTDC) while the homogenous mixture is yielded with partial direct injection ($SOI = 150$ deg BTDC). Therefore, the combustion process is faster in case of the stratified mixture due to the faster rate of combustion (Wimmer et al., 2005).

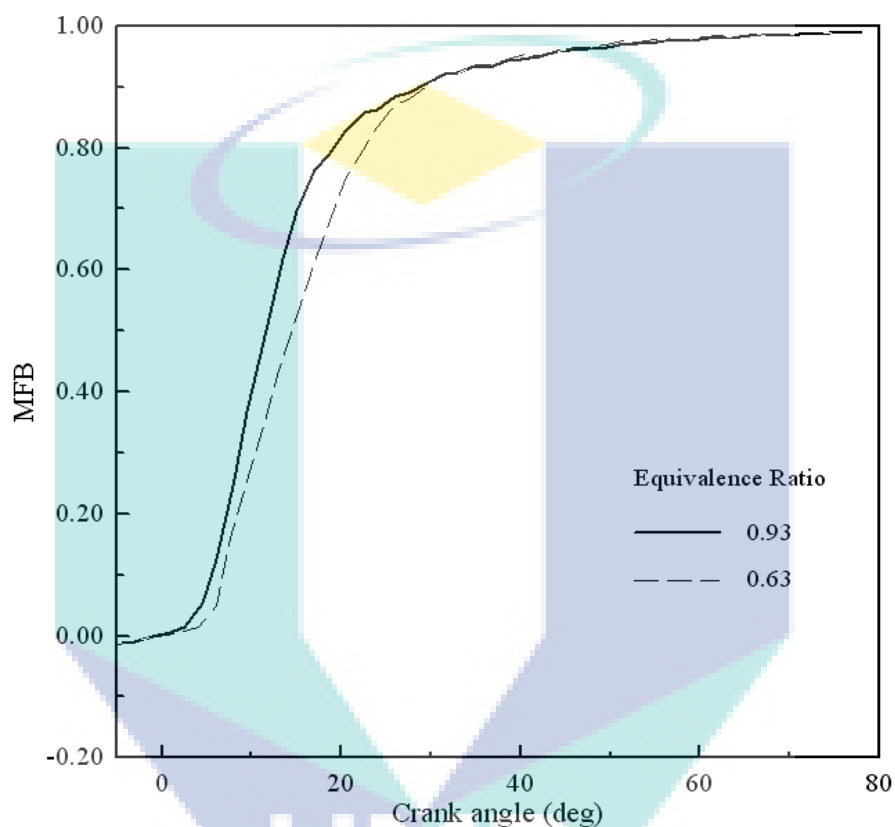


Figure 4.4: Variation of the mass fraction burned for different equivalence ratio at 3000 rpm and $SOI = 130$ deg BTDC at full-load condition.

The direct injection ($SOI = 130$ deg BTDC) seems to be a better injection timing at 1800 rpm condition, in which combustion duration shorter and combustion efficiency higher. In Figures 4.4 and 4.5, the MFB starts with almost -0.005 at spark timing, and then it starts to increase after that. The MFB approaches noticeably to its maximum value with an increase of crank angle. Essentially, at this point all the fuel chemical energy is almost released at the end of the combustion process. It can be seen that the maximum MFB, which essentially identifies the end of combustion, occurs later as the equivalence ratio decreases and the injection timing advances respectively. In general, based on the MFB trends, the overall combustion process is completed in the period

(0.1-0.9) within 20 deg. This short period is due to the fast burning speed for hydrogen fuel, which is the reason of the detonation behavior of hydrogen combustion (Das, 1996).

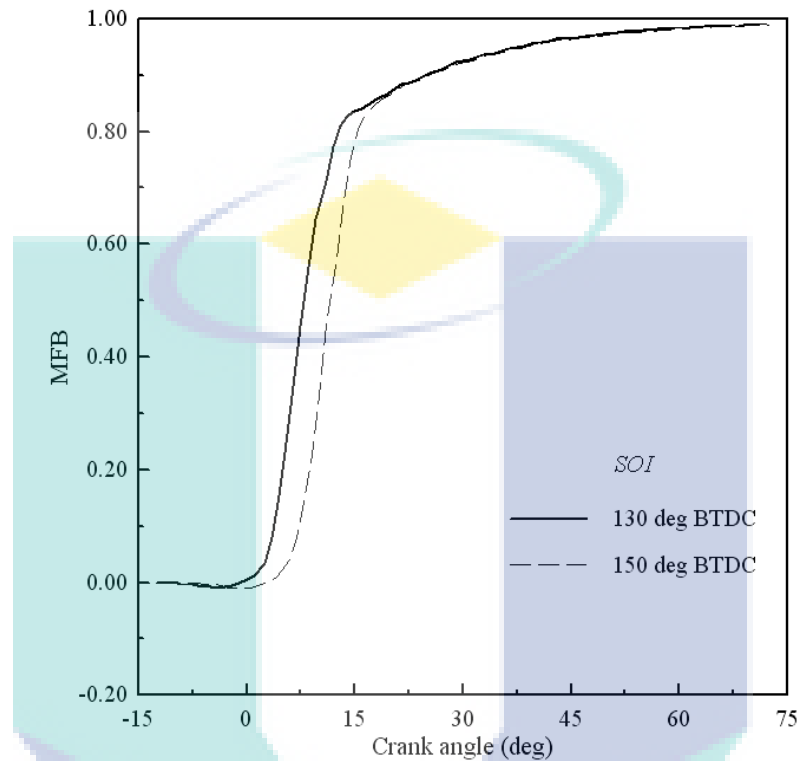


Figure 4.5: Variation of the mass fraction burned for different injection timing at 1800 rpm and stoichiometric condition ($\phi = 1.0$) at full-load condition.

4.2.3 Heat Release Rate

The in-cylinder pressure traces in conjunction with the cylinder volume can be used to estimate the instantaneous energy release from the combustion process with respect to crank angle (Martyr and Plint, 2007). There are many well-documented theories, which are fundamentally similar, depended on earlier work (Rassweiler and Withrow, 1938). This approach was adopted in the present study for estimating of the heat release rate from the in-cylinder pressure and volume data. Figure 4.6 presents the variation of heat release rate against the crank angle for the different equivalence ratio ($\phi = 0.63$ and $\phi = 0.93$) at 3000 rpm, $SOI = 130$ deg BTDC and the full-load condition. The heat release rate is based on the in-cylinder pressure-volume diagrams. Trends of

heat release rate are identical during the compression stroke. However, there are significant differences during the combustion and expansion stroke. The maximum rate of heat release is increased from 0.03 to 0.05 kJ/deg as the equivalence ratio increases from 0.63 to 0.93 due to more energy being fed into the engine (Boretta and Watson, 2009). This difference (40 %) is due to the reduction in the fuel amount per the intake charge. Besides that, the timing of peak rate is increased from 9 to 13 deg ATDC. Furthermore, the relation between the equivalence ratio and combustion rate and duration can be extracted from Figure 4.6. Combustion rate is increased as an increase of the equivalence ratio due to increase of the flame burning speed (Stefaan and Sebastian, 2005 and Verhelst and Sierens, 2003) and thus increase of the turbulent flame propagation (Wimmer et al., 2005). The heat release rate is faster increased and decreased during combustion and expansion strokes respectively in case of ($\phi = 0.93$). Therefore, there is interception between curves of the two cases. Combustion duration is decreased from 30 to 20 deg ATDC as the equivalence ratio increased from ($\phi = 0.63$) to ($\phi = 0.93$) due to the slower combustion for the leaner mixture. This behavior is well agreed with the previous observation reported by Ma et al. (2011), Wimmer et al. (2005) and Shudo et al. (2000b).

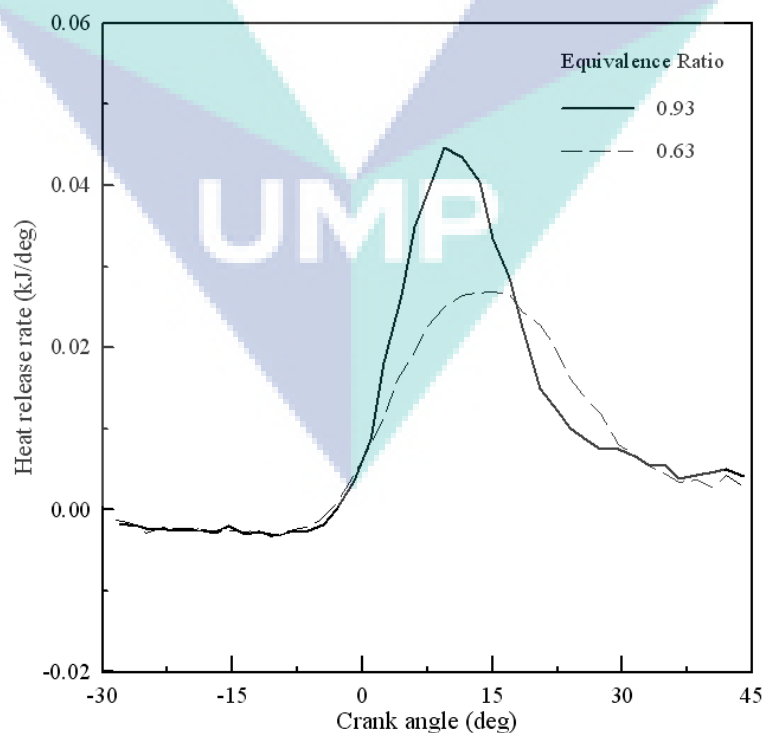


Figure 4.6: Variation of the heat release rate profiles for different equivalence ratio at 3000 rpm and $SOI = 130$ deg BTDC at full-load condition.

Figure 4.7 shows the variation of heat release rate for different injection timing ($SOI = 130$ and 150 deg BTDC) at the engine speed of 1800 rpm, equivalence ratio ($\phi = 1.0$) and the full-load condition. Trends of heat release rate are an identical during all strokes for both injection timings (130 and 150 deg BTDC). However, there is a small difference (7%) in the maximum rate of heat release and corresponding crank angle. The maximum rate is decreased from 0.1 to 0.093 kJ/deg and the corresponding crank angle of 9 and 13 deg ATDC, as SOI advanced from 130 to 150 deg BTDC. This is caused by the effect of charge stratification since the direct-injection timing ($SOI = 130$ deg BTDC) has a wider injection window after intake valve closed (Wimmer et al., 2005). It can also be seen that the maximum rates of heat release in Figure 4.7 are greater than Figure 4.6 due to the retardation in ignition timing (7 deg ATDC).

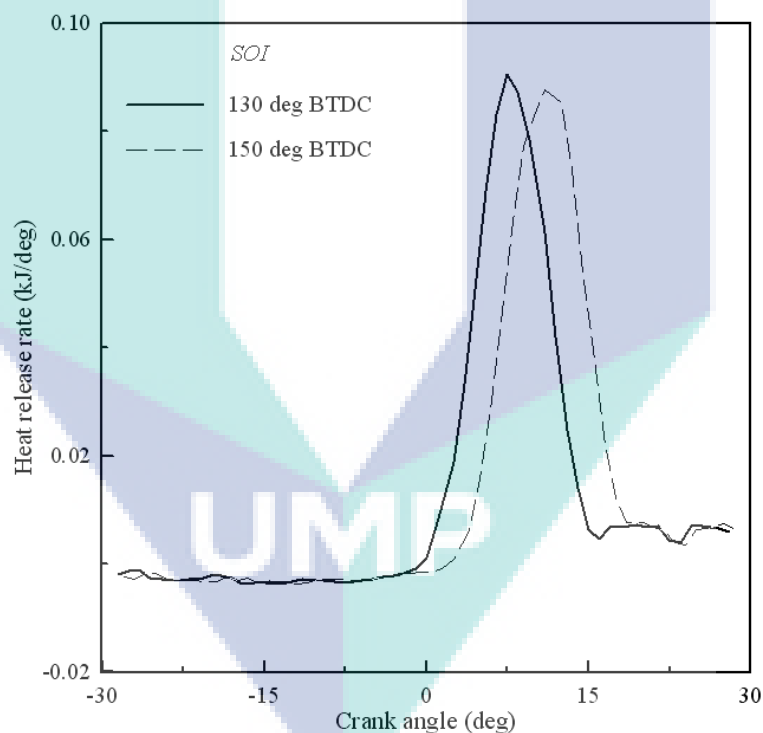


Figure 4.7: Variation of the heat release rate for different injection timing at 1800 rpm and stoichiometric mixture condition ($\phi=1.0$) at full-load condition.

4.3 ONE-DIMENSIONAL MODEL

One-dimensional model is developed based on gas dynamic approach. It is employed to characterize the TAHT of DIH₂ICE. The developed model is validated against the experimental results. One-dimensional model is validated for various engine

speed, equivalence ratio and *SOI*. It is performed in terms of the *IMEP*, the peak in-cylinder pressure, the volumetric efficiency, the engine brake torque and the engine brake power. Analysis of TAHT is based on the heat transfer rate, the percentage ratio of heat transfer rate, dimensionless parameters and correlation between the dimensionless parameters. It is considered the effect of engine speed, equivalence and *SOI*. Following sections present the results of the one-dimensional model.

4.3.1 Model Validation

The collected database from the experimental test rig was used to validate the baseline engine model. The baseline engine model was performed for a test rig of a single-cylinder PROTON CAMPRO engine. Model validation was performed for three operation parameters namely the engine speed, equivalence ratio and *SOI*. The developed model was validated in terms of the *IMEP*, the peak in-cylinder pressure and the engine brake torque for various engine speed and *AFR* at *SOI* = 130 deg BTDC. This injection timing is chosen to simulate the direct- injection case. Further retarding for *SOI* is unachievable experimentally due to the abnormal combustion. However, it was validated in terms of the volumetric efficiency, the brake torque and power for various engine speed and *SOI* at $\phi = 0.78$. Several calibration parameters, including friction, combustion, and heat transfer based on the Woschni's correlation were incorporated in the one-dimensional model. These calibration parameters are used to adjust the developed model with experimental results. Table 4.1 summarizes the calibration parameters, which are considered for one-dimensional model.

Table 4.1: Calibration parameters considered for the one-dimensional model

Calibration parameter	Values of best matching	Unit
<i>C</i>	0.43	bar
<i>PF</i>	0.0047	-
<i>MPSF</i>	0.086	bar/(m/s)
<i>MPSSF</i>	0.0011	bar/(m/s) ²
<i>a</i>	5	-
<i>n</i>	3	-
Woschni's correlation multiplier	1.13	-

Figure 4.8 presents the comparison between predicted (simulated) and experimental results of *IMEP* against *AFR* at *SOI* = 130 deg BTDC for engine speed of 1800 and 3000 rpm. It can be seen that the *IMEP* is decreased as *AFR* increased while there is a minor effect for the engine speed on the general trends. This general trend is coincidence with previous works reported by Boretti and Watson (2009), Boretti et al. (2007) and Eichlseder et al. (2003).

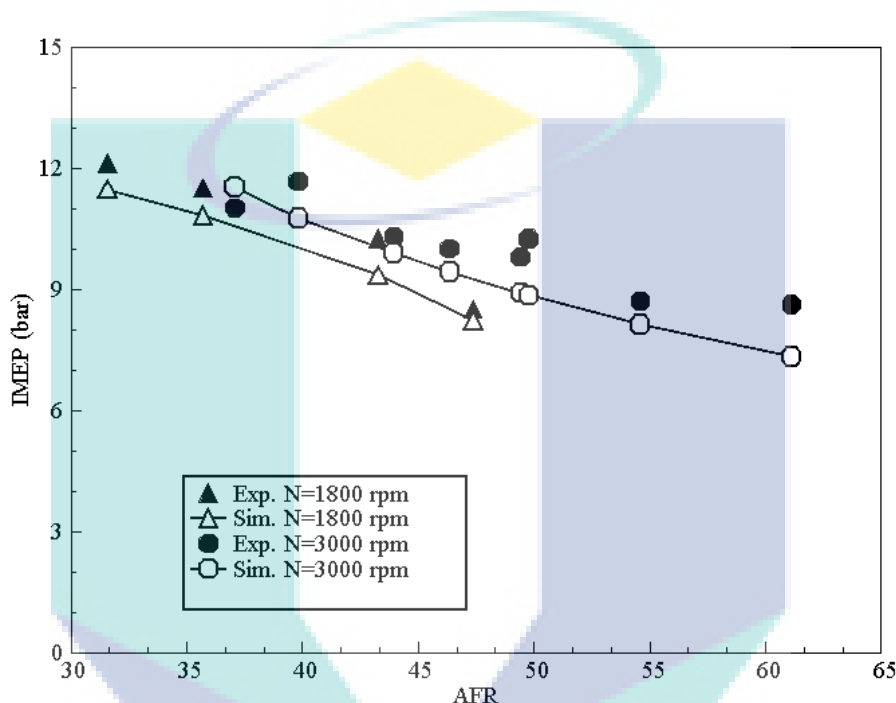


Figure 4.8: Comparison between predicted (simulated) and experimental results of *IMEP* for the baseline hydrogen engine at *SOI* = 130 deg BTDC

Figure 4.9 compares the predicted (simulated) with experimental results of the maximum in-cylinder pressure against *AFR* at *SOI* = 130 deg BTDC for engine speed of 1800 and 3000 rpm. It can be seen that the maximum in-cylinder pressure is decreased as *AFR* increased. This general trend is the coincidence with previous works reported by Boretti and Watson (2009), Boretti et al. (2007) and Verhelst et al. (2006b). However, its trends with the engine speed variation are fluctuated because of retarding the ignition timing with increasing of engine speed to prevent the pre-ignition phenomenon at high engine speed operation.

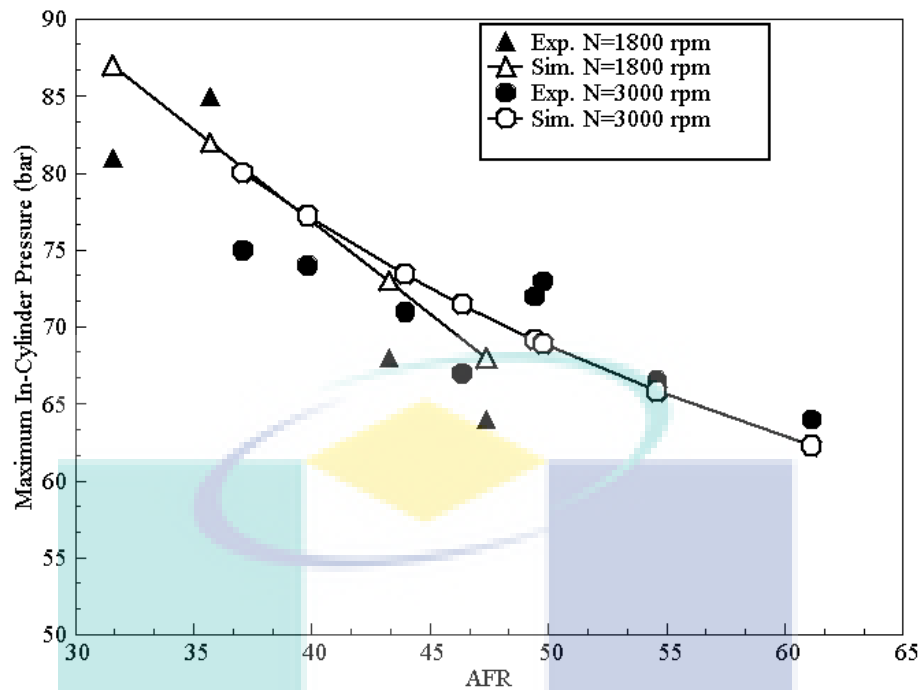


Figure 4.9: Comparison between predicted (simulated) with experimental results of the maximum in-cylinder pressure for the baseline hydrogen engine at $SOI = 130$ deg BTDC.

Figure 4.10 presents the comparison between the predicted (simulation) and experimental brake torque against AFR at $SOI = 130$ deg BTDC for engine speed of 1800 and 3000 rpm. It can be seen that the brake torque is decreased as AFR increased while minor influence for engine speed is appeared. This general trend is the coincidence with previous work reported by (Verhelst et al., 2008).

The start of injection timing is one of the main operation parameters for analysis of DIH_2ICE during the present investigation. The developed model is validated in terms of the volumetric efficiency, the engine brake torque and power for various SOI and engine speed at $\phi = 0.78$. The volumetric efficiency has vital importance for hydrogen engine because of a large amount of the incoming air displaces by the hydrogen fuel due to its low density (0.0824 kg.m^{-3} at 25°C and 1 atm.). These properties reduce the volumetric efficiency to a high extent.

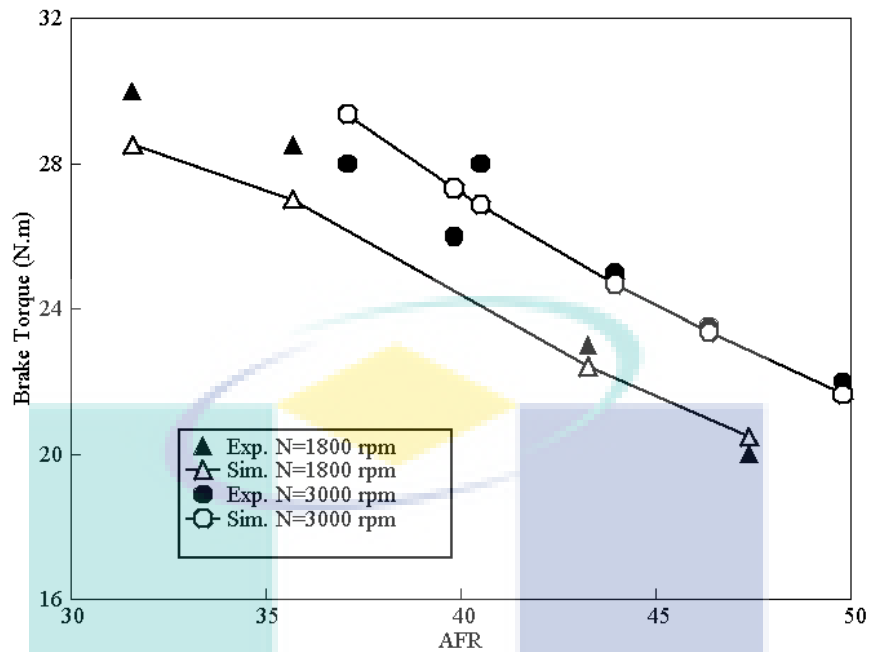


Figure 4.10: Comparison between predicted (simulation) and experimental brake torque for the baseline hydrogen engine at $SOI = 130$ deg BTDC.

Figure 4.11 shows the comparison between the predicted (simulated) and experimental results for the volumetric efficiency with respect to engine speed and SOI at $\phi = 0.78$. For all experimental tests, in cases of $SOI = 130$ and 150 deg BTDC, the engine operation at a speed above 3000 rpm was not achievable due to the long injection duration requirement (limitation by ignition event as well as cylinder pressure) (Abdullah and Rashid, 2009). The volumetric efficiency increases as the engine speed increases for all values of SOI . This is due to increase the vacuum at intake port as the engine speed increase. Thus, the large amount of air is charged to the combustion chamber. The volumetric efficiency is decreased dramatically from 85% to 55% as the SOI advanced from 130 to 300 deg BTDC. This is due to increase the displaced fresh air by hydrogen fuel within the combustion chamber at 300 deg BTDC. Both the experimental and simulation results are coincidence with the general trends of previous observation reported by (Lee et al., 1995 and Yi et al., 1996).

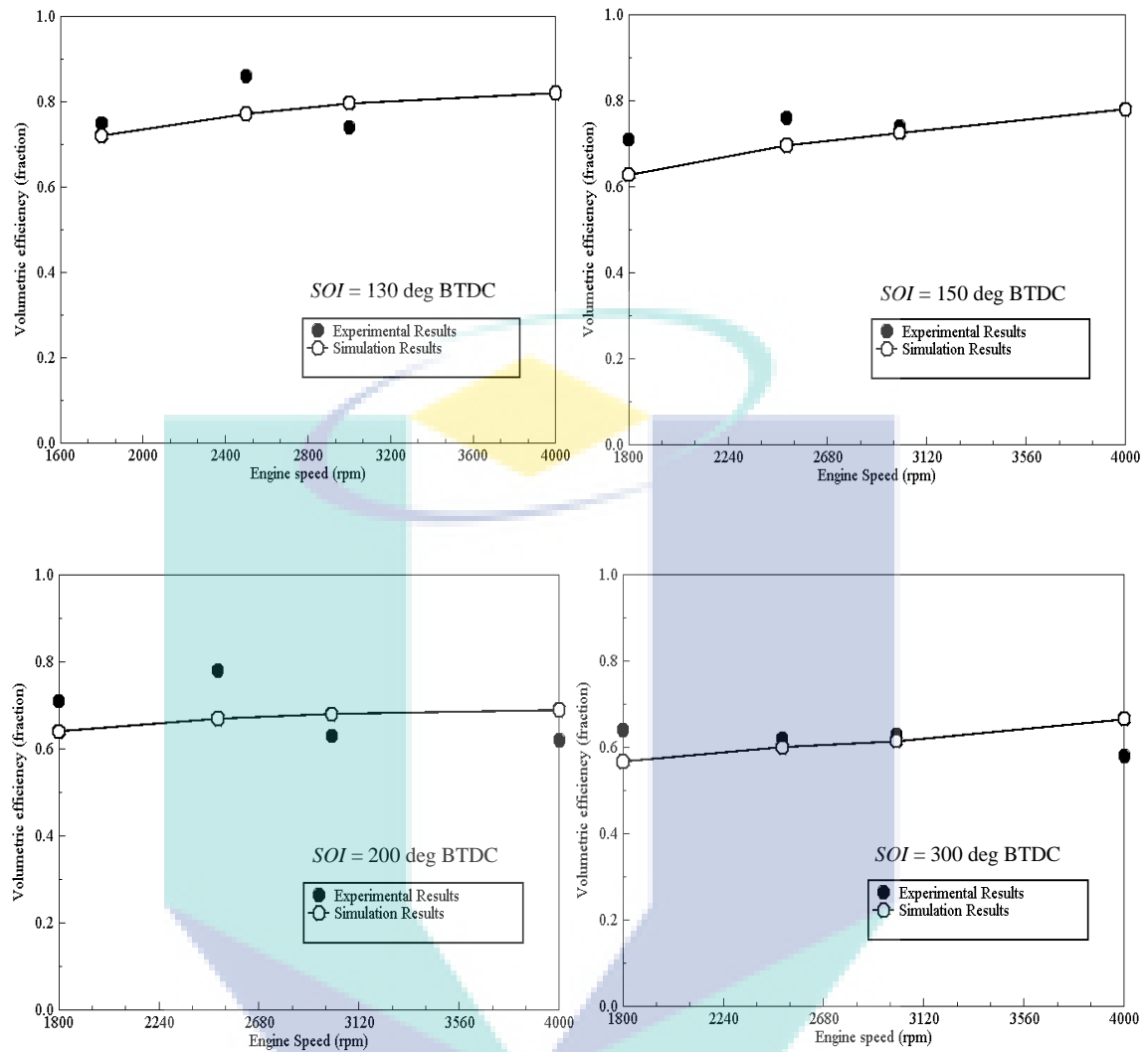


Figure 4.11: Comparison between measured and simulated volumetric efficiency for the baseline hydrogen engine at different engine speed and SOI .

Figure 4.12 presents the comparison between the predicted (simulated) and experimental results for brake torque against the engine speed for various SOI at $\phi = 0.78$. The engine brake torque increases as engine speed increases for all values of SOI . This general trend is coincidence with previous work reported by Kahraman et al. (2007). Furthermore, the engine brake torque decreases and tends to have the flat profile as the SOI advances from 130 to 300 deg BTDC.

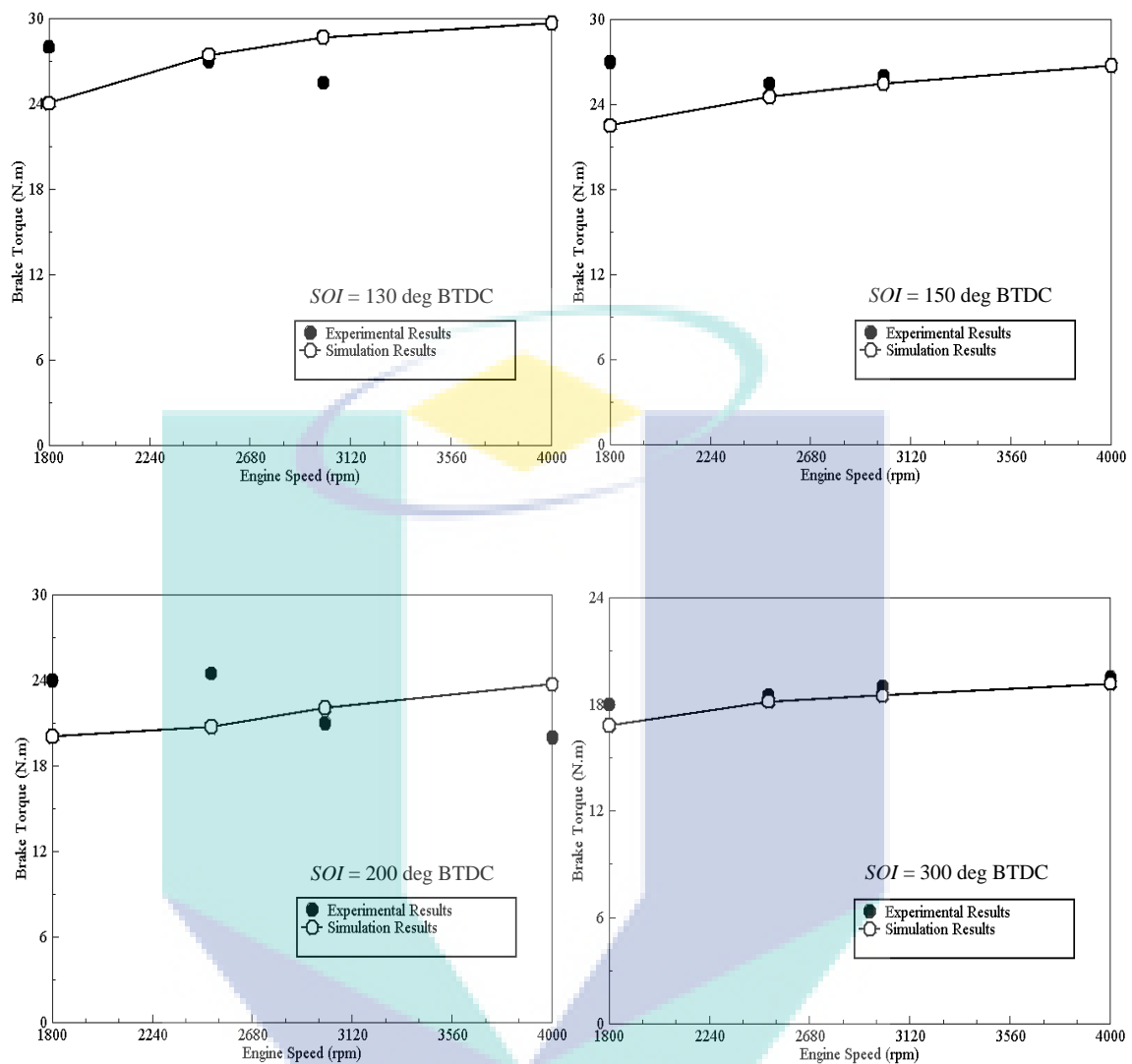


Figure 4.12: Comparison between measured and simulated engine brake torque for the baseline hydrogen engine at different engine speed and *SOI*.

Figure 4.13 compares between the predicted (simulation) and experimental results for engine brake power against the engine speed for various *SOI* at $\phi = 0.78$. Engine brake power increases linearly as the engine speed increases from 1800 to 4000 rpm. This general trend is coincidence with previous work reported by Verhelst et al. (2008) and Kahraman et al. (2007). Furthermore, the engine brake power decreases as the *SOI* advances from 130 to 300 deg BTDC. The influence of advancing *SOI* from 130 to 300 deg BTDC is caused in the reduction of the engine brake torque and power (see Figures 4.12 and 4.13). The rate of reduction for the torque and power is identical to volumetric efficiency.

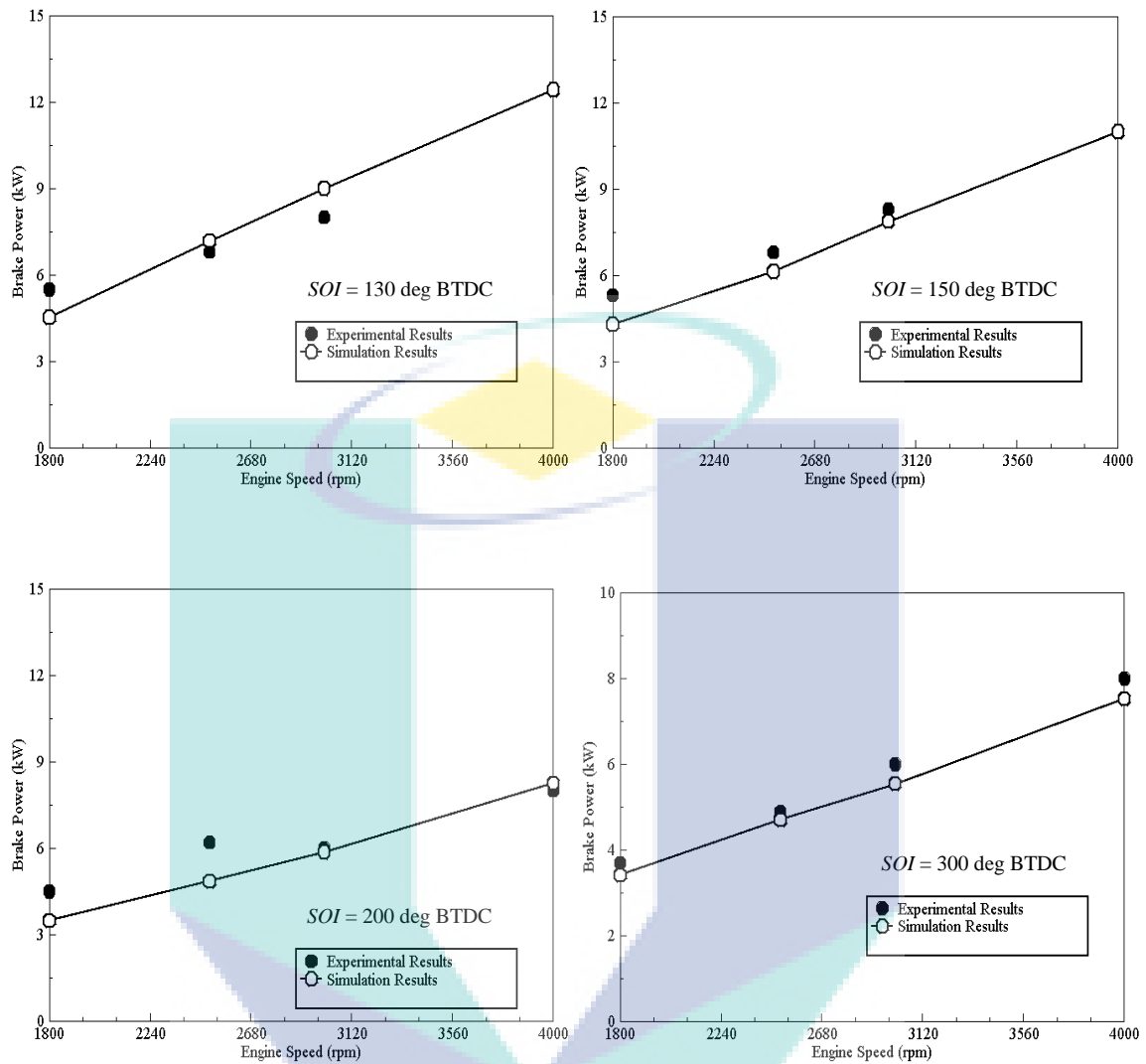


Figure 4.13: Comparison between measured and simulated engine brake power for the baseline hydrogen engine at different engine speed and *SOI*.

It can be seen a well tendency agreement between predicted and experimental results. However, there is a discrepancy between the predicted and experimental results, where the average deviation around 10 %. These deviations are appeared because of ignoring the effect of blow-by, leakage and cycle-to-cycle variation within the developed model. In spite of that, the adopted model is still capable of describing the engine performance. It can be seen obviously that the present one-dimensional model is capable to predict the engine performance of DIH₂ICE. Therefore, it can be extend to use for further estimation and optimization purpose.

4.3.2 Analysis of Time-Averaged Heat Transfer

Analysis of the time-averaged heat transfer is performed based on the one-dimensional gas dynamic model for DIH₂ICE with the different operation parameters namely the engine speed, equivalence ratio (ϕ) and injection timing (*SOI*). The engine speed is varied from 1800 to 5000 rpm with interval of 400 rpm. Equivalence ratio (ϕ) is varied from rich $\phi = 1.2$ to an ultra lean mixture $\phi = 0.2$ with interval of 0.1, which include large part from the flammability limit for the hydrogen ($0.1 \leq \phi \leq 7.1$) (Sierens and Verhelst, 2003 and Verhelst et al., 2006). The *SOI* is considered after the intake valves closed. It is varied from 70 to 130 deg BTDC with interval of 15 deg. These conditions are based on benchmarks of previous studies on the engine performance optimization (Mohammadi et al., 2007). The heat-transfer parameters, including the heat transfer rate, the percentage ratio as well as the dimensionless parameters are considered for analysis of TAHT. The correlations between the dimensionless parameters are also developed for time-averaged heat transfer. The following sub-section presents the detail's analysis of time-averaged heat transfer.

Heat Transfer Rate

Heat transfer rate is used to characterize the TAHT based on the operation parameters. The heat transfer rate within a combustion chamber has instantaneous behavior for ICE application (Eichelberg, 1939; Annand, 1963 and Woschni, 1967). However, the time-averaged of heat transfer provides valuable information for designing and optimizing of ICE (Taylor, 1985; Heywood, 1988 and Stone, 1999). The cyclic integral for the instantaneous rate of heat transfer from gases to combustion chamber walls under the time domain is used as an indicator. Variation of heat transfer rate in terms of the engine speed and ϕ for different *SOI* is demonstrated in Figure 4.14. The heat transfer rate increases with an increase of the engine speed as well as the equivalence ratio for all *SOI*. Heat transfer rate is boosted as the engine speed increased due to increase the driving force (forced convection) for the heat-transfer mechanism (Schubert et al., 2005).

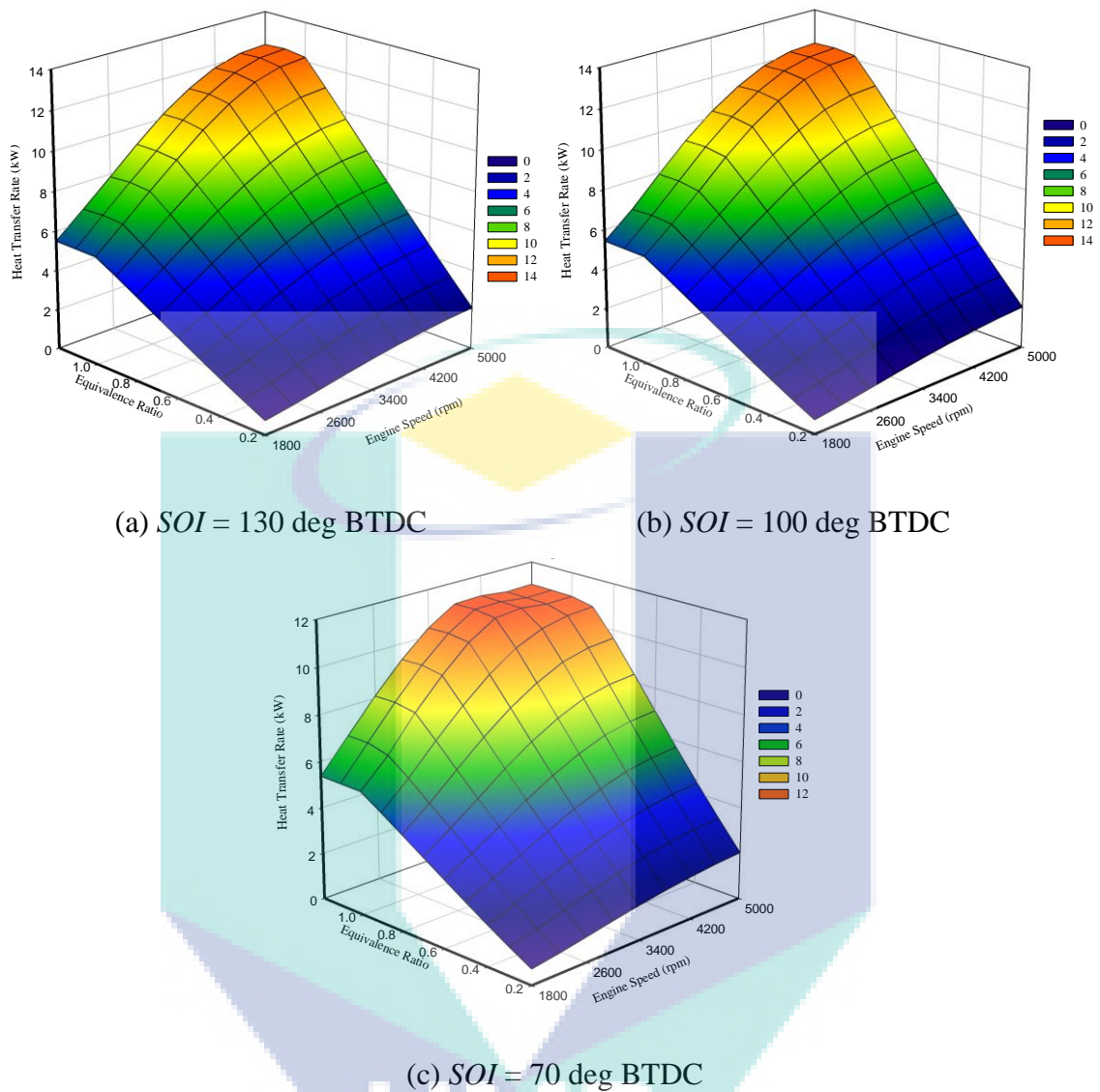


Figure 4.14: Variation of heat transfer rate against the engine speed and equivalence ratio for different *SOI*.

This behavior can be explained through the scrutiny deeply of the Woschni model for heat transfer. Heat transfer rate during the engine power cycle is divided into two stages based on the definition of characteristic velocity for the Woschni model (Woschni, 1967). The mean piston speed is used for the intake, compression, expansion and exhaust strokes. The turbulence level increases as the engine speed increases during these strokes (Ferguson and Kirkpatrick, 2001). Therefore, the heat transfer rate boosts as engine speed increases. The in-cylinder gas velocity is used for combustion stroke, which is mainly depended on the combustion pressure rise. It is noted that the raise pressure is directly boosted with increasing of engine speed (White, 2006). Thus, the

instantaneous heat transfer coefficient is increased directly with increasing engine speed. Finally, the heat transfer rate increased with increasing of engine speed. Accordingly, the effect of engine speed on the heat-transfer behavior is justifiable.

The increment of heat transfer rate at low engine speed (1800-2600) for the ultra-lean mixture is around (35 %) while it is (> 55 %) for the lean mixture until the stoichiometric limit. This is because of the energy content increases as the mixture becomes richer. Therefore, the combustion heat release is become higher. Consequently, the rate of heat transfer is increased significantly. Beyond the stoichiometric limit, the rate of increment is remained constant for the range of engine speeds (1800-3800 rpm). This is due to the insufficient amount of existing oxygen to complete the combustion process. This is an indication that a poor performance for the combustion process. For higher engine speeds, the low increment rate of heat transfer rate is observed, and the curve tends to be flatter. This combined effect between engine speed and ϕ is a crucial and unique influence on the heat-transfer process for H_2ICE .

For $SOI = 70$ deg BTDC, it can be seen that the range of the flatter area is increased as shown in Figure 4.14c. It can be explained by the perception of the relationship of the time required for injection with increasing of the engine speed. As the engine speed increased, it is difficult to provide the sufficient time for fuel injection. There is a short period between the end of fuel injection and start of the combustion process. This period is not enough to mix the fuel with air in a sufficient way to produce a homogenous mixture. An incomplete combustion process is occurred in this situation. The energy content is not fully converted due to the weakness of the combustion process. These trends for heat transfer rate are revealed the characteristics of TAHT inside the cylinder.

Percentage Ratio of Heat Transfer

The heat transfer as a percentage ratio of the fuel's chemical energy is usually used for characterization of the heat transfer in ICE (Heywood, 1988 and Yamin, 2007). Besides the heat transfer rate, the percentage ratio of heat transfer (PRHT) is used as another indicator for characterization of time-averaged heat transfer in DIH_2ICE . The

variation of PRHT against the engine speed and equivalence ratio for different *SOI* is shown in Figure 4.15.

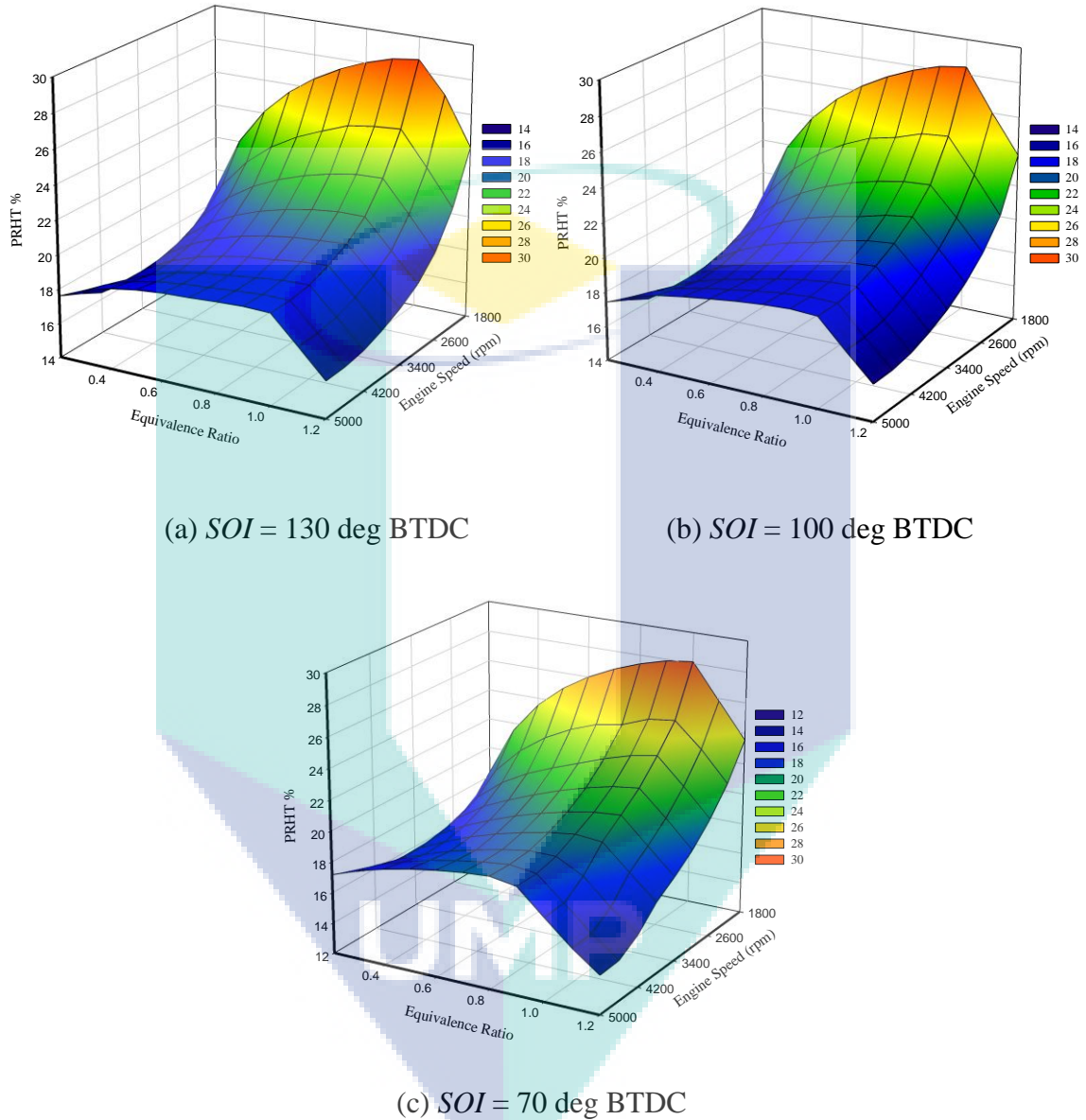


Figure 4.15: Variation of PRHT against the engine speed and equivalence ratio for different *SOI*.

It is decreased with increasing of the engine speed as well as the equivalence ratio beyond the stoichiometric limit. Before that, it is increased with increasing of the equivalence ratio for the entire range of engine speed. The same trends are observed in an earlier investigation (Yamin, 2007). This is due to the increment of time per power cycle at low engine speed and uncompleted combustion for the fuel-air mixture beyond

the stoichiometric limit (Heywood, 1988). For high engine speed (> 4000 rpm), the PRHT is constant for all the equivalence ratio range. The PRHT is strongly depended on the equivalence ratio at low engine speed. The maximum PRHT is obtained at the stoichiometric condition for all SOI as well as engine speed. The effect of the SOI on the PRHT is minor. However, for $SOI = 70$ deg BTDC some deviation is revealed at the rich and stoichiometric mixture condition due to the reduction of the time period for fuel injection at high engine speed (> 4000 rpm). It can be clearly seen a well consistence between the PRHT trends and heat transfer rate behavior during all injection timing.

Dimensionless Parameters

The dimensionless approach is employed to characterize the heat transfer of DIH_2ICE based on the one-dimensional gas dynamic model. The trends of the dimensionless parameters namely Nusselt number (Nu) and Reynold's number (Re) are considered for DIH_2ICE . Nusselt number is a dimensionless quantity represents the ratio of the convection to conduction resistance for heat transfer. Reynold's number is a dimensionless quantity represents the ratio of the inertia force to viscous force (Borman and Nishiwaki, 1987). Analysis is presented with respect to the engine speed, equivalence ratio and SOI .

Figure 4.16 illustrates the variation of Nu against the engine speed and equivalence ratio for different SOI . The Nu increases with an increase of the engine speed as well as the equivalence ratio for all SOI . This trend can be explained according to the physical definition of Nusselt number. Resistance of convection heat transfer is directly proportion to the heat-transfer coefficients. Heat transfer coefficient is intensified as the engine speed increased due to increase of the in-cylinder gas velocities (Chiodi and Bargende, 2001). Therefore, the convective resistance increases with an increase of the engine speed. Furthermore, the conductive resistance is also increased with an increase of the engine speed. However, the rate of increment of the convective resistance is greater than the conductive resistance. Besides that, the heat transfer is enhanced as the equivalence ratio increased due to the energy content increases as the mixture becomes richer. Therefore, the combustion heat release is become higher. Consequently, the Nu is enhanced significantly with an increase of the engine speed and

equivalence ratio. Moreover, it can be seen that the retarding of *SOI* to 70 deg BTDC is cased a reduction in the maximum Nu ($> 10\%$) for rich and stoichiometric mixture strength. This is because of decreasing the time between the end of injection and start of combustion. Therefore, the heat transfer rate per power cycle decreases.

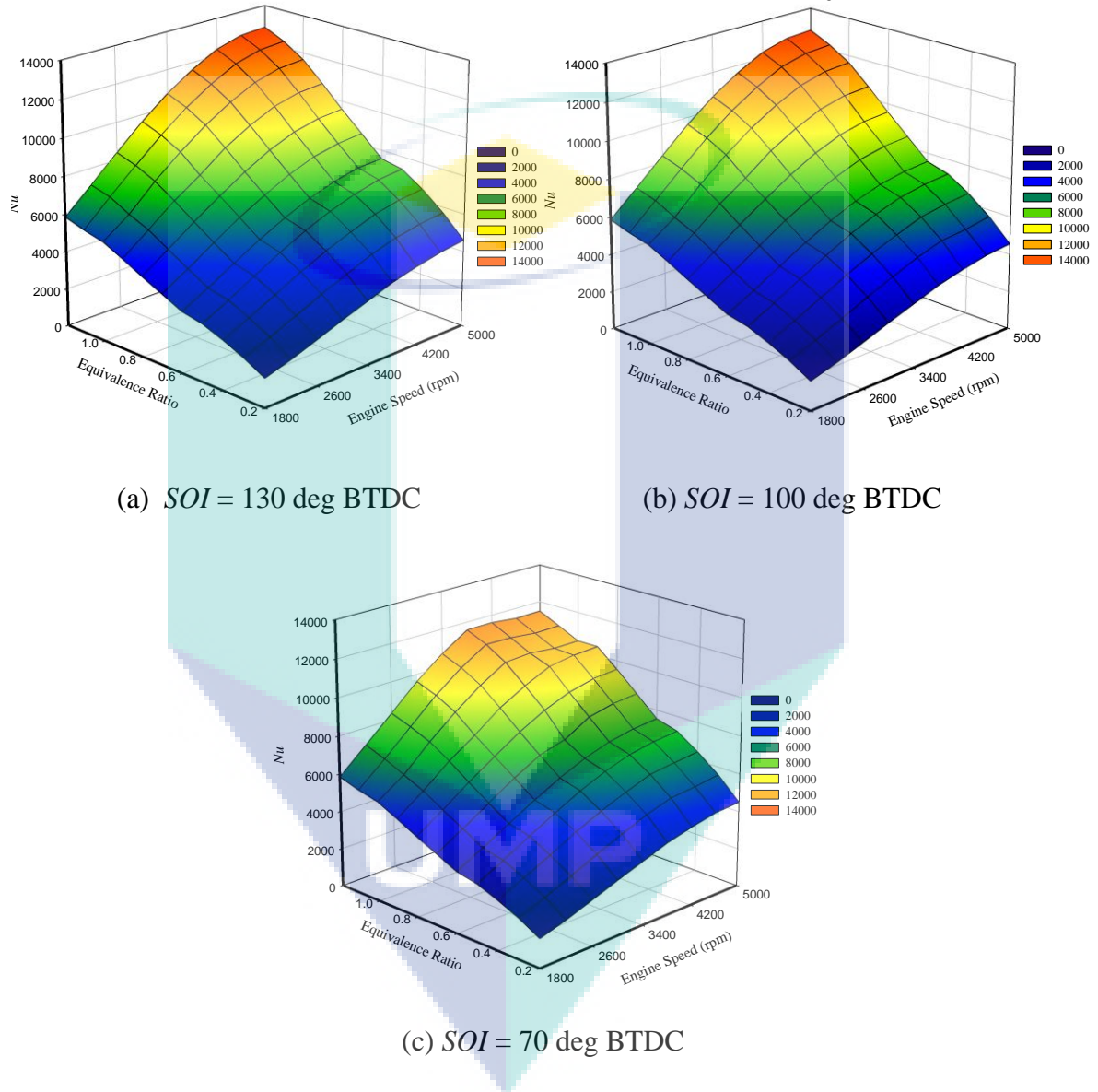


Figure 4.16: Variation of Nusselt number against the engine speed and equivalence ratio for different *SOI*.

Figure 4.17 demonstrates the variation of Reynold's number against the engine speed and equivalence ratio for different *SOI*. The Re increases with an increase of the engine speed for the entire ranges of the equivalence ratio and *SOI*. This is because of boosting of the forced convection as an increase of engine speed.

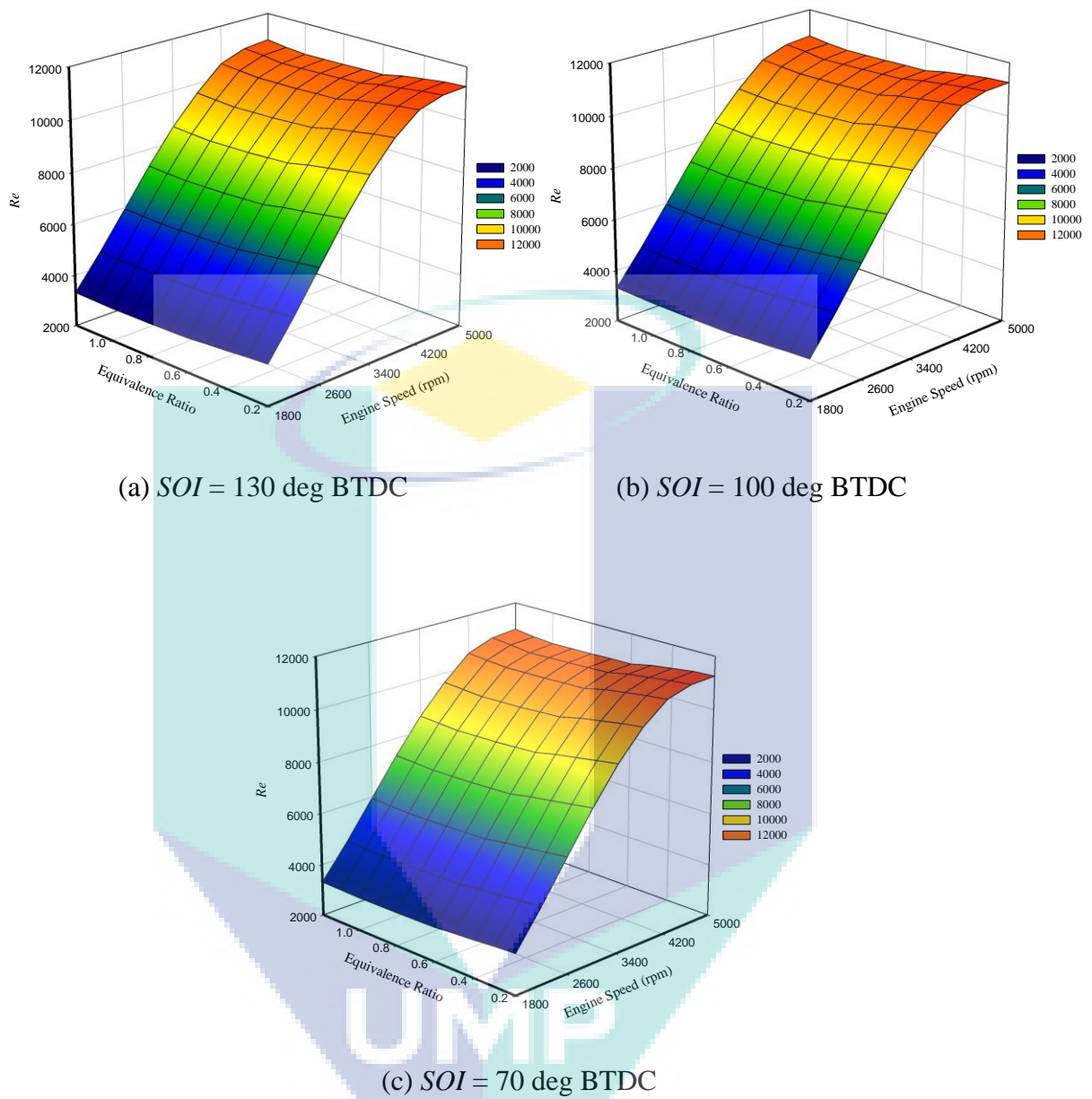


Figure 4.17: Variation of Reynolds number against the engine speed and equivalence ratio for different SOI .

However, the variation of Re with the equivalence ratio is insignificant. This trend can be explained according to the physical definition of Reynold's number. Mass flow rate and the dynamic viscosity are the governing variables of Re . For direct injection, the fuel is injected during all valves are closed. Therefore, the equivalence ratio is not affected the mass flow rate. Besides that, the mixture strength has a weak influence on dynamic viscosity in case of hydrogen fuel (Nefischer et al., 2009). Therefore, the equivalence ratio is not affected the trend of Re . Finally, the effect of SOI

on Re is negligible for the entire range of the engine speed and ϕ . It can be seen that the trend of Re is identical with all SOI .

4.3.3 Correlations between Dimensionless Parameters

Evaluation of the existing heat transfer correlations represents a prerequisite step for improving and developing an enhanced correlation for any application. The dominant mode for heat transfer from the in-cylinder gases to walls in ICEs applications is the convection (Borman and Nishiwaki, 1987 and Schubert et al., 2005). The convection mechanism is usually used to describe heat transfer from burning gas to a combustion chamber of SI engines (Torregrosa et al., 2008). Most of the previous studies were performed based on the dimensionless analysis theory (Taylor and Toong, 1957; Bargende, 1991 and Bohac et al., 1996). A dimensionless analysis is mainly carried out to correlate of the Nu and Re . An overview of the art state shows abundance of correlations for estimation of heat transfer in ICE. Classifying of these correlations can be made based on the type of averaging method, which is used for estimation the heat transfer coefficient (Heywood, 1988). This section is focused on the analysis TAHT for DIH₂ICE. These correlations were used for the estimation of the overall cycle of heat transfer rate to the wall. However, it was empirically developed from observations of engines fueled with gasoline or diesel fuel (Stone, 1999). Taylor (1985) was suggested one of the most familiar models for TAHT in ICEs. It was correlated both Nu and Re number, which is expressed as Eq. (4.1):

$$Nu = 10.4 \times Re^{0.75} \quad (4.1)$$

Comparison between the predicted (simulation) and Taylor's correlation results is considered as shown in Figure 4.18. It can be seen that this correlation is not valid to use for H₂ICE. Weakness of Taylor's correlation is very clear, especially for lean and ultra-lean mixture conditions. Taylor's correlation is over estimated of the prediction results. Even for the remaining equivalence ratio rang, it has a considerable deviation. However, in practical applications, it is very difficult to operate a H₂ICE at these conditions ($1.0 \leq \phi \leq 1.2$) due to the abnormal combustion phenomena (Tang et al., 2002; Heffel, 2003 and Liu et al., 2008). The wide range of flammability for hydrogen

fuel ($0.1 < \varphi < 7.1$) considers one of the most promising characteristics in operating of SI engine (Berckmüller et. al, 2003 and White, 2006). Taylor's correlation dependency on the mixture strength was not included during the formulation. Therefore, it is unsuitable to use Taylor's correlation under the lean as well as the ultra-lean conditions for H_2ICE .

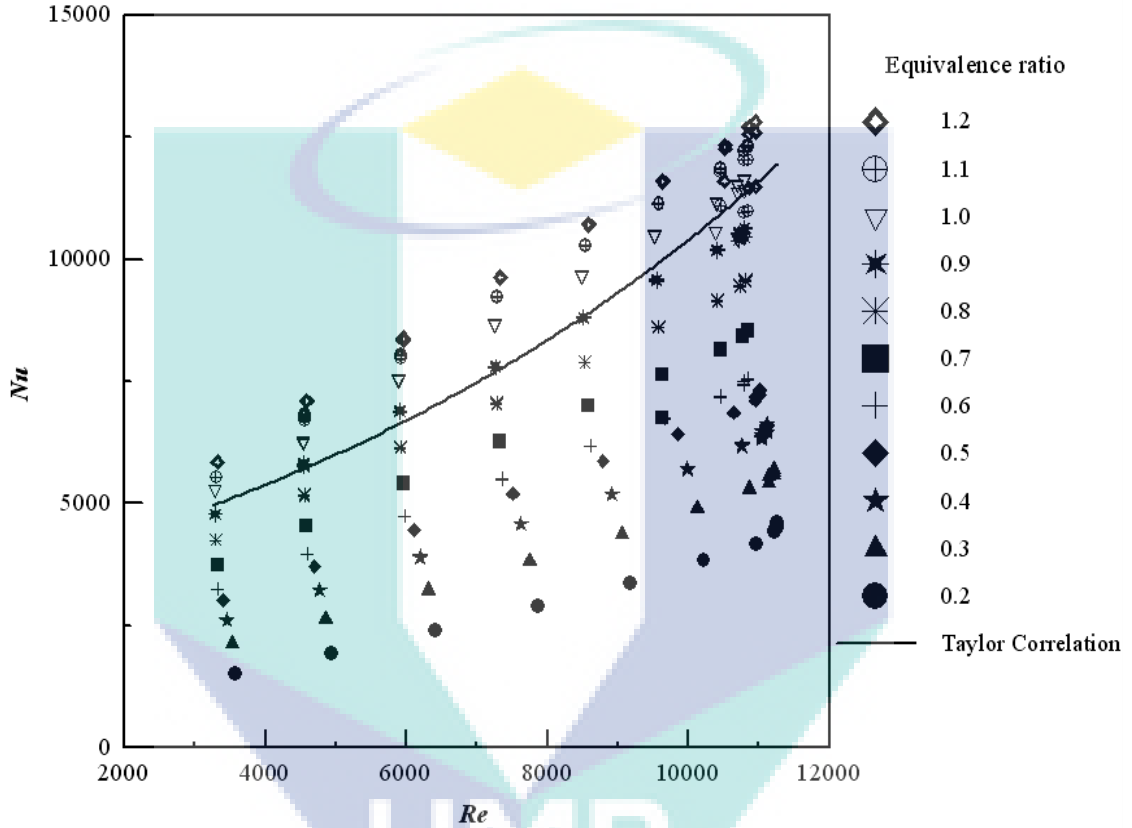


Figure 4.18: Comparison of the predicted (simulation) with Taylor's correlation results.

Figure 4.19 shows the relative errors of the predicted results based on Taylor's correlation in case of H_2ICE . The relative error decreases with an increase of the equivalence ratio. The maximum relative error is obtained (around 70 %) under the ultra-lean mixture strength ($\varphi = 0.2$) at low Reynolds number ($Re = 3580$). The relative error decreases from (70 %) to (20 %) as the equivalence ratio increases from the ultra-lean ($\varphi = 0.2$) to lean ($\varphi = 0.7$) mixture conditions. This is because of excluding the effect of the equivalence ratio in Taylor's correlation. The relative error in the remaining equivalence ratio range ($0.8 \leq \varphi \leq 1.2$) is confined within the range of ± 20 %. This is because the Taylor's correlation was formulated for the range near to

stoichiometric limit (the operating range of petrol and diesel engines ($0.8 \leq \varphi \leq 1.2$) (Taylor, 1985; Heywood, 1988). The relative error is tended to reduce with increasing of Reynolds number for all conditions of the mixture strength. However, the effect of Reynolds number on the relative error is insignificant compared to the equivalence ratio.

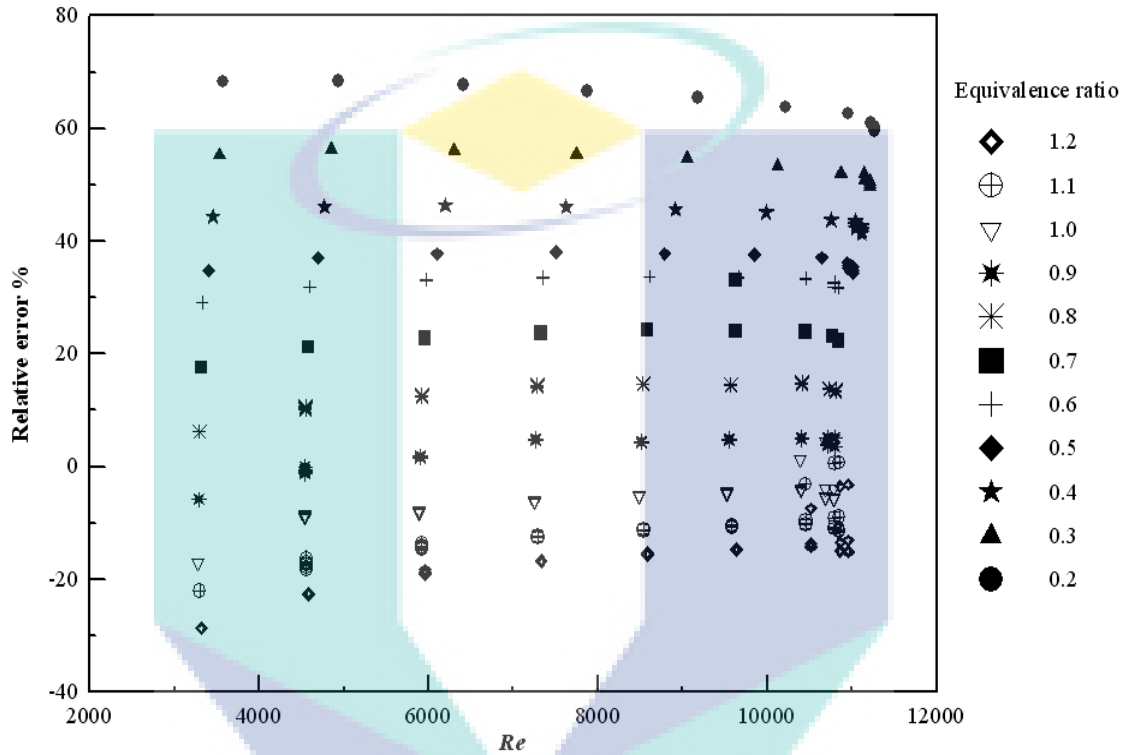


Figure 4.19: Relative error of the predicted results based on results of Taylor's correlation.

The most promising equivalence ratio range for operating the SI engine with hydrogen is ($0.3 \leq \varphi \leq 0.9$) (Eichlseder et. al, 2003; Berckmüller et. al, 2003 and Mohammadi et al., 2007). At this range, most of the optimization studies have been performed to achieve the highest efficiency as well as lowest NO_x emissions (Tang et. al, 2002 and Natkin et. al, 2003). Therefore, it is required to consider the effect of the equivalence ratio on the heat-transfer correlation in case of H₂ICE. Obviously, there was a substantial deviation between the existing model and predicted results, especially for the lean and ultra-lean mixture conditions because of excluding the influence of the equivalence ratio. Therefore, it is reasonable to take into account the equivalence ratio as a governing variable in the heat-transfer correlation. Up-to-date there is no

correlation developed considering the effect of the equivalence ratio to describe the heat transfer inside the combustion chamber (Wei et al., 2001; Schubert et al., 2005; Nefischer et al., 2009 and Demuynck et al., 2011) except Shudo and Suzuki (2002b) which it was for port-injection case. However, this correlation contains two calibration parameters are dependent on the ignition timing and equivalence ratio. These dependencies are stated to be the subject of further studies, so this correlation is still under development and not widely use, until now (Verhelst, 2005 and Demuynck et al., 2011).

The Newly Developed Correlations

Based on the above analysis, a new correlation will be proposed for TAHT. The new proposed heat transfer correlation depends on Reynold's number (Re) and the equivalence ratio (ϕ). The novelty of the new correlation is including of the equivalence ratio (ϕ) as a governing variable. Crucial influence for the equivalence ratio (ϕ) on the heat transfer is due to the wide flammability limit for hydrogen fuel ($0.1 < \phi < 7.1$) (Sierens and Verhelst, 2003 and Verhelst et al., 2006). The new correlation is expressed as Eq. (4.2):

$$Nu = C \times Re^m \times \phi^n \quad (4.2)$$

where C , m and n are correlation's constants.

The statistical analysis was performed using the capabilities of SPSS software to obtain the values of C , m and n . The statistical analysis is carried out based on the one-dimensional model results. These data are generated from execution of the model under the different operation parameters. The nonlinear regression approach is considered for the statistical analysis. Nonlinear regression is a technique of the relationship between the dependent variable and a set of independent variables. This technique evaluates the models with arbitrary relationships between the independent and dependent variables by iterative evaluation algorithms (Abraham and Ledolter, 2006). A Levenberg-Marquardt algorithm is considered for estimating the parameters of models (Marquardt, 1963). The convergence criterion is based on the relative reduction between successive residual

sums of squares. The statistical iterations were executed until this value is at most equal to 10^{-8} . Five values for each constant (C , m and n) are estimated by statistical processing for simulation results, as in Table 4.2. The proposed correlation formula can be evaluated statistically through measuring of the coefficient of determination (R^2 -value). The R^2 -value is a scale for the suitability of the regression model intended for fitting the test data (Abraham and Ledolter, 2006). The R^2 -value equal one implies perfect correlation as all the residuals (the difference between the estimated and the exact value at each test point) equal to zero. The proposed correlations have a very well performance, where the determination coefficient about 0.99.

Table 4.2: TAHT Correlations constants

<i>SOI</i>	<i>C</i>	<i>m</i>	<i>n</i>	<i>R</i> ²
70 deg BTDC	24.084	0.6570	0.6522	0.9844
85 deg BTDC	23.800	0.6613	0.6833	0.9846
100 deg BTDC	15.546	0.7088	0.6909	0.9906
115 deg BTDC	15.408	0.7098	0.6895	0.9902
130 deg BTDC	15.302	0.7107	0.6882	0.9901

The relationships between Nu , Re and ϕ are considered by fitting non-linear regression correlations to the simulated data. The F -test is used to identify the significance of the proposed correlations. This is equivalent to checking that no regression coefficients are zero. The checking statistic quantity is expressed as Eq. (4.3) (Field, 2009):

$$F = \frac{SS_M / k}{SS_R / (n - k - 1)} \quad (4.3)$$

where SS_M is the regression model sum of data squares

SS_R is the residual sum of data squares

k is the number of variables

n is the number of samples (data points)

For a given significance level p , its rejection region is $F \geq F_p(k, n-k-1)$ (Field, 2009). For a given significance level of $p = 5\%$, the significance of the correlation is

checked using the analysis of variance method. The results obtained for Eq. (4.3) are listed in Table 4.3. It can be seen that all the values of the F are greater than the $F_{p=0.05}(3, 96) = 2.70$ (Field, 2009), so the proposed regression correlations are significant, which means that the Re and ϕ significantly influence Nu . Therefore, all developed formulas proved significant due to the large F -values compared to $F_{p=0.05}$.

Table 4.3: Squares differences analysis

<i>SOI</i>	Technique	DF	Sum of squares	Mean of squares	<i>F</i>-test
70 deg BTDC	Regression	3	5142691094.36	1714230364.79	15083.6
	Residual	96	10910284.6419	113648.79835	
85 deg BTDC	Regression	3	5316190339.59	1772063446.53	4093.5
	Residual	96	41558243.4112	432898.36887	
100 deg BTDC	Regression	3	5403328225.06	1801109408.35	23175.8
	Residual	96	7460643.93998	77715.04104	
115 deg BTDC	Regression	3	5416177862.79	1805392620.93	22290.66
	Residual	96	7775350.21357	80993.23139	
130 deg BTDC	Regression	3	5426000896.71	1808666965.57	21908.72
	Residual	96	7925246.28806	82554.64883	

It can be seen that, the constant (C) in Table 4.2 has convergent values within two intervals; $100 \leq SOI \leq 130$ and $70 \leq SOI \leq 85$. It is impossible to merge all of correlations in one formula due to a large variation in constants' values between the two intervals. Besides that, one of the important goals for the new correlation is proposed to minimize the relative error as much as possible. The mathematical models based on the non-linear regression analysis are developed as Eq. (4.2) with different coefficients for each interval as listed in Table 4.4.

Table 4.4: Constants of the newly developed TAHT correlations

<i>No. of interval</i>	<i>SOI</i> (deg BTDC)	<i>C</i>	<i>m</i>	<i>n</i>	<i>R</i>²
1	$70 \leq SOI \leq 85$	24.084	0.6570	0.6522	0.985
2	$100 \leq SOI \leq 130$	15.302	0.7107	0.6882	0.9901

The newly developed models are validated using the simulation results. The comparison between the simulation results and Model 1 is presented in Figure 4.20. The dimensionless parameter $[f_1(Nu, \phi)]$ is expressed as Eq. (4.4):

$$f1(Nu, \varphi) = \left[\frac{Nu}{C_1 \times \varphi^{n_1}} \right]^{\left(\frac{1}{m_1} \right)} \quad (4.4)$$

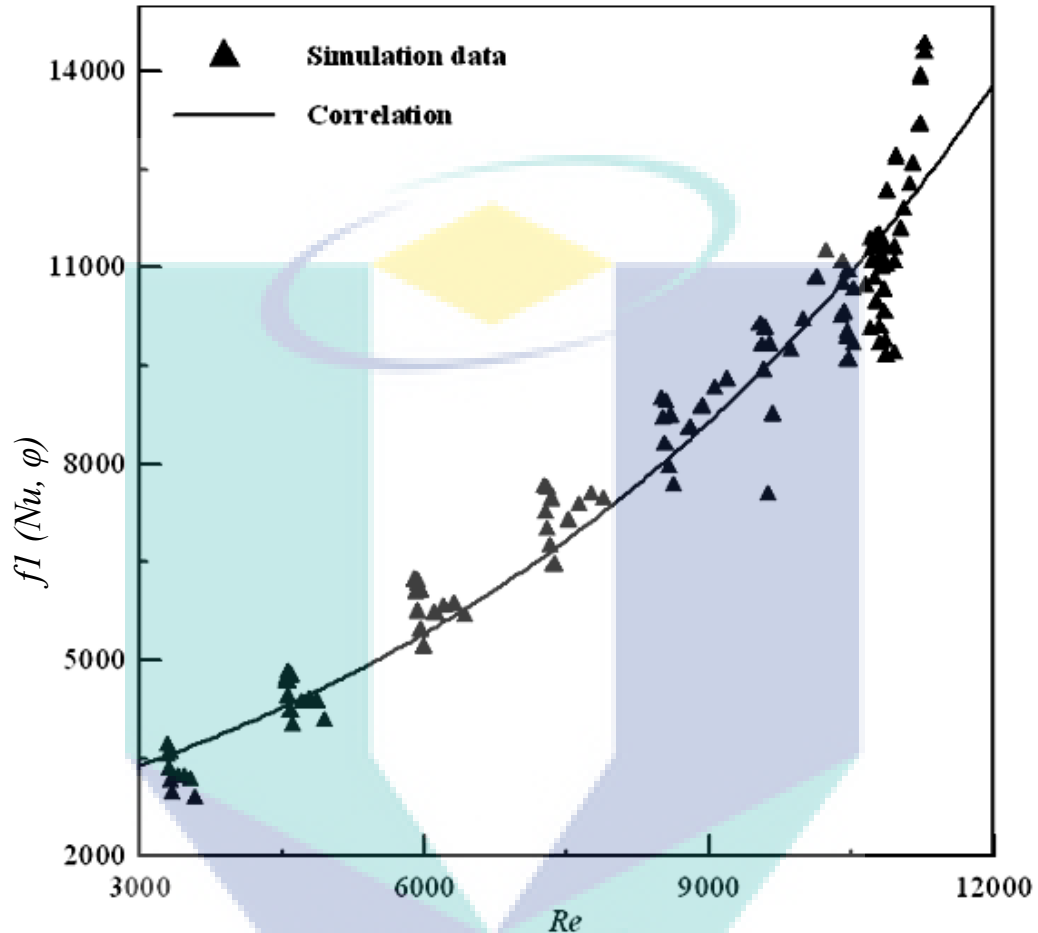


Figure 4.20: Comparison of simulation results and proposed correlation for $70 \text{ deg BTDC} \leq SOI \leq 85 \text{ deg BTDC}$.

It can observe the non-linear trends for the predicted (simulation) results as well as the Model 1. The new proposed correlation shows a well coincident trend with predicted (simulation) results for Model 1 when take into account the wide range of the equivalence ratio ($0.2 \leq \varphi \leq 1.2$). However, the predicted (simulation) results are deviated from the Model 1 with average error around 10 %. The deviation is increased as an increase of the Reynolds number (Re). Consequently, the deviations of some points are exceeded of 10 %.

The comparison between the simulation results and Model 2 is presented in Figure 4.21. The dimensionless parameter $[f^2(Nu, \varphi)]$ is expressed as Eq. (4.5):

$$f^2(Nu, \varphi) = \left[\frac{Nu}{C_2 \times \varphi^{n_2}} \right]^{\left(\frac{1}{m_2}\right)} \quad (4.5)$$

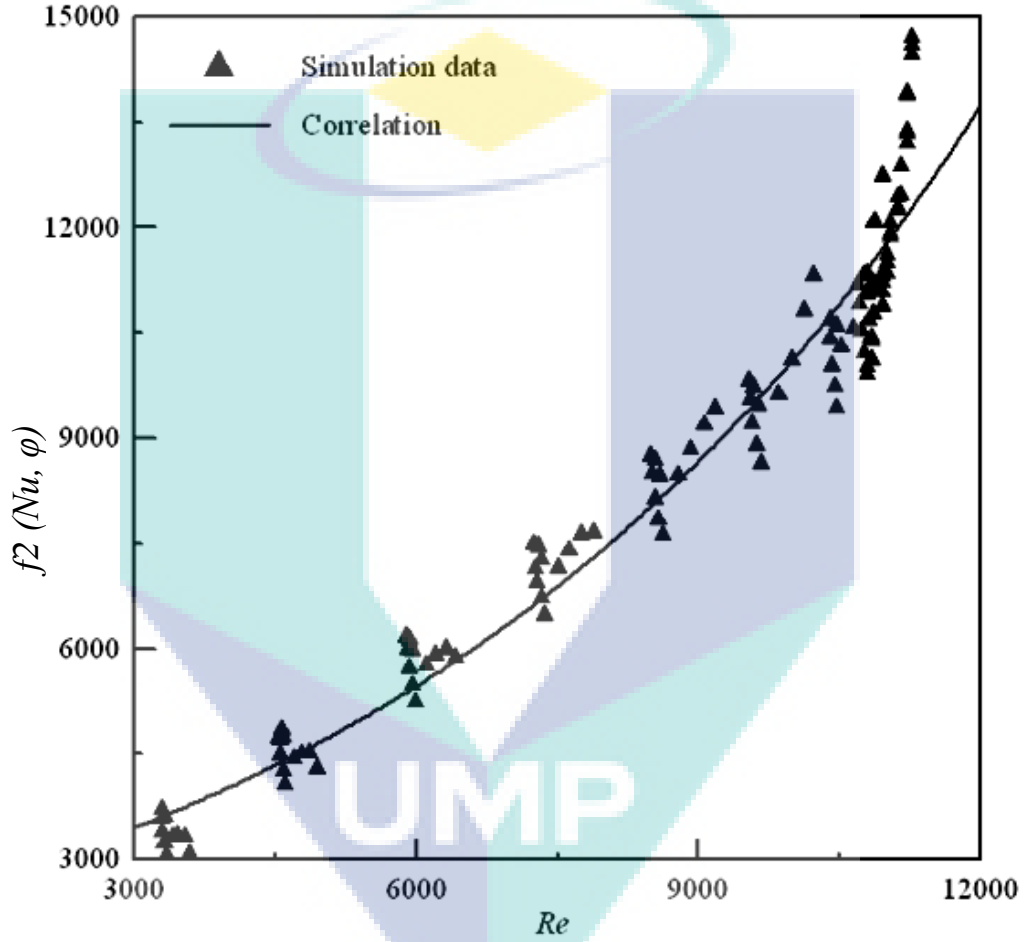


Figure 4.21: Comparison of simulation results and proposed correlation for $100 \text{ deg BTDC} \leq \text{SOI} \leq 130 \text{ deg BTDC}$.

It can notice the non-linear trends for the predicted (simulation) results as well as the Model 2. The new proposed correlation shows a well coincident trend with predicted (simulation) results for Model 2, when take into account the wide range of the equivalence ratio ($0.2 \leq \varphi \leq 1.2$). However, the predicted (simulation) results are deviated from the Model 2 with average error around 10 %. The deviation is increased as an increase of the Reynolds number (Re). Moreover, Model 2 is appeared to be more

accurate in comparison with Model 1 when take into account the number of points, which are exceeded of 10 %. This is due to the different behavior between two intervals of *SOI* (see Figures 4.14, 4.15 and 4.16). The trustworthiness of the new proposed correlations for representing the simulation results is revealed.

Minimizing the relative error as much as possible is one of the important aspects for new correlations. Figure 4.22 shows the relative error of predicted (simulation) results based on newly developed correlations (Model 1 and Model 2). A better verification for the predicted (simulation) results is confirmed for the proposed new correlations compared to performance of Taylor's correlation. More than 95 % of the predicted (simulation) results are within the margin of the relative error of 10 % for new correlations while less than 15 % for Taylor's correlation (see Figure 4.19).

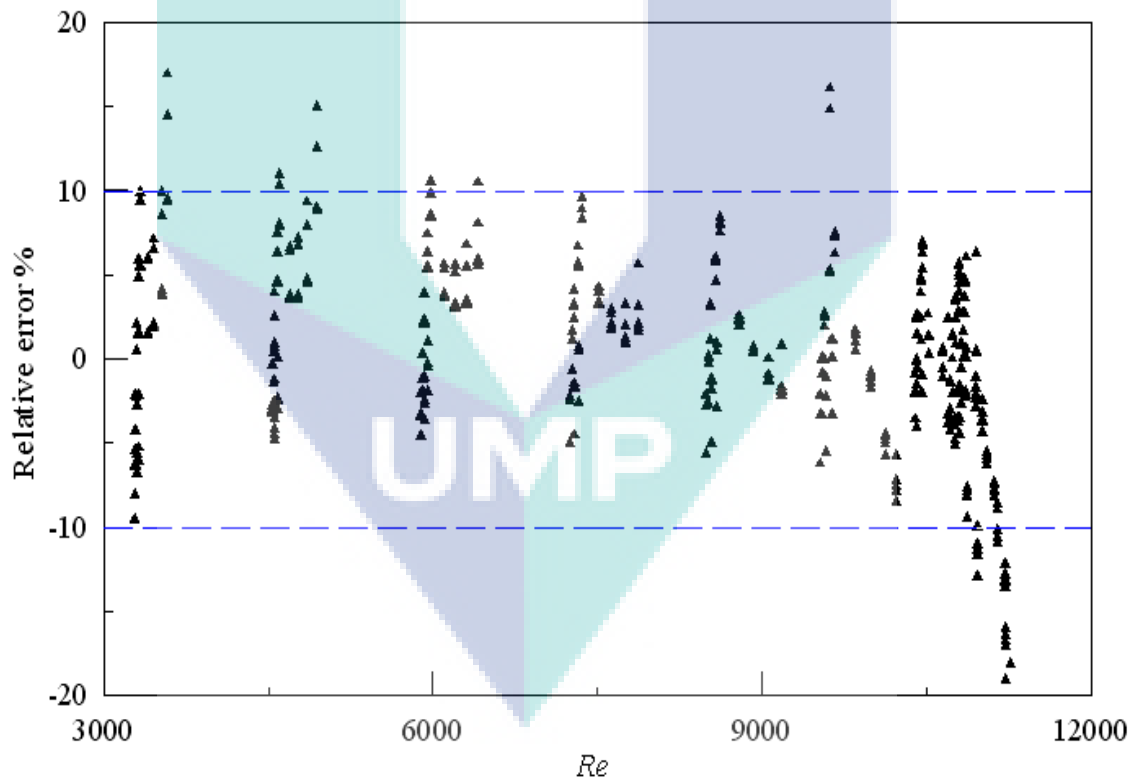


Figure 4.22: Relative error of predicted (simulation) results based on newly developed correlations (Model 1 and Model 2).

Both of newly developed correlations (Model 1 and Model 2) are shown the good consistency with the predicted results. Furthermore, the evaluation of these models

is revealed a significant reduction of the relative error ($> 50\%$) in comparison with Taylor's model. However, it can be performed the further experimental investigation to verify the developed models as well as to improve the relative error reduction.

4.3 MULTIDIMENSIONAL MODEL

The multidimensional model is developed based on the finite volume approach. It is employed to perform an investigation for the instantaneous heat transfer (IHT) in DIH₂ICE. The developed model is validated against the experimental results. The grid sensitivity analysis is carried out for multidimensional model based on the motoring condition. Multidimensional model is validated in terms of the in-cylinder pressure traces. It is performed for various engine speed and equivalence ratio at $SOI = 130^\circ$ BTDC, $IT = TDC$ under a full load condition. The developed model was used to carry out the parametric analysis for the IHT. The parametric analysis was performed in terms of the flow field, thermal field, trends of heat release rate, trends of heat loss and trends of the heat-transfer coefficients. It is considered the effect of engine speed, equivalence and SOI . Following sections present the results of the multidimensional model.

4.3.1 Model Validation

The collected database from the experimental test rig was used to validate the baseline engine model. The baseline engine model was performed for a test rig of a single-cylinder PROTON CAMPRO engine. The grid sensitivity analysis was carried out for multidimensional model based on the motoring condition at engine speed 2000 rpm. The developed model was validated experimentally based on the in-cylinder pressure traces. It was performed for three operation parameters namely the engine speed, equivalence ratio and SOI . Following sub-sections present the details of model's validation.

Grid Sensitivity Analysis

The grid sensitivity is analysed to eliminate the effect of grid dependency on the model's prediction. This is performed through reducing the grid element size. The

single-cylinder baseline engine was operated by the David McClure dynamometer at motoring condition for 2000 rpm. The numbers of cells are defined as coarse to fine mesh from 33291 to 52897 cells. The result's sensitivity on the spatial resolution is assessed through individually varying the resolution in the cylinder region. The intake and exhaust regions are excluded for the grid sensitivity analysis because of these two regions are not existed during the combustion phase. Figure 4.23 illustrates the computational domain with the hexahedron elements for multidimensional engine model at the TDC position. The developed model is executed using an adaptive time stepping scheme. The time step for the successive cycle is computed considering the solution of the previous cycle in view of various accuracy related constraints. The maximum time step is selected to be equal 10^{-5} seconds. The time interval is converted to be equivalent to a unit of crank angle degree. According to the accuracy constraint, the time step is reduced automatically as the mesh is refined.

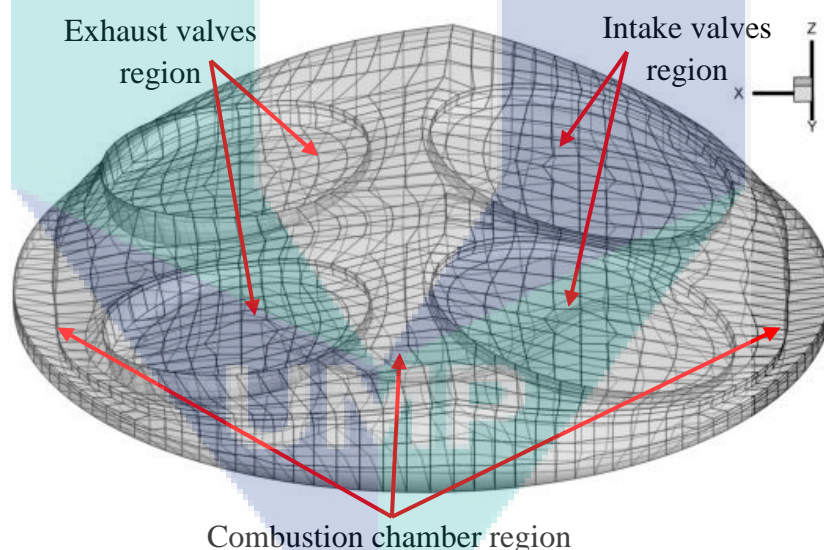


Figure 4.23: Computational domain with hexahedral element for multidimensional engine model at TDC position.

Figure 4.24 presents the results of grid sensitivity analysis. The in-cylinder pressure traces for experimental and model prediction results at 2000 rpm under motoring conditions are considered to investigate the sensitivity of mesh size. A significant sensitivity is observed in predictions of peak pressure with a minor difference in the corresponding crank angle. The prediction of in-cylinder pressure traces is approached from the experimental results as the grid size reduced. The last fine

grid distribution (52,897 cells) is the closest to the experimental results. Further refinement in the spatial domain leads to increase computational times with a negligible benefit regarding the results' accuracy. It reveals that the fine-mesh size is the best compromise between the time and accuracy. Hence, the fine-mesh distribution (52,897 cells) is selected for the present study. The requirements for spatial resolution are justified by using the fine-mesh distribution, as well as the temporal resolution is conceded with the accuracy criterion.

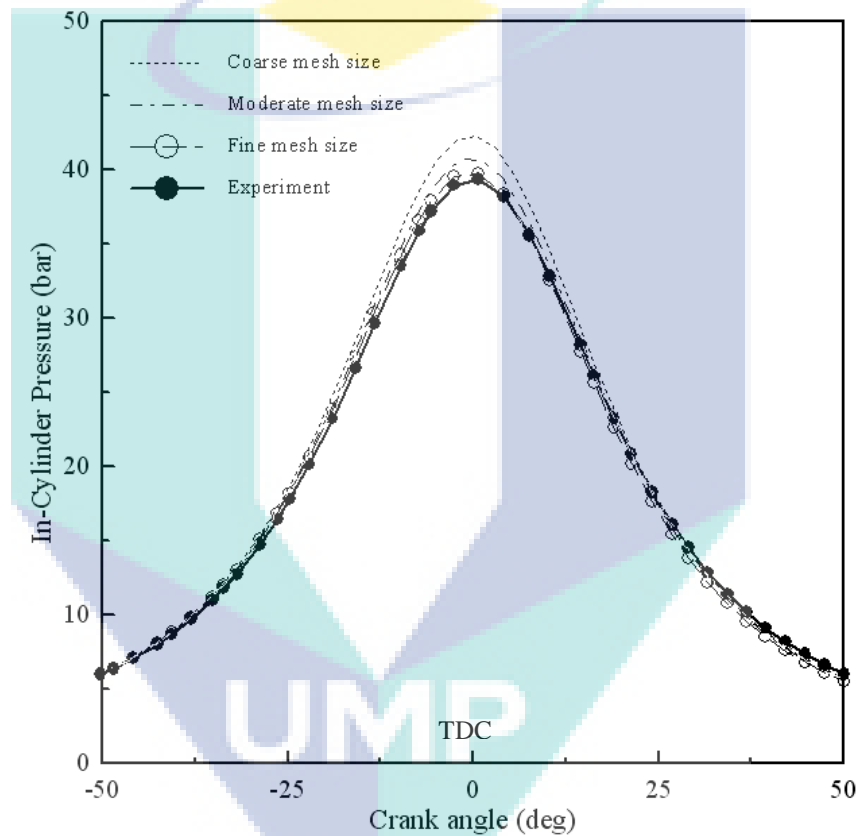


Figure 4.24: Effect of mesh size on the comparison between simulated and experimental in-cylinder pressure under the motoring condition with (2000 rpm).

Experimental Validation Tests

The developed model was validated experimentally in terms of the in-cylinder pressure traces. It is performed for various engine speed and equivalence ratio at $SOI = 130$ deg BTDC under the WOT and full-load condition. This injection timing is chosen

to simulate the direct-injection case. Further retarding for *SOI* is unachievable experimentally due to the abnormal combustion. Table 4.5 lists the different experimental conditions are used for the model validations. These conditions are included of both low and high engine speed as well as the ultra-lean and lean mixture strength. The engine was tested to yield sufficient torque (misfire limit) and avoid knocking noise.

Table 4.5: The experimental operating points of the cases utilized for validating of the multidimensional model.

Case	Engine Speed	ϕ	<i>SOI</i>	Load Condition
Case 1	1800 rpm	0.65	130 deg BTDC	Full Load
Case 2	1800 rpm	0.97	130 deg BTDC	Full Load
Case 3	3000 rpm	0.78	130 deg BTDC	Full Load
Case 4	3000 rpm	0.41	130 deg BTDC	Full Load

Figure 4.25 illustrates the comparisons between the experimental and predicted (simulation) results of the in-cylinder pressure for different engine speed and various mixture strength under WOT and full-load conditions. It can be elucidated that there are good agreements between the predicted (simulation) and experimental results for all tested conditions. However, there are some deviations in terms of the in-cylinder pressure (about 5 %) and the locations of peak pressure (around 10 %). The deviation of the in-cylinder pressure traces is appeared during the end of the compression stroke and combustion stroke. The predicted results are slightly over-estimated during the end of the compression stroke. This is due to the uncertainty of the compression ratio (Knop et al., 2008). Although the compression ratio, for computational as well as experimental, are considered constant, while the real compression ratio for the experiment appears to fluctuate. Therefore, it is caused some uncertainty in the predicted results during this interval. It can notice that an increase in the discrepancy between the predicted and experimental results with initiation of the combustion until the expansion stroke. It can be seen that the predicted results show a too slow combustion at the beginning and a rapid combustion near the peak in-cylinder pressure. Consequently, the initiation timing of the predicted results is retarded than the experimental. This is because of a simplified single-step oxidation was used that converts hydrogen and oxygen to water in multidimensional modelling.

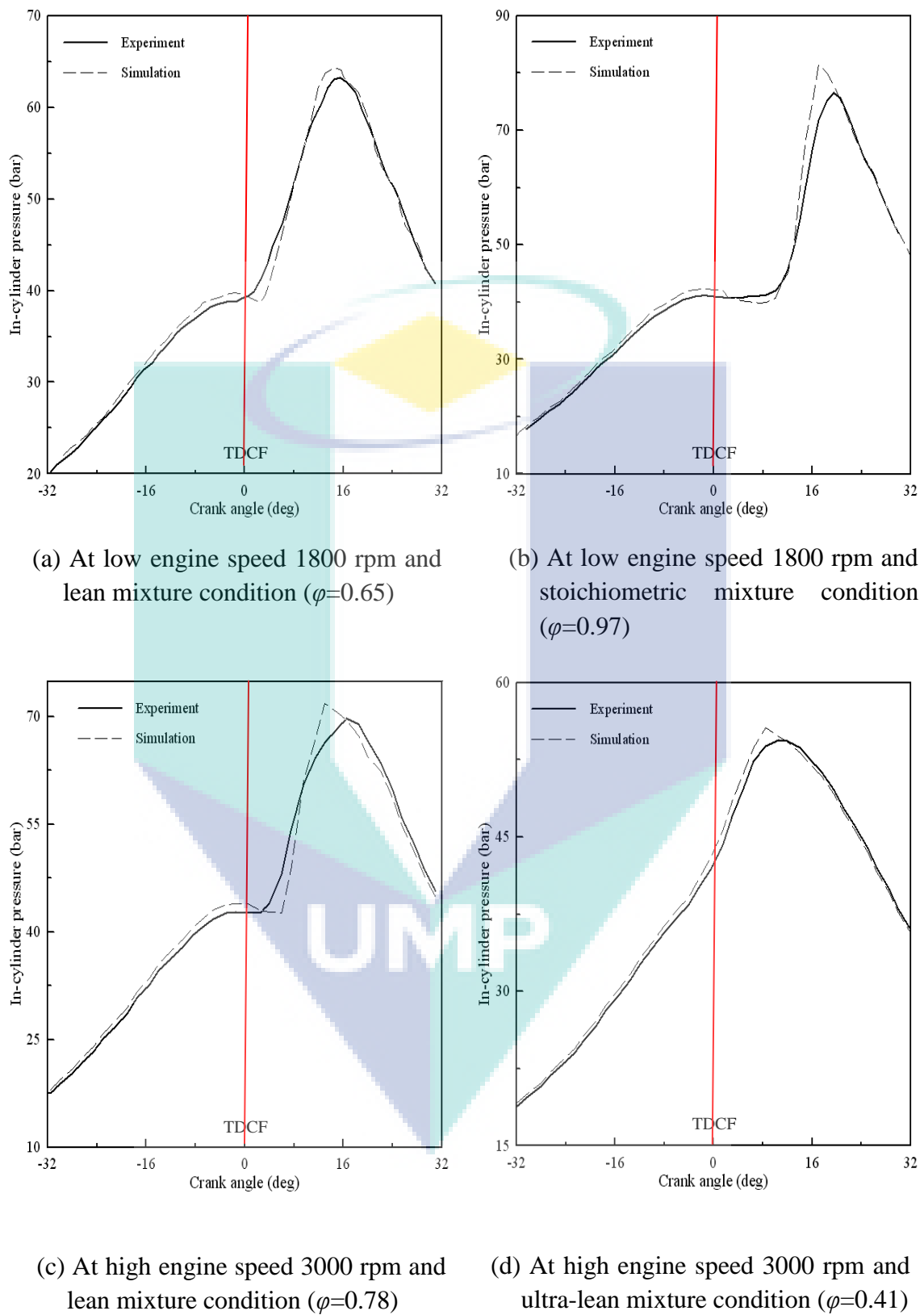


Figure 4.25: Comparison between the experiment and predicted (simulation) results of the in-cylinder pressure traces for different engine speed and mixture strength under WOT and full-load conditions.

Furthermore, the results discrepancy is increased with an increase of the equivalence ratio due to retarding of SI timing to avoid the abnormal combustion. The deviations of the above presented results are due to the following reasons:

- i. The developed model is considered the kinetic reaction sub-model, which is depending on the fuel characteristics. It needs to provide the forward pre-exponential factor (k_{fr}), and the integral stoichiometric coefficients (a_{mr} and b_{mr}) which are fuel characteristics. These characteristics are usually evaluated empirically to be appropriate for any application. An excessive rate of heat release is produced when chosen too high values for these characteristics. However, the combustion is not sustained due to insufficient heat release when considered low values (Amsden, 1993). The values of these characteristics are considered in the present study according to previous reported works (Marinov et al., 1995 and Kumar et al., 2011). These values were revealed a degree of uncertainty in prediction of the laminar flame speed. Therefore, it tends to be one of the sources for the discrepancy.
- ii. The experimental pressure traces are taken as ensemble-averaged over 100 consecutive cycles while the developed model is estimated the result only in one cycle.

It can conclude that the agreement between experiment and computation is reasonable whatever the level of mixture strength and engine speed. Therefore, it is suitable to consider the developed model for further investigation of the combustion process.

4.3.2 Parametric Analysis

Multidimensional analysis of IHT for the in-cylinder of four strokes SI DIH₂ICE model is performed for the three operational parameters namely the engine speed, equivalence ratio (ϕ) and injection timing (*SOI*). The engine speed is varied from 2000 to 5000 rpm with change step equals to 1000 rpm. Equivalence ratio is varied within the

range $0.3 \leq \phi \leq 0.9$ with change step equals to 0.2. The injection timing is selected within the range $70 \text{ deg BTDC} \leq SOI \leq 130 \text{ deg BTDC}$ with change step equals to 30 deg. The parametric analysis was performed in terms of the flow field, thermal field, trends of heat release rate, trends of heat loss and trends of the heat-transfer coefficients. Following sub-section presents the details of the parametric analysis.

Flow Field

The in-cylinder flow field for DIH₂ICE is presented to clarify the fuel-injection process in a gaseous state, and its interaction based on the modified KIVA code. Pattern of the flow field combined with the history of hydrogen concentration inside the combustion chamber during the injection phase is used to capture of hydrogen injection. Figure 4.26 presents the flow field with hydrogen concentration of the injection process for different engine speed 3000 and 5000 rpm, $\phi = 0.7$ and $SOI = 100 \text{ deg BTDC}$ at 80 deg BTDC. The proper instants are selected to reveal the hydrogen injection based on the boundary conditions of the injection region ($SOI = 100 \text{ deg BTDC}$ and injection duration of 50 deg). Therefore, it is selected during the opening period of the gas injector. The identical distribution for the hydrogen concentration is observed because of the hydrogen fuel in the gaseous state has a very low density and remarkably high diffusivity (Verhelst and Sierens, 2001a and Shudo, 2005). Besides that, the hydrogen fuel is injected within the combustion chamber during the closing period of the valves. There is no flow coming into the combustion chamber during this period. Accordingly, the mixing process between fuel and fresh air within the combustion chamber is mainly depended on the physical properties of the fuel. Furthermore, it can be noticed that the velocity vectors are greater size as well as coarser distribution near to the piston surface at higher engine. This is because of increasing the turbulence level as an increase of the engine speed (Heywood, 1988 and Ferguson and Kirkpatrick, 2001).

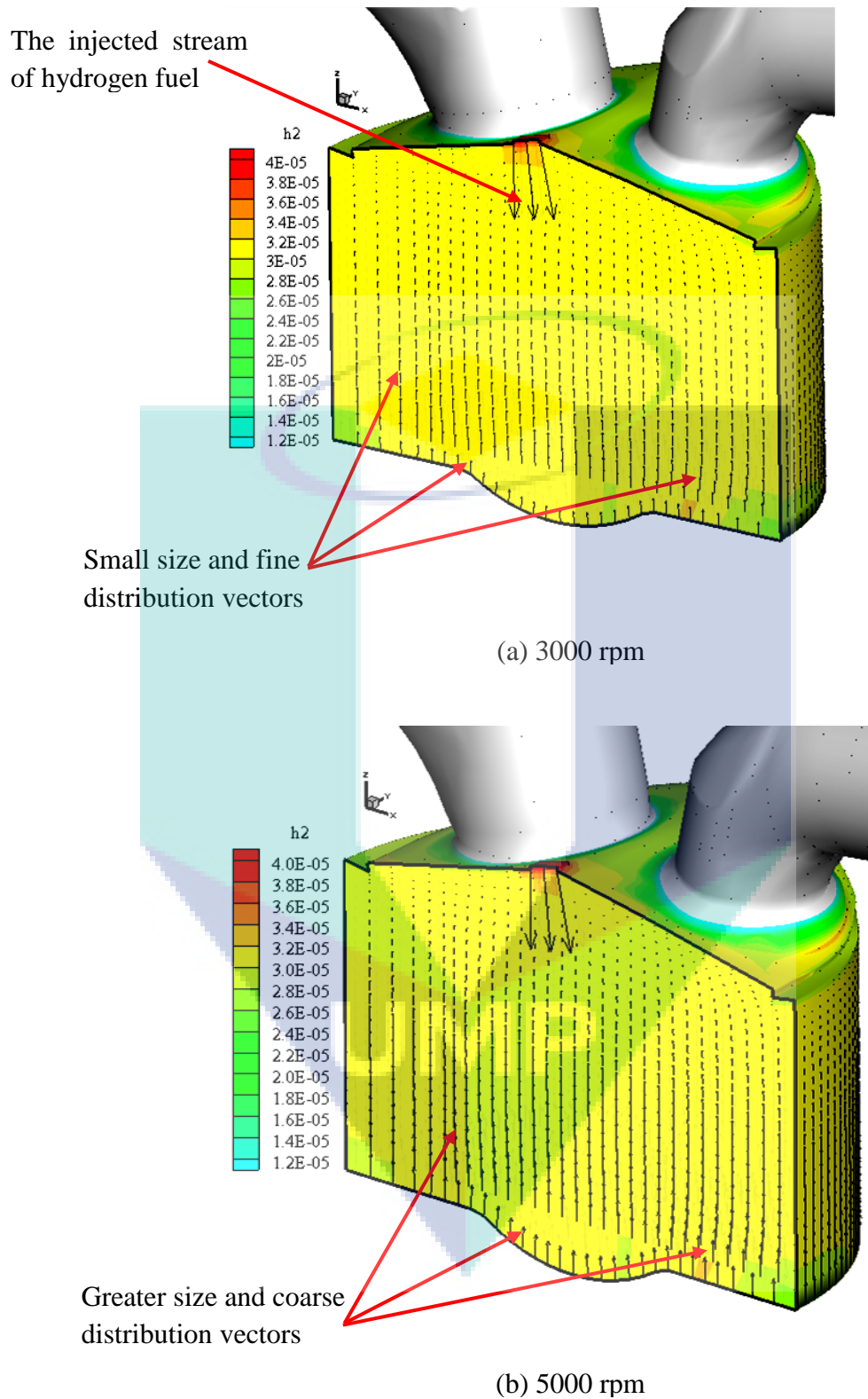


Figure 4.26: The flow field with hydrogen concentration of the injection process for different engine speed, $\phi = 0.7$ and $SOI = 100$ deg BTDC at 80 deg BTDC. (Isometric view)

Figure 4.27 presents the flow field with hydrogen concentration of the injection process for different instants, 3000 rpm, $\phi = 0.5$ and $SOI = 100$ deg BTDC. Two instants (70 and 80 deg BTDC) are considered to illustrate the progress of the fuel-injection process with piston movement. It can be seen that an adverse behavior is taken place as the crank angle advanced where the gradient of concentration for the hydrogen fuel increases progressively. The maximum hydrogen concentration is increased from (3.2×10^{-5}) to (3.8×10^{-5}) as the crank angle advanced from 80 to 70 deg BTDC respectively, while the minimum concentration is remained constant (1.0×10^{-5}). That means the heterogeneous in hydrogen distribution is increased within the computational domain. This is because of increasing the injected amount of hydrogen fuel as the piston level gradually increases. Even the total amount of hydrogen fuel is increased within the combustion chamber, but it is still not enough to acquire a homogenous distribution.

Figure 4.28 presents the flow field with hydrogen concentration of the injection process for the different equivalence ratio $\phi = 0.5$ and 0.7 , 3000 rpm and $SOI = 100$ deg BTDC at 80 deg BTDC. The maximum hydrogen concentration (4×10^{-4}) is obtained at higher mixture strength ($\phi = 0.7$). It can be seen that the mixture is become more homogeneous as an increase of mixture strength due to increasing the amount of hydrogen. Therefore, it is increased the total injected amount of hydrogen inside the combustion chamber per unit time.

Thermal Field

Thermal field represents a local distribution of the temperature within the computational domain. Figure 4.29 presents the description of the temperature contour at TDC position, which is the ignition timing point. It reveals the essential elements from the combustion chamber, including the spark plug position, intake ports, exhaust ports and fuel injection regions.

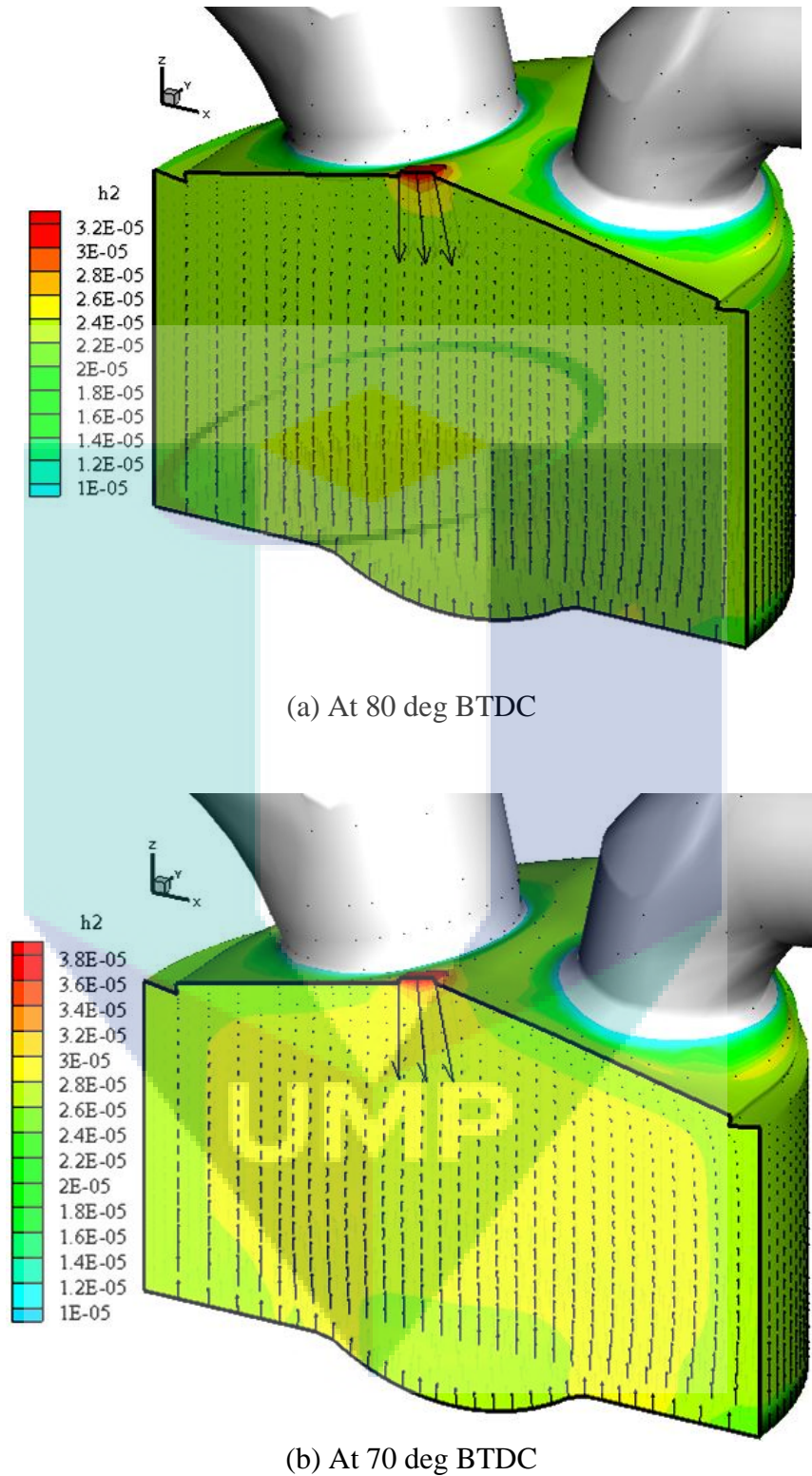


Figure 4.27: The flow field with hydrogen concentration of the injection process for different instants, 3000 rpm, $\phi = 0.5$ and $SOI = 100$ deg BTDC. (Isometric view)

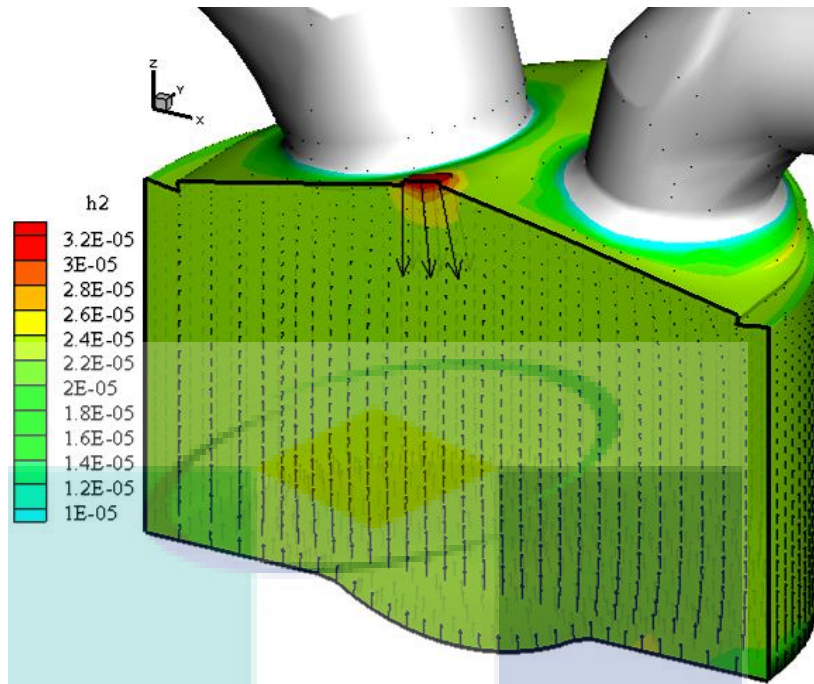
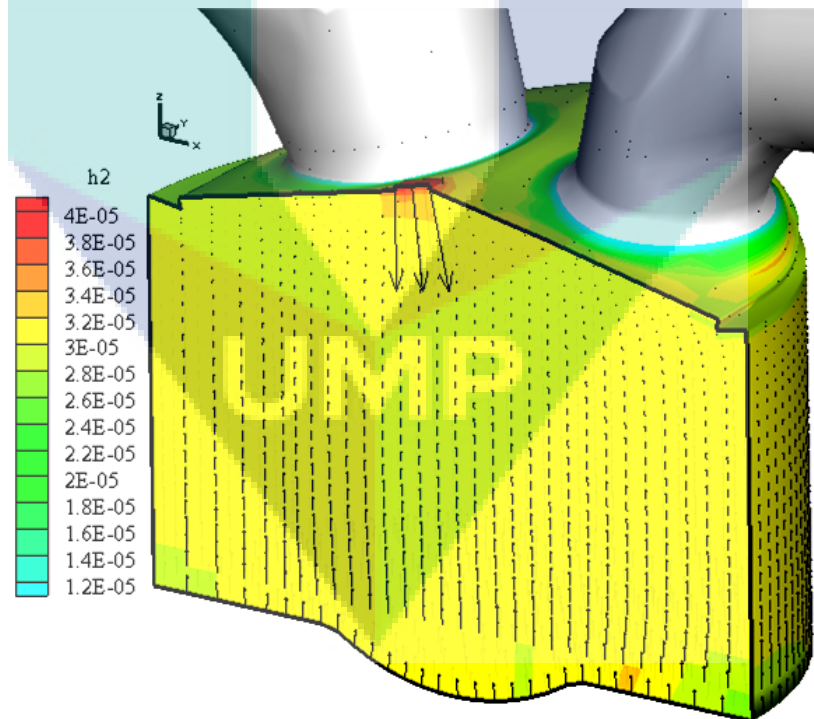
(a) For $\phi = 0.5$ (b) For $\phi = 0.7$

Figure 4.28: The flow field with hydrogen concentration of the injection process for different equivalence ratio, 3000 rpm and $SOI = 100$ deg BTDC at 80 deg BTDC. (Isometric view)

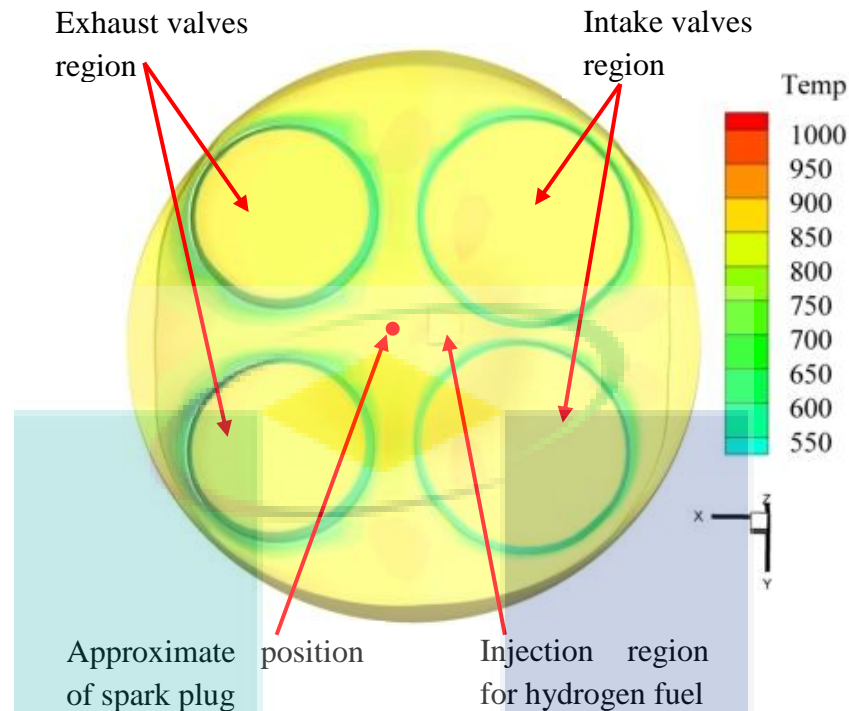


Figure 4.29: The temperature contour at TDC position (isometric view).

Figure 4.30 demonstrates the temperature contours for different engine speed (2000 and 4000 rpm) and instants (5, 10, 15 and 20 deg ATDC) at $\phi = 0.7$ and $SOI = 100$ deg BTDC. These four instants are selected to differentiate the progress of the combustion events as well as analyzing the heat-transfer phenomenon. The first instant (5 deg ATDC) is immediately after the start of the ignition process, which reveals a hot spot at the spark plug position. At this stage, the temperature distributions are almost identical with the engine speed. This is because of the flame propagation is in the initiation stage. At the second instant (10 deg ATDC), the growth of flame becomes more developed and covers wider space from the combustion chamber. The temperature levels also are increased as the crank angle advanced due to increase of the amount burning mixture. These growths and development are increased continuously for the next two instants (15 and 20 deg ATDC). It can also be seen that the growth of flame to cover wider space is rapidly increased as an increase of the engine speed. The temperature levels as well as are increased as an increase of the engine speed. The differences are clearer in terms of the instants of 10 and 15 deg ATDC.

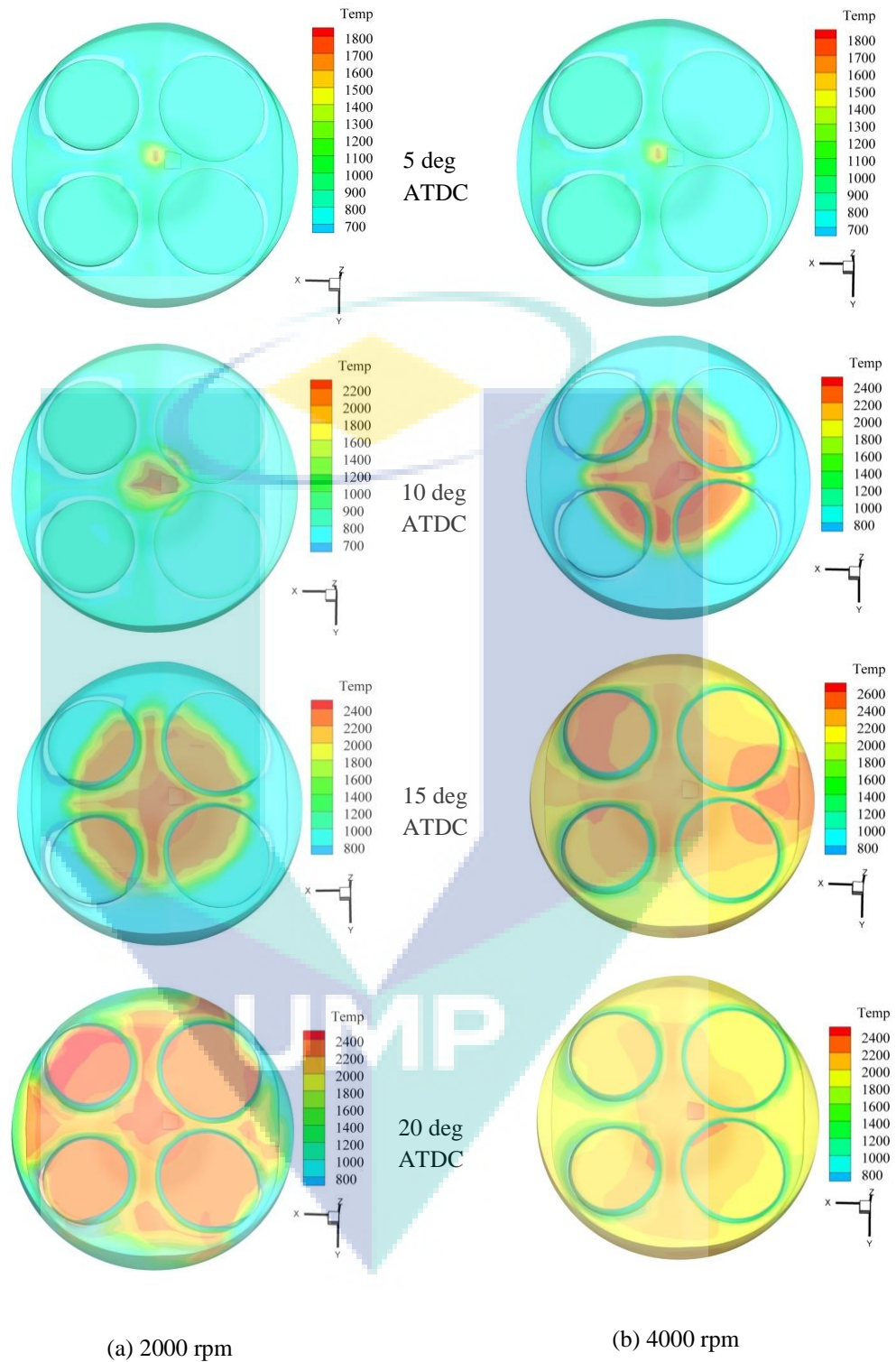


Figure 4.30: The temperature contours for different engine speed and instants at $\phi = 0.7$, IT = TDC and SOI = 100 deg BTDC.

The maximum local temperature is obtained 2400 and 2600 °K for 4000 rpm at the instants of 10 and 15 deg ATDC respectively. This is because of the increase the reaction rate as an increase of the engine speed, which is caused higher level of turbulence (Heywood, 1988 and Ferguson and Kirkpatrick, 2001). This difference in the temperature distributions for both engine speeds continues with the further progress in piston movement. The difference also still exists even in the temperature levels. Besides that, there is a delay to complete the combustion process in case of the 2000 rpm. Again, the direct effect of the engine speed on the turbulence level that leads to direct impact on the flame propagation and reaction rate represent the main reason for this delay. This behavior for the local distributions of the temperature within the combustion chamber produces the same trends for spatial heat transfer. This is because of a direct relationship between the distribution of temperature and the nature of the process of heat transfer. These results are achieved according to the improved wall function for definitions of the velocity and temperature within the region vicinity to the walls.

Figure 4.31 demonstrates the temperature contours for the different equivalence ratio ($\phi = 0.3, 0.5, 0.7$ and 0.9) and instants (10 and 15 deg ATDC) at the engine speed of 3000 rpm and $SOI = 100$ deg BTDC. These two instants are selected based on the observed behavior in Figure 4.30. It can be classified the results here into the ultra-lean ($\phi = 0.3$ and 0.5) and lean ($\phi = 0.7$ and 0.9) mixture strength ranges. There is a considerable difference in distribution of the temperature levels and the space of the burnt mixture for the ultra-lean range. It can be seen that, the higher local temperature distribution as well as, a wider burning space is observed at $\phi = 0.5$. The maximum temperature is obtained (2000 °K) at the stronger mixture strength ($\phi = 0.5$) and second instant (15 deg ATDC). This is due to a direct relationship between the flame speed and mixture strength. As the hydrogen has a significantly higher dependency for the laminar flame speed on mixture strength condition (Natkin et. al, 2003). Therefore, the combustion rate becomes faster for the stronger mixture condition. At the first instant with lean mixture strength ($\phi = 0.7$ and 0.9), the temperature contours are almost an identical. However, the temperature contours are differentiated for the second instant.

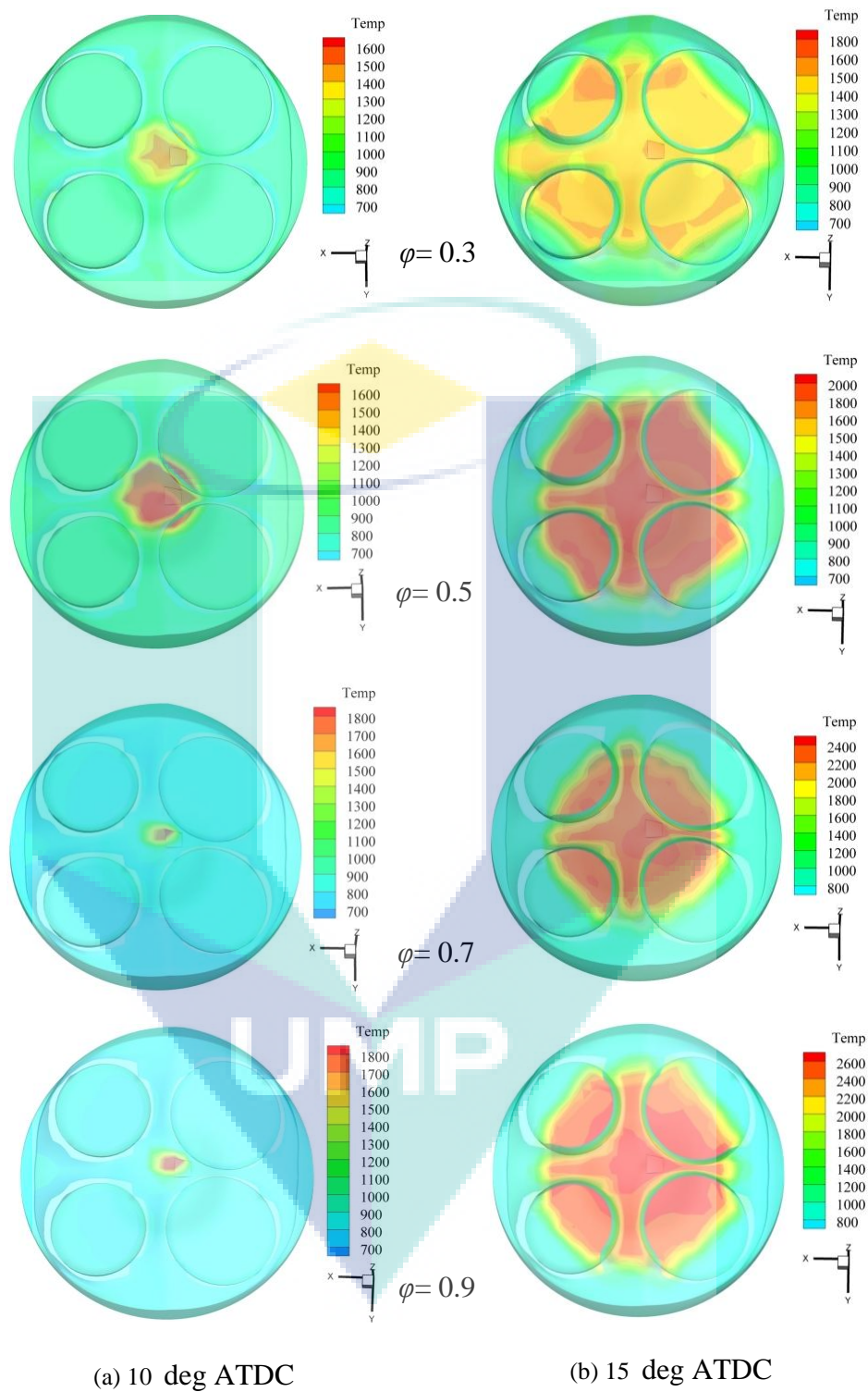


Figure 4.31: The temperature contours for different equivalence ratio and instants at engine speed of 3000 rpm, IT = TDC and SOI = 100 deg BTDC.

The maximum temperature (2600 °K) is obtained in case of the richer mixture strength ($\phi = 0.9$). This is because of the laminar flame speed for the hydrogen fuel increases dramatically as an increase of the equivalence ratio (Natkin et al., 2003). Therefore, the richer mixture strength produces a faster burning rate, which means a quicker flame development and thus higher heat release. Accordingly, the heat transfer rate has to be a higher with the richer mixture strength.

It is seen that, the trend of temperature distribution is non-uniform for the ultra-lean and lean mixture strength. This is due to the nature of the combustion model in the multidimensional modelling. It is based on the kinetic controlled and equilibrium reactions mechanisms. These mechanisms for the combustion modelling depend on some properties of fuel that are employed within the model formulation. The forward pre-exponential factor (k_{fr}), and the stoichiometric coefficients (a_m and b_m) are the most important properties (Amsden, 1993). These characteristics are usually evaluated empirically to be appropriate for any application. An excessive rate of heat release is produced when chosen too high values for these characteristics. However, the combustion is not sustained due to insufficient heat release when considered low values (Amsden, 1993). The values of these characteristics are considered in the present study according to previous reported works (Marinov et al., 1995 and Kumar et al., 2011). However, these values were revealed a degree of uncertainty in prediction of a laminar flame speed. The predicted flame speed well represented the experimental data for only the 0.55 - 1.1 equivalence ratio range. Predictions by the global reaction mechanism were considered poor outside this equivalence ratio range. The poor prediction is attributed to chemical and thermal structure changes in the flame as the stoichiometry varies, which could not, be properly accounted for in the global reaction model.

The impact of injection timing on the temperature distribution is desired to clarify. Figure 4.31 demonstrates the temperature contours for different injection timing ($SOI = 70$ and 130 deg BTDC) and instants (5, 10, 15 and 20 deg ATDC) at the engine speed of 3000 rpm, $\phi = 0.7$ and $IT = TDC$. It can be seen that there is no pronounced difference for the temperature distribution between different injection timing, even with advance stages of the combustion process. This is because of the injection process

completed with a sufficient time earlier the ignition event, even for the retarded injection timing ($SOI = 70$ deg BTDC). Therefore, there is no effect on heat transfer.

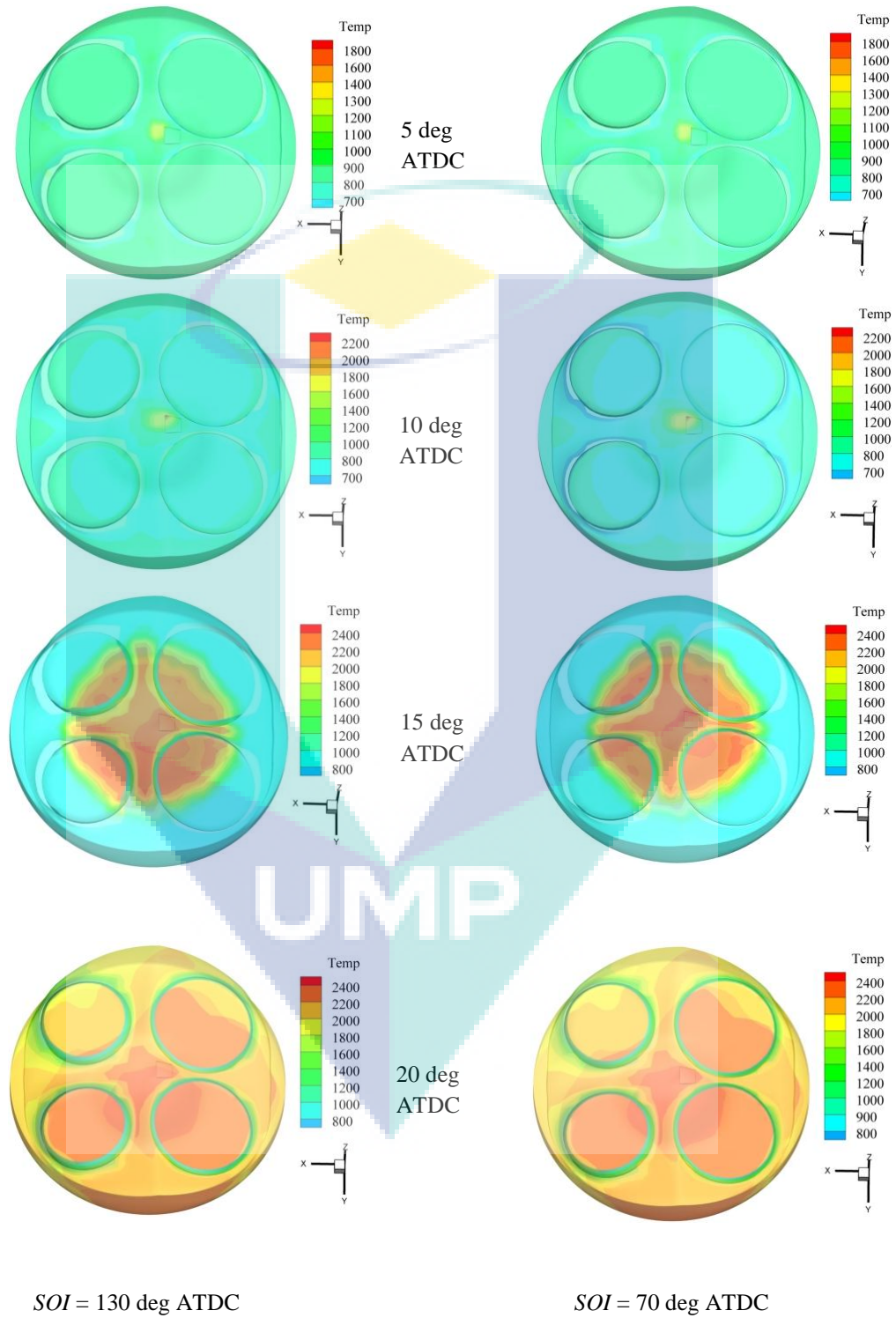


Figure 4.32: The temperature contours for different SOI and instants at engine speed of 3000 rpm, $\phi = 0.7$ and IT = TDC.

Trends of Heat Release

Heat release during combustion is used for characterization the heat transfer of ICEs. The heat release rate is determined based on kinetic controlled and equilibrium reactions for multidimensional modelling. Figure 4.33 presents the variation of heat release rate against crank angle for different engine speed of 2000 and 5000 rpm at ($\phi = 0.7$), IT = TDC and $SOI = 100$ deg BTDC. It can be seen that there is no variation in heat release rate during compression and expansion strokes. However, the variation of heat release rate is significant during combustion strokes. The heat release rate is increased with an increase of engine speed. The peak rate of heat release was around 65 and 140 J/deg at 2000 and 5000 rpm respectively. Moreover, the crank angle corresponding to the peak rate is become nearest to TDC position with an increase of engine speed. The peak point is appeared at 19 and 10 deg ATDC for 2000 and 5000 rpm respectively. It can be also seen that the combustion process is taken placed in a shorter period with an increase of engine speed. That means the hydrogen fuel combustion is boosted with an increase of engine speed increased. This is because of increasing of engine speed leads to intensify of turbulence level within the combustion chamber (Heywood, 1988 and Ferguson and Kirkpatrick, 2001).

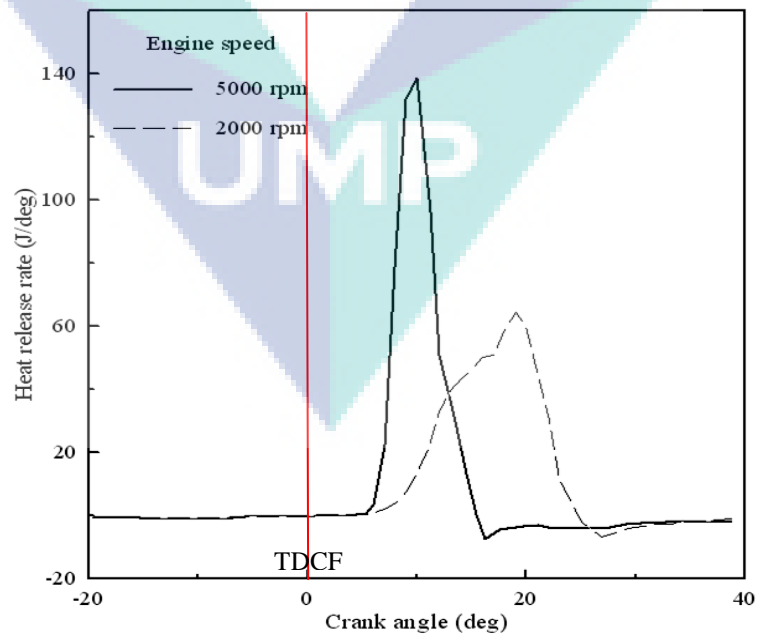


Figure 4.33: Variation of heat release rate against crank angle for different engine speed at $\phi = 0.7$, IT = TDC and $SOI = 100$ deg BTDC.

Figure 4.34 presents the variation of heat release rate against crank angle for different equivalence ratio ($\phi = 0.5$ and $\phi = 0.7$) at engine speed of 3000 rpm, IT = TDC and $SOI = 100$ deg BTDC. The identical trends are revealed during compression, combustion and expansion strokes. It can be seen that the rate of heat release increases with an increase of the equivalence ratio. The peak rate of heat release was around 62 and 116 J/deg at $\phi = 0.5$ and $\phi = 0.7$ respectively. Moreover, the crank angle corresponding to the peak rate is almost identical (16 deg ATDC). It can be also seen that the combustion process is taken placed in a shorter period with an increase of the equivalence ratio. Combustion duration is decreased from 18 to 12 deg as the equivalence ratio increased from ($\phi = 0.5$) to ($\phi = 0.7$) due to the slower combustion for the leaner mixture. This is because of increasing of flame development due to increase of laminar flame speed (Natkin et al., 2003). Therefore, mixture is burned faster because the burning rate depends mainly on the flame development (Stefaan and Sebastian, 2005 and Verhelst and Sierens, 2003). This result is agreed with the general trends of the experimental results (see Figure 4.6) as well as the previous observation reported by Shudo et al. (2003), Wimmer et al. (2005) and Ma et al. (2011).

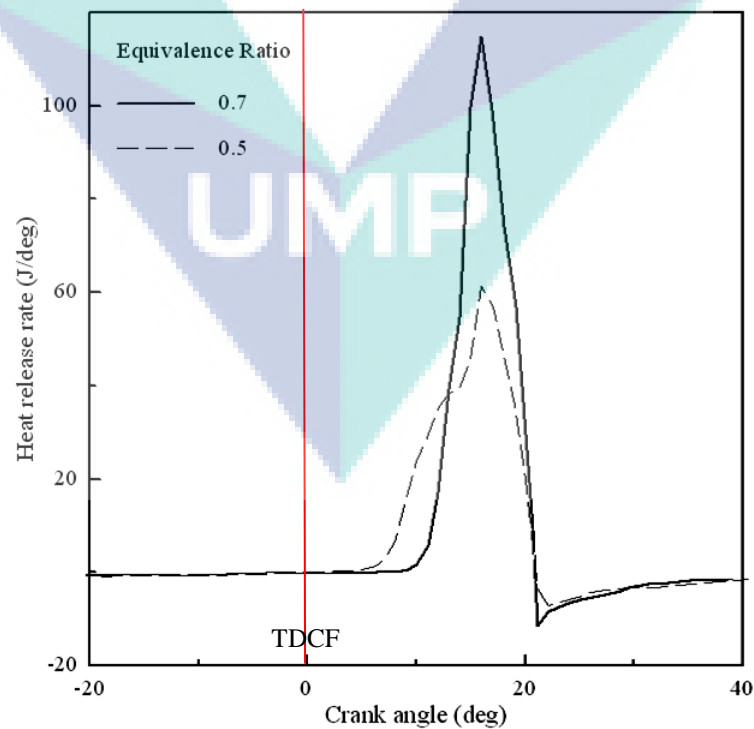


Figure 4.34: Variation of heat release rate against crank angle for different equivalence ratio at engine speed of 3000 rpm, IT = TDC and $SOI = 100$ deg BTDC.

Figure 4.35 demonstrates the variation of heat release rate against crank angle for different injection timing ($SOI = 70, 100$ and 130 deg BTDC) at engine speed of 3000 rpm, $\phi = 0.7$ and $IT = TDC$. The identical trends are revealed during compression, combustion and expansion strokes. The variation of SOI is not caused any impact on the trends of heat release rate because of the absence of the interaction between of the injection and ignition events even for the latter timing ($SOI = 70$ deg BTDC). It can be seen that there is a negative heat release is appeared after complete the combustion process as shown in Figures 4.33-4.35. The negative values imply that combustion products absorb of heat from the surround. The negative rate is appeared because of the heat release model is based on chemical reactions (Amsden, 1993). This behavior is disappeared as engine speed increased because of reducing the available time. This finding has also reported by Shudo et al. (2003) and Demuynck et al. (2009).

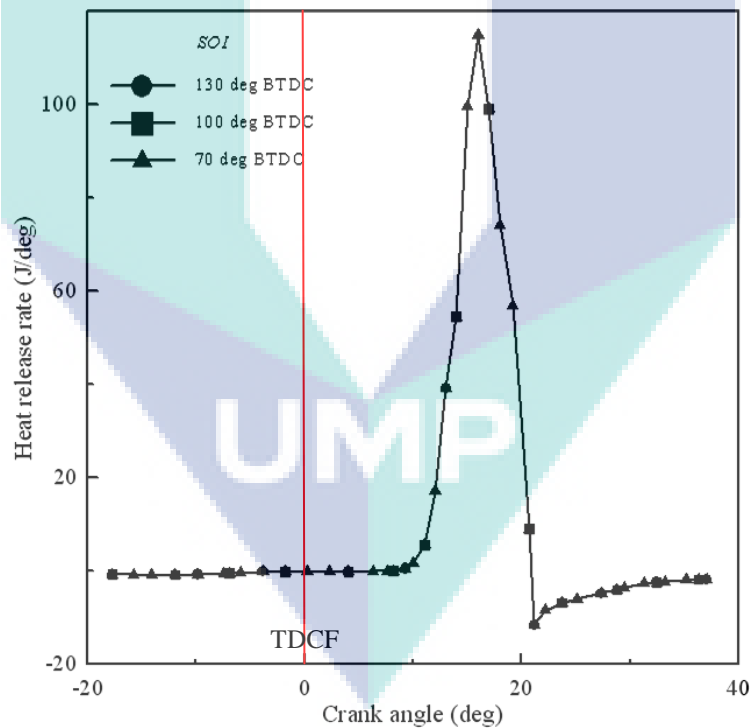


Figure 4.35: Variation of heat release rate against crank angle for different SOI at engine speed of 3000 rpm, $\phi = 0.7$ and $IT = TDC$.

Trends of Instantaneous Heat Loss

The correct estimation for instantaneous rate of heat loss is a decisive issue for the heat-transfer analysis of the multidimensional model. The instantaneous rate of heat loss is considered as an indicator for the trends of instantaneous heat transfer (IHT). The instantaneous rate of heat loss is the instant energy waste during combustion. It is spatially averaged of the heat loss, as modeled by Eq. (3.56), for the entire domain of the combustion chamber. Figure 4.36 shows the instantaneous rate of heat loss against crank angle for different engine speeds of 2000, 3000, 4000 and 5000 rpm at ($\phi = 0.7$), IT = TDC and SOI = 100 deg BTDC. The instantaneous rate of heat loss is increased at the late stage of the compression stroke. However, it is rapidly increased during the combustion stroke immediately after TDC due to the detonation of hydrogen fuel (Das, 1996).

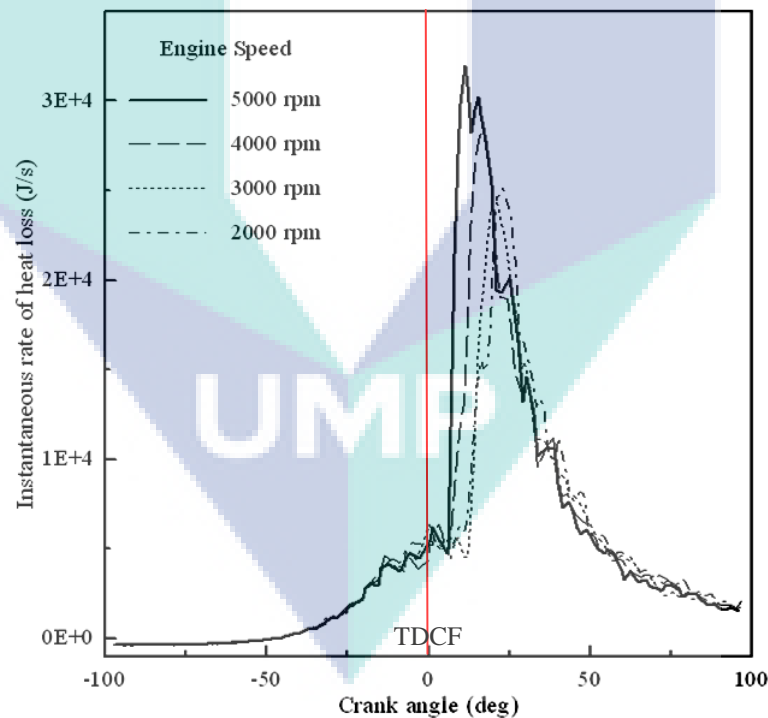


Figure 4.36: Variation of the instantaneous rate of heat loss against crank angle for different engine speed at $\phi = 0.7$, IT = TDC and SOI = 100 deg BTDC.

It can be seen that the instantaneous rate of heat loss is increased with an increase of engine speed. The higher engine speed (5000 rpm) produces a greater peak value (around 32300 J/s) for the instantaneous rate of heat loss due to increase the

velocities of the in-cylinder gases. The percentage of increment in peak value is around 35 % as engine speed increased from 2000 to 5000 rpm. That means; the higher value of engine speed causes a larger heat loss, since the in-cylinder gas motion is promoted by increasing of the engine speed (Karamangil et al., 2006). Furthermore, it can be seen that the start of increasing, and peak points are appeared earlier (nearest to TDC) with an increase of engine speed. This is because of developing of the combustion flame is faster in case of the higher engine speed as appeared in temperature contours (see Figure 4.30).

Figure 4.37 demonstrates variation the instantaneous rate of heat loss against crank angle for different equivalence ratio ($\phi = 0.3, 0.5, 0.7$ and $\phi = 0.9$) at engine speed of 3000 rpm, IT = TDC and SOI = 100 deg BTDC.

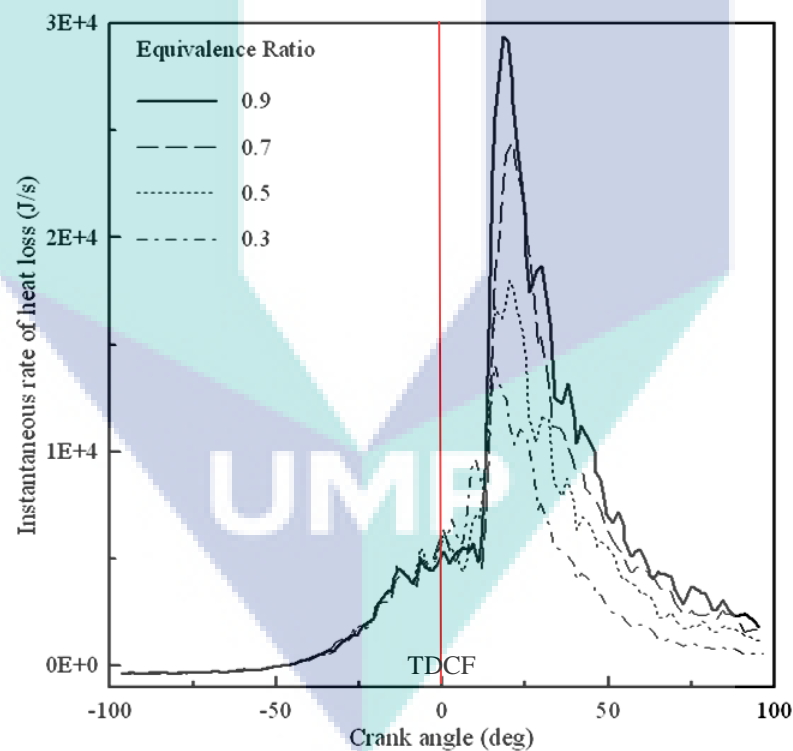


Figure 4.37: Variation of the instantaneous rate of heat loss against crank angle for different equivalence ratio at engine speed of 3000 rpm, IT = TDC and SOI = 100 deg BTDC.

The identical general trends are revealed during compression, combustion and expansion strokes. It shows that the equivalence ratio has an intense effect on the instantaneous rate of heat loss. The largest difference (around 50 %) is observed around

the peak value of heat loss in favor of richer mixtures ($\phi = 0.9$). This is because of increasing the amount of the released energy during combustion as the mixture becomes richer due to increase of mixture energy content (Boretti and Watson, 2009). Furthermore, the range of the high rate becomes wider as the mixture strength increases due to the longer time consumed for cooling the combustion chamber. Moreover, it is clearly understood from the temperature contours as shown in Figure 4.31. The richer mixture is produced higher temperature and covered larger space from the combustion chamber. Accordingly, the temperature difference between the wall and the adjacent gas layer become higher. Therefore, the main driving force for the heat flux is directly increased the rate of instantaneous heat loss.

Figure 4.38 demonstrates the variation the instantaneous rate of heat loss against crank angle for different injection timing ($SOI = 70, 100$ and 130 deg BTDC) at engine speed of 3000 rpm, $\phi = 0.7$ and $IT = TDC$. The identical trends are revealed during compression, combustion and expansion strokes. The variation of SOI is not caused any impact on the trends of the instantaneous rate of heat loss. This behavior is supporting the previous indications for the instantaneous modes for the temperature distributions and heat release rate. This is because of completing of hydrogen injection earlier than of the ignition event with sufficient time. For example, at $SOI = 70$ deg BTDC there are 20 deg between the end of injection and start of ignition. That means there is no interaction between of the injection and ignition events even for the latter timing. Figures 4.36, 4.37 and 4.38 illustrate the rates of instantaneous heat absorbed or rejected against crank angle, for various cases. It can clearly be seen the phenomenon related to such instantaneous systems with heat necessarily flowing in and out of the body periodically. This is because of the temperature difference between gas and wall surface temperatures become sometimes positive and other times negative due to their phasing. It can also be seen that the instantaneous rate of heat loss appears a fluctuation mode during the late stage of compression and combustion stroke. This reflects the nature of the local variations for wall heat fluxes as well as the boosting of flame propagation due to increasing of the squish zone (Mugele et al., 1999).

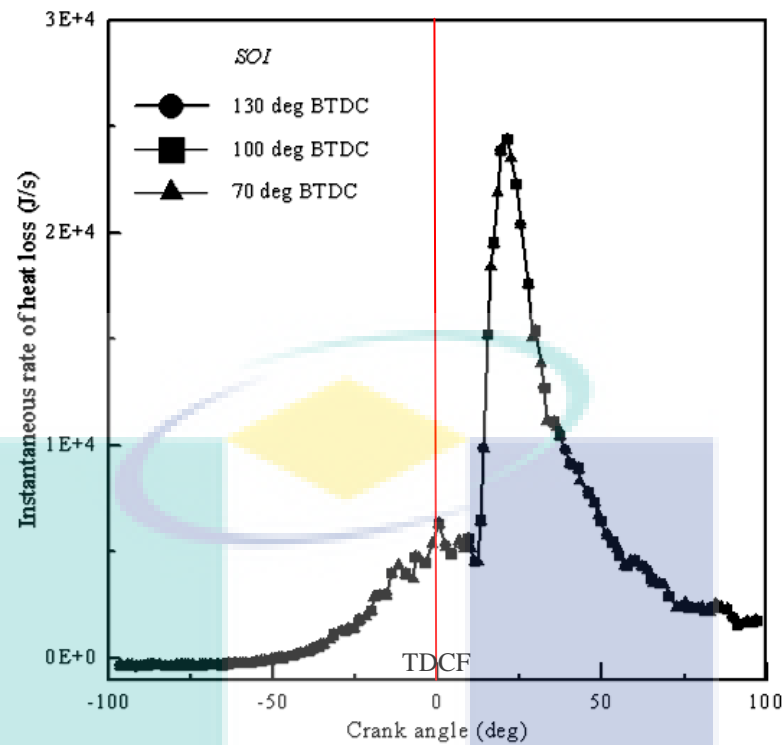


Figure 4.38: Variation of the instantaneous rate of heat loss against crank angle for different *SOI* at engine speed of 3000 rpm, $\phi = 0.7$ and IT = TDC.

Trends of Cumulative Heat Loss

The cumulative heat loss is a global integral for the rate of instantaneous heat loss. Figure 4.39 shows the instantaneous rate of heat loss against crank angle for different engine speeds of 2000 and 5000 rpm at ($\phi = 0.7$), IT = TDC and *SOI* = 100 deg BTDC. There is no variation during the compression stroke due to lacking the energy source. The variations of the cumulative heat losses are not significant due to the small temperature gradient. It is also observed that the negative values of cumulative heat losses during the compression stroke. This is because of the heat is transferred to the gases in the combustion chamber. This tendency takes place because of the temperature of the fresh charge is lower than the cylinder wall temperature. However, the process is inverted as the temperature of the charge increased, when the pressure increases gradually in the combustion phase. The cumulative heat loss is rapidly increased when the flame front is sufficiently developed. This is because of increasing the released energy rapidly during the combustion phase due to the detonation nature for hydrogen fuel. The gradient of cumulative heat loss is decreased during the late stage of

combustion due to the depletion of the contribution from the released energy. It becomes flatter during the expansion stroke due to insignificant thermal energy lost from the system.

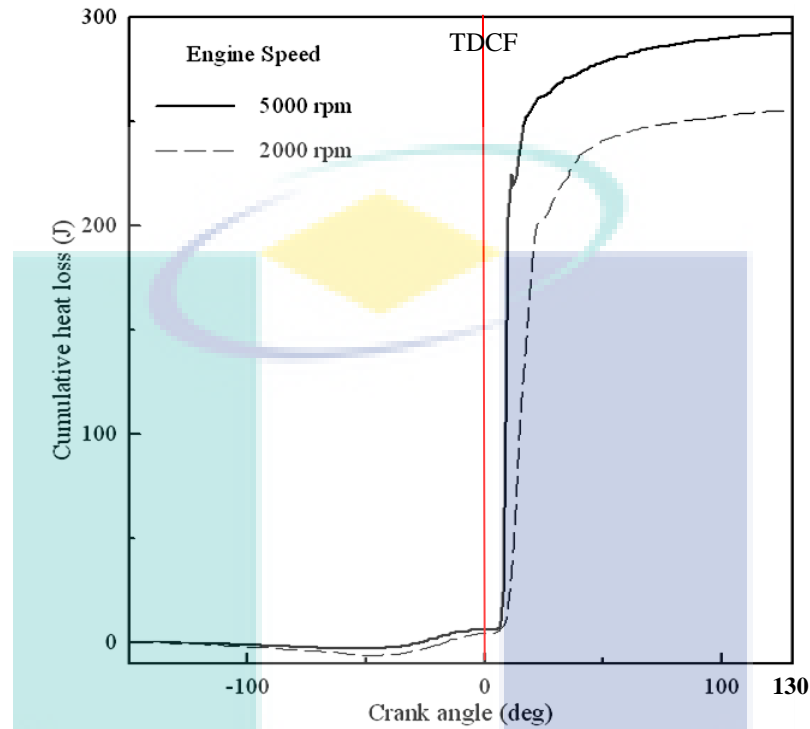


Figure 4.39: Variation of the cumulative heat loss against crank angle for different engine speed at $\phi = 0.7$, IT = TDC and $SOI = 100$ deg BTDC.

Influence of engine speed can be seen clearly during and after the combustion process. For higher engine speed, the cumulative heat loss is appeared to have a sharper gradient during the combustion process as well as is presented greater values. At the crank angle of 130 deg ATDC, the cumulative heat loss increased about around 10 % with an increase of the engine speed from 2000 to 5000 rpm. This is because of enhancing the convection heat transfer to cylinder walls with an increase of the engine speed, which boosts the turbulence level and reduces the boundary-layer thickness (Heywood, 1988 and Ferguson and Kirkpatrick, 2001).

Figure 4.40 demonstrates the variation of the cumulative heat loss against crank angle for the different equivalence ratio ($\phi = 0.5$ and $\phi = 0.7$) at engine speed of 3000 rpm, IT = TDC and $SOI = 100$ deg BTDC. The selected values for the equivalence ratio (ϕ) are based on the range of the finest engine operation for DIH_2ICE

(Mohammadi et al., 2007). Trends of the cumulative heat loss with variation of the equivalence ratio are identical with variation of engine speed. It can be seen that the cumulative heat losses increase with an increase of the equivalence ratio during combustion as well as expansion strokes. This is due to the higher heat rejection from the combustion chamber. Richer mixtures produce higher temperatures inside the cylinder (as Figure 4.31 shows) and faster flame speed. The temperature gradient of heat transfer, as well as the approach velocity of the hot plume to the wall is increased. Therefore, the cumulative heat loss increases with an increase of the equivalence ratio due to the higher heat rejection. The cumulative heat loss increased around 35 % with an increase of the equivalence ratio from ($\phi = 0.5$) to ($\phi = 0.7$) at the crank angle of 130 deg ATDC.

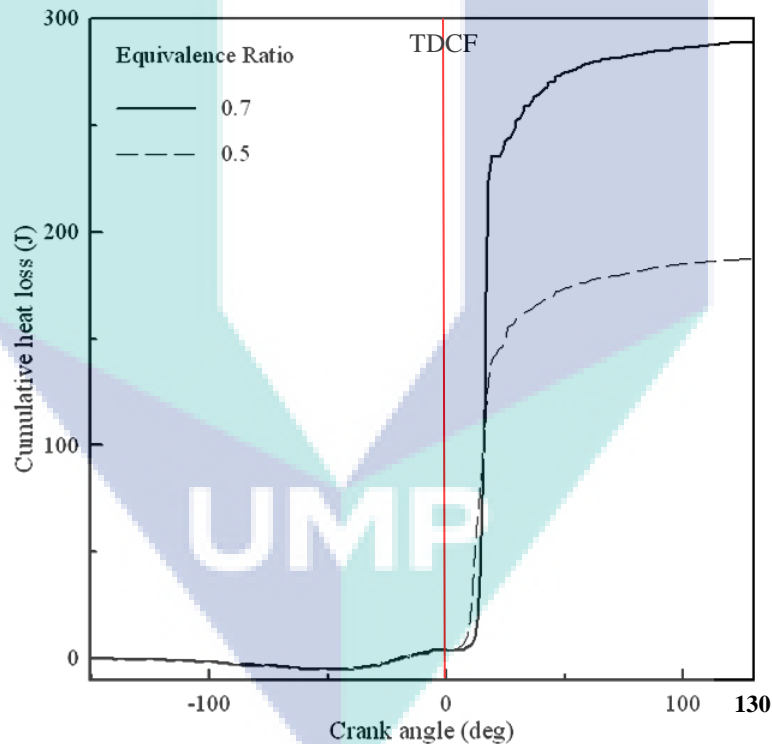


Figure 4.40: Variation of the cumulative heat loss against crank angle for different equivalence ratio at engine speed of 3000 rpm, IT = TDC and $SOI = 100$ deg BTDC.

Figure 4.41 demonstrates the variation of the cumulative heat loss against crank angle for different injection timing ($SOI = 70, 100$ and 130 deg BTDC) at engine speed of 3000 rpm, $\phi = 0.7$ and IT = TDC. Trends of the cumulative heat loss with variation of injection timing (SOI) are identical with variation of the engine speed and

equivalence ratio. As mentioned previously, an advance of *SOI* is not caused any pronounceable change in the profiles of the instantaneous rate of heat loss. Therefore, it is not caused any impact on the cumulative heat loss. In brief, the cumulative heat loss is a main parameter has a direct effect on the estimation of the engine power. The influence of the equivalence ratio (ϕ) is substantial for estimating of IHT in DIH₂ICE. The effect of engine speed comes subsequent while the effect of *SOI* is negligible within the investigated range.

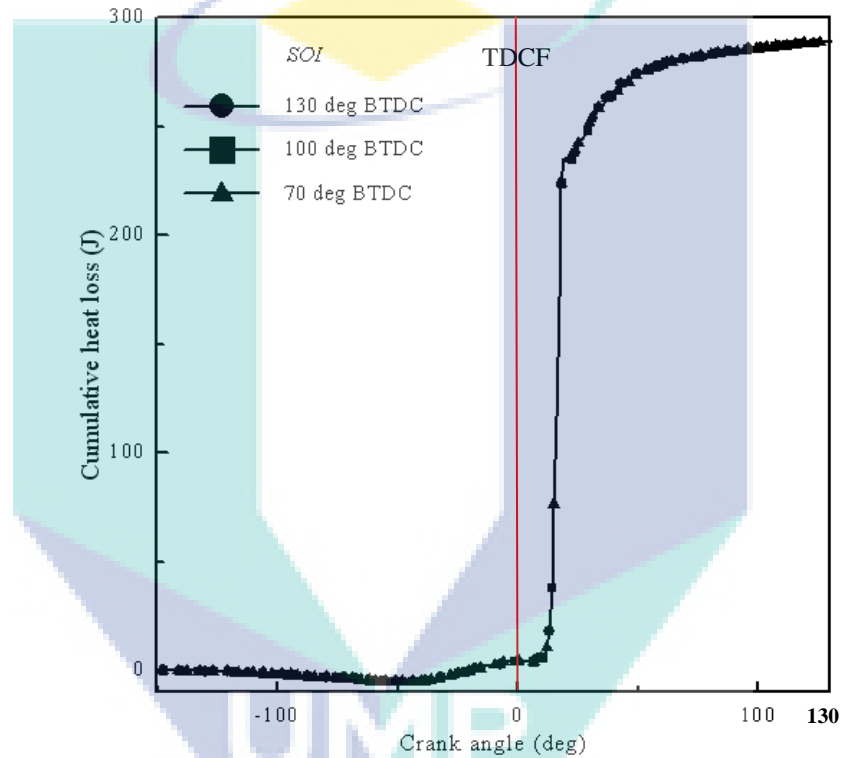


Figure 4.41: Variation of the cumulative heat loss against crank angle for different *SOI* at engine speed of 3000 rpm, $\phi = 0.7$ and IT = TDC.

Trends of Heat Transfer Coefficient

Estimation of the heat-transfer coefficient in the multidimensional model is based on the modified wall function (Eq. 3.56). It is considered for characterizing of IHT in DIH₂ICE. A parametric study is performed to reveal the influence of operation parameters on trends of the heat-transfer coefficients. Figure 4.42 shows the prediction of the multidimensional model for the heat-transfer coefficient for engine speeds of 2000 and 5000 rpm at ($\phi = 0.7$), IT = TDC and *SOI* = 100 deg BTDC.

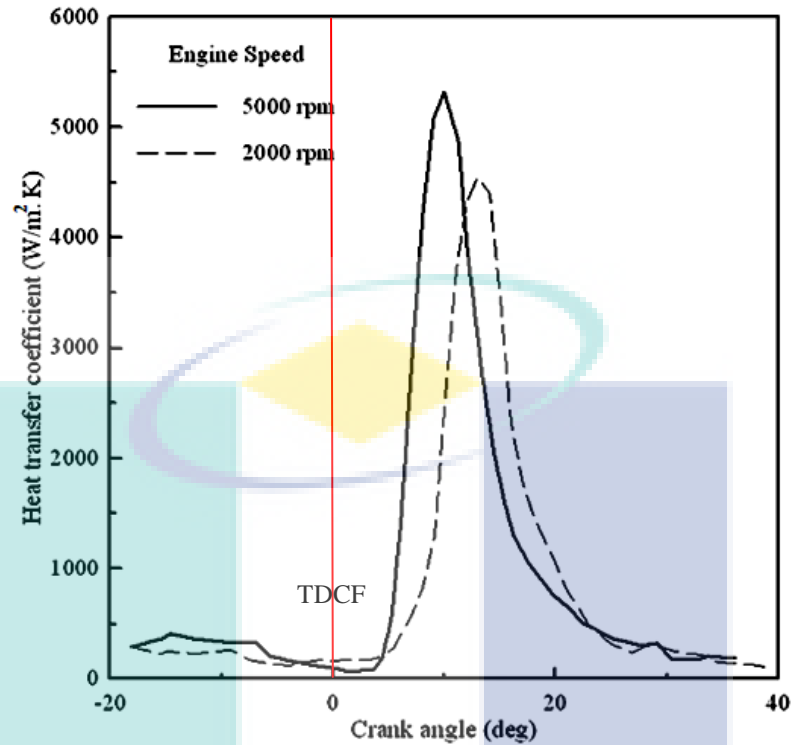


Figure 4.42: Variation of the heat transfer coefficient against crank angle for different engine speed at $\phi = 0.7$, IT = TDC and SOI = 100 deg BTDC.

The effect of engine speed on the heat-transfer coefficient is apparent clearly. It can be seen that the heat transfer coefficient increases with an increase of the engine speed. The maximum heat transfer coefficient was around 4700 and 5300 W/m².K at 13 and 10 deg ATDC for 2000 and 5000 rpm respectively. The percentage of increment is around 10 % as engine speed increased from 2000 to 5000 rpm. This is because of enhancing the convection heat transfer to cylinder walls with an increase of the engine speed, which boosts the turbulence level and reduces the boundary-layer thickness (Heywood, 1988 and Ferguson and Kirkpatrick, 2001). The location of maximum value is appeared earlier in case of higher engine speed due to the faster development of the flame front as appeared in temperature contours (see Figure 4.30).

Figure 4.43 demonstrates the variation of the heat-transfer coefficient against crank angle for the different equivalence ratio ($\phi = 0.5$ and $\phi = 0.7$) at engine speed of 3000 rpm, IT = TDC and SOI = 100 deg BTDC. The selected values for the equivalence ratio (ϕ) are based on the range of the finest engine operation for DIH₂ICE

(Mohammadi et al., 2007). It can be seen that the heat transfer coefficient increase with an increase of the equivalence ratio due to increase of the released energy and temperature gradient. This is because of increasing of the mixture energy content with an increase of the equivalence ratio (Boretti and Watson, 2009). Furthermore, the combustion rate increases with an increase of the equivalence ratio due to increase of the flame burning speed (Verhelst and Sierens, 2003 and Stefaan and Sebastian, 2005) and thus increase of the turbulent flame propagation (Wimmer et al., 2005).

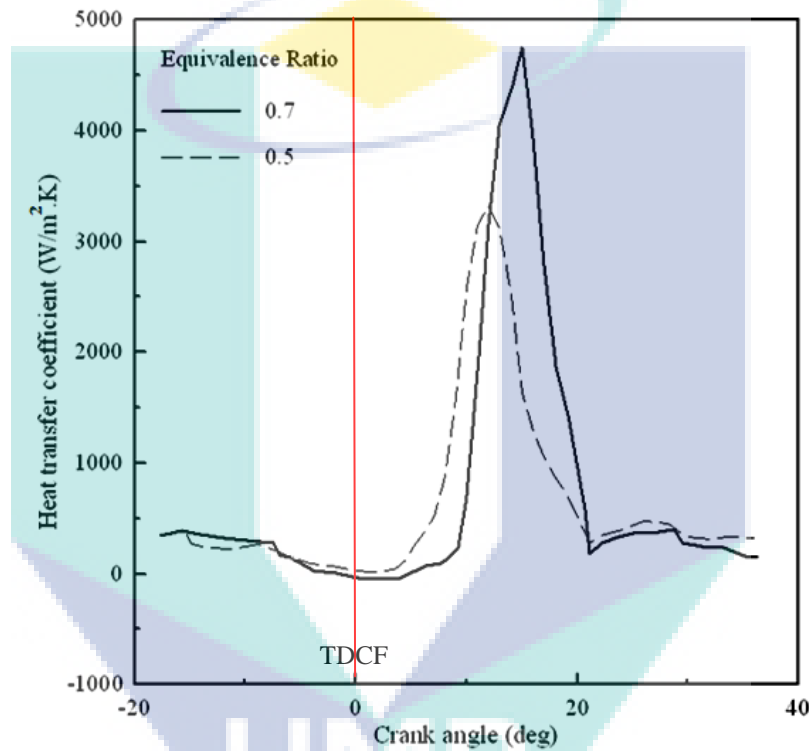


Figure 4.43: Variation of the heat transfer coefficient against crank angle for different equivalence ratio at engine speed of 3000 rpm, IT = TDC and SOI = 100 deg BTDC.

It can be seen that, the maximum heat transfer coefficient increases with an increase of the equivalence ratio (ϕ). It was around 3300 and 4800 W/m².K at 12 and 16 deg ATDC for $\phi = 0.5$ and $\phi = 0.7$ respectively. The percentage of increment is around 35 % as the equivalence ratio increased from 0.5 to 0.7. This is due to increase of the released energy from the burnt mixture because of increasing the energy content per intake charge. Moreover, the crank angle corresponding to the peak value is delayed with an increase of the equivalence ratio (ϕ) due to the non-uniform trends of

temperature distribution for the ultra-lean and lean mixture strength (see Figure 4.31). This is due to the nature of the combustion model in the multidimensional modelling.

Figure 4.44 presents the prediction of the multidimensional model for the heat-transfer coefficient for different injection timing ($SOI = 70, 100$ and 130 deg BTDC) at engine speed of 3000 rpm, $\phi = 0.7$ and $IT = TDC$. The identical trends are revealed during compression, combustion and expansion strokes. As mentioned previously, an advance of SOI does not cause any pronounceable change in the profiles of the instantaneous rate of heat loss. Therefore, it is not caused any impact on the heat transfer coefficient. In brief, the influence of the equivalence ratio (ϕ) is substantial for estimating of IHT in DIH₂ICE. The effect of engine speed comes subsequent while the effect of SOI is negligible within the investigated range.

Figures 4.42-4.44 are shown that the heat-transfer coefficient is suddenly increased to its peak value within a period less than 10 deg. This is due to the detonation nature for burning of hydrogen fuel (Das, 1996). The same behaviour for H₂ICEs were reported by Wei et al. (2001) and Shudo and Suzuki (2002a, b). Therefore, they have been proposed a new equation for estimating of heat transfer in case of H₂ICEs. It was employed a new term to account for this increment in the heat transfer coefficient. The apparent heat release term instead of the pressure difference term in the Woschni equation is used (Shudo and Suzuki, 2002a). However, the new correlation contains two calibration parameters. It was used for adjusting the effect of the ignition timing and equivalence ratio. These dependencies are stated to be the subject of further studies. Thus, this correlation is still under development (Verhelst, 2005; Safari et al., 2009; Verhelst and Wallner, 2009 and Demuyne et al., 2011).

One-dimensional and multidimensional modeling are revealed that the equivalence ratio (ϕ) has a substantial influence on heat transfer in case of H₂ICE. This effect is come from the wide flammability limit for hydrogen fuel ($0.1 \leq \phi \leq 7.1$). With this range, there is a wide variation in combustion proprieties of hydrogen fuel. Among these proprieties including the flame speed, quenching distance and energy content has a direct impact on the heat transfer phenomena. These proprieties produce the unique behaviour for hydrogen combustion. Consequently, it has unique trends for TAHT and

IHT in comparison with fossil fuel. Finally, it can be concluded that considering of φ as a parameter for any development in heat transfer correlations is a necessary step for successful description in H₂ICE.

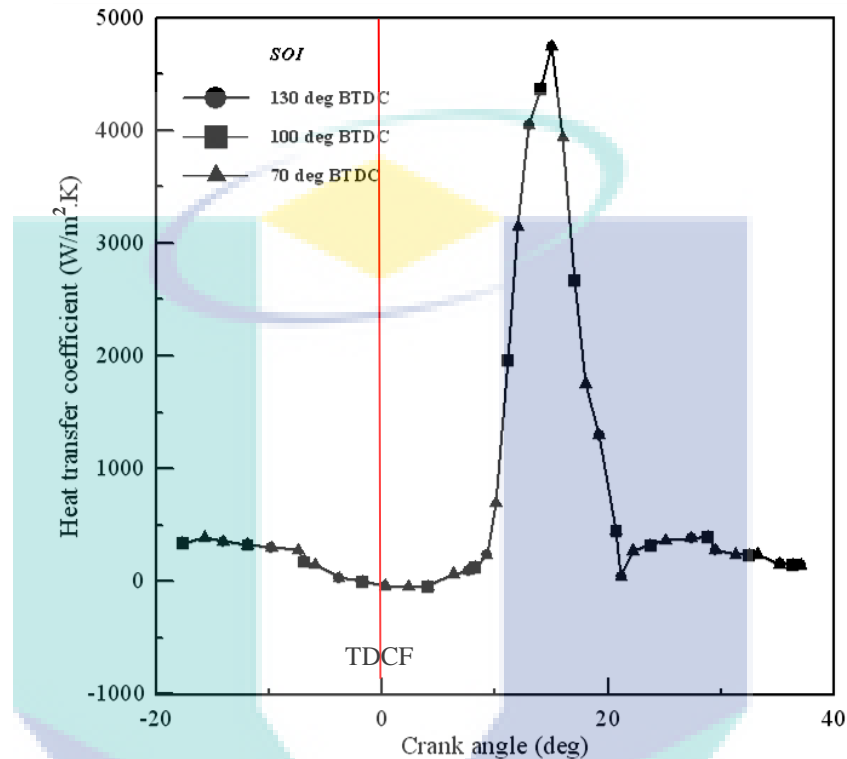
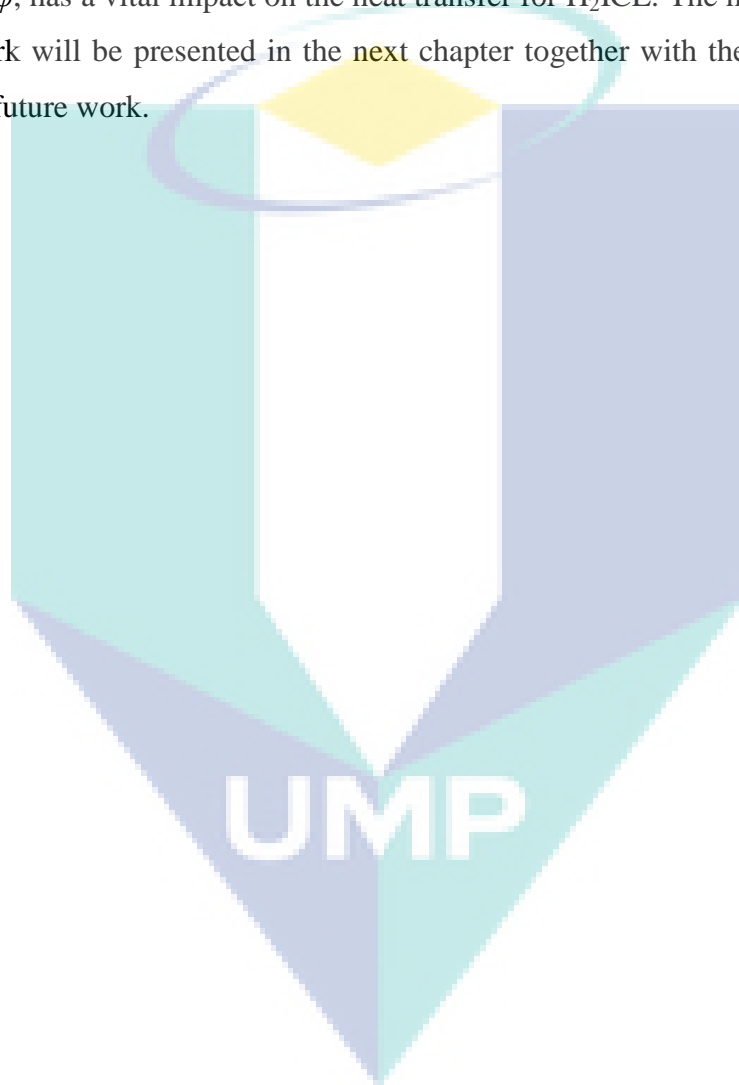


Figure 4.44: Variation of the heat transfer coefficient against crank angle for different *SOI* at engine speed of 3000 rpm, $\varphi = 0.7$ and IT = TDC.

4.6 SUMMARY

The results obtained from the experimental tests, and numerical models were presented. The experimental results were employed to identify the combustion characteristics for DIH₂ICE. Furthermore, the experimental tests were used for the calibration and validation of the numerical models. One-dimensional engine model based on gas dynamic approach was executed for the different conditions. Its result was presented and assessed for the evaluation of time-averaged heat-transfer trends. It has been shown that the equivalence ratio and engine speed has a vital effect on the time-averaged heat transfer of DIH₂ICE. Therefore, the existing correlation for estimating the time-averaged heat-transfer in the fossil-fueled engine was unsuitable for H₂ICE. Accordingly, new correlations were developed for describing the time-averaged heat-

transfer. A well prediction was achieved by adopting the new developed correlations. Multidimensional engine model based on finite volume approach was executed for various operation conditions, including the engine speed, equivalence ratio, and *SOI*. Its result was presented and assessed for describing the hydrogen-injection and evaluating the IHT trends. A parametric analysis was performed for qualifying and quantifying the influence of the operation parameters on IHT. It was shown that the neglected parameter, ϕ , has a vital impact on the heat transfer for H_2ICE . The main findings of the present work will be presented in the next chapter together with the recommendations for further future work.



CHAPTER FIVE

CONCLUSIONS AND FUTURE WORK

5.1 INTRODUCTION

The time averaged heat transfer and instantaneous heat transfer in the direct-injection hydrogen-fueled engine have been studied numerically as well as experimentally to expand new knowledge about the effect of the specified operation parameters on their behaviors. To achieve these goals, the capabilities of one dimensional and the multidimensional models were used. This chapter presents the summary of the main findings from the work carried out in this research. It also proposes recommendations for future development in each of the areas covered during this research.

5.2 SUMMARY OF FINDINGS

One-dimensional as well as the multidimensional models were developed for characterizing the time averaged heat transfer and instantaneous heat transfer in the direct-injection hydrogen-fueled engine. The main findings are summarized in this section. The results obtained through this research can be classified into two groups as follows:

5.2.1 One-dimensional Modeling

A one-dimensional model for the direct-injection hydrogen-fueled engine was developed based on gas dynamics approach to represent the flow and heat transfer in the

different components of the engine. The aim of this model was to perform a diagnostic study for assessing the influence of operation parameters on TAHT characteristics. This model was validated experimentally utilizing the collected database. It was capable to predict the engine performance within a reasonable accuracy around 10 %. The obtained results of the engine speed and equivalence ratio were shown the several pairs of operation points that produce a crucial gradient for TAHT characteristics. A significant impact for the equivalence ratio on TAHT characteristics was revealed. This is a unique behavior appears in case of the H_2 ICE due to the wide flammability range. A notable deterioration of the TAHT characteristics was revealed as retarding of *SOI*. This was caused due to the short period between the end of fuel injection and start of the combustion process.

A new correlation for the time-averaged heat transfer was developed. The novelty of this newly developed correlation is included the equivalence ratio as a governing variable. Therefore, the newly correlation depends on the Reynold's number as well as the equivalence ratio. It accounts for the decisive influence for the equivalence ratio on the time-averaged heat transfer due to the wide flammability limit for hydrogen fuel. The well-recognized Taylor's correlation applicable to the hydrocarbon-fuel of ICE has also been performed for hydrogen-fueled engine. Taylor's correlation was revealed the weak performance for estimating the time-averaged heat transfer of the direct-injection hydrogen-fueled engine. The relative error was confined within the range of 70% to 20% for the ultra-lean and lean mixture ($0.2 \leq \phi \leq 0.8$). The newly correlations were developed based on the nonlinear regression approach using the results of one-dimensional gas dynamic model. According to the *SOI*, two correlations were proposed. The effectiveness of the developed correlations was evaluated statistically. The proposed correlations have a remarkably satisfactory performance for all simulation data, where the determination coefficient (R^2) about 0.99. Moreover, the newly developed correlations were also validated with the simulation data. More than 95% of the simulation data were within the limits of the relative error of 10%. The new correlations were more reliable than Taylor's correlation for representing the actual data by reducing the relative error more than 50 %. The newly developed correlations are hypothetical to be suitable even for the hydrocarbon-fuel because of its general form. The amount of heat loss can be estimated

accurately using the newly developed correlations. It is a powerful design procedure for the automotive industries by improving thermal efficiencies; engine parts protection and reduction emissions.

5.2.2 Multidimensional Modelling

The multidimensional modelling for describing the trends of instantaneous heat transfer (IHT) in the direct-injection hydrogen-fueled engine was developed using the finite volume approach. The validation measurements were conducted using PROTON CAMPRO single cylinder engine. The performance of the multidimensional model was adequately accurate with some justifiable discrepancy (error < 10 %). The effect of operation parameters, including of the engine speed, equivalence ratio and *SOI* on IHT was identified qualitatively as well as quantitatively. The prediction of the multidimensional model for IHT trends were demonstrated in terms of the heat release rate, instantaneous rate of heat loss, cumulative heat loss as well as the heat-transfer coefficients. The influence of the equivalence ratio was substantial for trends of IHT in DIH₂ICE. The predictions of IHT parameters were increased around 35% when increasing the equivalence ratio within the range of the finest operation. While only 10% increment was acquired for the entire engine speed range. The effect of *SOI* is negligible within the investigated range. Therefore, the influence of ϕ is more importance parameters in identification of IHT in DIH₂ICE. It can be concluded that, including of ϕ as a parameter in the development of heat-transfer correlation is a powerful approach for estimating the heat transfer in H₂ICE. There was no identified effect for the *SOI* due to no interaction between the injection and ignition events even for the latter timing.

An integrated program for simulating of hydrogen injection in the gaseous state in DIH₂ICE was developed. This program was implemented in the multidimensional model. The flow pattern of a typical early injection was revealed for the DIH₂ICE. The flow fields were appeared to have greater vectors size and coarser distribution with increasing of engine speed. The heterogeneous distribution was obtained for the ultra-lean mixture condition ($\phi \leq 0.5$) due to insufficient the injected amount of hydrogen. The heterogeneity was decreased with increasing of ϕ because of increasing the total

injected amount of hydrogen inside the combustion chamber per unit time. There was no pronounced influence for *SOI* on the flow field pattern and mixture homogeneity because only the early period of injection was considered. The multidimensional model with the integrated injection program is a practical strategy for alternative-fuel development in automotives sectors. It is promising to perform optimization of the mixture formation and combustion analysis by 3D-CFD simulation.

5.3 CONTRIBUTIONS OF THE STUDY

The contributions of this study are summarized as follows:

- i. New predictive correlations are developed using a non-linear regression approach to estimate the rate of TAHT for DIH₂ICE applications. The existing correlations in this direction are only suitable for the hydrocarbon fuels. The available correlations are not taken into account for the influence of the equivalence ratio (φ) which identified as a crucial variable in case of H₂ICE. The newly developed correlations are hypothetical that might be suitable for the hydrocarbon-fuel. It is influential design procedure by improving thermal efficiencies; engine parts protection and reduction emissions for the automotive industries.
- ii. The influences of operation parameters on the IHT trends in DIH₂ICE are identified qualitatively as well as quantitatively. It is specified the key parameters that need to be included in the development of the heat transfer correlations for instantaneous heat transfer estimation.
- iii. An integrated computer program (SETVELIN) is developed for simulating of the hydrogen injection process in DIH₂ICE. This program is a convenient technique when incorporated with multidimensional modelling for hydrogen engine development. It is capable of adjusting fuel supply pressure, temperature, *SOI*, injection duration and rate of the injection stream. It can be easily to perform optimization of the inner mixture formation by means of 3D-CFD simulation.

- iv. A one-dimensional model is established based on gas dynamics approach. This model is analyzed the TAHT characteristics and also investigated its response to parameter's variation.

5.4 RECOMMENDATIONS FOR FUTURE WORK

During this research, there are several areas of interest highlighted, which could be of interest and worthwhile to investigate more thoroughly. These are outlined as the follows:

- i. Study the validity of the newly developed correlations based on the hydrocarbon fuels as well as compared to the experimental measurements.
- ii. Developing a new IHT correlation for DIH₂ICE by considering ϕ as a substantial parameter.
- iii. Coupling of the multidimensional model with the detailed chemical kinetics mechanism (like CHEMKIN) to simulate the combustion process for H₂ICE.
- iv. Study of NO_x formation in DIH₂ICE by using the coupled multidimensional model with the detailed chemical kinetic's mechanism.

REFERENCES

- Abdel-Aal, H.K., Sadik, M., Bassyouni, M. and Shalabi, M. 2005. A new approach to utilize hydrogen as a safe fuel. *International Journal of Hydrogen Energy*. **30**(13-14): 1511-1514.
- Abdullah, M.A. 2009. *Engine performance and combustion characteristics of hydrogen in a direct injection engine*. M.Sc. Thesis, Universiti Teknologi PETRONAS, Malaysia.
- Abraham, B. and Ledolter, J. 2006. *Introduction to regression modeling*. Thomson Brooks/Cole.
- Abdullah, M.A. and Rashid, A.A. 2009. An experimental investigation of hydrogen combustion in a direct injection spark ignition natural gas engine. *SAE Technical Paper No. 2009-01-1499*.
- Alkidas, A.C. 1980. Heat transfer characteristics of a spark-ignition engine. *ASME Journal of Heat Transfer*. **102**(2): 189-193.
- Amsden, A. A. 1993. KIVA-3: A KIVA program with block-structured mesh for complex geometries. *Los Alamos National Laboratory report no. LA-12503-MS*.
- Amsden, A. A. 1997. KIVA-3V: A block-structured KIVA program for engines with vertical or canted valves. *Los Alamos National Laboratory report no. LA-13313-MS*.
- Amsden, A. A. 1999. KIVA-3V, release 2, improvements to KIVA-3V. *Los Alamos National Laboratory report no. LA-13608-MS*.
- Amsden, A. A., O'Rourke, P. J. and Butler, T. D. 1989. KIVA-II: A computer program for chemically reactive flows with sprays. *Los Alamos National Laboratory report no. LA-11560-MS*.
- Amsden, A.A., Ramshaw, J.D., O'Rourke, P.J. and Dukowicz, J.K. 1985. KIVA: A computer program for two and three-dimensional fluid flows with chemical reactions and fuel sprays. *Los Alamos National Laboratory Report LA-10245-MS*.
- Annand, W.J. 1963. Heat transfer in the cylinders of reciprocating internal combustion engines. *Proceedings of Institution of Mechanical Engineers*. **177**(36): 973-990.
- Annand, W.J.D. 1986. Heat transfer in the cylinder and porting. in Horlock J. H. and Winterbone, D.E. (Editors), *The Thermodynamics and Gas Dynamics of Internal Combustion Engines*, Vol. II. *Oxford University Press*.
- Ball, M. and Wietschell, M. 2008. The future of hydrogen—opportunities and challenges. *International Journal of Hydrogen Energy*. **34**(2): 615-627.

- Bargende, M. 1991. *A correlation equation for calculating the heat transfer losses in high pressure spark ignition engines*. PhD Thesis. Technical University Darmstadt, Germany.
- Berckmüller, M., Rottengruber, H., Eder, A., Brehm, N., Elsässer, G., Alander, G. M. and Schwarz, C. 2003. Potentials of a charged SI-hydrogen engine. *SAE Technical Paper No. 2003-01-3210*.
- Blair, G. P. 1999. *Design and simulation of four-stroke engines*. Warrendale, Pa.: Society of Automotive Engineers, Inc. (SAE).
- Bohac, S. V., Baker, D. M. and Assanis, D. N. 1996. A global model for steady-state and transient SI engine heat transfer studies. *SAE Technical Paper No. 960073*.
- Boretti, A. A. and Watson, H. C. 2009, Enhanced combustion by jet ignition in a turbocharged cryogenic port fuel injected hydrogen engine. *International Journal of Hydrogen Energy*. **34**(5): 2511-2516.
- Boretti, A.A., Brear, M.J. and Watson, H.C. 2007. Experimental and numerical study of a hydrogen fuelled I.C. engine fitted with the hydrogen assisted jet ignition system. *Sixteenth Australasian Fluid Mechanics Conference*, Crown Plaza, Gold Coast, Australia, 2-7 December, pp. 1142-1147.
- Borgnakke, C., Puzinauskas, P. and Xiao, Y. 1986. Spark ignition engine simulation models. *University of Michigan report No. UM-MEAM-86-35*.
- Borman, G. and Nishiwaki, K. 1987. Internal combustion engine heat transfer. *Progress in Energy Combustion Sciences*. **13**(1): 1-46.
- Borman, G. L. 1990. In-cylinder heat transfer research at the U. W. engine research center. *International Symposium COMODIA 90*: 1-10.
- Brunt, M. F. J. and Emtage A. L. 1997. Evaluation of burn rate routines and analysis errors. *SAE Technical Paper No. 970037*.
- Buttsworth, D. R., Agrira, A., Malpress, R. and Yusaf, T. 2011. Simulation of instantaneous heat transfer in spark ignition internal combustion engines - unsteady thermal boundary layer modelling. *Journal of Engineering for Gas Turbines and Power*, **133**(2): 022802-022806.
- Chang, J., Güralp, O., Filipi, Z., Assanis, D., Kuo, T., Najt, P. and Rask, R. 2004. New heat transfer correlation for an HCCI engine derived from measurements of instantaneous surface heat flux. *SAE Technical Paper No. 2004-01-2996*.
- Chen, S. K. and Flynn, P. F. 1965. Development of a single cylinder compression ignition research engine. *SAE Technical Paper No. 650733*.
- Chiodi, M. 2011. *An innovative 3D-CFD approach towards virtual development of internal combustion engines*. First ed. 2011, Springer, Germany.

- Chiodi, M. and Bargende, M. 2001. Improvement of engine heat transfer calculation in the three-dimensional simulation using a phenomenological heat transfer model. *SAE Technical Paper No.2001-01-3601*.
- Ciulli, E. 1993. A review of internal combustion engine losses part 2: studies for global evaluations. *Proceedings of the Institution of Mechanical Engineers, Part D: Journal of Automobile Engineering*. **207**(3): 229-240.
- Cordaway, A. W. 2004. *Characteristics of hydrogen and operation of a hydrogen fueled internal combustion engine*. M.Sc. Thesis. Mechanical engineering department. Texas Technical University, USA.
- Courant, R., Friedrichs, K. and Lewy, H. 1928, On the partial difference equations of mathematical physics. *IBM Journal*. pp. 215-234, English translation of the 1928 German original.
- Crabtree, G., Dresselhaus, M. and Buchanan, M. 2004. The hydrogen economy. *Physics Today*. **57**(12): 39-44.
- Das, L. M. 1990. Hydrogen engines: a view of the past and look into the future. *International Journal of Hydrogen Energy*. **15**(6): 425-446.
- Das, L. M. 1991. Exhaust emission characterization of hydrogen operated engine system; nature of pollutants and their control technique. *International Journal of Hydrogen Energy*. **16**(11): 765-775.
- Das, L. 1996. Hydrogen-oxygen reaction mechanism and its implication to hydrogen engine combustion. *International Journal of Hydrogen Energy*. **21**(8): 703-715.
- Das, S. and Dent, J.C. 1995. Simulation of the mean flow in the cylinder of a motored 4-valved spark ignition engine. *SAE Technical Paper No. 952384*.
- Demuynck, J., De Paepe, M., Huisseune, H., Sierens, R., Vancoillie, J. and Verhelst, S. 2011. On the applicability of empirical heat transfer models for hydrogen combustion engines. *International Journal of Hydrogen Energy*. **36**(1): 975-984.
- Demuynck, J., De Paepe, M., Sierens, R. and Verhelst, S. 2010. Heat transfer comparison between methane and hydrogen in a spark ignited engine. *World Hydrogen Energy Conference*. Essen, Germany.
- Demuynck, J., Raes, N., Zuliani, M., De Paepe, M., Sierens, R. and Verhelst, S. 2009. Local heat flux measurements in a hydrogen and methane spark ignition engine with a thermopile sensor. *International Journal of Hydrogen Energy*. **34**(24): 9857-9868.
- Demuynck, J., Pauwels, S., Verhelst, S., De Paepe, M. and Sierens R. 2008. Experimental Research on the Heat Transfer Inside a Hydrogen Combustion

Engine: Evaluation and Construction of Measurement Methods. *In: Proceedings of the FISITA 2008 World Automotive Congress*, Paper no. F2008-SC-037.

- Dent, J. C. and Suliaman, S. J. 1977. Convective and radiative heat transfer in a high swirl direct injection diesel engine. *SAE Technical Paper No. 770407*.
- Dresselhaus, M., Crabtree, G. and Buchanan, M. Eds. 2003. *Basic research needs for the hydrogen economy*. Office of Basic Energy Sciences, Department of Energy, Washington, DC. www.sc.doe.gov/bes/reports/abstracts.html#NHE (Accessed 11 April 2010).
- Eichelberg, G. 1939. Some new investigations on old combustion engine problems. *Engineering*. **148**: 463-547.
- Eichlseder, H., Wallner, T., Freymann, R. and Ringler, J. 2003. The potential of hydrogen internal combustion engines in a future mobility scenario. *SAE Technical paper No. 2003-01-2267*.
- EPM (Emerson Process Management). 2006. Product Datasheets Micro Motion® Meters Specification Summaries.
- EIA (Energy information administration). 2011. *International energy outlook*. USA.
- Ferguson, C. R. 1986. *Internal combustion engines: applied thermosciences*. First ed. New York: John Wiley and Sons, Inc.
- Ferguson, C. R. and Kirkpatrick, A. T. 2001. *Internal combustion engine: applied thermosciences*. Second ed. New York: John Wiley and Sons, Inc.
- Field, A. 2009. *Discovering statistics using SPSS*. SAGE Publications
- Fiene, J., Braithwaite, T., Boehm, R. and Baghzouz, Y. 2002. Development of a hydrogen engine for a hybrid electric bus. *SAE Technical Paper No. 2002-01-1085*.
- Finol, C.A. and Robinson, K. 2006. Thermal modelling of modern engines: a review of empirical correlations to estimate the in-cylinder heat transfer coefficient. *Proceedings of the Institution of Mechanical Engineers, Part D: Journal of Automobile Engineering*, **220**(121): 765-1781.
- Finol Parra, C.A. 2008. *Heat transfer investigations in a modern diesel engine*. Ph. D. Thesis, Department of Mechanical Engineering, University of Bath, UK.
- Finol, C.A. and Robinson, K. 2011. Thermal modelling of modern diesel engines: proposal of a new heat transfer coefficient correlation. *Proceedings of the Institution of Mechanical Engineers, Part D: Journal of Automobile Engineering*, **225**, online 18 July 2011.

- Gadallah, A. H., Elshenawy, A. E., Elzahaby, A. M., El-Salmawy, H.A. and Bawady, A. H. 2009. Effect of in-cylinder water injection strategies on performance and emissions of a hydrogen fuelled direct injection engine. *SAE Technical Paper No.* 2009-01-1925.
- Galindo, J., Luján, J., Serrano, J., Dolz, V. and Guilain, S. 2006. Description of a heat transfer model suitable to calculate transient processes of turbocharged diesel engines with one-dimensional gas-dynamic codes. *Applied Thermal Engineering*. **26**(1): 66-76.
- Gamma Technologies, 2004 GT-Power User Manual. Gamma Technologies, Inc.
- Grabner, P., Eichlseder, H., Gerbig, F. and Gerke, U. 2006. Optimisation of a hydrogen internal combustion engine with inner mixture formation. *First International Symposium on Hydrogen Internal Combustion Engines*, Graz University of Technology, Austria.
- Grief, R., Namba, T. and Nikanham, M. 1979. Heat transfer during piston compression including side wall and convection effects. *International Journal of Heat and Mass Transfer*. **22**(6): 901-997.
- Guezennec, Y. G. and Hamama, W. 1999. Two zone heat release analysis of combustion data and calibration of heat transfer correlation in an internal combustion engine. *SAE Technical Paper No.* 1999-01-0218.
- Halmari, J. J. 2005. *Computer simulation of a hydrogen fueled internal combustion engine*. M.Sc. Thesis. Mechanical engineering department. Texas Technical University, USA.
- Han, S. B., Chung, Y. J. and Lee, S. 1997. Empirical formula for instantaneous heat transfer coefficient in spark ignition engine. *SAE Technical Paper No.* 972995.
- Han, Z. and Reitz, R. D. 1997. A temperature wall function formulation for variable-density turbulent flows with application to engine convective heat transfer modeling. *International Journal of Heat and Mass Transfer*. **40**(3): 613-625.
- He, X. 2001. *Development and validation of a hybrid electric vehicle with hydrogen internal combustion engine*. Ph.D. Thesis. Texas Technical University, USA.
- Heffel, J. W. 2003. NO_x emission reduction in a hydrogen fueled internal combustion engine at 3000 rpm using exhaust gas recirculation. *International Journal of Hydrogen Energy*. **28**(11): 1258-1292.
- Heywood, J. B. 1988. *Internal combustion engine fundamentals*. New York: McGraw-Hill.
- Hirt, C. W., Amsden, A. A. and Cook, J. L. 1974. Arbitrary Lagrangian-Eulerian computing method for all flow speeds. *Journal of Computational Physics*. **14**(3): 227-253.

- Holst, M. J. 1992. Notes on the KIVA-II software and chemically reactive fluid mechanics. *Lawrence Livermore National Laboratory*.
- Incropera, F. P. and DeWitt, D. P. 1990. Introduction to heat transfer. Second Ed. *John Wiley & Sons Inc.*
- Isshiki, N. and Nishiwaki, N. 1970. Study on laminar heat transfer of inside gas with cyclic pressure change on an inner wall of a cylinder head. *Proceedings of the Fourth International Heat Transfer Conference*. FC3.5:1-10.
- Jorach, R., Enderle, C. and Decker, R. 1997. Development of a low-NO_x truck hydrogen engine with high specific power output. *International Journal of Hydrogen Energy*. **22**(4): 423-427.
- Kahraman, E. 2005. *Analysis of a hydrogen fueled internal combustion engine*. M.Sc. Thesis. İzmir Institute of Technology, Turkey.
- Kahraman, E., Ozcanli, C. and Ozerdem, B. 2007. An experimental study on performance and emission characteristics of a hydrogen fuelled spark ignition engine. *International Journal of Hydrogen Energy*. **32**(12): 2066–2072.
- Karamangil, M. I., Kaynakli, O. and Surmen, A. 2006. Parametric investigation of cylinder and jacket side convective heat transfer coefficients of gasoline engines. *Energy Conversion and Management*. **47**(6): 800-816.
- Kim, Y. Y., Lee, J. T. and Caton, J. A. 2006. The development of a dual-Injection hydrogen-fueled engine with high power and high efficiency. *Journal of Engineering for Gas Turbines and Power, ASME*. **128**(1): 203-212.
- Knop, V., Benkenida, A., Jay, S. and Colin, O. 2008. Modelling of combustion and nitrogen oxide formation in hydrogen-fuelled internal combustion engines within a 3D CFD code. *International Journal of Hydrogen Energy*. **33**(19): 5083-5097.
- Krieger, R. B. and Borman, G. L. 1966. The computation of apparent heat release for internal combustion engines. *ASME Paper no: 66-WA/DGP-4*.
- Kumar, P., Franchek, M., Grigoriadis, K. and Balakotaiah, V. 2011. Fundamentals-based low-dimensional combustion modeling of spark-ignited internal combustion engines. *AIChE Journal*. **57**(9): 2472–2492.
- Launder, B. E. and Spalding, D. B. 1974. The numerical computation of turbulent flows. *Computer Methods in Applied Mechanics and Engineering*. **3**(2):269-89.
- Lee, S. J., Yi, H. S. and Kim, E. S. 1995. Combustion characteristics of intake port injection type hydrogen fueled engine. *International Journal of Hydrogen Energy*. **20**(4): 317-322.

- LeFeuvre, T., Myers, P. S. and Ueyehara, O. A. 1969. Experimental instantaneous heat fluxes in a diesel engine and their correlation. *SAE Technical Paper No. 690464*.
- Li, H. and Karim, G. A. 2006. Hydrogen fueled spark-ignition engines predictive and experimental performance. *Transactions of the ASME*. **128**(1): 230-236.
- Liu, X., Liu, F., Zhou, L., Sun, B. and Schock, H, 2008. Backfire predication in a manifold injection hydrogen internal combustion engine. *International Journal of Hydrogen Energy*. **33**(14): 3847- 3855.
- Liu, Y. and Reitz, R. D. 1997. Multidimensional modeling of engine combustion chamber surface temperatures. *SAE Technical Paper No.971593*.
- Lounici, M. S., Loubar, K., Balistrrou, M. and Tazerout, M. 2011. Investigation on heat transfer evaluation for a more efficient two-zone combustion model in the case of natural gas SI engines. *Applied Thermal Engineering*. **31**(2-3): 319-328.
- Ma, F., He, Y., Deng, J., Jiang, L., Naeve, N., Wang, M. and Chen, R. 2011. Idle characteristics of a hydrogen fueled SI engine. *International Journal of Hydrogen Energy*. **36**(7): 4454-4460.
- Ma, J., Su, Y., Zhou, Y. and Zhang, Z. 2003. Simulation and prediction on the performance of a vehicle's hydrogen engine. *International Journal of Hydrogen Energy*. **28**(1): 77-83.
- Marinov, N. M., Westbrook, C. K. and Pitz, W. J. 1995. Detailed and global chemical kinetics model for hydrogen. In: *Eighth International Symposium on Transport Properties*. San Francisco, USA, paper no. UCRL-JC-120677 CONF-9510158-1.
- Marquardt, D. W. 1963. An algorithm for least-squares estimation of nonlinear parameters. *Journal of the Society for Industrial and Applied Mathematics*. **11**(2): 431-441.
- Martyr, A. J. and Plint, M. A. 2007. *Engine Testing*. Third Ed. SAE international.
- Masood, M., Ishrat, M. M. and Reddy, A. S. 2007. Computational combustion and emission analysis of hydrogen-diesel blends with experimental verification. *International Journal of Hydrogen Energy*. **32**(13): 2539-2547.
- Mohammadi, A., Shioji, M., Nakai, Y., Ishikura, W. and Tabo, E. 2007. Performance and combustion characteristics of a direct injection SI hydrogen engine. *International Journal of Hydrogen Energy*. **32**(2): 296-304.
- Mohammadi, A., Yaghoubi, M. and Rashidi, M. 2008. Analysis of local convective heat transfer in a spark ignition engine. *International Communications in Heat and Mass Transfer*. **35**(2): 215–224.

- Mohammadi, A. and Yaghoubi, M. 2010. Estimation of instantaneous local heat transfer coefficient in spark-ignition engines. *International Journal of Thermal Sciences*, **49**(7): 1309-1317.
- Morel, T. and Keribar, R. 1985. A model for predicting spatially and time-resolved convective heat transfer in bowl-in-piston combustion chambers. *SAE Technical Paper No.850204*.
- Morel, T., Fort, E. and Blumerg, P. 1985. Effect of insulation strategy and design parameters on diesel heat rejection and performance. *SAE Technical Paper No.850506*.
- Mugele, M., Worret, R. and Spicher, U. 1999. Comparison of measured and predicted combustion characteristics using an improved quasi-dimensional model. *ICE99-Fourth International Conference on Internal Combustion Engines: Experiments and Modelling*, Capri, Naples, Italy, September 12-16, pp. 173-181.
- Natkin, R. J., Tang, X., Boyer, B., Oltmans, B., Denlinger, A. and Heffel, J. W. 2003. Hydrogen IC engine boosting performance and NO_x study, *SAE paper no. 2003-01-0631*.
- Nefischer, A., Hallmannsegger, M., Wimmer, A. and Priker, G. 2009. Application of a flow field based heat transfer model to hydrogen internal combustion engines. *SAE Technical Paper No. 2009-01-1423*.
- Nijeweme, D. J., Kok, J. B. W., Stone, C. R. and Wyszynski, L. 2001. Unsteady in-cylinder heat transfer in a spark ignition engine: experiments and modelling. *Proceedings of the Institution of Mechanical Engineering, Part D: J. Automobile Engineering*, **215**: 747-760.
- Nikuradse, J. 1937. Laws of flow in rough pipes. *NACA Tech. Mem.* 1292.
- Nishiwaki K. 1998. Modeling engine heat transfer and flame-wall interaction. In: *Proceedings of Fourth international symposium on diagnostics and modelling of combustion in internal combustion engines. (COMODIA 1998)*. Kyoto, Japan; July. Pp: 35-44.
- Oguri, T. 1960. On the coefficient of heat transfer between gases and cylinder walls of the spark-ignition engine. *JSME*. **3**(11): 363-369.
- Ollivier, E. 2006. Contribution to the characterization of heat transfer in spark ignition engines (in French). Application to knock detection. Ph.D. Thesis, ENSTIM de Nantes.
- O'Rourke, P. J. and Amsden, A. A. 1986. Implementation of a conjugate residual iteration in the KIVA computer program. *Los Alamos National Laboratory*. Report no. LA-10849-MS.

- Padiyar, S. 1985. Properties of hydrogen. In: *Proceedings of summer school of hydrogen energy*, IIT Madras, Chennai, India.
- Patankar, S. V. 1980. *Numerical heat transfer and fluid flow*. McGraw-Hill: New York.
- Polasek, M., Macek, J., Takats, M. and Vitek, O. 2002. Application of advanced simulation methods and their combination with experiments to modeling of hydrogen fueled engine emission potentials. *SAE Technical Paper No. 2002-01-0373*.
- Poulos, S. G. and Heywood, J. B. 1983. The effect of chamber geometry on spark-ignited engine combustion. *SAE Technical Paper No. 830334*.
- Pracht, W. E. 1975. Calculating three-dimensional fluid flows at all speeds with an Eulerian-Lagrangian computing mesh. *Journal of Computational Physics*. **17**(2): 132-159.
- Pulkrabek, W. W. 2003. *Engineering fundamentals of the internal combustion engine*. Second Ed. New Jersey: Prentice Hall.
- Rakopoulos, C. D., Kosmadakis, G. M. and Pariotis, E. G. 2010. Critical evaluation of current heat transfer models used in CFD in-cylinder engine simulations and establishment of a comprehensive wall-function formulation. *Applied Energy*. **87**(5): 1612–1630.
- Rassweiler, G. M. and Withrow, L. 1938. Motion pictures of engine flames correlated with pressure cards. *SAE Technical Paper No. 380139*.
- Ringler, J., Gerbig, F., Eichlseder, H. and Wallner, T. 2004. Insights into the development of a hydrogen combustion process with internal mixture formation. *Proceedings of the Sixth International Symposium on Internal Combustion Diagnostics*. Baden Baden Germany.
- Safari, H., Jazayeri, S.A. and Ebrahimi, R. 2009. Potentials of NO_x emission reduction methods in SI hydrogen engines- Simulation study. *International journal of Hydrogen Energy*. **34**(2): 1015-1025.
- Sanli, A., Sayin, C., Gumus, M., Kilicaslan, I. and Canakci, M. 2009. Numerical evaluation by models of load and spark timing effects on the in-cylinder heat transfer of a SI engine. *Numerical Heat Transfer*. **56**(5): 444-458.
- Schubert, C., Wimmer, A. and Chmela, F. 2005. Advanced heat transfer model for CI engines. *SAE Technical Paper No. 2005-01-0695*.
- Shayler, P. J., Chick, J. P. and Ma, T. 1997. Correlation of engine heat transfer for heat rejection and warm-up modelling. *SAE Technical Paper No. 971851*.
- Shudo, T. 2005. Thermophysical properties of working fluid and heat transfer in hydrogen. *JSME Transactions B*. **71**(702): 730-736.

- Shudo, T. 2007. Improving thermal efficiency by reducing cooling losses in hydrogen combustion engines. *International journal of Hydrogen Energy*. **32**(17): 4285-4293.
- Shudo, T. and Nabetani, S. 2001. Analysis of degree of constant volume and cooling loss in a hydrogen fuelled SI engine. *SAE Technical Paper No. 2001-01-3561*.
- Shudo, T. and Suzuki, H. 2002a. Applicability of heat transfer equations to hydrogen combustion. *JSAE Review*. **23**(3): 303-308.
- Shudo, T. and Suzuki, H. 2002b. New heat transfer equation applicable to hydrogen-fuelled engines. *ASME Fall Technical Conference*. New Orleans, Louisiana. Paper no. ICEF2002-515.
- Shudo, T. and Suzuki, H. 2002c. Heat transfer from burning gas to the cylinder wall in a hydrogen engine. *JSME*. **68**(673): 2650-2656.
- Shudo, T. and Tsuga, K. 2001. Analysis of direct injection SI stratified combustion in hydrogen lean mixture-combustion promotion and cooling loss by hydrogen. *International Journal of Automotive Technology*. **2**(3): 85-91.
- Shudo, T., Cheng, W.K., Kuninaga, T. and Hasegawa, T. 2003. Reduction of cooling loss in hydrogen combustion by direct injection stratified charge. *SAE Technical Paper No. 2003-01-3094*.
- Shudo, T., Futakuchi, T. and Nakajima, Y. 2000a. Thermal efficiency analysis in hydrogen premixed combustion engine. *JSME Review*. **21**(2): 177-182.
- Shudo, T., Tsuga, K. and Nakajima, Y. 2000b. Analysis of direct injection spark ignition combustion in hydrogen lean mixture. *Seoul 2000 FISITA World Automotive Congress* Paper no. F2000A085, June 12-15, Seoul, Korea.
- Shudo, T., Nabetani, S. and Nakajima, Y. 2001a. Analysis of the degree of constant volume and cooling loss in a spark ignition engine fuelled with hydrogen. *International Journal of Engine Research*. **2**(1): 81-92.
- Shudo, T., Nabetani, S. and Nakajima, Y. 2001b. Influence of specific heats on indicator diagram analysis in a hydrogen-fuelled SI engine. *JSAE Review*. **22**(2): 224-226.
- Sierens, R. and Verhelst, S. 2003. Influence of the injection parameters on the efficiency and power output of a hydrogen fueled engine. *Journal of Engineering for Gas Turbines and Power, ASME*. **125**(2): 444-450.
- Smith, J. R. and Aceves, S. M. 1997. Hybrid and conventional hydrogen engine vehicles that meet EZEVE emissions. *SAE Technical Paper No. 970290*.

- Soyhan, H. S., Yasar, H., Walmsley, H., Head, B., Kalghatgi, G. T. and Sorousbay, C. 2009. Evaluation of heat transfer correlations for HCCI engine modeling. *Applied Thermal Engineering*. **29**(2-3): 541–549.
- Stefaan, V., Roger, S. and Sebastian, V. 2005. A high speed single cylinder hydrogen fuelled internal combustion engine. *World Automotive Congress*, 23-27 May, Barcelona, Spain, pp. 1-10.
- Stockhausen, W. F., Natkin, R. J., Kabat, D. M., Reams, L., Tang, X. Hashemi, S., Szwabowski, S. J. and Zanardelli, V. P. 2002. Ford P2000 hydrogen engine design and vehicle development program. *SAE Technical Paper No. 2002-01-0240*.
- Stone, R. 1999. *Introduction to internal combustion engines*. Third Ed. MacMillan Publisher: Great Britain.
- Subramanian, V., Mallikarjuna, J. M. and Ramesh, A. 2005. Performance, emission and combustion characteristics of a hydrogen fuelled SI Engine: an experimental study. *SAE Technical Paper No. 2005-26-349*.
- Subramanian, V., Mallikarjuna, J. M. and Ramesh, A. 2006. Improvement of combustion stability and thermal efficiency of a hydrogen fuelled SI engine at low loads by throttling. *National Conference on Advances in Energy Research*. IIT Bombay, pp. 1-6.
- Subramanian, V. Mallikarjuna, J.M. and Ramesh, A. 2007. Effect of water injection and spark timing on the nitric oxide emission and combustion parameters of a hydrogen fuelled spark ignition engine. *International Journal of Hydrogen Energy*, **32**(9): 1159–1173.
- Suzuki, T., Oguri, Y. and Yoshida, M. 2000. Heat transfer in the internal combustion engines. *SAE Technical Paper No. 2000-01-0300*.
- Swain, M. R., Swain, M. N. and Adt, R. R. 1988. Considerations in the design of an inexpensive hydrogen-fueled engine. *SAE Technical Paper No. 881630*.
- Takats, M., Macek, J., Polasek, M., Kovar, Z., Beroun, S. and Schloz C. 1998. Hydrogen fueled reciprocating engine as an automotive prime mover. *FISITA World Automotive Congress*. Paris, France. Paper No. F98T/P693.
- Tang, X. G., Daniel, M. K., Robert, J. N., Stockhausen, W. F. and Heffel, J. 2002. Ford P2000 hydrogen engine dynamometer development. *SAE Technical Paper, No. 2002-01-0242*.
- Taylor, C. F. 1985. *The internal combustion engine in theory and practice*. Second Ed. revised volume1. MIT Press, Cambridge, Massachusetts.
- Taylor, C.F. and Toong, T.Y. 1957. Heat transfer in internal combustion engines. *ASME paper no. 57-HT-17*.

- Torregrosa, A.J., Olmeda, P.C. and Romero, C.A. 2008. Revising engine heat transfer. *Annals of Faculty Engineering-HUNEDOARA-International Journal of Engineering*. **6**(3): 245-265.
- Van Leer, B. 1979. Towards the ultimate conservative difference scheme v. a second-order sequel to Godunov's method. *Journal of Computational Physics*. **32**(1):101-136.
- Verhelst, S. 2005. *A study of the combustion in hydrogen-fuelled internal combustion engines*. Ph.D. Thesis. Mechanical engineering department. Ghent University, Belgium.
- Verhelst, S. and Sierens, R. 2001a. Hydrogen engine-specific properties. *International Journal of Hydrogen Energy*. **26**(9): 377-382.
- Verhelst, S. and Sierens, R. 2003. A laminar burning velocity correlation for hydrogen/air mixtures valid at spark-ignition engine conditions. In: *Spring technical conference of the ASME internal combustion engine division*, paper no ICES2003-555, Salzburg, Austria, pp. 35-43.
- Verhelst, S., Sierens, R. and Verstraeten, A. 2006a. A critical review of experimental research on hydrogen fueled spark ignition engines. *SAE Technical Paper No. 2006-01-0430*.
- Verhelst, S., Sierens, R. and Verstraeten, A. 2006b. Calculation of the power cycle of hydrogen IC engine. *Sixteenth Worldwide Hydrogen Conference of Energy*, Lyon, France 13-16 June, pp. 1-9.
- Verhelst, S. and Sierens, R. 2007. A quasi-dimensional model for the power cycle of a hydrogen-fuelled ICE. *International Journal of Hydrogen Energy*. **32**(15): 3545-3554.
- Verhelst, S., Landtsheere, J. D., Smet, F. D., Trenson, A. and Sierens, R. 2008. Effects of supercharging, EGR and variable valve timing on power and emissions of hydrogen internal combustion engines. *SAE Technical Paper No. 2008-01-1033*.
- Verhelst, S. and Wallner, T. 2009. Hydrogen-fueled internal combustion engines. *Progress in Energy and Combustion Science*. **35**(6): 490-527.
- Verhelst, S., Demuynck, J., Sierens, R. and Huyskens, P. 2010. Impact of variable valve timing on power, emissions and backfire of a bi-fuel hydrogen/gasoline engine. *International Journal of Hydrogen Energy*. **35**(9): 4399-4408.
- Watson, N. and Janota, M. S. 1982. Turbo charging the internal combustion engine. *Macmillan Education Ltd*.
- Watson, H. C. and Milkins, E. F. 1978. Some problems and benefits from the hydrogen-fuelled spark ignition engine. *SAE Technical Paper No. 789212*.

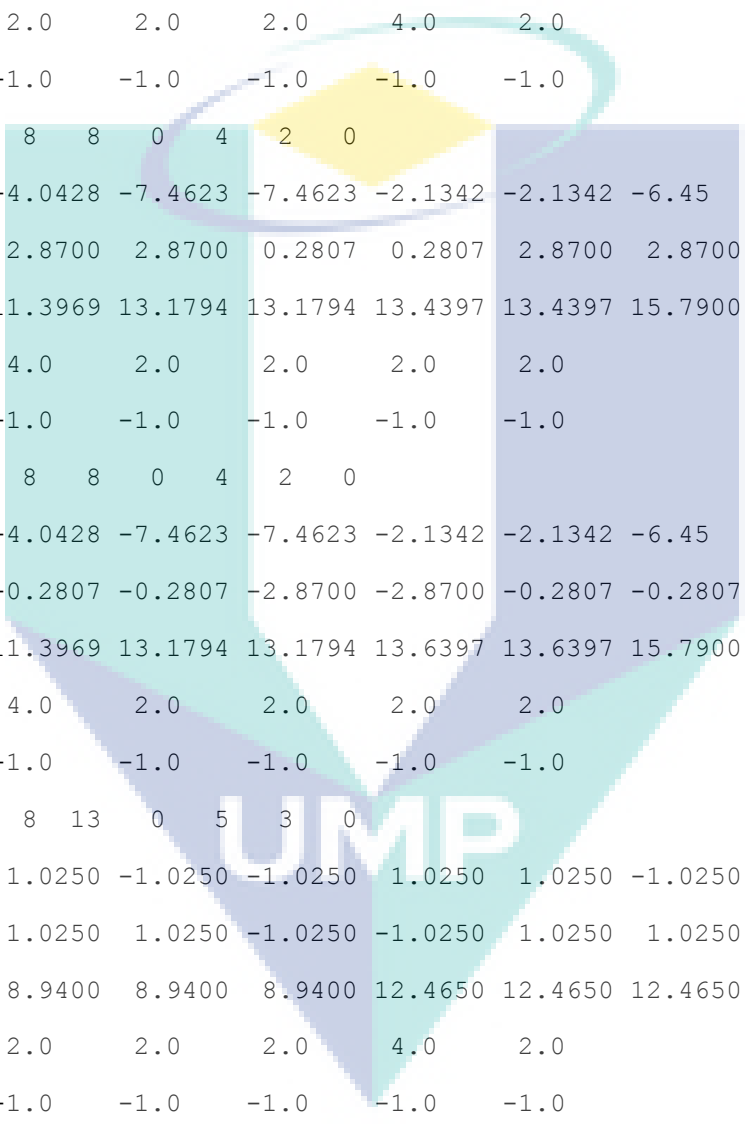
- Wei, S. W., Kim, Y. Y., Kim, H. J. and Lee, J. T. 2001. A study on transient heat transfer coefficient of in cylinder gas in the hydrogen fueled engine. *Journal of the Korean Hydrogen Energy Society*. **12**(4): 267-275.
- White, C. M., Steeper, R. R. and Lutz, A. E. 2006. The hydrogen-fueled internal combustion engine: a technical review. *International Journal of Hydrogen Energy*. **31**(10): 1292–1305.
- Wimmer, A., Wallner, T., Ringler, J. and Gerbig, F. 2005. H₂-direct injection- a highly promising combustion concept. *SAE Technical Paper No. 2005-01-0108*.
- Woschni, G. 1967. A universally applicable equation for the instantaneous heat transfer coefficient in the internal combustion engine. *SAE Technical Paper No. 670931*.
- Wu, Y. Y., Chen, B. C. and Hsieh, F. C. 2006. Heat transfer model for small-scale air-cooled spark-ignition four-stroke engines. *International Journal of Heat and Mass Transfer*. **49**(21-22): 3895–3905.
- Wu, Y. Y., Chen, B. C., Hsieh, F. C. and Ke, C. T. 2009. Heat transfer model for small-scale spark-ignition engines. *International Journal of Heat and Mass Transfer*. **52**(7-8): 1875–1886.
- Xin, J., Shih, S., Itano E. and Maeda, Y. 2003. Integration of 3D combustion simulations and conjugate heat transfer analysis to quantitatively evaluate component temperatures. *SAE Technical Paper No. 2003-01-3128*.
- Xin, Q. 2009. Theoretical analysis of internal combustion engine miscellaneous heat losses. *SAE Technical Paper No. 2009-01-2881*.
- Yamin, J. A. 2007. Heat losses minimization from hydrogen fueled 4-stroke spark ignition engines. *Journal of the Brazilian Society of Mechanical Sciences and Engineering*. **29**(1): 109-114.
- Yamin, J. A. and Hamdan, M. A. 2010. The performance of hydrogen-powered 4-stroke SI engine using locally designed fuel regulator. *Journal of the Brazilian Society of Mechanical Sciences and Engineering*. **32**(3): 195-199.
- Yang, J. and Martin, J. K. 1989. Approximate solution one-dimensional energy equation for transient, compressible, low Mach number turbulent boundary layer flows. *Journal of Heat Transfer*. **111**(3): 619-624.
- Yi, H. S., Lee, S. J. and Kim, E. S. 1996. Performance evaluation and emission characteristics of in-cylinder injection type hydrogen fueled engine. *International Journal of Hydrogen Energy*. **21**(7): 617-624.
- Yi, H. S., Min, K. and Kim, E. S. 2000. The optimised mixture formation for hydrogen fuelled engines. *International Journal of Hydrogen Energy*. **25**(7): 685-690.

APPENDIX A

IPREP FILE

K3PREP/ 4-valve pent-roof engine

```
bore      7.6
stroke    8.8
squish     0.115
thsect    360.0
nblocks   32
  1  30  30  20  0  2  1  0
  3.8000  3.8000 -3.8000 -3.8000  3.8000  3.8000 -3.8000 -3.8000
-3.8000  3.8000  3.8000 -3.8000 -3.8000  3.8000  3.8000 -3.8000
  0.0     0.0     0.0     0.0     8.8150  8.8150  8.8150  8.8150
  2.0     2.0     2.0     2.0     1.0     2.0
-1.0     -1.0    -1.0    -1.0     0.0    -1.0
  2  28  30  1  0  4  1  0
  3.5000  3.5000 -3.5000 -3.5000  3.5000  3.5000 -3.5000 -3.5000
-3.5000  3.5000  3.5000 -3.5000 -3.5000  3.5000  3.5000 -3.5000
  8.8150  8.8150  8.8150  8.8150  8.8900  8.8900  8.8900  8.8900
  2.0     2.0     2.0     2.0     4.0     4.0
-1.0     -1.0    -1.0    -1.0    -1.0    -1.0
  3  28  30  1  0  4  1  0
  3.5000  3.5000 -3.5000 -3.5000  3.5000  3.5000 -3.5000 -3.5000
-3.5000  3.5000  3.5000 -3.5000 -3.5000  3.5000  3.5000 -3.5000
  8.8900  8.8900  8.8900  8.8900  8.9400  8.9400  8.9400  8.9400
  2.0     2.0     2.0     2.0     4.0     2.0
-1.0     -1.0    -1.0    -1.0    -1.0    -1.0
  4   8   8  13  0  5  2  0
  1.3250  1.3250 -1.3250 -1.3250  1.3250  1.3250 -1.3250 -1.3250
-1.3250  1.3250  1.3250 -1.3250 -1.3250  1.3250  1.3250 -1.3250
  8.9400  8.9400  8.9400  8.9400 14.0900 14.0900 14.0900 14.0900
```



2.0	2.0	2.0	2.0	4.0	2.0		
-1.0	-1.0	-1.0	-1.0	-1.0	-1.0		
5	8	8	13	0	5	2	0
1.3250	1.3250	-1.3250	-1.3250	1.3250	1.3250	-1.3250	-1.3250
-1.3250	1.3250	1.3250	-1.3250	-1.3250	1.3250	1.3250	-1.3250
8.9400	8.9400	8.9400	8.9400	14.0900	14.0900	14.0900	14.0900
2.0	2.0	2.0	2.0	4.0	2.0		
-1.0	-1.0	-1.0	-1.0	-1.0	-1.0		
6	10	8	8	0	4	2	0
-4.0428	-4.0428	-7.4623	-7.4623	-2.1342	-2.1342	-6.45	-6.45
0.2807	2.8700	2.8700	0.2807	0.2807	2.8700	2.8700	0.2807
11.3969	11.3969	13.1794	13.1794	13.4397	13.4397	15.7900	15.7900
9.0	4.0	2.0	2.0	2.0	2.0		
-1.0	-1.0	-1.0	-1.0	-1.0	-1.0		
7	10	8	8	0	4	2	0
-4.0428	-4.0428	-7.4623	-7.4623	-2.1342	-2.1342	-6.45	-6.45
-2.8700	-0.2807	-0.2807	-2.8700	-2.8700	-0.2807	-0.2807	-2.8700
11.3969	11.3969	13.1794	13.1794	13.6397	13.6397	15.7900	15.7900
9.0	4.0	2.0	2.0	2.0	2.0		
-1.0	-1.0	-1.0	-1.0	-1.0	-1.0		
8	8	8	13	0	5	3	0
1.0250	1.0250	-1.0250	-1.0250	1.0250	1.0250	-1.0250	-1.0250
-1.0250	1.0250	1.0250	-1.0250	-1.0250	1.0250	1.0250	-1.0250
8.9400	8.9400	8.9400	8.9400	12.4650	12.4650	12.4650	12.4650
2.0	2.0	2.0	2.0	4.0	2.0		
-1.0	-1.0	-1.0	-1.0	-1.0	-1.0		
9	8	8	13	0	5	3	0
1.0250	1.0250	-1.0250	-1.0250	1.0250	1.0250	-1.0250	-1.0250
-1.0250	1.0250	1.0250	-1.0250	-1.0250	1.0250	1.0250	-1.0250
8.9400	8.9400	8.9400	8.9400	12.4650	12.4650	12.4650	12.4650
2.0	2.0	2.0	2.0	4.0	2.0		
-1.0	-1.0	-1.0	-1.0	-1.0	-1.0		

10	10	8	8	0	4	3	0
8.02	8.02	3.70	3.70	7.50	7.50	2.50	2.50
0.583	2.6240	2.6240	0.583	0.583	2.6240	2.6240	0.583
12.5361	12.1150	10.8850	10.8850	14.2150	14.2150	12.4650	12.4650
4.0	10.0	2.0	2.0	2.0	2.0		
-1.0	-1.0	-1.0	-1.0	-1.0	-1.0		
11	10	8	8	0	4	3	0
8.02	8.02	3.70	3.70	7.50	7.50	2.50	2.50
-2.6240	-0.583	-0.583	-2.6240	-2.6240	-0.583	-0.583	-2.6240
12.1150	12.5361	10.8850	10.8850	14.2150	14.2150	12.4650	12.4650
4.0	10.0	2.0	2.0	2.0	2.0		
-1.0	-1.0	-1.0	-1.0	-1.0	-1.0		
12	2	2	1	0	4	4	0
-0.2800	-0.2800	-0.7200	-0.7200	-0.2980	-0.2980	-0.7200	-0.7200
-0.2500	0.2500	0.1900	-0.1900	-0.2500	0.2500	0.1900	-0.1900
9.8600	9.8600	9.7200	9.7200	9.9100	9.9100	9.7700	9.7700
2.0	2.0	2.0	2.0	4.0	7.0		
-1.0	-1.0	-1.0	-1.0	-1.0	-1.0		
13	10	10	20	0	2	1	0
1.4500	1.4500	-1.4500	-1.4500	1.4500	1.4500	-1.4500	-1.4500
-1.4500	1.4500	1.4500	-1.4500	-1.4500	1.4500	1.4500	-1.4500
0.0	0.0	0.0	0.0	8.8150	8.8150	8.8150	8.8150
4.0	4.0	4.0	4.0	1.0	1.0		
-1.0	-1.0	-1.0	-1.0	0.0	1.0		
14	10	10	1	0	2	2	1
1.4500	1.4500	-1.4500	-1.4500	1.4500	1.4500	-1.4500	-1.4500
-1.4500	1.4500	1.4500	-1.4500	-1.4500	1.4500	1.4500	-1.4500
8.8150	8.8150	8.8150	8.8150	8.8900	8.8900	8.8900	8.8900
2.0	2.0	2.0	2.0	1.0	1.0		
-1.0	-1.0	-1.0	-1.0	1.0	2.0		
15	10	10	1	0	2	2	0
1.4500	1.4500	-1.4500	-1.4500	1.4500	1.4500	-1.4500	-1.4500

-1.4500	1.4500	1.4500	-1.4500	-1.4500	1.4500	1.4500	-1.4500
8.8900	8.8900	8.8900	8.8900	8.9400	8.9400	8.9400	8.9400
4.0	4.0	4.0	4.0	1.0	2.0		
-1.0	-1.0	-1.0	-1.0	2.0	-1.0		
16	8	8	20	0	2	1	0
1.2750	1.2750	-1.2750	-1.2750	1.2750	1.2750	-1.2750	-1.2750
-1.2750	1.2750	1.2750	-1.2750	-1.2750	1.2750	1.2750	-1.2750
0.0	0.0	0.0	0.0	8.8150	8.8150	8.8150	8.8150
4.0	4.0	4.0	4.0	1.0	1.0		
-1.0	-1.0	-1.0	-1.0	0.0	1.0		
17	8	8	1	0	2	2	1
1.2750	1.2750	-1.2750	-1.2750	1.2750	1.2750	-1.2750	-1.2750
-1.2750	1.2750	1.2750	-1.2750	-1.2750	1.2750	1.2750	-1.2750
8.8150	8.8150	8.8150	8.8150	8.8900	8.8900	8.8900	8.8900
2.0	2.0	2.0	2.0	1.0	1.0		
-1.0	-1.0	-1.0	-1.0	1.0	2.0		
18	8	8	1	0	2	2	0
1.2750	1.2750	-1.2750	-1.2750	1.2750	1.2750	-1.2750	-1.2750
-1.2750	1.2750	1.2750	-1.2750	-1.2750	1.2750	1.2750	-1.2750
8.8900	8.8900	8.8900	8.8900	8.9400	8.9400	8.9400	8.9400
4.0	4.0	4.0	4.0	1.0	4.0		
-1.0	-1.0	-1.0	-1.0	2.0	-1.0		
19	2	2	20	0	2	1	0
0.3500	0.3500	-0.3500	-0.3500	0.3500	0.3500	-0.3500	-0.3500
-0.3500	0.3500	0.3500	-0.3500	-0.3500	0.3500	0.3500	-0.3500
0.0	0.0	0.0	0.0	8.8150	8.8150	8.8150	8.8150
4.0	4.0	4.0	4.0	1.0	1.0		
-1.0	-1.0	-1.0	-1.0	0.0	1.0		
20	2	2	1	0	2	2	1
0.3500	0.3500	-0.3500	-0.3500	0.3500	0.3500	-0.3500	-0.3500
-0.3500	0.3500	0.3500	-0.3500	-0.3500	0.3500	0.3500	-0.3500
8.8150	8.8150	8.8150	8.8150	8.8900	8.8900	8.8900	8.8900

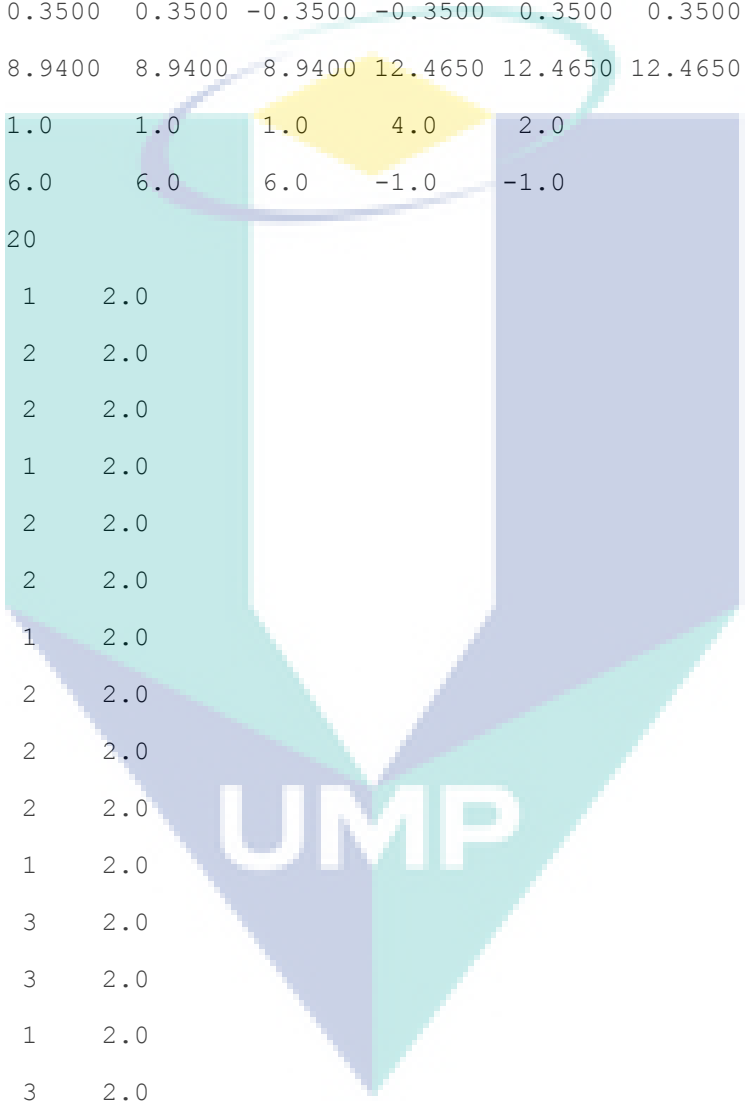
2.0	2.0	2.0	2.0	1.0	1.0		
-1.0	-1.0	-1.0	-1.0	1.0	2.0		
21	2	2	1	0	2	2	1
0.3500	0.3500	-0.3500	-0.3500	0.3500	0.3500	-0.3500	-0.3500
-0.3500	0.3500	0.3500	-0.3500	-0.3500	0.3500	0.3500	-0.3500
8.8900	8.8900	8.8900	8.8900	8.9400	8.9400	8.9400	8.9400
1.0	1.0	1.0	1.0	1.0	4.0		
2.0	2.0	2.0	2.0	2.0	-1.0		
22	2	2	13	0	5	2	1
0.3500	0.3500	-0.3500	-0.3500	0.3500	0.3500	-0.3500	-0.3500
-0.3500	0.3500	0.3500	-0.3500	-0.3500	0.3500	0.3500	-0.3500
8.9400	8.9400	8.9400	8.9400	14.0900	14.0900	14.0900	14.0900
1.0	1.0	1.0	1.0	4.0	2.0		
2.0	2.0	2.0	2.0	-1.0	-1.0		
23	10	10	20	0	2	1	0
1.2500	1.2500	-1.2500	-1.2500	1.2500	1.2500	-1.2500	-1.2500
-1.2500	1.2500	1.2500	-1.2500	-1.2500	1.2500	1.2500	-1.2500
0.0	0.0	0.0	0.0	8.8150	8.8150	8.8150	8.8150
4.0	4.0	4.0	4.0	1.0	1.0		
-1.0	-1.0	-1.0	-1.0	0.0	5.0		
24	10	10	1	0	2	3	1
1.2500	1.2500	-1.2500	-1.2500	1.2500	1.2500	-1.2500	-1.2500
-1.2500	1.2500	1.2500	-1.2500	-1.2500	1.2500	1.2500	-1.2500
8.8150	8.8150	8.8150	8.8150	8.8900	8.8900	8.8900	8.8900
2.0	2.0	2.0	2.0	1.0	1.0		
-1.0	-1.0	-1.0	-1.0	5.0	6.0		
25	10	10	1	0	2	3	0
1.2500	1.2500	-1.2500	-1.2500	1.2500	1.2500	-1.2500	-1.2500
-1.2500	1.2500	1.2500	-1.2500	-1.2500	1.2500	1.2500	-1.2500
8.8900	8.8900	8.8900	8.8900	8.9400	8.9400	8.9400	8.9400
4.0	4.0	4.0	4.0	1.0	2.0		
-1.0	-1.0	-1.0	-1.0	6.0	-1.0		

26	8	8	20	0	2	1	0
1.0250	1.0250	-1.0250	-1.0250	1.0250	1.0250	-1.0250	-1.0250
-1.0250	1.0250	1.0250	-1.0250	-1.0250	1.0250	1.0250	-1.0250
0.0	0.0	0.0	0.0	8.8150	8.8150	8.8150	8.8150
4.0	4.0	4.0	4.0	1.0	1.0		
-1.0	-1.0	-1.0	-1.0	0.0	5.0		
27	8	8	1	0	2	3	1
1.0250	1.0250	-1.0250	-1.0250	1.0250	1.0250	-1.0250	-1.0250
-1.0250	1.0250	1.0250	-1.0250	-1.0250	1.0250	1.0250	-1.0250
8.8150	8.8150	8.8150	8.8150	8.8900	8.8900	8.8900	8.8900
2.0	2.0	2.0	2.0	1.0	1.0		
-1.0	-1.0	-1.0	-1.0	5.0	6.0		
28	8	8	1	0	2	3	0
1.0250	1.0250	-1.0250	-1.0250	1.0250	1.0250	-1.0250	-1.0250
-1.0250	1.0250	1.0250	-1.0250	-1.0250	1.0250	1.0250	-1.0250
8.8900	8.8900	8.8900	8.8900	8.9400	8.9400	8.9400	8.9400
4.0	4.0	4.0	4.0	1.0	4.0		
-1.0	-1.0	-1.0	-1.0	6.0	-1.0		
29	2	2	20	0	2	1	0
0.3500	0.3500	-0.3500	-0.3500	0.3500	0.3500	-0.3500	-0.3500
-0.3500	0.3500	0.3500	-0.3500	-0.3500	0.3500	0.3500	-0.3500
0.0	0.0	0.0	0.0	8.8150	8.8150	8.8150	8.8150
4.0	4.0	4.0	4.0	1.0	1.0		
-1.0	-1.0	-1.0	-1.0	0.0	5.0		
30	2	2	1	0	2	3	1
0.3500	0.3500	-0.3500	-0.3500	0.3500	0.3500	-0.3500	-0.3500
-0.3500	0.3500	0.3500	-0.3500	-0.3500	0.3500	0.3500	-0.3500
8.8150	8.8150	8.8150	8.8150	8.8900	8.8900	8.8900	8.8900
2.0	2.0	2.0	2.0	1.0	1.0		
-1.0	-1.0	-1.0	-1.0	5.0	6.0		
31	2	2	1	0	2	3	1
0.3500	0.3500	-0.3500	-0.3500	0.3500	0.3500	-0.3500	-0.3500

```

-0.3500  0.3500  0.3500 -0.3500 -0.3500  0.3500  0.3500 -0.3500
 8.8900  8.8900  8.8900  8.8900  8.9400  8.9400  8.9400  8.9400
 1.0      1.0      1.0      1.0      1.0      4.0
 6.0      6.0      6.0      6.0      6.0     -1.0
32  2    2  13    0    5    3    1
 0.3500  0.3500 -0.3500 -0.3500  0.3500  0.3500 -0.3500 -0.3500
-0.3500  0.3500  0.3500 -0.3500 -0.3500  0.3500  0.3500 -0.3500
 8.9400  8.9400  8.9400  8.9400 12.4650 12.4650 12.4650 12.4650
 1.0      1.0      1.0      1.0      4.0      2.0
 6.0      6.0      6.0      6.0     -1.0     -1.0
ncopy    20
13  33    1    2.0
14  34    2    2.0
15  35    2    2.0
16  36    1    2.0
17  37    2    2.0
18  38    2    2.0
19  39    1    2.0
20  40    2    2.0
21  41    2    2.0
22  42    2    2.0
23  43    1    2.0
24  44    3    2.0
25  45    3    2.0
26  46    1    2.0
27  47    3    2.0
28  48    3    2.0
29  49    1    2.0
30  50    3    2.0
31  51    3    2.0
32  52    3    2.0
tiltflag    4

```



```

2  2  -3.80    0.0    8.814
2  3   0.0    +3.80    8.814
3  2  -3.80    0.0    8.814
3  3   0.0    +3.80    8.814

pentflag    3

1 16 20
2 15 19
3 15 19

wedgflag    0
translate   44

4    -1.42    1.55    0.0
5    -1.42   -1.55    0.0
8     +1.66    1.60    0.0
9     +1.66   -1.60    0.0
13   -1.42    1.55    0.0
14   -1.42    1.55    0.0
15   -1.42    1.55    0.0
16   -1.42    1.55    0.0
17   -1.42    1.55    0.0
18   -1.42    1.55    0.0
19   -1.42    1.55    0.0
20   -1.42    1.55    0.0
21   -1.42    1.55    0.0
22   -1.42    1.55    0.0
23    +1.66    1.60    0.0
24    +1.66    1.60    0.0
25    +1.66    1.60    0.0
26    +1.66    1.60    0.0
27    +1.66    1.60    0.0
28    +1.66    1.60    0.0
29    +1.66    1.60    0.0
30    +1.66    1.60    0.0

```

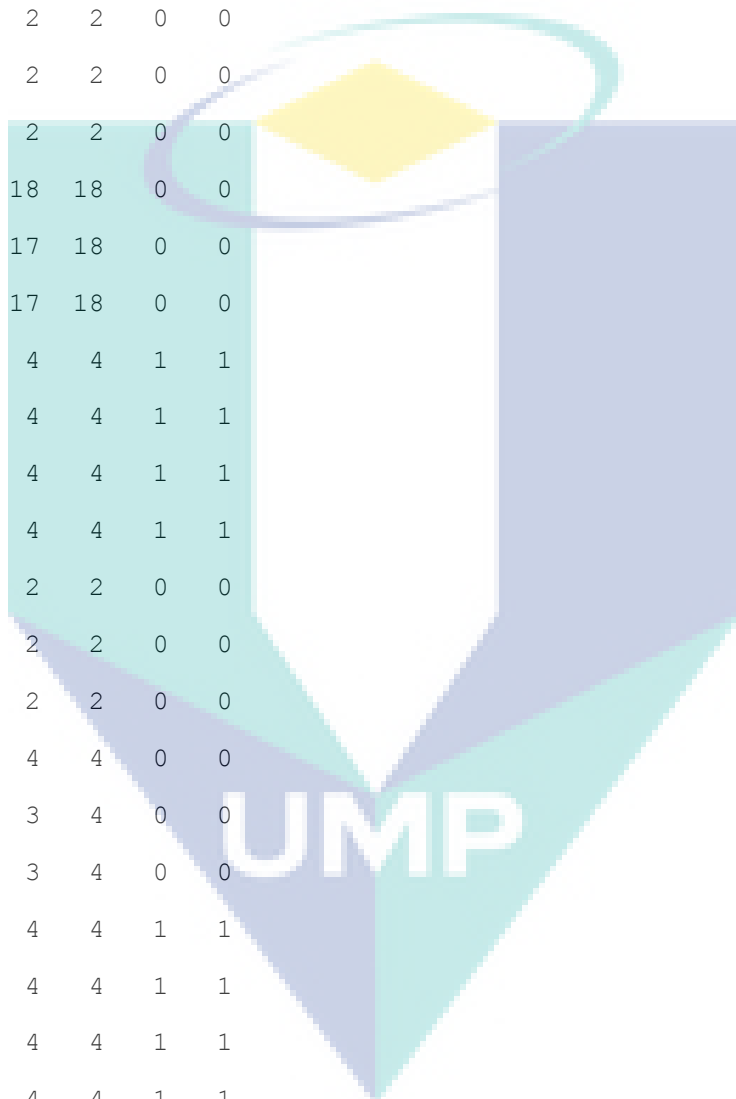
31	+1.66	1.60	0.0
32	+1.66	1.60	0.0
33	-1.42	-1.55	0.0
34	-1.42	-1.55	0.0
35	-1.42	-1.55	0.0
36	-1.42	-1.55	0.0
37	-1.42	-1.55	0.0
38	-1.42	-1.55	0.0
39	-1.42	-1.55	0.0
40	-1.42	-1.55	0.0
41	-1.42	-1.55	0.0
42	-1.42	-1.55	0.0
43	+1.66	-1.60	0.0
44	+1.66	-1.60	0.0
45	+1.66	-1.60	0.0
46	+1.66	-1.60	0.0
47	+1.66	-1.60	0.0
48	+1.66	-1.60	0.0
49	+1.66	-1.60	0.0
50	+1.66	-1.60	0.0
51	+1.66	-1.60	0.0
52	+1.66	-1.60	0.0

nlocxy 0

reshape 40

19	16	4	4	1	1
20	17	4	4	1	1
21	18	4	4	1	1
22	4	4	4	1	1
16	13	2	2	0	0
17	14	2	2	0	0
18	15	2	2	0	0
13	1	4	18	0	0

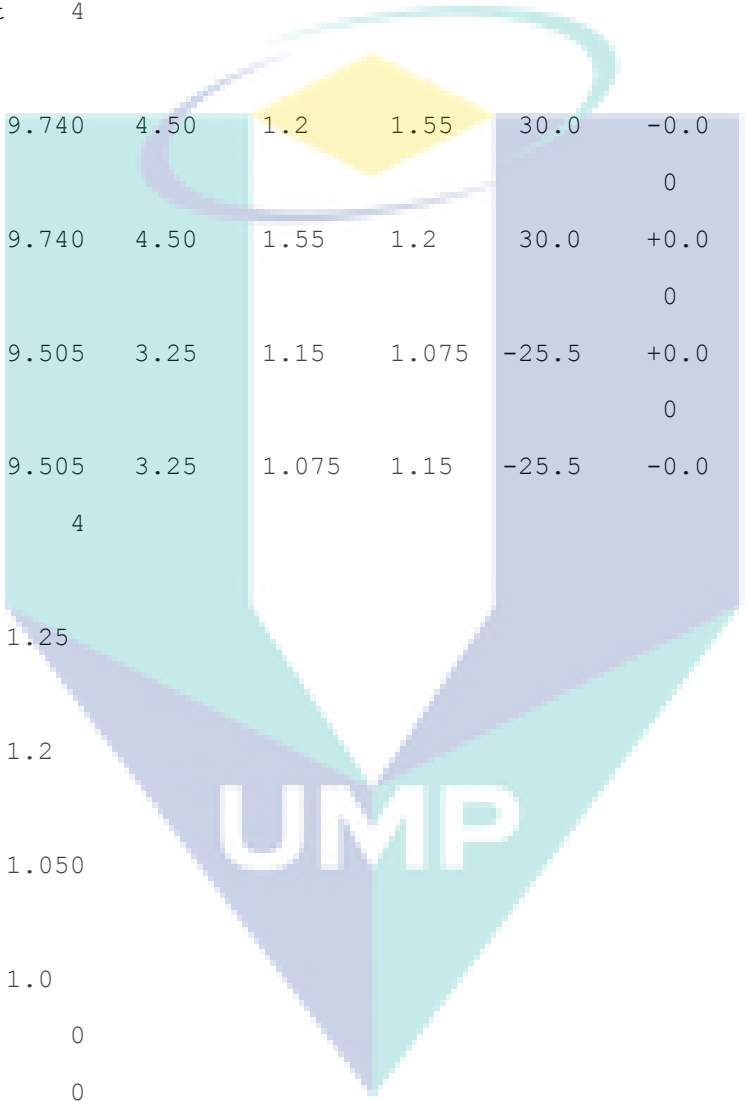
14	2	3	18	0	0
15	3	3	18	0	0
29	26	4	4	1	1
30	27	4	4	1	1
31	28	4	4	1	1
32	8	4	4	1	1
26	23	2	2	0	0
27	24	2	2	0	0
28	25	2	2	0	0
23	1	18	18	0	0
24	2	17	18	0	0
25	3	17	18	0	0
39	36	4	4	1	1
40	37	4	4	1	1
41	38	4	4	1	1
42	5	4	4	1	1
36	33	2	2	0	0
37	34	2	2	0	0
38	35	2	2	0	0
33	1	4	4	0	0
34	2	3	4	0	0
35	3	3	4	0	0
49	46	4	4	1	1
50	47	4	4	1	1
51	48	4	4	1	1
52	9	4	4	1	1
46	43	2	2	0	0
47	44	2	2	0	0
48	45	2	2	0	0
43	1	18	4	0	0
44	2	17	4	0	0
45	3	17	4	0	0



```

straightx0    0
straighty0    1
npentxy       2
  1   2   1   0
  1   3   1   0
nvguide       0
nvalvport     4
  4
-4.40  9.740  4.50  1.2   1.55  30.0  -0.0
  5
-4.40  9.740  4.50  1.55  1.2   30.0  +0.0
  8
+3.65  9.505  3.25  1.15  1.075 -25.5  +0.0
  9
+3.65  9.505  3.25  1.075  1.15 -25.5  -0.0
nrunner       4
  6   4
  1.2  1.25
  7   5
  1.25  1.2
 10   8
  1.0  1.050
 11   9
  1.050  1.0
nsiamese      0
nround        0
  npatch     11
  2   5   1   2   1   1
  3   5   2   1   1   2
  4   5   3   4  19   3
  5   5   3   4   5   3
  8   5   3  18  19   3

```



```

9   5   3  18   5   3
6   2   4   1   6   6
7   2   5   1   6   7
10  1   8   1   6  10
11  1   9   1   6  11
12  5   3  12  15   3

```

```
nrelaxb    0
```

```
nprovtop   4
```

```

2   1   2  13  14
-1.5135  1.5614  1.3250
0.35    1.0
0.36    0.89
0.38    0.80
0.40    0.752
0.45    0.665
0.50    0.60
0.55    0.545
0.60    0.50
0.65    0.47
0.70    0.445
0.75    0.42
0.80    0.40
1.25    0.15
1.3250  0.0
4   1   2  13  14
-1.5135 -1.5363  1.3250

```

```
0.35    1.0
```

```
0.36    0.89
```

```
0.38    0.80
```

```
0.40    0.752
```

```
0.45    0.665
```

```
0.50    0.60
```



UMP

0.55 0.545

0.60 0.50

0.65 0.47

0.70 0.445

0.75 0.42

0.80 0.40

1.25 0.15

1.3250 0.0

6 1 2 13 13

1.7201 1.6218 1.2750

0.35 1.1

0.40 0.95

0.45 0.82

0.50 0.73

0.55 0.61

0.62 0.51

0.76 0.44

0.89 0.38

1.0 0.33

1.05 0.29

1.13 0.26

1.20 0.22

1.2750 0.0

8 1 2 13 13

1.7201 -1.5816 1.2750

0.35 1.1

0.40 0.95

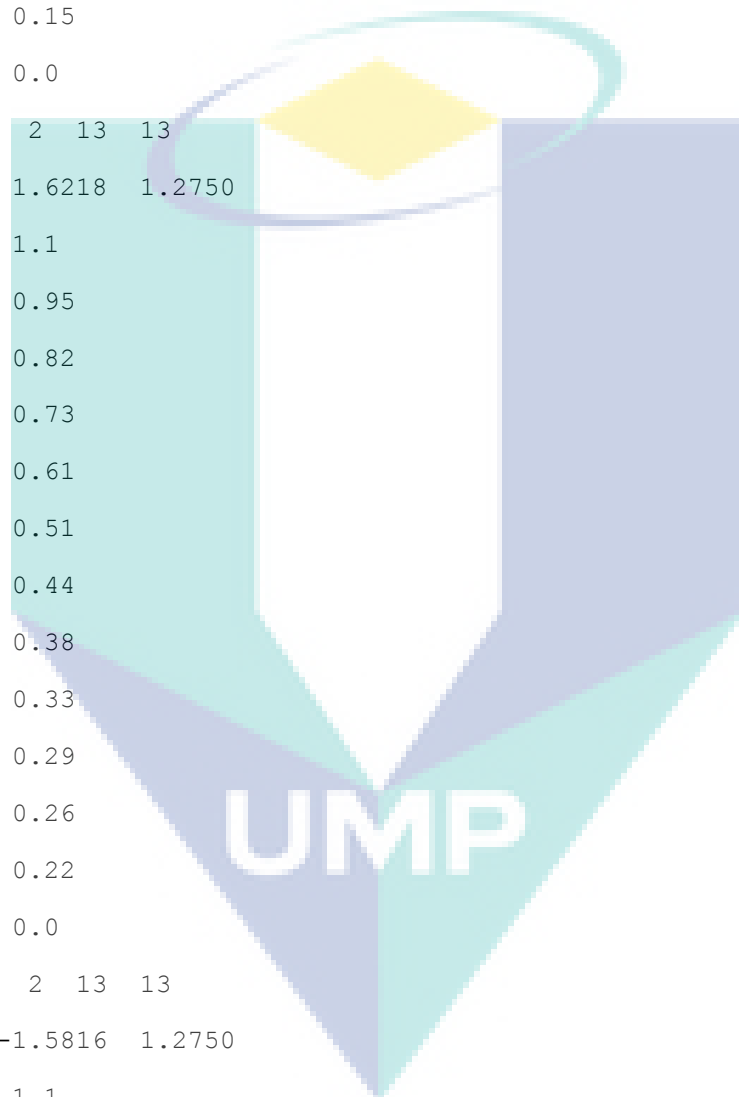
0.45 0.82

0.50 0.73

0.55 0.61

0.62 0.51

0.76 0.44



0.89 0.38
1.0 0.33
1.05 0.29
1.13 0.26
1.20 0.22
1.2750 0.0

nprovfce 0

nzcylwall 21

0.0

0.7385

1.3771

2.1156

2.7542

3.3927

4.0313

4.6698

5.3083

5.9469

6.5854

7.2240

7.8625

7.99234

8.18218

8.34202

8.50186

8.6617

8.73833

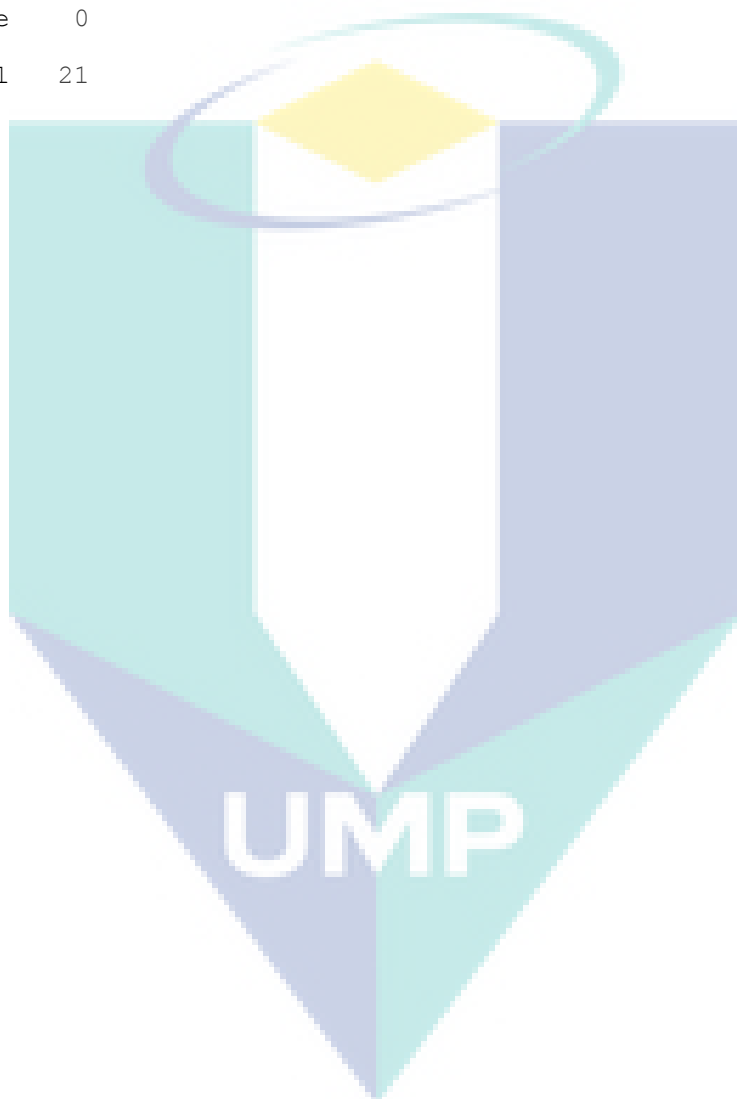
8.77666

8.815

tilt 2

4

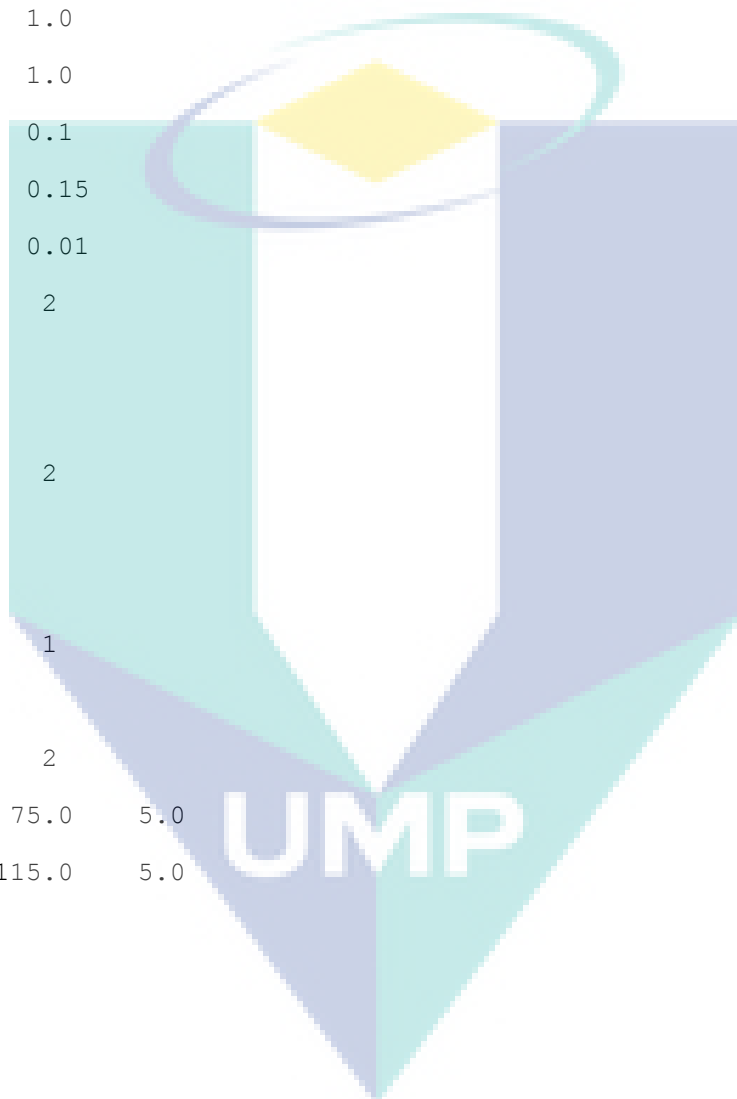
3 +3.10 8.815 +19.0



```

    2  -3.10  8.815  -18.0
ndish      1
0.49    1.95    1.890
nscallop   0
xoffset    0.0
yoffset    0.0
write17    1.0
plotmesh   1.0
xband      0.1
yband      0.15
zband      0.01
nxplots    2
-2.00
+2.50
nyplots    2
0.0
1.95
nzplots    1
0.0
nvhide     2
45.0    75.0    5.0
225.0   115.0   5.0

```



APPENDIX B

CALIBRATION AND TESTING PROCEDURE

B.1 CALIBRATION

To ensure the accuracy in the data the calibration process is used. In the following experiment, routine calibration was mainly done to the dynamometer, the pressure data acquisition system, the injector with the ECU system and the exhaust gas analyzer.

B.1.1 Dynamometer

The dynamometer was calibrated using calibrated weights as reference. The weights are put on one side of dynamometer and the reading is noted down from the control panel. After every reading the weights are increased in a sequential manner as shown in the Table B.1. When the dynamometer achieves its maximum reading (i.e. 48 Nm) weights are unloaded. The reading on the control panel should be zero when all the loads are removed. Same procedure is repeated for other arm of dynamometer.

Table B.1: Load Sequence for Dynamometer Calibration Process

No	Weight (kg)	Torque (N.m)
1	1	4
2	2	8
3	5	20
4	10	40
5	12	48

B.1.2 Pressure Data Acquisition Systems

Pressure data acquisition system is calibrated by using pressure testing device for engine. The system for the acquisition of in-cylinder pressure is composed of:

- i. Piezo electric cylinder pressure sensor- AVL QH32D, gain 25.28 pc/bar range 0-200bar
- ii. Charge amplifier- AVL3066AO
- iii. Shaft position encoder-AVL364C

The procedure for pressure sensor calibration was:

- i. Turn-on all systems
- ii. Unplug the spark plug from its position
- iii. Install the manual pressure testing device on the spark position
- iv. Motor the engine in a low rpm condition (<300 rpm)
- v. Measure the reading by data acquisition systems
- vi. Compare both results from manual pressure device and pressure sensor reading

The maximum pressure was compared using this procedure. The manual pressure reading device showed pressure gauge reading. If the pressure sensors shows the same reading with pressure gauge, than in order to get absolute pressure reading, the whole pressure sensor reading need to be added by 1atm.

B.1.3 Fuel Injector

Initially, the injector and the ECU system had been developed for natural gas investigations. Therefore, the injector and the ECU have been calibrated for hydrogen fuel usage. This was to correct for the mass flow of fuel in relation to the injection duration. Water displacement method, as shown in Figure B.1, has been employed by (Abdullah, 2009) for that purpose. Basically, the injector has been designed to operate on the choked flow. Hence, the calibration can be done with outlet pressure in atmospheric conditions. Ten injections have been made at several injection durations. The mass of the water displaced has been weighed, and the volume has been calculated with the density of water assumed to be unity. So that, this volume was equal to the hydrogen volume. Hence, the mass of hydrogen per injection duration has been known. Figure B.2 displays, the calibration curve for the injector and the ECU system with hydrogen fuel.

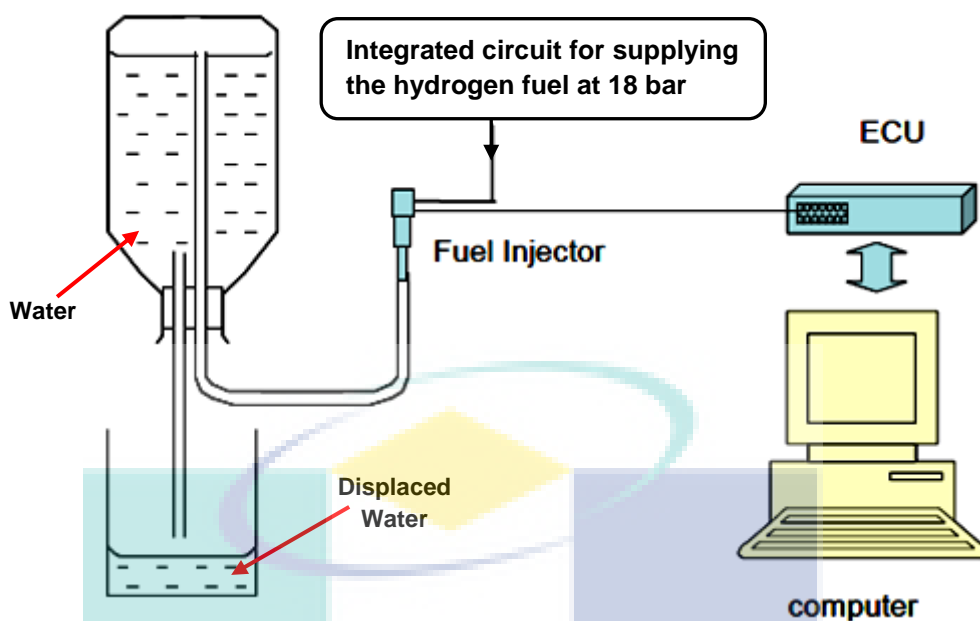


Figure B.1: The set up for calibration of the injector and the ECU system

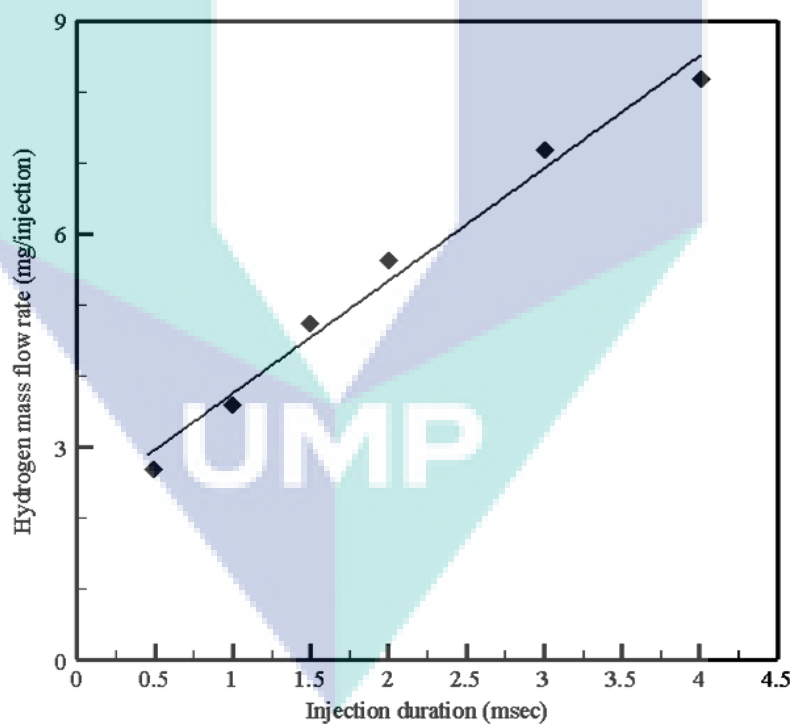


Figure B.2: Hydrogen mass flow rate against the injection duration for injector calibration test

Although the injector calibration corrected the amount of fuel delivered per injection as given by the ECU, more accurate measure of fuel flow was given by the micro-motion fuel flow meter. Thus, while this calibration helped the running of the test

by having ‘feed forward’ value of air fuel ratio and fuel delivery, the more accurate readings for analysis would be from mass flow meters of fuel and air. Another source of air fuel ratio measurement was from the oxygen gas analyzer.

B.1.4 Exhaust Gas Analyzer

Exhaust gas analyzer is calibrated before starting any experimental works. GASMET exhaust gas analyzer is already equipped with self calibration procedure. This calibration procedure is called zero calibration. Zero calibration is necessary to be done before starting the experiment. It measures the background spectrum for subsequent sample spectrum measurement. Zero calibration can only be valid if the instrument is in steady state condition with certain cell temperature and interferometer temperature.

For zero calibration, the sample must be filled with pure substance such as N_2 to make sure that there is no unwanted sample in the test cell. FTIR system will create background data base of the pure substance analysis as the base line for the measurement process. A typical background spectrum is presented in Figure B.3. The background spectrum represents the actual absolute intensity of infrared radiation that is transmitted through zero gas filled sample.

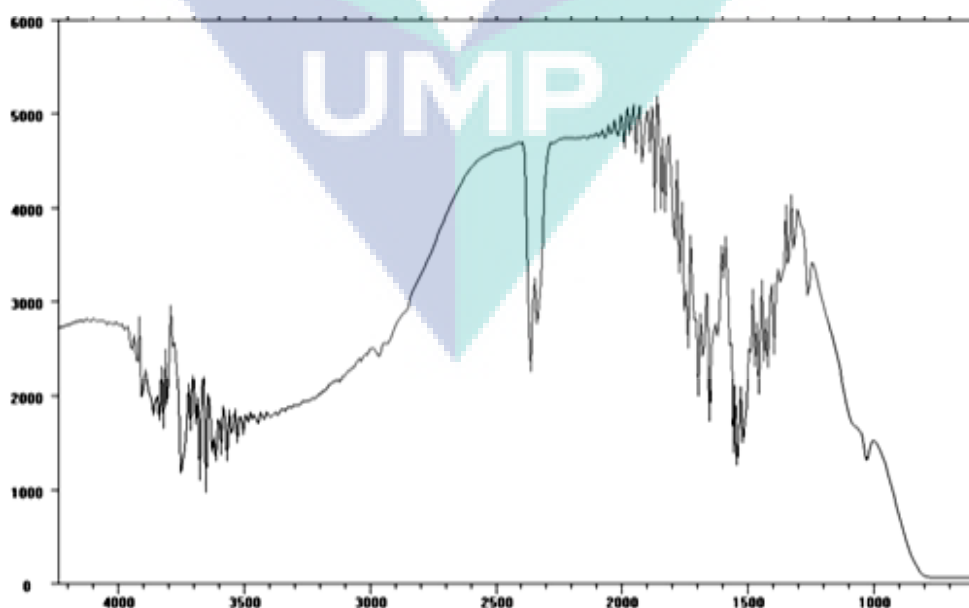


Figure B.3: Calibration spectrums on FTIR system for emission analysis

B.2 PROCEDURE FOR THE EXPERIMENTAL TESTING

Before conducting any test, the engine needs to be warming up. This is to make sure that the engine had reached operating temperatures and had stabilized. As hydrogen cost was substantially higher than other fuels, the engine warm up was done on natural gas. Since a common fuel line was used, this process would result in potential cross contamination of the fuel being tested. Experiments have been conducted after running the engine until it reached steady state, with oil temperature at 60°C and cooling water temperature 70°C. After that, the natural gas line has been turned off and replaced by opening the hydrogen fuel line. Then the data recording has been started after running the engine with hydrogen fuel.

All tests are run on MBT ignition timing in order to get comparable data. The research has mainly carried out at wide open throttled (WOT). The spark timing has been settled at MBT points for all tests. The following values have been used for start injection timing: 130, 150, -200 and 300 deg BTDC. It has been inspected the direct and partially direct injection as well the port injection schemes. Mixture strength has been varied to be including the rich, stoichiometric, lean and ultra-lean conditions. The mixture strength has been obtained by setting from the “Gasmeter gas analyzer” which contains an oxygen sensor. In terms of the engine speed, the tests comprise of 1800 and 3000 rpm were being utilized.

APPENDIX C

LIST OF PUBLICATIONS

C.1 INTERNATIONAL JOURNALS

1. M. M. Rahman, **Khalaf I. Hamada**, Rosli A. Bakar and M. A. Maleque. 2011. Heat transfer analysis inside exhaust port for a hydrogen fueled port injection engine. *Advanced Science Letters* (accepted), (SCI Indexed, IF=1.258).
2. M. M. Rahman, **Khalaf I. Hamada** and A. Rashid A. Aziz. 2011. Multidimensional computational modeling of direct injection for hydrogen fueled engine. *Advanced Science Letters* (accepted), (SCI Indexed, IF=1.258).
3. M. M. Rahman, **Khalaf I. Hamada** and K. Kadirgama. 2011. Heat transfer of intake port for hydrogen fueled port injection engine: A steady state approach. *International Journal of Physical Sciences*, **6**(16): 4036-4043 (SCI Indexed, IF=0.554).
4. M. M. Rahman, **Khalaf I. Hamada**, K. Kadirgama and Rosli A. Bakar. 2011. Cycle analysis of in-cylinder heat transfer characteristics for hydrogen fueled engine. *Scientific Research and Essays*, (in press) (SCI Indexed, IF=0.448).
5. **Khalaf I. Hamada**, M.M. Rahman and A. Rashid A. Aziz. 2011. Development of a computational fluid dynamics model for direct injection hydrogen fueled engine. *Applied Mechanics and Materials* (ISI and SCOPUS Indexed) (Accepted).
6. M.M. Rahman, **Khalaf I. Hamada**, M.M. Noor, K. Kadirgama, Rosli A. Bakar and M.F.A. Rahim. 2011. Heat transfer characteristics in exhaust port for hydrogen fueled port injection engine: a transient approach. *Advanced Materials Research*, **152-153**: 1909-1914. (Scopus Indexed).
7. M.M. Rahman, **Khalaf I. Hamada**, M.M. Noor, K. Kadirgama, M.A. Maleque and Rosli A. Bakar. 2010. Heat transfer characteristics of intake port for spark ignition engine: A comparative study. *Journal of Applied Sciences*, **10**(18): 2019-2016. (ISI Thomson and Scopus Indexed).
8. M.M. Rahman, **Khalaf I. Hamada**, M.M. Noor, Rosli A. bakar, K. Kadirgama and M.A. Maleque. 2010. In-cylinder heat transfer characteristics of hydrogen fueled engine: a steady state approach. *American Journal of Environmental Sciences*, **6**(2): 124-129. (Scopus Indexed).
9. M.M. Rahman, **Khalaf I. Hamada**, M.M. Noor, Rosli A. Bakar, K. Kadirgama and M.A. Maleque. 2010. Transient in-cylinder gas flow characteristics of single cylinder port injection hydrogen fueled engine. *American Journal of Applied Sciences*, **7**(10): 1364-1371, 2010. (ISI Thomson indexing/ Scopus Indexing).

10. **Khalaf I. Hamada**, M.M. Rahman, M A. Abdullah and A. Rashid A. Aziz. 2011. Time-averaged heat transfer correlation for DI hydrogen fueled engine. *International Journal of Hydrogen Energy*, (under review).
11. **Khalaf I. Hamada**, M.M. Rahman and A. Rashid A. Aziz. 2011. A critical review on engine heat transfer correlations and their applicability for a hydrogen fueled engine. *Thermal Science*, (under review).
12. **Khalaf I. Hamada**, M.M. Rahman, M A. Abdullah and A. Rashid A. Aziz. 2011. Influence of engine speed, equivalence ratio and injection timing on combustion characteristics of a direct injection hydrogen fueled engine. *Energy Conversion and Management*, (under review).
13. **Khalaf I. Hamada**, M.M. Rahman and A. Rashid A. Aziz. 2011. Computational modeling, validation and utilization for DI hydrogen fueled engine. *Thermal Science*, (under review).

C.2 INTERNATIONAL AND NATIONAL CONFERENCES

14. **Khalaf I. Hamada**, M.M. Rahman and A. Rashid A. Aziz. 2012. Injection timing optimization in term of in-cylinder heat transfer analysis for DI H₂ICE. *International Conference on Applications and Design in Mechanical Engineering (ICADME 2012)*, 27-28February 2012, Bayview Hotel, Penang, Malaysia. (accepted)
15. **Khalaf I. Hamada**, M.M. Rahman and A. Rashid A. Aziz. 2011. Experimental study on combustion analysis for a direct injection hydrogen fueled engine. *First International Conference on Mechanical Engineering Research (ICMER2011)*, 5-7 December, M.S. Garden Hotel, Kuantan, Malaysia, (accepted).
16. **Khalaf I. Hamada**, M.M. Rahman, Rosli A. Bakar and I. Ali, 2011. Trend of heat transfer parameters in the in-cylinder of hydrogen fueled engine. *Third International Conference on Mechanical and Electrical Technology. (ICMET2011)*, 26 to 27 August, Dalian, China, 681-687.
17. M. M. Rahman, **Khalaf I. Hamada**, M. M. Noor and K. Kadirgama, Effect of intake conditions on heat transfer characteristics for port injection hydrogen fueled engine, 2010 *International Conference on Mechanical and Electrical Technology (ICMET 2010)*, Singapore. September 10-12, 2010 (accepted) (IEEE Proceedings, ISI proceedings indexing), pp. 549-554.
18. **Khalaf I. Hamada**, M.M. Rahman, M.M.Noar, K. Kadirgama and Rosli A. Bakar. 2010. Influence of engine speed and injection timings on in-cylinder heat transfer for port injection hydrogen fueled engine. *Proceedings of Second National Conference in Mechanical Engineering for Research and Postgraduate Studies (2nd NCMER)*, pp. 183-194.
19. **Khalaf I. Hamada**, M.M. Rahman, M.M.Noar, K. Kadirgama and Rosli A. Bakar. 2010. Influence of engine speed and injection timings on in-cylinder heat transfer for port injection hydrogen fueled engine. *National Conference in Mechanical Engineering*

Research and Postgraduate Studies, 3-4December, Faculty of Mechanical Engineering, UMP Pekan, Kuantan, Pahang, Malaysia; pp. 183-194.

20. M.M. Rahman, **Khalaf I. Hamada**, M.M. Noor and K, Kadirgama, 2009. Influence of engine speed on heat transfer characteristics of port injection hydrogen fueled engine. *Eighth International Conference on Mechanical Engineering (ICME)* 2009, 26-28 December, BUET, Dhaka, Bangladesh, pp. 1-7.

